Stress-strain-sorption behaviour of coal matrix material exposed to CO_2

Sander Hol

UTRECHT STUDIES IN EARTH SCIENCES
Nº 008

Members of the dissertation committee:

Prof. dr. J. Bruining
Technische Universiteit Delft
Nederland

Prof. dr. S. Durucan
Imperial College London
United Kingdom

Prof. dr. D. Elsworth
Penn State University
United States of America

Prof. dr. S. Harpalani
Southern Illinois University
United States of America

Prof. dr. M. Mazzotti
Eidgenössische Technische Hochschule Zürich
Schweiz

The research reported in this thesis was carried out under the program Earth Materials: Properties and Processes of the Vening Meinisz Research School of Geodynamics (VMSG). The project was funded by Shell International.

The research was carried out at:
High Pressure and Temperature Laboratory
Faculty of Geosciences, Utrecht University
Budapestlaan 4, 3584 CD Utrecht
The Netherlands
www.uu.nl/geo/hpt

Printed by: Gildeprint, Enschede

Copyright © Sander Hol

All rights reserved. No parts of this publication may be reproduced in any form, by print or photo print, microfilm or other means, without written permission by the author.

ISBN/EAN: 978-90-6266-289-0

Stress-strain-sorption behaviour of coal matrix material exposed to CO_2

Spanning-vervorming-sorptiegedrag
van steenkool bij blootstelling aan CO_2
(met een samenvatting in het Nederlands)

Proefschrift
ter verkrijging van de graad van doctor aan de Universiteit Utrecht op gezag van de rector magnificus, prof.dr. G.J. van der Zwaan, ingevolge het besluit van het college voor promoties in het openbaar te verdedigen op vrijdag 2 december 2011 des middags te 12.45 uur
door

Sander Hol
geboren op 26 oktober 1979, te Amsterdam

Promotor: **Prof.dr. C.J. Spiers**
Co-promotor: **Dr. C.J. Peach**

Dit proefschrift werd mogelijk gemaakt met financiële steun van Shell

Music is not only entertainment,
instead, it is really creative power for us to survive this world.

Masaaki Suzuki,
Conductor

Chapter 1:
General introduction 9

1.1. Motivation for this study: Enhanced Coalbed Methane production 11
1.2. Nature and behaviour of coal-CO2 systems 14
1.3. Stress-strain-sorption behaviour of coal: an unsolved issue 17
1.4. Scope and aims of this thesis 19

Chapter 2:
Applied stress reduces the CO_2 sorption capacity of coal **21**

2.1. Introduction 23
2.2. Experimental method 26
2.3. Results 37
2.4. Discussion 41
2.5. Conclusion 52

Chapter 3:
Competition between adsorption-induced swelling and elastic compression of coal at CO_2 pressures up to 100 MPa **55**

3.1. Introduction 57
3.2. Experimental method 59
3.3. Results 71
3.4. Discussion 75
3.5. Conclusion 91

Chapter 4:
Direct determination of total CO_2 uptake by coal: A new technique compared to the manometric method **93**

4.1. Introduction 95
4.2. Experimental methods 97
4.3. Results 111
4.4. Discussion 116
4.5. Conclusions 129

Chapter 5:
Effect of 3-D stress state on adsorption of CO_2 by coal **131**

5.1. Introduction 133
5.2. Adsorption under stress-free conditions 136
5.3. Adsorption under stressed conditions 144
5.4. Experimental test of the effect of hydrostatic stress on adsorption of CO_2 by coal 154
5.5. Constitutive equation for stress-strain-sorption behaviour of coal 160
5.6. Conclusions 165

Chapter 6:
Microfracturing of coal due to interaction with CO_2 under unconfined conditions **167**

6.1. Introduction 169
6.2. Experimental methods 171
6.3. Results 179
6.4. Discussion 190
6.5. Conclusions 198

Chapter 7:
Conclusions and suggestions for future research **201**

7.1. Main conclusions 204
7.2. Implications for ECBM production 208
7.3. Suggestions for future research 210

Bibliography **213**

Summary **225**

Samenvatting voor een algemeen publiek **231**

Acknowledgements **237**

Curriculum Vitae **240**

1

General introduction

Sander Hol, Christopher J. Spiers

1.1. Motivation for this study: Enhanced Coalbed Methane production

Coal deposits form as the result of thermal degradation of buried peat bog or swamp vegetation. Prime factors controlling this process, known as "coalification", are the biological and chemical properties of the vegetation, the conditions under which degradation occurs (such as depth, temperature and water content), and the depositional history and architecture of the enclosing sedimentary sequence. As coalification proceeds, layers of accumulated material compact to form coal beds consisting of a dense structure of more or less homogeneous microscopic lithotypes. These microlithotypes are called "macerals" and are analogous to minerals in inorganic rocks (van Krevelen, 1993). Three maceral groups are defined, namely vitrinite, inertinite and liptinite, the origin of which is related to specific vegetation sources. Woody material (*e.g.* bark) gives rise to vitrinite, non-woody plant materials (*e.g.* spores) to liptinite, and oxidised material (*e.g.* burnt wood) to inertinite. The chemical composition of these maceral types shows slight differences in carbon, oxygen and hydrogen content (Bustin et al., 1985; van Krevelen, 1993). Aside from the maceral and preserved cellular microstructure exhibited by coals, coal beds generally show a well-developed mm- or cm-scale joint, or "cleat" system that transects the coal into cubic blocks of coal matrix material (Fig. 1) (Laubach et al., 1998).

Coalification results in an increase in carbon content of the deposits, which in turn is a measure of the degree of coalification, or "rank" of the coal (van Krevelen, 1993). The increase in carbon content is accompanied by the generation of substantial amounts of natural gas that generally consists of about 90 % CH_4 (Kim, 1973). Most of this natural gas migrates out of the internal porosity, through the cleat system, into the overlying strata to form conventional gas fields or else ultimately escapes to the atmosphere. However, a substantial amount generally remains in the coal seam where it formed, adsorbed in the internal nanoscale pores of the coal matrix and trapped as a free phase in larger pores (Rice et al., 1989; Strapoc et al., 2006)IJCG. This coalbed methane or CBM poses, on the one hand, the well-known "fire-damp" risk for mining operations (Beamish and Crosdale, 1998; Wold et al., 2008), but on the other hand offers a major unconventional gas resource. For example, in the United States, in 2000, CBM reserves were estimated to be 0.444 Tm^3, which represented 8.9 % of the total domestic gas reserves, while estimates of worldwide CBM reserves were in the range 84.38-262.21 Tm^3 (White et al., 2005).

In the period 1960-1980, major research efforts were undertaken to find ways of extracting CH_4 trapped in coal seams, with the aim both of improving mining safety (Cervik, 1969; Elder, 1969; Muchnik, 1974), and of commercially producing the trapped natural gas (Terry, 1978). In the United States, extraction of coalbed methane has proven economically feasible, and, since 1990, production has increased steadily, reaching ~2000 $BCF \cdot y^{-1}$ in recent years (USEIA, 2010). The commercial development

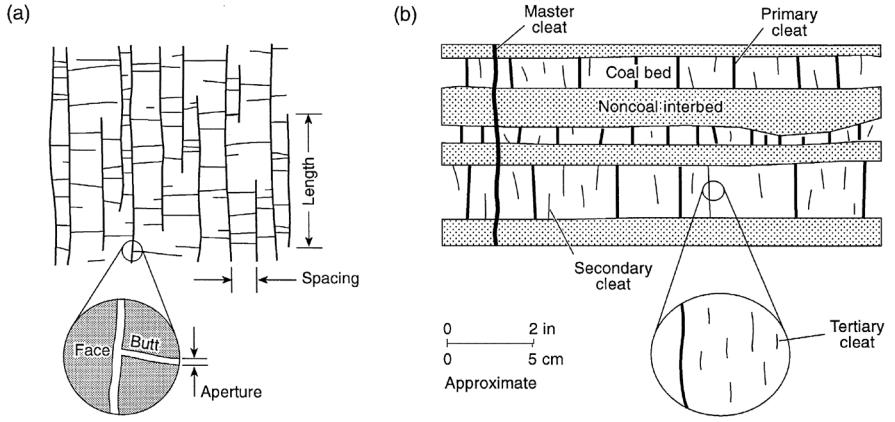

Fig. 1. Schematic diagram showing the typical structure displayed by coal beds, including the internal cleat-matrix system (taken from Laubach et al., 1998). a) Plan view of coal layer showing long face cleats interconnected by butt cleats. The aperture and connectivity of the cleats are important in determining the permeability of the coal seam as a whole, i.e. in determining the feasibility of injection and production of fluids. b) Cross-section of a coal layer, interbedded with other sediments. Several different scales of cleats are shown, namely the master, primary, and secondary cleats.

of CBM plays has also proven modestly feasible in other countries such as Australia, Canada and Russia. Despite this success, CBM production is usually limited to only 50 % of the estimated reserves (Rice et al., 1993), leaving large quantities of CH_4 adsorbed in the coal seams. In many fields, CBM has not been successful at all (Murray, 1996).

These difficulties with CBM production have driven other development. In practice, experiments performed on crushed coal (Every and Dell'osso Jr., 1972) and coal cores (Fulton et al., 1980; Reznik et al., 1984), have shown that CO_2 can displace CH_4 from coal material. This has led to the concept of Enhanced Coalbed Methane production (ECBM), which involves injection of preferentially sorbing CO_2 into the target coal seam, coupled with recovery of the desorbed CH_4 (Puri and Yee, 1990; Reeves, 2001; White et al., 2005). ECBM thus offers not only a promising way of producing CH_4 from coalbeds but also a potential means of geologically storing CO_2, and hence reducing CO_2 emissions (White et al., 2005). This is particularly interesting in view of the fact that the CO_2 adsorption potential of coal is approximately two times the CH_4 adsorption potential (Chaback et al., 1996). The ECBM concept has accordingly attracted much interest, not least as a possible zero-emission-method of energy production. Since 1995, pilot ECBM operations have been conducted in Japan (Yamaguchi et al., 2006) GHGT8, Poland (van Bergen et al., 2006), Canada (Mavor et al., 2004) and the USA (Reeves, 2001), with varying degrees of success. Methane was produced in all of these field trials, but CO_2 injectivity of the coal seams decreased drastically in each case,

pointing towards blocking or closure of the transport paths in the coal seam. This effect has been attributed to adsorption-induced swelling of the coal matrix, leading to build up in stress, closure of the cleat system, and sealing of the formation (e.g. van Bergen et al., 2006).

The injectivity reductions experienced during ECBM imply that a strong coupling exists between sorption behaviour, changes in the mechanical state of coal and changes in its transport properties. Understanding the mechanisms and processes underlying this coupling in coal-CO_2 systems under *in situ* stress conditions is crucial for predicting reservoir behaviour and hence for assessing the feasibility of ECBM operations and for selecting optimum performance conditions. To date, however, the coupling that determines the stress-strain-sorption behaviour of coal has received only limited attention (with a few exceptions: Karacan, 2007; Pone et al., 2009b; Harpalani and Mitra, 2010; Wang et al., 2011) and insufficient understanding exists to model coal reservoir response to CO_2 injection in terms of the detailed physical processes operating. The motivation for the present thesis was to help fill this knowledge gap, providing a basis to advance existing ECBM reservoir "simulators" towards predictive reservoir models.

1.2. Nature and behaviour of coal-CO_2 systems

At the sub-maceral scale, coal matrix material consists of a macromolecular network, built up of aliphatic- and aromatic-bonded carbon (50-96 %C) plus mainly organically bonded oxygen and hydrogen. As the carbon content increases with coal rank during progressive coalification, the proportion of aromatic structures strongly increases, ultimately yielding a graphite-like arrangement of carbon crystallites at carbon contents higher than 95 %. In such crystallites, the spacing between individual polyaromatic sheets is of the order of ~0.34 nm (Hirsch, 1954). The corresponding intersheet regions or sheet pores form the smallest void spaces in coal. The amount of nanoscale and polyaromatic porosity in this size range has been shown via sorption experiments to increase linearly with crystalline carbon content.

The total porosity present in virgin coal matrix material (*i.e.* in the macerals) reflects pore sizes ranging from the nanoscale to the microscale. Though somewhat inconsistent with nanoscience terminology, the pores are usually classified as micro- (<2 nm) meso- (2-50 nm) and macropores (>50 nm), following the IUPAC convention for colloid and surface chemistry. Interestingly, the pore size distribution seen in different maceral types is slightly different. For example, vitrinite appears to be more abundant in micropores than inertinite (Unsworth et al., 1989). In this study, we will refer to the micro- and mesopores as "nanopores" thereby including nanoscale intermolecular voids, *i.e.* sheet pores between polyaromatic sheets. Cleats, the joint-like features in coal layers (Laubach et al., 1998), which cut the matrix into cubes, form as the result of matrix dehydration and shrinkage during coalification, with their orientation being related to the tectonic stress field present during their formation (Solano-Acosta et al., 2007). Access of CO_2 to the cleat-matrix system is crucial for ECBM operations to be successful.

The uptake and physical state of gases such as CO_2 and CH_4 in the pores and cleats of coal has long been the subject of experimental investigation, the aim of such studies being to improve understanding of the interactions occurring, and to produce improved ways of extracting energy from coals (*e.g.* Briggs and Sinha, 1932; Ruff and Geselle, 1936; Moffat and Weale, 1955; Perkins and Cervik, 1969; Reucroft and Patel, 1986; Stevenson et al., 1991; Clarkson et al., 1997; Karacan and Okandan, 2001; Schroeder et al., 2002; Busch et al., 2004; Goodman et al., 2005; Mirzaeian and Hall, 2006; Sakurovs et al., 2007; Melnichenko et al., 2009; Pini et al., 2010). Some investigators infer that CO_2 dissolves in coal causing changes in the macromolecular structure (*i.e.* plasticisation - Larsen, 2004; Mirzaeian and Hall, 2006), putting these forward to explain the volumetric contraction of CO_2 bearing coal seen upon heating (Khan and Jenkins, 1985) and the alterations in transport behaviour seen upon exposure to CO_2 (Goodman et al., 2006). However, most work shows that CO_2 is predominantly

adsorbed by the coal matrix (Goodman et al., 2005; Melnichenko et al., 2009) with some remaining as a free phase occupying the macropores and cleats and obeying the Equation of State (EoS). Several workers have recently addressed the issues of a) how the free and adsorbed phases partition themselves between the IUPAC pore scale classes, *i.e.* between the macro-, meso- and micropores (Bae and Bhatia, 2006; Steriotis et al., 2008; Melnichenko et al., 2009), and b) what the physical nature of the adsorbed CO_2 is (Melnichenko et al., 2009)IJCG. The work by Melnichenko et al. (2009) IJCG, who used small angle neutron scattering techniques, points to increased CO_2 densities in pores below 30 nm aperture, *i.e.* to the presence of a condensed CO_2 phase adsorbed on the nanopore surfaces, *i.e.* on the micro- and mesopore, as well as on the macromolecular surfaces. These results further imply that CO_2 exists mainly as a free phase in the macropores, cleats and cracks. Since molecular interactions between the coal and CO_2 play no role at this scale, the injected CO_2 merely fills and pressurises the macropore and cleat system, the EoS of bulk CO_2 will be obeyed and Darcy-type flow is expected through the pore/cleat network. Accordingly, the poroelastic equation (Biot, 1941; Wang, 2000) is expected to describe the stress-strain changes that take place purely due to changes in fluid pressure *P*, within the macropore and cleat network, as a result of the injection of CO_2 and the production of CH_4 and/or H_2O (Yi et al., 2009)IJCG. By contrast, in the pores with dimensions <30 nm, the thermophysical behaviour of the CO_2 is affected by surface forces that attract and physically adsorb CO_2 in a reversible manner (Goodman et al., 2005; Melnichenko et al., 2009; Radlinski et al., 2009a). Due to these molecular interactions with the solid, the adsorbed CO_2 trapped in the fine-scale pores and molecular interstices will not obey the equation of state for bulk CO_2 (Melnichenko et al., 2009)IJCG. It is these interaction forces between the solid surfaces (molecules) and CO_2 that are responsible for adsorption and for swelling of coal upon adsorption (Goodman et al., 2005). This is quite different in origin from the poroelastic effect.

The physical adsorption of CO_2 by coal, but also of CH_4 and H_2O, occurs due to long-range van der Waals forces, attracting CO_2 into the nanoscale porosity of the coal matrix, and onto the surfaces of larger pores and cleats (Goodman et al., 2005; Radlinski et al., 2009b). The adsorption of CO_2 by coal is generally described by Langmuir-type behaviour, *i.e.* filling of available adsorption sites, and is known to be affected by a number of physical factors, including: a) partial pressure of CO_2, b) temperature, c) coal rank, and d) water content (Busch and Gensterblum, 2011)IJCG. An increase in temperature and water content decreases CO_2 adsorption, whereas increasing CO_2 partial pressure increases adsorption. Coal rank has a variable effect, *i.e.* low rank shows a slight decrease in adsorption capacity with increasing coal rank, whereas high rank coal shows a slight increase in adsorption capacity with increasing coal rank. This is attributed to the micropore density, which, for dry coal, exhibits a similar dependence on rank (Prinz and Littke, 2005). Gruszkiewicz et al. (2009)IJCG demonstrate that sample size strongly affects the rate of equilibration at temperatures

of 35 and 40 °C, and CO_2 pressures up to 6.9 MPa. At about 2-3 MPa CO_2 pressure, crushed samples, with a particle size of 45-150 μm, equilibrated in roughly 10-40h whereas a larger-size fraction of 1-5 mm required 60-300 h. Similar results were obtained by Busch et al. (2004). Water decreases the adsorption capacity only of low rank coals by maximum 80 % relative to the dry state (Busch and Gensterblum, 2011). Other authors, however, show that complete saturation of high volatile bituminous coal substantially lengthens the equilibration time, although the final maximum adsorption capacities are comparable to those of dry coals (Gruszkiewicz et al., 2009). The adsorption of CH_4 by coal exhibits a similar dependence on pressure, temperature, coal rank and water content as CO_2. However, the adsorption capacities are generally 1.5-3 times lower than for coal.

Swelling is the most important mechanical effect of CO_2 adsorption exhibited by coal matrix material. Numerous laboratory studies have been performed to determine the magnitude of coal swelling. In these studies, unconfined coal samples are typically exposed to CO_2 at pressure and temperature conditions relevant to ECBM operations (*e.g.* Day et al., 2008; Durucan et al., 2009; van Bergen et al., 2009; Day et al., 2010; Majewska et al., 2010). Such work has shown that the observed swelling of coal is directly related to the CO_2 pressure and to the amount of CO_2 adsorbed, generally in a non-linear manner (Astashov et al., 2008; Day et al., 2008; Kelemen and Kwiatek, 2009; Pini et al., 2009; Day et al., 2010).

On the basis of the numerous studies that have been performed on the uptake of CO_2 by coal (reviewed by Busch and Gensterblum, 2011), adsorption is regarded as the dominant storage mechanism under *in situ* conditions relevant to ECBM, *i.e.* under the conditions pertaining in coal seams at depths of 1000-2000 m, temperatures of 20-50 °C, and fluid pressures of ~10-20 MPa (White et al., 2005). Adsorption is hence expected to substantially influence the response of coal beds to injected CO_2 in terms of CO_2 storage capacity, methane exchange, swelling and injectivity. In modelling ECBM reservoir behaviour, all of these aspects of system response need to be accounted for.

1.3. Stress-strain-sorption behaviour of coal: an unsolved issue

While the elastic response of coal (stress-strain-fluid pressure behaviour) to the free CO_2 injected into coal may be quantitatively understood through the poroelastic equation (Biot, 1941; Wang, 2000), little is known about the coupling between stress, strain and CO_2 adsorption. It is important to note, that the swelling response is not poroelastic in nature, and hence does not follow a stress-strain relationship predicted by the poroelastic equation (Biot, 1941; Wang, 2000). Instead, the volumetric response to adsorption is one of expansion, and thus opposite to a typical poroelastic response with increasing fluid pressure. As a result of this swelling, the volume of the coal matrix is increases by several percent at typical *in situ* fluid pressure and temperature conditions, reducing open cleat space, and drastically reducing permeability. ECBM operations to date have encountered injectivity problems caused by coal swelling (e.g. van Bergen et al., 2006). Hence, it is essential to understand this effect under *in situ* conditions, *i.e.* including the effect of *in situ* stress state. Since swelling under *in situ* conditions will require work to be done against the stress supported by the solid coal matrix, it is likely that the *in situ* stress will reduce the adsorbed concentration of CO_2 at otherwise fixed conditions. Similar effects are seen in adsorption-swelling of clays exposed to water (Low, 1987; Heidug and Wong, 1996; Renard and Ortoleva, 1997). This implies that a constitutive description must be sought describing coupled stress-strain-sorption effects in coal exposed to CO_2. Such understanding is crucial for the prediction of the *in situ* mechanical behaviour of the coal matrix during ECBM, and is also important in the development of new coalbed methane plays.

Experimental investigations of the mechanical behaviour of coal-CO_2 systems to date include the determination of the effects of CO_2 on the apparent elastic behaviour of coal (Viete and Ranjith, 2006), and on the brittle failure strength (Ates and Barron, 1988; Aziz and Ming-li, 1999; Ranjith et al., 2010). The relationship between swelling and stress has been considered (Ruff and Geselle, 1936; Karacan, 2007; Pone et al., 2009a; Harpalani and Mitra, 2010), and evidence presented for that the application of an effective stress reduces coal swelling. More specific, Harpalani and Mitra (2010) TPM inferred from their experiments on coal cores, equilibrated with CO_2 pressures at 2.1 MPa, that only by application of effective stress of the order of four times the CO_2 pressure (*i.e.* more than 8 MPa effective stress) the lateral swelling strain could be reduced back to zero. Other studies suggest that adsorption of CO_2 by coal matrix material may cause a) a reduction of yield (brittle failure) strength in uniaxial loading (Ranjith et al., 2010)FUEL, and b) a reduction of apparent Young's modulus (Viete and Ranjith, 2006). Most of these studies, however, have neglected the possibility of a direct coupling between stress, strain and adsorbed amount of CO_2, of the type seen in clays adsorbing water (Heidug and Wong, 1996; Renard and Ortoleva, 1997), so that interpretations may be incomplete. Moreover, most such experiments were performed

using cm-scale coal cores. Large cores include large pores, cleats and cracks, which can strongly influence the bulk stress, strain, transport and sorption behaviour. Such complications drastically impede obtaining a general description of the effects of CO_2 on coal matrix response, and render direct application of experimental results to ECBM reservoirs questionable.

An additional issue in determining the coupled stress-strain-adsorption response of coal matrix material exposed to CO_2 is the need to accurately determine the sorption capacity. This is done by conducting either manometric or gravimetric sorption tests on powdered coal samples flooded with CO_2 under unconfined, isostatic conditions (Bae and Bhatia, 2006; Goodman et al., 2007; Gensterblum et al., 2010; Pini et al., 2010). These techniques are usually applied to determine the excess sorption, or Gibbs Surface Excess (GSE), *i.e.* the amount of CO_2 adsorbed in the nanoporous coal matrix in excess of any free, bulk phase present at constant pressure and temperature (Sircar, 1999). However, as recently discussed by Sakurovs et al. (2009), Yu et al. (2008), Ross and Bustin (2007), Condon (2006) and Romanov et al. (2006b), methodological uncertainties may affect the accuracy of determinations of the CO_2 sorption capacity of coal. These uncertainties include a) errors in correcting for volumetric effects of coal swelling (Ozdemir et al., 2002; Siemons and Busch, 2007), b) the question whether the application of the He-pycnometry method to determine the free CO_2 volume or mass present in coal samples is reliable (Ross and Bustin, 2007), and c) the extreme sensitivity of the thermophysical properties of CO_2 to the presence of chemical impurities near the critical point (Zhang et al., 2002). Despite attempts made to minimise uncertainties associated with GSE sorption determination methods for coal-CO_2 systems (Ozdemir et al., 2003; Pini et al., 2006; Romanov et al., 2006a; van Hemert et al., 2009), these three issues are extremely difficult to resolve, as they are inherent to the assumptions made in the application of the manometric and gravimetric methods to the measurement of physical adsorption (Condon, 2006). To assess the importance of the accompanying uncertainties, an independent, direct method of determining CO_2 uptake by coal is needed.

1.4. Scope and aims of this thesis

This thesis focuses on the mechanisms, processes and thermodynamics that determine the stress-strain-sorption behaviour of dry coal matrix material under isothermal conditions, including the effects of free and adsorbed CO_2. Effects addressed include coal swelling, elastic compression, changes in apparent elastic modulus, and effects of stress state on adsorbed concentration. The broad aim of this study is to improve understanding of the interplay between a) amount of stored CO_2 (adsorbed and/or free), b) CO_2 pressure, c) effective stress state, and d) volumetric strain response of the coal material, and to explain how and why these quantities are related. The implications for the behaviour of coal under *in situ* ECBM conditions are also considered.

The specific aims of the thesis are:

1. To determine whether the CO_2 sorption capacity of crushed coal matrix material, as commonly determined using the manometric or gravimetric method, is influenced by the application of an effective stress to the solid framework of the coal matrix. An attempt is made to investigate whether these effects are reversible, and to explain and model the effects of applied stress in terms of the underlying thermodynamics (see Chapter 2).
2. To quantify and explain the volumetric response of coal matrix material to exposure to high pressure CO_2 (up to 100 MPa) under unconfined conditions. Addressed here is the competition between a) adsorption-induced swelling and b) elastic compression by the free CO_2 phase, and the relative importance of these two components (see Chapter 3).
3. To determine the total uptake of CO_2 by coal matrix material (*i.e.* the sum of pore filling and adsorption capacity), independently of the standard manometric and gravimetric methods which rely on the EoS for CO_2, and without the need to apply volumetric corrections to account for sample swelling (see Chapter 4).
4. To develop a full thermodynamic model on the effect of a general 3-D stress state on the adsorbed concentration, as observed in Chapter 2, and to test this model further on a cm-scale cylindrical coal sample. The theory is then finalised with a constitutive equation describing the full coupling between stress, strain and adsorption in coal matrix material exposed to CO_2 (see Chapter 5).
5. To determine whether irreversible effects in the coal matrix such as permanent swelling and changes in equilibration time, occur in response to exposure to CO_2. And, to establish the microphysical process underlying these, in order to predict whether these effects are likely to occur under *in situ* conditions of stress (see Chapter 6).

All experiments reported in this thesis were performed on Brzeszcze high volatile bituminous coal (seam 364) to allow a comparison with results from the ECBM pilot project RECOPOL in Poland. Small, matrix-scale samples (*i.e.* crushed samples, or mm-sized cylinders or blocks) were used to eliminate any effect related to the presence of cleats. This was done to obtain purely matrix-related understanding of the response of coal to CO_2. Such understanding is also highly relevant for the mechanical behaviour of other unconventional gas plays such as shale gas reservoirs, and also for the integrity of shale caprocks in the context of geological storage of CO_2 to reduce greenhouse gas emissions.

2

Applied stress reduces the CO_2 sorption capacity of coal

Sander Hol, Colin J. Peach,
Christopher J. Spiers

International Journal of Coal Geology, 85(1): 128-142

Abstract

Though the adsorption of CO_2 by coal has been extensively studied in experiments, few systematic studies have been done on the effects of the stress state within the coal on CO_2 sorption. To investigate whether or not the CO_2 sorption capacity of coal is influenced by the application of an effective stress to its solid framework, we performed five experiments on pre-compacted, porous aggregates of crushed coal matrix material, at a fixed temperature of 40 °C and at varying CO_2 pore pressures between 10 and 20 MPa. The samples were loaded in a stepwise manner up to an applied effective stress of 35 MPa in excess of the CO_2 pressure in the pores, while the volume expelled from the samples was monitored using a syringe pump. One control experiment was conducted using non-adsorbing Helium at 15 MPa. Our data show that CO_2 is reversibly expelled from our samples by the application of an effective stress, and that this is accompanied by reversible compaction, with both effects being partly time-dependent. Analysis of these data, assuming the maximum versus the minimum possible reduction of pore volume occupied by free CO_2 during compaction of the aggregates, demonstrates that the CO_2 sorption capacity of our samples was reduced by an amount in the range between 0.0014 to 0.014 $mmol \cdot g_{coal}^{-1} \cdot MPa^{-1}$. Under the temperature and CO_2 pressure conditions investigated, this is equivalent to a reduction of about 5-50 % of the initial sorption capacity at zero applied effective stress. The observed desorption was accompanied by a reduction in apparent axial stiffness of the samples by about ⅓ from 1.52 to 0.95 GPa. The microphysical mechanism responsible for desorption was investigated by deriving a simplified (hydrostatic) thermodynamic model representing the coal as an adsorbent with a finite density of adsorption sites, interacting with CO_2 (the adsorbate). Our model is based on the principle that the free energy change associated with adsorption of a single CO_2 molecule in stressed coal, is increased, relative to the unstressed state, by an amount reflecting the extra mechanical work done due to swelling of the coal per adsorbed molecule. This model predicts a reduction in CO_2 sorption capacity and in apparent axial stiffness of the samples, of similar magnitude to those observed in our experiments, suggesting that the basic physics of the effect of stress on sorption are successfully captured by the model. In coal basins considered for ECBM production, the overburden stress increases with depth, and self-stressing of coal seams will occur due to swelling after CO_2 injection. As current reservoir models do not consider the effects of stress on adsorption, our observations and modelling results may have important implications for predictions of *in situ* CO_2 storage capacity.

2.1. Introduction

It is now widely acknowledged that anthropogenic greenhouse gas emissions are driving global changes in climate (IPCC, 2007). To limit long-term impact, industrialised countries are moving to reduce their emissions significantly, in the case of the European Union by up to 20% of 1990 levels by 2020 and 50% by 2050 (Commission of the European Communities, 2008). One of the most promising possibilities under consideration worldwide involves CO_2 capture at source followed by geological storage in depleted reservoirs or deep saline aquifers (Davison et al., 2001; Bradshaw et al., 2007; Bachu, 2008; van der Meer and Egberts, 2008). However, a commercially more attractive niche scenario is offered by Enhanced Coalbed Methane (ECBM) production from unmineable coal seams. This involves injection and storage of preferentially sorbing CO_2, coupled with recovery of desorbed CH_4 (Puri and Yee, 1990; Reeves, 2001; White et al., 2005). ECBM pilot operations have recently been conducted in Japan (Yamaguchi et al., 2006), Poland (van Bergen et al., 2006), Canada (Mavor et al., 2004) and the USA (Reeves, 2001), with varying degrees of success. Although CH_4 was produced in all of these field trials, the injectivity of the coal seams decreased drastically in each case. This was attributed to adsorption-induced swelling of the coal matrix (*e.g.* van Bergen et al., 2006).

To predict the behaviour of a coal reservoir during ECBM operations, in particular the CH_4 production rate, the CO_2 storage capacity and the geo-mechanical response to CO_2 injection, a fundamental understanding of the mechanisms controlling exchange and transport of CO_2 in the pore system of coals is needed. Numerous laboratory experiments and modelling studies have addressed these issues, and have revealed two classes of mechanisms (Palmer and Mansoori, 1998; Pan and Connell, 2007; Palmer, 2009) operating at the different pore scales inherent to coal (e.g. Rouzaud, 1990; van Krevelen, 1993; Prinz et al., 2004; Radlinski et al., 2004; Prinz and Littke, 2005). At the scale of large pores, cleats and cracks (>30 nm), in which CO_2 exists as a free fluid with bulk CO_2 properties, injected CO_2 merely fills and pressurises the pore system, having a mechanical effect described by poroelastic theory (Biot, 1941; Wang, 2000). Molecular interactions between the coal and CO_2 play no role at this scale. Therefore Darcy-type flow is expected through the corresponding pore/cleat network and the poroelastic equation (Biot, 1941; Wang, 2000) predicts that volume changes take place due to in-seam changes in fluid pressure P, driven by the production of CH_4 and H_2O (P decrease), and by injection of CO_2 (P increase). On the other hand, in the small pores and nanoscale intermolecular voids between polyaromatic sheets in the coal matrix (<30 nm), intermolecular forces operate that influence the thermophysical behaviour of the CO_2 that diffuses into such locations. These forces attract and physically adsorb CO_2, as demonstrated by studies using Fourier Transform Infrared (FTIR) microscopy (Goodman et al., 2005) and Small-Angle X-Ray Scattering (SAXS) techniques (Melnichenko et al., 2009; Radlinski et al., 2009). The adsorption process

is reversible (Goodman et al., 2005). Due to molecular interaction with the solid, adsorbed CO_2 does not obey the equation of state for bulk CO_2 (Melnichenko et al., 2009). In addition, the molecular interaction associated with adsorption causes (differential) swelling of coal, such that the state of stress changes when the material is confined (e.g. Ruff and Geselle, 1936; Ceglarska-Stefanska and Czaplinski, 1991; Ceglarska-Stefanska and Czaplinski, 1993; Levine, 1996; Karacan, 2003; Karacan and Mitchell, 2003; Karacan, 2007; Day et al., 2008). Thus, CO_2 in coal will in general be present in bulk form in the coarser pores and cleats, and in adsorbed form in the intervening, nanoporous matrix. This means that the volumetric behaviour of coal seams, changes in *in situ* stress, and changes in stress-dependent transport properties will generally be determined by the interaction of both poroelastic and adsorption effects.

The interplay between poroelasticity and physical adsorption in coal samples equilibrated with CO_2 and CH_4, under unconfined conditions at constant temperature, has been considered in detail by Pan and Connell (2007). These authors derived a model that relates volumetric response to changes in bulk fluid pressure, chemical potential, the amount of fluid stored as a free phase in open pores (>30 nm), and the amount stored as an adsorbate in the matrix (<30 nm). The model can be successfully fitted to trends seen in experimental studies on swelling induced by the saturation of coal with CO_2 (Levine, 1996) as well as CH_4 (Moffat and Weale, 1955). However, it does not take into account the possible effects on adsorption of the *in situ* stress present in coal seams, or of changes in the *in situ* stress due to confined swelling.

From experiments on coal-CO_2 systems, two broad effects of stress state have been suggested. First of all, stress-induced changes in transport properties can influence the time a sample takes to reach equilibrium when exposed to CO_2. Such effects have recently been reported by Siriwardane et al. (2009), who showed that the application of a confining pressure P_c of 50 MPa to coal reduces its permeability, which must therefore increase the time taken for CO_2 to access such samples and reach equilibrium. Secondly, stress may influence the adsorption process itself. This is indirectly suggested by the work of Ruff and Geselle (1936) and Walker Jr. et al. (1988), who report a reduction in adsorption-induced swelling due to effective stress. Similarly, Viete and Ranjith (2006) report a reduction in the elastic stiffness of brown coal exposed to CO_2, which may also indirectly suggest an effect of stress on adsorption. In addition, Pone et al. (2009) and Hile (2006) recently claimed to have observed a direct effect of stress on the adsorption of CO_2 by coal cores. Their evidence, however, does not take into account the reduction in permeability that others have reported, which makes the basis for their claim unclear. Thus, while there are indications in the literature for a possible effect of stress on the adsorption of CO_2 by coal, there is no direct proof or quantitative evidence for such an effect or its magnitude. It is well-known, however, that stress affects the adsorption of water and other volatiles at the surfaces of clays (e.g. Heidug and Wong, 1996; Bennethum and Weinstein, 2002; Abou Najm et al., 2009) and other crystalline materials (Feuerstein and John, 1969; Baer et al., 1984).

In this study, we investigate directly the effect of stress on the physical adsorption of CO_2 by coal matrix material. We aim to demonstrate whether or not the CO_2 sorption capacity of coal is influenced by the application of an effective stress to the solid framework of the coal, and if so to explain the responsible microphysical mechanism. Our aims relate to interaction processes at the nanoscale, *i.e.* to the effects of stress on the pure sorption process, which can only be investigated if effects of stress on transport properties and accessible porosity are ruled out. To eliminate such effects, we have conducted uniaxial compaction experiments on pre-consolidated aggregates of crushed coal matrix material, prepared with ~20 % porosity and with sufficiently fine grain size a) to be free of internal cleats and fractures, and b) to allow rapid diffusion of CO_2 into and out of the individual matrix grains. Our results show that significant amounts of CO_2 are desorbed from our samples with increasing applied effective stress. They further suggest that the effective stress state pertaining *in situ* during ECBM operations may substantially lower CO_2 storage predictions made by conventional thermodynamic and reservoir models.

2.2. Experimental method

2.2.1. Basic approach

In this study, a uniaxial or oedometer-type compaction apparatus was used to apply an axial effective stress to pre-compacted aggregates of finely crushed coal matrix material prepared from high volatile bituminous coal. The pre-compacted samples were first allowed to equilibrate with CO_2 under load-free conditions. The samples were then loaded axially in a stepwise manner and changes in sample CO_2 content were measured using a servo-controlled, high pressure syringe pump connected to the compaction vessel. The experiments were carried out at 40 °C and a CO_2 pressure of 10.0-20.0 MPa, *i.e.* using supercritical CO_2.

2.2.2. Samples

2.2.2.1. Origin and preparation

The experiments were performed on high volatile bituminous coal from the Upper Silesian Basin of Poland (Nowak, 2004). The material used was kindly provided by the Central Mining Institute of Poland in the form of a large (~200 kg) block taken from Seam 364, exposed in the Brzeszcze Mine (Longwall No. 105) at a depth of 640-740 m. Note that CO_2 was injected into this layer in 2004 at a distance of 5 km from the mine, as a part of the ECBM pilot project 'RECOPOL' (van Bergen et al., 2006).

A 10 cm fragment, selected from the large block of coal, was crushed and sieved ('as received') to obtain a coal matrix fraction of 63-212 μm in grain diameter. Crushing was performed using a Retsch ZM-200 centrifugal mill, while sieving was performed using a Retsch AS-200 sieve shaker. Prior to use, the sieved fraction was manually homogenised by stirring and a 10 g sample was selected for each experiment. The chosen grain size fraction was fine enough to ensure compositional homogenisation and the elimination of cleats, while being sufficiently coarse to maintain the micrometre and nanometre-scale structure and hence properties of the coal matrix particles.

2.2.2.2. Composition and properties

As reported by Busch et al. (2004) and Hower (2008), sieving of coal samples leads to maceral fractionation. Petrological and chemical analyses were therefore performed on the selected grain size fraction, at the Geochemical Laboratory of the Netherlands Organization for Applied Scientific Research (TNO), in Utrecht (Table 1), to yield an accurate description of the sample composition and properties. Maceral counting was performed using a polished block of resin-impregnated, granular sample material. This showed that the samples contained 60.1 % vitrinite, 9.8 % liptinite and 30.1 % inertinite (all vol%). The sample material exhibited a vitrinite reflectance (R_0) of 0.77

± 0.05 %, determined on the basis of 50 spot measurements. Proximate analyses (in wt%) were performed accordance to ASTM-standard D5142 using a LECO TGA-601 Thermo Gravimetric Analyser, and showed that the coal contained 2.93 % of moisture, 31.21 % of volatile matter, 5.16 % of ash and 60.70 % of fixed carbon. Ultimate analyses (wt%) were performed using a LECO CHN-1000 analyser to determine the content of carbon, hydrogen and nitrogen. Carbon and sulphur contents were determined using a LECO SC-144 analyser. The samples were found to contain 74.14 % carbon, 5.27 % hydrogen, 1.44 % nitrogen, 0.70 % sulphur and the remaining 18.45 % was assumed to be oxygen ('by difference').

The mean density of the matrix material under unconfined conditions was derived from the mass and volume of three, cleat-free, right-ground, cylindrical cores of coal matrix measuring ~ 5 mm in length by 3.8 mm in diameter. The cores were taken from a coal fragment adjacent to that used to prepare the crushed coal samples. This procedure yielded an average matrix density ρ_{matrix} of 1343 ± 15 kg·m^{-3}, which compares well with the densities of high volatile bituminous coals as obtained using He-pycnometry by Dormans et al. (1957) for various Polish coals (1270-1380 kg·m^{-3}) and by Huang et al. (1995) for U.S. coals (1312.7-1463.7 kg·m^{-3}). Since the average density obtained for our matrix cores (density of solid coal including pores) falls in the higher range of He-densities (approx. solid coal density) reported by Dormans et al. (1957) and Huang et al. (1995), the percentage of pore space in our samples must be very small. A hypothetical He-porosity of 2.6 % in our samples would yield a He-density of 1380 kg·m^{-3}, which is the upper limit of the densities determined by Dormans et al. (1957) for samples from Polish coal basins. From this we infer that the He-accessible porosity in our Brzeszcze high volatile bituminous coal (Poland) can only be a few percent at most.

Organic Petrology	Vitrinite reflectance R_o	0.77
	Vitrinite %	60.1
	Liptinite %	9.8
	Inertinite %	30.1
Proximate Analysis	Moisture %	2.93
	Volatile Matter %	31.21
	Ash %	5.16
	Fixed Carbon %	60.70
Ultimate Analysis	Carbon %	74.14
	Hydrogen %	5.27
	Nitrogen %	1.44
	Sulfur %	0.70
	Oxygen % ("by difference")	18.45

Table 1. Organic petrology, proximate analysis and ultimate analysis performed on the 63-212 µm fraction of Brzeszcze high volatile bituminous coal used as sample material in the present study. The analyses were performed at the Geochemical Laboratory of the Netherlands Organization for Applied Scientific Research (TNO).

2.2.3. Apparatus and calibration

2.2.3.1. Experimental set-up

The experimental set-up used consists of a uniaxial, oedometer-type compaction cell, constructed of Monel K-500 alloy (Schutjens, 1991), mounted in an Instron 8862 servo-mechanical loading frame to apply axial load, and connected to an ISCO 65D high pressure syringe pump to control pore fluid pressure (Fig. 1). The Instron 8862 loading frame can be operated in either position control (allowing fixed vessel volume) or load control modes. Ram position is measured in the drive unit using a Linear Variable Differential Transformer (LVDT) with accuracy of ± 0.05 mm. The Instron's electro-mechanical actuator and servo-system allow position control with an accuracy of ± 0.0016 mm. Applied axial load is measured external to the compaction vessel using a 100 kN capacity Instron loadcell (model 2518-111), which allows load control to within ± 0.23 kN.

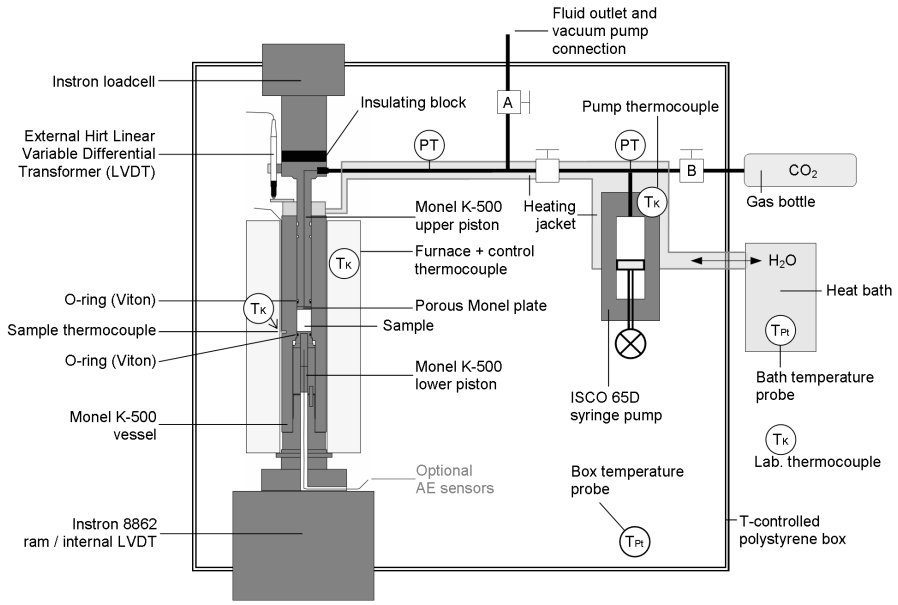

Fig. 1. Experimental set-up consisting of a uniaxial compaction vessel, constructed of Monel K-500, located in an Instron loading frame. Pore fluid pressure (CO_2) is held constant using an ISCO syringe pump connected to the compaction vessel via a bore in the axial loading piston. T_K = Type K thermocouple; T_{Pt} = Pt100 element

The Monel compaction cell (internal diameter 20 mm), at the centre of the set up, consists of an externally heated pressure vessel equipped with an upper, moveable Monel piston and a fixed, lower Monel piston. The top piston contains a central bore, providing access for CO_2 to the sample, through a 1.2 mm thick, porous Monel plate at its tip. Both loading pistons are sealed against the vessel wall using Viton o-rings. In the present experiments, displacement of the upper piston relative to the top of the compaction cell was measured using a Peter Hirt GmbH T102F LVDT (measuring stroke ± 2 mm, repeatability 0.01 μm).

The ISCO 65D servo-mechanical syringe pump, used to control CO_2 pressure, consists of a piston-cylinder assembly with a maximum internal volume of 68.07 ml, that can be operated either in constant pressure mode (up to 137.9 MPa) or constant flow rate mode (up to 30 ml·min^{-1}). Pressure within the pump is measured and controlled using a Honeywell TJE 0-137.90 MPa (20000 psi) pressure transducer, located at the top of the syringe pump cylinder, having an absolute accuracy of ±0.6895 MPa (100 psi). Volume changes in the pore fluid system can be derived from the pump displacement calculated from stepper-motor drive increments (resolution 2.55 nl). To check on the sensitivity of the Honeywell pressure transducer, a separate MSI 0-35 MPa (± 0.035 MPa) pressure transducer was attached to the pore fluid system near the compaction cell to attain better resolution and accuracy. This, taken together with independent tests on the temperature and power stability of the signal obtained from the MSI transducer (*i.e.* the drift characteristics of the MSI transducer), showed that the syringe pump could maintain constant pressure to within ±0.049 MPa. Taking into account errors in measuring and controlling the pressure, and errors in measuring pump displacement, the total volumetric resolution of the pump varied between 0.01 ml (at a CO_2 pressure of 20.0 MPa) and 0.06 ml (at a CO_2 pressure of 10.0 MPa), which is equivalent to a total absolute resolution of 0.019-0.086 mmol per gram coal (mmol·g_{coal}^{-1}) for CO_2 pressure in the range 20.0-10.0 MPa.

To control the air temperature around the setup, and to minimise thermal drift and noise, a 1.5 m^3 foam-polystyrene box was constructed around the compaction vessel, syringe pump, pore fluid system and temperature-sensitive conditioner/control modules (Fig. 1). The temperature inside the box was measured using a Pt100-element and kept constant at 30 °C (± 0.1 °C) by means of a digital CAL 9900 PID-controller, coupled to a 60 W light bulb. A powerful fan, operating at constant speed was installed to homogenise the air temperature in the box.

Vessel temperature was controlled using an external furnace and CAL 9900 PID-controller. Temperature was measured using type-K thermocouples located inside the vessel wall (sample temperature), inside the syringe pump jacket (pump temperature), in the furnace (to regulate the furnace temperature) and in the laboratory (to monitor room temperature fluctuations). Thermocouple signals were conditioned using a module based on an Analog Devices AD595C cold junction compensation integrated

circuit. All temperature signals were calibrated using a multifunction reference thermometer accurate to 0.6 °C, and were individually scaled using a sixth-order polynomial.

All of the present experiments were performed at a sample and vessel temperature of 40 °C. To ensure a uniform temperature of 40 °C in the entire pore fluid system, a Lauda heat bath, controlled at 40 °C (± 0.05 °C), was employed to circulate water through a jacket enclosing the ISCO pump cylinder, the pore fluid pipes, and the Monel vessel top. This ensured that the temperature in the entire closed fluid system was above the critical temperature of CO_2 (31.1 °C) and that no CO_2 phase boundaries existed in the system.

2.2.3.2. Data acquisition systems

Load and position signals, obtained from the Instron loadcell and internal Instron LVDT, plus the temperature, fluid pressure and piston position (Hirt LVDT) signals were converted at 16-bit resolution using a National Instruments, 16-channel data acquisition system. The signals were then logged digitally at 60 s intervals by the logging computer using National Instruments VI Logger software. The syringe pump volume was logged at a resolution of 2.55 nl using a special National Instruments Labview control module and a serial connection (RS-232) between the syringe pump and the logging computer.

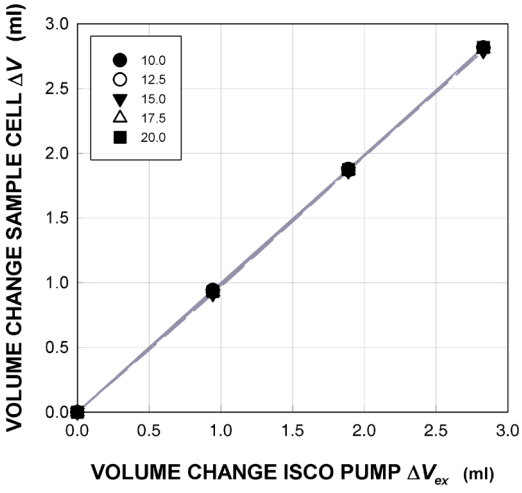

Fig. 2. Volume change of sample cell (ΔV) versus volume change of pump (ΔV_{ex}) measured for an empty sample cell at 40°C and CO_2 pressures of 10.0, 12.5, 15.0, 17.5 and 20.0 MPa. Data corrected for background leak measured at each pressure. Notice that the data points directly overlie each other, regardless of CO_2 pressure, and that a 1:1 relation between cell and pump volume change is obtained for all pressures investigated.

Exp. / Sample N°	Fluid	Fluid pressure *P*	Temp. *T*	Starting porosity (Porosity after pre-compaction)	Loading rate during stress increments	Leak rate correction	Max. error in expelled amount of CO_2 due to volumetric inaccuracies in pump
		MPa	°C	%	MPa·min^{-1}	µl·h^{-1}	mmol·g$_{coal}^{-1}$
1	CO2	10.0	40.0	17.87	0.83	16.02	0.09
2	CO2	12.5	40.0	21.88	0.50	5.09	0.09
3	CO2	15.0	40.0	20.54	0.50	4.89	0.03
4	CO2	17.5	40.0	21.37	0.50	5.00	0.04
5	CO2	20.0	40.0	20.27	1.00	3.72	0.01
6	He	15.0	40.0	18.81	0.50	-	-

Table 2. List of the complete set of experiments conducted on the 63-212 µm fraction of Brzeszcze high volatile bituminous coal. Each pre-compacted sample was loaded in a stepwise manner to applied effective stresses of 5, 10, 20, 30 and 35 MPa and rapidly unloaded. Two such loading cycles or "runs" were conducted in each case.

2.2.3.3. Volumetric calibrations

The loading frame and compaction cell pistons inevitably experience minor elastic deformation when any sample is loaded (apparatus stiffness effect). To obtain the true sample dimensions and hence volume at a given load, the position and displacement measurements obtained from the Instron ram LVDT (used to determine starting length sample) and external Hirt LVDT (used to measure length change) were corrected using appropriate stiffness calibrations. These were obtained from runs performed using a free-standing, stainless steel (AISI 316) dummy sample with a known Young's modulus, loaded axially in the compaction cell at pressure-temperature (*P-T*) conditions identical to those used in the experiments on our coal samples. Based on a sixth order polynomial fit to the Instron LVDT and the external (Hirt) LVDT data, a position correction function was developed for each set of *P-T* conditions investigated. The maximum error in sample length due to inaccurate correction or hysteresis was 10 µm in starting length (correction to the Instron ram data) and 1.35 µm during loading (correction to the external LVDT data). The latter corresponds to an error in displaced volume of CO_2 in an empty vessel of 0.000151 mmol·g$_{coal}^{-1}$ at the highest CO_2 pressure used (20.0 MPa).

Despite the presence of advanced dynamic o-ring sealing systems in both the compaction vessel and ISCO pump, the pore fluid system suffered minor leaks. For each CO_2 pressure used in the experiments, the leak rate was measured from ISCO pump volume data obtained from long duration leak tests (12-24 h) at constant pressure and temperature. A linear fit was obtained describing the decrease in pump volume versus time for each CO_2 pressure tested, and applied to correct the experimental data. Leak rates ranged from 3.72 µl·h^{-1} at a CO_2 pressure of 20.0 MPa to 16.02 µl·h^{-1} at a CO_2 pressure of 10.0 MPa (Table 2) and were used to correct the experimental data continuously as a function of time (at fixed CO_2 pressure and temperature). Errors

introduced by inaccurate leak rate corrections are considered in the total volumetric resolution of the pump as described in section 2.2.3.1. Note that the o-rings present in the equipment did not release or take up significant amounts of CO_2 during the sample loading procedure employed in our experiments. This was inferred from the pump volume data obtained during the stiffness tests described above, which showed no measurable changes in CO_2 volumes whatsoever (*i.e.* due to loading or any other effects).

With no sample present in the vessel, and after leak correction, the volume of fluid expelled due to piston movement equalled the volume change measured by the ISCO pump, within 15 µl or 0.16 % of the standard coal sample volume of ~9.26 ml, at given temperature and CO_2 pressure conditions (Fig. 2). This means that, independently of stiffness correction, changes in CO_2 volume in the sample cell could be directly measured at the pump, with a maximum error of 0.005 mmol·g_{coal}^{-1} at the highest CO_2 pressure used (*i.e.* at 20.0 MPa). Combined with inaccuracies in correcting piston displacement for machine stiffness during sample loading, the maximum error in CO_2 volume change measured by the ISCO pump was therefore 0.005 mmol·g_{coal}^{-1}.

2.2.4. Experimental procedure

2.2.4.1. Sample pre-compaction

In setting up each experiment, ten grams of the chosen 63-212 µm coal fraction were placed in the vessel and the upper piston inserted lightly, such that sufficient space was left between the upper piston and the sample to permit unconstrained swelling of the sample upon CO_2 addition. The vessel was then placed in the Instron loading frame and connected to the pore fluid system. A touch point was then established between the Instron loading frame and the upper piston, and the sample-pump system was evacuated for ~1.5 h. Valve A in Fig. 1 was then closed and liquid CO_2 was injected into the vessel at 5.8 MPa, directly from the CO_2 supply bottle via valve B (Fig. 1). The vessel and pore fluid system, including the syringe pump, were subsequently isolated from the CO_2 bottle, by closing valve B, and the entire pore fluid system and vessel were heated to 40 °C. This temperature increase led to a pressure increase in the system to approximately 8.0 MPa, with full thermal and pressure equilibration taking about four hours. The CO_2 pressure was then increased to the experimentally required setting (10.0, 12.5, 15.0, 17.5 or 20.0 MPa), using the ISCO syringe pump, and the system was left to equilibrate for ~18 hours. Manometric sorption experiments conducted by Siemons and Busch (2007) on crushed Brzeszcze 364 coal with a grain size < 200 µm, at 45 °C and CO_2 pressures of 0-20 MPa showed pressure equilibration times between 1 h and 20 h, which depended on coal type, particle size and CO_2 pressure. We therefore assume that our samples reached equilibrium with the injected CO_2 within ~18 h. The samples were then pre-compacted at fixed effective stress to achieve a (near-)

reproducible starting state. To do this, the applied axial effective stress ($\sigma_e=\sigma_a-P$) was increased linearly with time to 40 MPa, over a period of either 20 min (P = 20.0 MPa) or 30 min (P = 10.0-17.5 MPa), and subsequently held constant for ~18 h. Here, σ_a represents total axial stress while P represents CO_2 pressure. Active loading resulted in 36 to 40 % compaction, followed by virtually zero creep once constant load was att After this pre-compaction stage, the applied effective stress (σ_e) was fully removed from the sample by moving the upper piston away from it (unloading in 1-2 min), while maintaining the CO_2 pressure constant. The sample was then allowed to re-equilibrate with the CO_2 in the unloaded condition. The volume fraction of coal matrix grains present in the sample after re-equilibration (including intragranular pores) was estimated for each experiment on the basis of the density of the matrix (ρ_{matrix} – described in section 2.2.2.2), as measured under atmospheric conditions, the unloaded sample length and the sample mass. This was done ignoring a likely 1-2% swelling of the matrix grains caused by exposure to CO_2 (van Bergen et al., 2009b), as well as any permanent grain compaction effects of similar magnitude that may have occurred due to loading (van Bergen et al., 2009a). In this way, the intergranular porosity of the individual samples after pre-compaction was estimated at values between 17.9 and 21.9 % (Table 2). Note that this represents the starting porosity for subsequent testing.

2.2.4.2. Determining the effect of axial loading on CO_2 content of the samples

To investigate the possible influence of applied effective stress (σ_e) on the sorption capacity of our samples, five pre-compacted samples (experiment 1-5) were each reloaded, in a stepwise manner, to applied effective stresses (σ_e) of 5, 10, 20, 30 and 35 MPa, at a constant incremental loading rate in the range 0.5-1.0 MPa·min^{-1} (Table 2). These five experiments were carried out at CO_2 pressures of 10.0, 12.5, 15.0, 17.5 and 20.0 MPa respectively. Note that the maximum applied effective stress (σ_e) of 35 MPa was chosen to be below the stress applied during pre-compaction (40 MPa). This was done to prevent additional permanent deformation by stress-dependent grain rearrangement and/or grain failure. After applying each stress increment, the sample was allowed to settle and equilibrate. The change in CO_2 volume accompanying loading (σ_e) was monitored through the volume change recorded by the ISCO syringe pump and approached a constant (equilibrium) value in 0.5-4.0 h after each stress increment. After the final loading stage at 35 MPa, the sample was rapidly unloaded to zero applied effective stress (σ_e) to allow re-equilibration with CO_2. In this procedure, the upper piston was retracted to a position above the sample. The axial loading procedure was then repeated, yielding a total of two loading cycles or "runs" per experiment. Any permanent strain of the sample after the first cycle was revealed by the difference in touch point at the start of the second compared to the first cycle. For control purposes, an identical experiment (experiment 6) was performed using Helium at 15.0 MPa, instead of CO_2 (Table 2). This was conducted to examine any dependence of volumetric behaviour on fluid type and because He is known to exhibit little or no adsorption by coal (as discussed by Sakurovs et al., 2009).

2.2.5. Data processing

The raw position, volume, and force data, scaled and logged as described in section 2.2.3.2, were processed to yield data on axial strain (*e*, *i.e.* the volumetric strain of the sample), expelled CO_2 volume (ΔV_{ex}, the leak corrected change in ISCO pump volume) and applied effective stress (σ_e) versus time (t). These were in turn used to construct e vs. σ_e and ΔV_{ex} vs. t data sets. Axial or volumetric strain was calculated using the definition $e = \Delta L/L_0 = \Delta V/V_0$ where ΔL is sample shortening at time t, ΔV is the corresponding volumetric compaction, and L_0 and V_0 are the length and volume of the sample at the onset of the first loading cycle. Expelled CO_2 volume (ΔV_{ex}) was taken as a positive quantity. Compressive axial stress σ_a and effective axial stress $\sigma_e = \sigma_a - P$) were also taken positive.

Using the data from the Instron LVDT, the length (L_0) and volume (V_0) of the sample at the onset of loading were derived from the difference between the position when the upper Monel piston touched the top of the sample, and the position when the upper Monel piston was in contact with the lower Monel piston with no sample present, multiplying by the internal area of the Monel vessel to obtain sample volume. The absolute volume of the sample during the experiment (solid plus all porosity), the change in sample volume (ΔV) and the sample shortening (ΔL), were calculated using the position data obtained from the external (Hirt) LVDT, corrected for apparatus distortion as described in section 2.2.3.3. The volume of CO_2 expelled upon loading of the sample (ΔV_{ex}) was derived from the volume change recorded by the ISCO syringe pump, corrected for leaks continuously as a function of time as described in section 2.2.3.3.

The expelled amount of CO_2 was also expressed in moles per unit mass of coal sample (Δn_{ex}, $mmol \cdot g_{coal}^{-1}$), using CO_2 densities derived from the Equation of State (EoS) for CO_2 (Span and Wagner, 1996), combined with the molar mass of CO_2 plus the known mass of the samples (10 g). Since the pressure and temperature conditions used in our experiments were well above the critical point of CO_2, errors in the EoS density values, due to impurities (Zhang et al., 2002) or temperature inaccuracies, are expected to be minor.

Finally note that the gas volumes expelled during loading of the He-saturated sample could not be reliably corrected because of excessive leakage of He through the o-ring seals. For this reason, the data from the single control test performed using He are not used, except for the mechanical data.

Table 3. Axial strain response and expelled amount of CO_2 measured under asymptotic (near-equilibrium) conditions after each increment in σ_e applied in the present experiments. Because reversibility of the mechanical response was not determined after the second loading cycle, e_{perm} could not be determined, and was assumed to be zero in order to calculate C_{app}.

Exp. / Sample N°		Fluid / Pressure	Total strain achieved at max. load	Apparent stiffness modulus	Total *t*-dep. creep strain achieved at max. load	Total permanent strain on removal of all load	Expelled amount of CO_2 at applied effective stress σ_e Amount is expressed as ΔV_{ex} in ml and as Δn_{ex} (mmol·g_{coal}^{-1})				
		P	e_{max}	C_{app}	e_{creep}	e_{perm}	σ_e = 5 MPa	σ_e = 10 MPa	σ_e = 20 MPa	σ_e = 30 MPa	σ_e = 35 MPa
		MPa	%	GPa	%	%	ml (mmol·g_{coal}^{-1})	ml (mmol·g_{coal}^{-1})	ml (mmol·g_{coal}^{-1})	ml (mmol·g_{coal}^{-1})	ml (mmol·g_{coal}^{-1})
Cycle/Run 1	1	CO_2 / 10.0	3.91	0.96	0.77	~0.3	0.090 (0.13)	0.195 (0.28)	0.307 (0.44)	0.372 (0.53)	0.420 (0.60)
	2	CO_2 / 12.5	4.33	0.86	0.67	~0.3	0.060 (0.10)	0.142 (0.24)	0.275 (0.46)	0.360 (0.60)	0.395 (0.66)
	3	CO_2 / 15.0	3.81	1.00	0.60	~0.2	0.062 (0.11)	0.130 (0.23)	0.254 (0.45)	0.327 (0.58)	0.367 (0.65)
	4	CO_2 / 17.5	3.97	0.95	0.63	~0.3	0.059 (0.11)	0.124 (0.23)	0.249 (0.46)	0.341 (0.63)	0.395 (0.73)
	5	CO_2 / 20.0	3.44	1.03	0.67	~0.1	0.040 (0.08)	0.103 (0.20)	0.220 (0.42)	0.310 (0.59)	0.362 (0.69)
	6	He / 15.0	2.29	1.52	0.13	0.0	-	-	-	-	-
Cycle/Run 2	1	CO_2 / 10.0	4.07	0.93	0.60	assumed 0.0	0.154 (0.22)	0.217 (0.31)	0.300 (0.43)	0.378 (0.54)	0.428 (0.61)
	2	CO_2 / 12.5	4.39	0.86	0.67	assumed 0.0	0.105 (0.17)	0.150 (0.25)	0.280 (0.47)	0.384 (0.64)	0.385 (0.64)
	3	CO_2 / 15.0	4.00	0.92	0.58	assumed 0.0	0.118 (0.21)	0.175 (0.31)	0.327 (0.58)	0.400 (0.71)	0.434 (0.77)
	4	CO_2 / 17.5	4.10	0.92	0.60	assumed 0.0	0.103 (0.19)	0.173 (0.32)	0.249 (0.46)	0.346 (0.64)	0.400 (0.74)
	5	CO_2 / 20.0	3.51	1.03	0.65	assumed 0.0	0.080 (0.15)	0.128 (0.24)	0.222 (0.42)	0.314 (0.60)	0.362 (0.69)

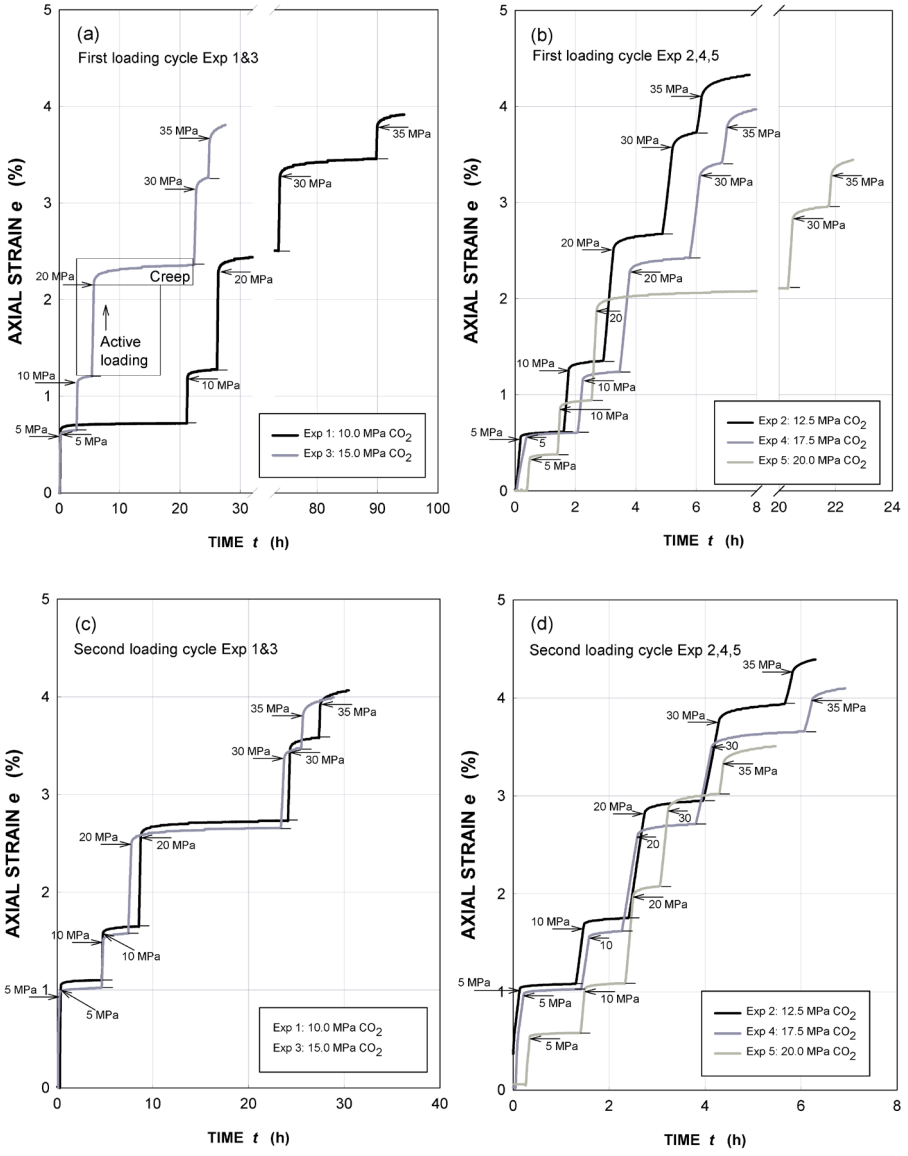

Fig. 3. Compaction data for all samples. Axial strain (e) versus time (t) for the first and second loading cycles – see (a)&(b) and (c)&(d) respectively, with small horizontal lines indicating onset of active loading, and arrows indicating the point at which loading was achieved. The numbers given next to the arrows specify the applied effective stress at the indicated point. e, f) see top page 32.

2.3. Results

2.3.1. Axial compaction data

The five samples tested with CO_2 (Experiments 1-5 - Table 2) a sharp, near-linear increase in axial compressive strain (e) with time during active incremental loading, plus minor compaction creep towards an asymptotic strain value during the intervening periods when the applied effective stress (σ_e) was held constant (Fig. 3a-d). Since the load increments were applied at constant loading rate, all samples also showed a near-linear relation between axial strain and applied effective stress during each loading step (Fig. 3e, f). Closely similar behaviour was observed in both the first and the second loading cycles. In each run, a total axial strain of 3-4 % was attained at maximum load (σ_e = 35 MPa), with an axial strain of ~0.5 % and ~1% being accumulated in individual loading steps of 5 and 10 MPa respectively. Creep occurring in the intervals of constant applied effective stress (σ_e) accounted for a strain of 0.1-0.2 % per interval, contributing a total of 0.60-0.77 % strain to the total axial strain achieved during the first loading sequence, and 0.50-0.77 % during the second (Fig. 3, Table 3). About 0.1-0.3% axial strain was found to be permanent after the first loading sequence (*i.e.* at the onset of the second loading cycle), which is much less than the total creep strain accumulated during loading (Fig. 3, Table 3). Most of the imposed deformation (90-97 % of it) was therefore reversible, including most of the time-dependent (creep) strain accumulated during loading.

From the e versus σ_e data presented in Fig. 3e and f. it is clear that loading up to 10 MPa applied effective stress (σ_e) resulted in a similar axial strain response for all tests performed with CO_2 except for the test at 20.0 MPa CO_2 pressure, which deformed slightly less (Fig. 3e, f). Above 10.0 MPa applied effective stress (σ_e), the e - σ_e curves diverge and the axial strain achieved generally tends to increase with decreasing CO_2 pressure. At the maximum applied effective stress (σ_e) of 35 MPa, this trend becomes the most apparent, and occurred during both cycles of the experiments (*cf.* Fig. 3e vs. f). Note, however, that a clear exception to this trend is seen in the experiment performed at a CO_2 pressure of 10.0 MPa. On the basis of the axial strain (e_{max}) attained at the maximum applied effective stress ($\sigma_{e\,max}$) of 35 MPa, an apparent tangent stiffness modulus, defined $C_{app}=\sigma_{e\,max}/e_{max}$, was calculated for all samples, *i.e.* all CO_2 pressures investigated (Experiments 1-5). The data obtained are shown in Table 3. These show a mean value of 0.95 GPa plus a slight tendency to increase with increasing CO_2 pressure, reflecting the lower total strains attained at the highest CO_2 pressures.

The single control experiment performed using He (Experiment 6 - Table 2) at a pressure of 15.0 MPa, and following an identical loading sequence to the experiments done using CO_2, showed fully reversible deformation with a maximum axial compressive strain of 2.2 % - *i.e.* around ½ to ⅔ of that achieved using CO_2 (Table 3). The apparent stiffness C_{app} of this sample was correspondingly much higher (1.7 x)

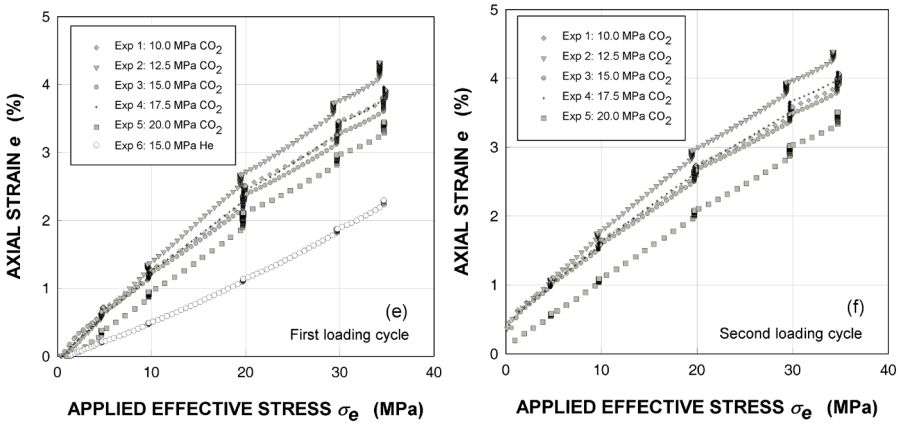

Fig. 3e and f) Axial strain (e) versus applied effective stress (σ_e) for the first and the second loading cycles. Note that the He control test was subjected to only one loading cycle (e). The apparent stiffness moduli derived from the data represented in (e) and (f) are tangent moduli defined following $C_{app}=\sigma_{e\,max}/e_{max}$.

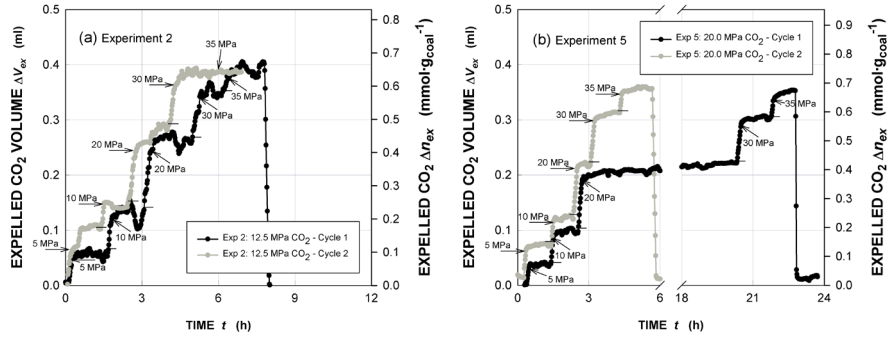

Fig. 4. Representative data showing CO_2 volume expelled (ΔV_{ex}) versus time in the present experiments using CO_2. a) Experiment 2 at 12.5 MPa CO_2 pressure, and b) Experiment 5 at 20.0 MPa CO_2 pressure. Data from the first loading cycle are indicated in black, and from the second in grey. Note that the expelled volume of CO_2 (ΔV_{ex}) is the expelled volume measured by the ISCO syringe pump, corrected for background leak rate, and is consequently calculated with respect to the onset of the first loading cycle. The expelled amount of CO_2 is also represented in terms of expelled amount Δn_{ex} in mmol per gram of coal sample (right hand vertical axis). Further, the small horizontal lines indicate the onset of active loading, and arrows indicate the point at which loading was achieved. The numbers given next to the arrows specify the applied effective stress at the indicated point.

than in the CO_2 runs, taking a value of 1.52 GPa (Table 3). In addition to this mean or tangent stiffness contrast, the axial strain (e) versus applied effective stress (σ_e) curve shows a clear increase in slope or decrease in stiffness with increasing strain (Fig. 3), in the case of the He experiment. This tendency is also seen in the CO_2-saturated samples during the stages of active loading, but is less marked. Finally, the e versus time and e versus σ_e curves for the He test (Fig. 3) show almost no time-dependent deformation (creep) during the intervals of constant applied effective stress, in sharp contrast to the tests with CO_2.

2.3.2. CO_2 expulsion data

Representative CO_2 expulsion versus time curves for the CO_2-saturated samples (experiments 1-5) are shown in Fig. 4. The expelled amounts of CO_2 are expressed in terms of expelled CO_2 volume (ΔV_{ex}) at test pressure and temperature, and in moles of CO_2 per gram of coal sample (Δn_{ex}). The curves obtained for both loading cycles all show rapid, near linear expulsion of fluid during the increments of active loading, followed by sharp deceleration towards much slower or zero expulsion during the intervening periods where the applied effective stress (σ_e) was held constant and the sample approached a new equilibrium state. Unloading at the end of the first loading cycle shows a more or less complete recovery of expelled fluid volume, indicating that expulsion and re-uptake of CO_2 are reversible. The expulsion curves obtained in the second loading cycle are approximately the same as in the first loading cycle, though in general the data obtained in the second cycle are smoother. The sudden drop in expelled volume seen in a few curves, towards the end of periods of constant applied effective stress (σ_e), reflects the point at which correction for background leak rate sometimes became inaccurate in comparison with the fluid expulsion rate, in the approach to equilibrium. Since leak rates at the higher CO_2 pressures (≥ 15.0 MPa) were systematically lower than at low CO_2 pressures (Table 2), the errors and hence fluctuations introduced by leak rate correction are least in the higher pressure experiments.

The results in Fig. 4 clearly show that the expelled volume correlates with the application of effective stress applied to the samples. During each constant applied effective stress step, the samples re-equilibrate with the CO_2, *i.e.* they slowly release CO_2 (after loading) or take up CO_2 (after unloading). Equilibrium values of ΔV_{ex} per step were taken as the average of the volumetric data obtained over a period of 30 minutes, prior to the onset of any non-oscillatory (monotonic) reversals in the expelled volume data, below a plateau value. The resulting total expelled CO_2 volumes at equilibrium are given in Table 3. Bear in mind here, that the onset of the first loading cycle is the reference point for all changes occurring in our samples during the first and the second loading cycle, *i.e.* the reference point for the measured changes in volume of the sample cell (ΔV) and the pump (ΔV_{ex}). The changes in volume of the pump (ΔV_{ex}) were recalculated to amounts of expelled CO_2 per gram of coal sample (mmol·g_{coal}^{-1})

and were plotted against the corresponding level of applied effective stress (σ_e) in Fig. 5, for both loading cycles used. The equilibrium expulsion data (in mmol·g_{coal}^{-1}) show that the amount of CO_2 expelled from our samples of crushed coal matrix material, at (or near) equilibrium, increases with increasing applied effective stress (σ_e), following a nearly linear trend (Fig. 5). The mean rate of expulsion per unit applied effective stress is ~0.02 mmol·$gcoal^{-1}$·MPa^{-1} for both loading cycles. No major difference in the effect of stress on expelled amount is observed as a function of CO_2 pressure (Fig. 5). Moreover, as already evident from Fig. 4 and Table 3, the measured expulsion and subsequent re-uptake upon unloading is largely reversible. As indicated earlier, we were unfortunately unable to obtain expulsion data for He as the leak rate in the He control test (experiment 6) was too high to accurately correct for.

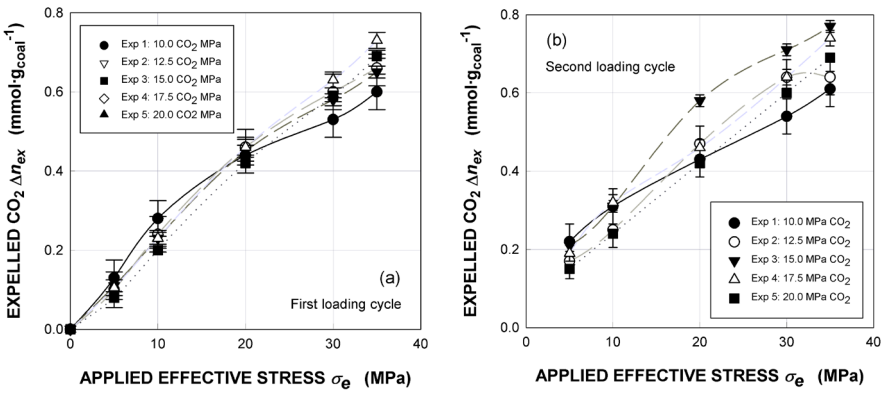

Fig. 5. Expelled amount of CO_2 (Δn_{ex}) at (or near) equilibrium versus applied effective stress (σ_e) during a) the first and b) the second loading cycle of the experiments. Expelled amounts were recalculated from the volume change measured by the ISCO syringe pump at equilibrium, as described under section 2.3.2 (i.e. with respect to the onset of the first loading cycle), using the Span and Wagner Equation of State (EoS) for CO_2 (Span and Wagner, 1996).

2.4. Discussion

The present data for pre-compacted samples saturated with CO_2 have shown a reversible effect of applied effective stress (σ_e) on CO_2 expulsion. This eliminates irreversible compaction mechanisms such as grain breakage and permanent rearrangement, leaving only poroelastic effects and reversible, stress-induced desorption as viable CO_2 expulsion mechanisms. We attempt to discriminate between these, and to evaluate any role of stress-induced desorption, by considering the change in pore and/or grain volumes that can occur in three hypothetical compaction scenarios. This results in upper and lower bound estimates of desorption, which unambiguously demonstrate a significant stress-induced desorption effect. Having identified how much CO_2 is released by stress-induced desorption, we go on to identify the thermodynamic origin of the effect.

2.4.1. Effect of stress on expelled CO_2 volume – evidence for desorption

Reversible, sorption-independent effects in our experiments can, in theory, involve volumetric reduction of intergranular pore space due to poroelastic deformation of the solid skeleton as well as poroelastic compression of the individual coal grains. Since direct, *in situ* measurements of the reduction of pore and solid volumes cannot be made during our experiments, we will identify an upper and lower limit of desorption via the following microscale volumetric response scenarios to mechanical loading, namely a minimum desorption scenario, a maximum possible desorption scenario, and (a more likely) constant porosity, maximum desorption scenario.

2.4.1.1. Minimum desorption scenario

In this case, the nanoporous solid grains are assumed (hypothetically) to be elastically deformable, but volumetrically incompressible, so that all expelled CO_2 volume results from compression of the open (*i.e.* intergranular), CO_2-filled pores. This scenario thus corresponds to maximum intergranular pore space reduction, hence maximum possible expulsion of free CO_2, during loading. From the 1:1 relation between the pump and vessel volume presented in the methods section (2.2.3.3), the maximum volume of free CO_2 driven out of the sample in this scenario is equal to the volume swept by the piston in an empty sample cell. Subtracting that swept volume from the measured amount of CO_2 expelled from our samples (Δn_{ex}) yields an excess amount of expelled CO_2 (Δn) at all applied effective stresses investigated, though the excess is small at the highest CO_2 pressures (Fig. 6). The excess CO_2 expelled amounts to 0.01-0.11 mmol·g_{coal}^{-1} at an applied effective stress (σ_e) of 35 MPa (Fig. 6), and implies a mean excess expulsion rate with respect to stress of 0.0003-0.0031 mmol·g_{coal}^{-1}·MPa^{-1}. If the solid grains in this scenario were volumetrically compressible, not incompressible, as they will always be in reality, the amount of adsorbed CO_2 released from them would be greater than shown in Fig. 6. It can therefore be concluded, that reduction only

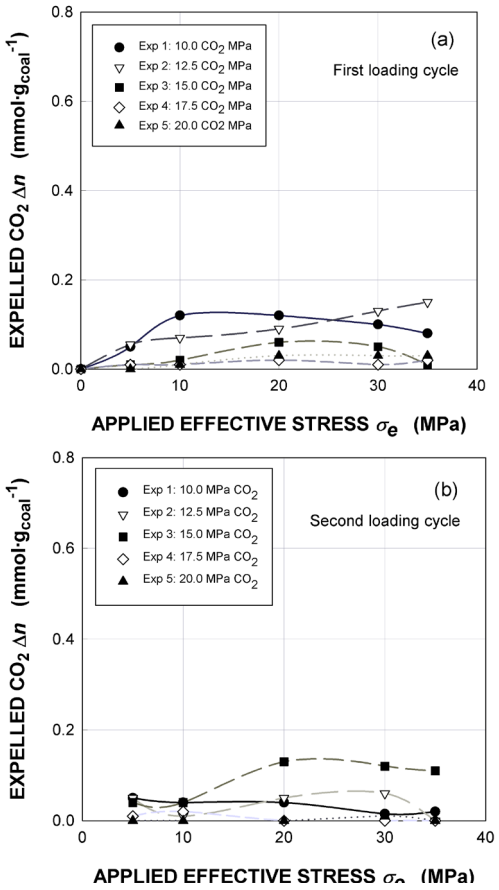

Fig. 6. Expelled amount of CO_2 due to desorption (Δn) versus applied stress (σ_e) during the first (a) and second (b) loading cycles of each experiment, calculated following the minimum desorption scenario (section 2.4.1.1), i.e. assuming constant solid-grain volume and hence maximum intergranular pore space reduction during loading. All data are calculated with respect to the onset of the first loading cycle.

in CO_2-bearing intergranular pore volume is unable to explain the measured CO_2 expulsion. This proves that at least part of the initial amount of CO_2 adsorbed in the nanopore system within the solid matrix grains is desorbed by the applied effective stress (σ_e), at a minimum mean rate of 0.3-3.1 $\mu mol \cdot g_{coal}^{-1} \cdot MPa^{-1}$.

2.4.1.2. Maximum possible desorption scenario

Maximum desorption of CO_2 from our samples in response to loading would occur in the hypothetical case where the intergranular pore volume containing free CO_2 is unable to change during loading. In this scenario, all volume change is achieved by volumetric compression of the nanoporous coal grains. All CO_2 driven out of the sample, as shown in Fig. 4 and Fig. 5, would then have to be desorbed due to particle compression, while the free CO_2 pore space remains constant. This implies a maximum desorption (Δn) totalling 0.8-0.9 $mmol \cdot g_{coal}^{-1}$ at 35 MPa loading, and thus an average

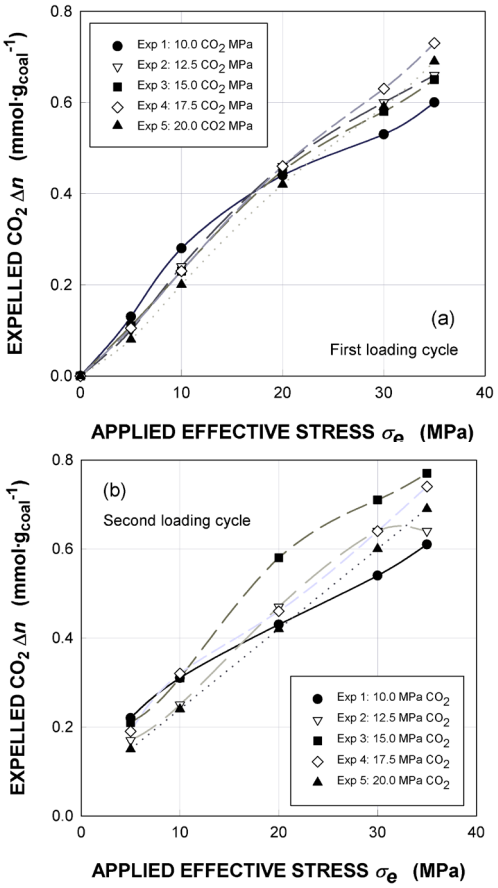

Fig. 7. Expelled amount of CO_2 due to desorption (Δn) versus applied stress (σ_e) during the first (a) and second (b) loading cycles of each experiment, calculated following the maximum desorption scenario (section 2.4.1.2), i.e. by assuming zero volume change of open, intergranular pores, and hence maximum desorption. All data are calculated with respect to the onset of the first loading cycle.

desorption rate of 0.02 $mmol \cdot g_{coal}^{-1} \cdot MPa^{-1}$ (Fig. 7). An unrealistic consequence of this scenario is, however, that the fraction of open pore space, *i.e.* the porosity, must increase during loading, whereas in reality it is expected to either decrease or stay constant.

2.4.1.3. Constant porosity desorption scenario

A much more realistic upper limit on stress-induced desorption can be set by assuming that the porosity (pore volume fraction) of the aggregates remains constant during loading, due to homogeneous poroelastic deformation of the solid grains and pores. From the dimensional change of the aggregate, the reduction of absolute intergranular pore volume, and hence the amount of CO_2 expelled from the open pores in the sample, can then be computed. Any volume of CO_2 measured in addition, must be desorbed. Assuming the initial porosity of our samples (17.87-21.88 % after pre-

compaction - Table 2) remains constant, the amount of desorption (Δn) predicted by this model is as shown in Fig. 8, and is approximately 0.5 mmol·g_{coal}^{-1} at the maximum applied effective stress (σ_e) of 35 MPa for all CO_2 pressures studied. As an outcome of the constant porosity scenario, we infer that the maximum mean desorption rate in our experiments was 0.014 mmol·g_{coal}^{-1}·MPa^{-1}.

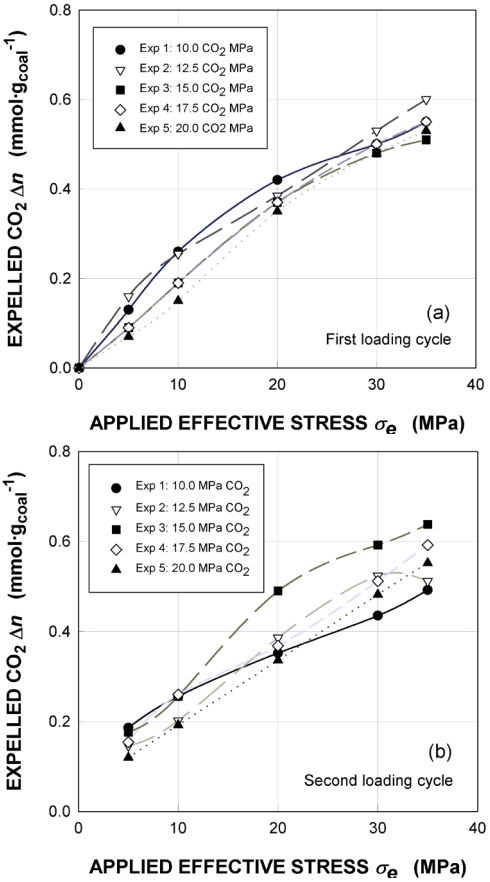

Fig. 8. Expelled amount of CO_2 due to desorption (Δn) versus applied stress (σ_e) during the first (a) and second (b) loading cycles of each experiment, calculated following the constant porosity desorption scenario (section 2.4.1.3). All data are calculated with respect to the onset of the first loading cycle. In this scenario, the total amount of expelled CO_2 is a combination of pore volume reduction and desorption, which both contribute significantly.

2.4.1.4. Magnitude and quantitative significance of the desorption effect

For the CO_2 pressures (P) investigated here, and for similar temperatures (45 °C), Siemons and Busch (2007) determined a Gibbs Surface Excess of adsorbed CO_2 amounting to ~1.0 mmol·g_{coal}^{-1} for Brzeszcze coal. Their measurements were done on powdered coal, fully immersed in CO_2, *i.e.* at hydrostatic conditions of zero effective stress. As demonstrated by our experiments and the analyses presented above, stress-induced desorption must have played a significant role in our tests, corresponding to a minimum of 0.0014 mmol·g_{coal}^{-1}·MPa^{-1} and a maximum of 0.014 mmol·g_{coal}^{-1}·MPa^{-1}. The maximum applied effective stress (σ_e) of 35 MPa used in our experiments thus reduced the sorption capacities by 5-50 % compared to the values determined by Siemons and Busch (2007) for unstressed Brzeszcze coal under similar conditions. Our results thus show that stress-induced desorption could be highly significant in coal under conditions relevant to ECBM, where *in situ* mean stresses would be around 25 MPa at 1 km depth, for example.

2.4.1.5. Effect of CO_2 sorption/desorption on mechanical behaviour

Because our crushed coal samples were all pre-compacted at an applied effective stress (σ_e) that was significantly higher than the maximum stress used in the subsequent loading cycles, all stress-dependent permanent compaction by sliding and cracking of grains should have been eliminated from the load cycling stages of the experiments. This is confirmed by the largely reversible mechanical behaviour of our samples. Nonetheless, samples saturated with CO_2 and He showed different compaction behaviour. In principle, this can reflect differences in either the poroelastic or adsorption behaviour of the samples. We now briefly consider the relative role of these effects.

Compression of the bulk structure of a poroelastic solid is typically a combination of pore space reduction and a decrease in solid skeleton volume and is thus greatly influenced by the amount of porosity (*e.g.* Munro, 2001). Since adsorption of He by coal is expected to be minor (as discussed by Sakurovs et al., 2009), drained poroelastic behaviour (Wang, 2000) is expected to occur in our He-saturated sample. This sample could be compressed instantly upon loading, and showed a near-linear and reversible dependence of compaction strain (e) on the applied effective stress (σ_e), with an apparent axial stiffness modulus C_{app} of 1.52 GPa (Table 3). No significant creep was observed during the stages of constant load. We therefore assume that this sample is representative for pure, poroelastic compression of our samples.

By contrast, the apparent stiffness C_{app} of the CO_2-saturated samples was of the order of only 0.9-1.0 GPa, as described in section 2.3.1. More specifically, for the applied effective stress (σ_e) range of 5-20 MPa, lower values of C_{app} of 0.7-0.9 GPa were computed, compared to the range σ_e = 20 to 35 MPa, where C_{app} was 0.9-1.1 GPa.

The stiffness of the CO_2-saturated coal samples was therefore significantly lower than the He-saturated sample due to the presence of adsorbed CO_2, especially at the lower applied stresses. Such an effect was reported previously by Viete and Ranjith (2006), who interpreted it as a reduction in elastic stiffness. However, the effect can be equally well explained by stress-induced desorption, leading to de-swelling of the coal. In this interpretation, removal of CO_2 from the coal structure by the application of an effective stress, leads to decrease in the apparent stiffness modulus, and the (reversible) time-dependent deformation (creep) observed after each stress increment would reflect diffusion of CO_2 out of the sample as it desorbs. The reduction in stiffness and the reversible creep observed in our CO_2 tests imply that adsorbed CO_2 has an effect on the mechanical response of our samples. As yet, however, we cannot determine unambiguously whether this reflects the influence of stress on desorption or an effect of CO_2 on mechanical properties, or both. Since CO_2 adsorption is known to cause swelling of unstressed coal, we infer at this point that stress-driven desorption is probably the main effect. We will attempt to elucidate this matter in section 2.4.2.

2.4.2. Thermodynamic origin of the effect of stress

The present experiments have shown that the application of a positive effective stress σ_e ($=\sigma_a - P$) to granular coal samples in contact with $scCO_2$ at a pore fluid pressure P leads to stress-induced expulsion of adsorbed CO_2, *i.e.* to desorption. Since coal swells significantly when CO_2 is adsorbed, this effect is not surprising and would appear to be a simple expression of Le Chatelier's Principle. To explain the effect more rigorously, we examine the thermodynamics of adsorption, first under unstressed conditions where the coal is exposed to CO_2 at pressure P, and then when an additional hydrostatic effective stress σ_e is applied to the solid.

We start by considering a small, cubic particle of coal matrix material of mass m and containing n_s adsorption sites. The concentration of potential adsorption sites can thus be defined as $C_s = n_s/m$ sites per kg of coal, which is presumably a constant for a given coal type. The cube is chosen to be so small (≤ 1 mm) that it is free of cleats and consists entirely of nanoporous coal matrix material. Optical and SEM observations on the fine grains samples used in the present experiments confirmed that this is a reasonable assumption for the individual grains in our samples, which are only 50-200 μm in mean diameter. The particle is accordingly free of pores allowing Darcy flow or storage of free CO_2 and can take up CO_2 only by diffusion and adsorption.

The coal particle is now exposed to CO_2 at pressure P. Following numerous authors (*e.g.* Tuin and Stein, 1995), but focusing on free energy changes at constant pressure and temperature, adsorption of a single CO_2 molecule is associated with a change in Gibbs energy equal to the "attachment energy", written

$$\Delta G_a = \Delta F_a + P\Delta V_a = \Delta F_a + P\left(\Omega_0 - \Omega_f\right) \tag{1}$$

This represents the total Gibbs energy that must be supplied to remove an adsorbed molecule of CO_2 from the potential well associated with the adsorbed (attached) state into a state that is in equilibrium with the free CO_2 phase, or, conversely, the free energy released when a single CO_2 molecule is adsorbed into the trapping potential well from the free phase. It includes all partition function terms present in the statistical mechanics description of adsorption (*cf.* Tuin and Stein, 1995). The term ΔF_a is similarly the Helmholtz free energy of attachment (which includes any changes in elastic energy stored in coal) and $\Delta V_a=(\Omega_0-\Omega_f)$ is the difference between the partial or effective molecular volume (Ω_0) of CO_2 in the adsorbed state and its molecular volume (Ω_f) in the free phase. With Ω_0 defined in this way, Ω_0 represents the volume change (swelling) of the coal per molecule of adsorbed CO_2 and the $P\Delta V_a$ term represents the pressure-volume work associated with adsorption of a single molecule.

If n molecules are now adsorbed, the total change in free energy contributed by the adsorbed phase is given

$$\Delta G = n\Delta G_a - kT\ln W \tag{2}$$

where k is the Boltzmann constant and $k\ln W$ is the configurational entropy associated with the W different ways that the n molecules of CO_2 can be distributed over the n_s adsorption sites present in the coal particle. Taking $W=n_s!/n!(n_s-n)!$, applying the standard (Stirling) approximation that $x!\approx x\ln x-1$, and differentiating ΔG with respect to n leads to the result

$$\frac{\partial \Delta G}{\partial n} = \Delta G_a - kT\ln\left[\frac{1-\theta}{\theta}\right] \tag{3}$$

where $\theta=n/n_s$ (c.f. Tuin and Stein, 1995). By definition, this derivative represents the chemical potential μ_a of the adsorbed CO_2 phase, measured in J·molecule^{-1}. If adsorption is allowed to proceed until equilibrium is reached with the free CO_2 surrounding the particle, then the potential $\mu_a=\partial G/\partial n$ of the adsorbed CO_2 will become equal to the potential μ_f of the free CO_2 phase. From the thermodynamics of fluid systems

$$\mu_f = \mu_{f0} + RT\ln a_f \tag{4}$$

where $a_f=a_f(P)$ is the chemical activity of the free CO_2 at pressure P and μ_{f0} is the potential in the reference state $a_f=1$ (Prausnitz et al., 1986). Hence, we can write $\mu_f=\partial\Delta G/\partial n$, which from (3) leads to the result

$$\theta = \frac{a_f \exp\left(\dfrac{\mu_{f0}-\Delta G_a}{kT}\right)}{1+a_f \exp\left(\dfrac{\mu_{f0}-\Delta G_a}{kT}\right)} \tag{5}$$

This gives the concentration θ of adsorbed CO_2 molecules as a fraction of the number of adsorption sites n_s present in the coal particle. Using equations (3) and (4), and writing the forward rate of the adsorption reaction as $r_+=k_+(1-\theta)a_f$ and the reverse rate as $r_-=k_-\theta$ following Masel (1996), (Eq. 5) now yields

$$\theta = \frac{Ka_f}{1+Ka_f} \tag{6}$$

where $K=k_+/k_-=\theta/(1-\theta)a_f = \exp[(\mu_{f0}-\Delta G_a)/kT]$ is the equilibrium constant for the adsorption reaction.

If the free fluid phase outside the coal particle behaves as an ideal gas, then $a_f=P$ and equation (6) reduces to the classical Langmuir adsorption isotherm (Langmuir, 1918). However, CO_2 is far from ideal in its behaviour, and the concentration of CO_2 adsorbed by coal is usually measured in mmol·g_{coal}^{-1}, *i.e.* mol·kg^{-1}. Therefore, for present purposes, equations (5) and (6) are best written in the form

$$C = C_s\theta = \frac{C_s a_f \exp\left(\dfrac{\mu_{f0}-\Delta G_a}{kT}\right)}{1+a_f \exp\left(\dfrac{\mu_{f0}-\Delta G_a}{kT}\right)} \tag{7}$$

where C is the equilibrium concentration of adsorbed CO_2 in mmol·g^{-1} or mol·kg^{-1} and where $C_s=n_s/m$ was defined at the start of our analysis as the (constant) number of potential adsorption sites per kg of coal.

Having determined an expression for the concentration of CO_2 that adsorbs in coal exposed to CO_2 at pressure P and activity a_f, we now consider the effect of applying a hydrostatic stress σ to the solid coal particle, in excess of the external CO_2 pressure by an amount $\sigma_e=(\sigma-P)$, while still allowing access of CO_2 to the coal particle, *e.g.* by diffusion. In this case, the free energy change, or attachment energy ΔG_σ associated with adsorption of a single CO_2 molecule is increased relative to ΔG_a by an amount equal to $\sigma_e\Omega_0$, which is the pressure-volume (stress-strain) work associated with swelling the coal by an amount Ω_0 per molecule against the applied effective stress σ_e. This term is analogous to the $P\Delta V_a=P(\Omega_0-\Omega_f)$ work term in equation (1), which expresses the net work done on the system when a single molecule is a) removed from the CO_2 phase, which decreases its volume by an amount Ω_f under the action of the pressure P, thus liberating work $P\Omega_f$, and b) adsorbed by the coal, which causes an expansion Ω_0 of the coal against the applied CO_2 pressure P, thus consuming work $P\Omega_0$. By contrast, however, when the solid coal particle is subjected to a hydrostatic stress σ which exceeds the CO_2 pressure P by an amount $\sigma_e=\sigma-P$, then expansion of the coal by the amount Ω_0 accompanying adsorption of a single CO_2 molecule, will require an extra amount of work to be done on the system of magnitude $\sigma_e\Omega_0$. The free

energy change ΔG_σ associated with adsorption in the stressed case can accordingly be written $\Delta G_\sigma = \Delta G_a + \sigma_e \Omega_0$. Substituting this for ΔG_a in the above analysis, and assuming that Ω_0 is independent or insensitive to σ_e (as classically assumed with respect to P in the Langmuir approach), now leads to the result

$$C_\sigma = \frac{C_s a_f \exp\left(\frac{\mu_{f0} - \Delta G_\sigma}{kT}\right)}{1 + a_f \exp\left(\frac{\mu_{f0} - \Delta G_\sigma}{kT}\right)} \tag{8}$$

or

$$C_\sigma = \frac{C_s a_f \exp\left(\frac{\mu_{f0} - \Delta G_a}{kT}\right)\exp\left(-\frac{\sigma_e \Omega_0}{kT}\right)}{1 + a_f \exp\left(\frac{\mu_{f0} - \Delta G_a}{kT}\right)\exp\left(-\frac{\sigma_e \Omega_0}{kT}\right)} \tag{9}$$

where C_σ is the equilibrium concentration of adsorbed CO_2 in $mol \cdot kg^{-1}$ in the coal particle, under conditions where the solid supports a hydrostatic effective stress σ_e.

Equation (9) clearly predicts that the adsorption capacity of coal matrix material in contact with CO_2 at pressure P decreases with increasing effective stress σ_e applied to the solid. This result is not directly applicable to our samples, as the individual coal matrix material particles in our granular aggregates are loaded at grain-to-grain contacts and do not support a uniform effective stress over their surface. Nonetheless, equation (9) does illustrate the effect that an applied effective stress is expected to have on adsorption capacity and is in qualitative agreement with our experimental observations.

To assess in a more quantitative way whether the magnitude of the effect of stress predicted by (9) agrees with that seen in our experiments requires values for the parameter C_s and $K = \exp[(\mu_{f0} - \Delta G_a)/kT]$, for which we have no data for the present samples. Moreover, the granular nature of our samples means that the applied effective stress gives only a crude estimate of the mean value of σ_e acting over grain surfaces. Nonetheless, a first, rough comparison between theory and experiment can be conducted for our experiments at the lowest CO_2 pressure used (10.0 MPa) by assuming that the adsorbed CO_2 concentration, written as $\theta = n/n_s$ is low compared with the saturation value of 1. In this case, $(1-\theta) \rightarrow 1$ in (3) and the denominator in equations 5 to 9 approaches 1 also. Though rough, this assumption can be justified by recognising that even though coal samples become saturated with CO_2 at any given pressure, this does not mean that all possible adsorption sites (n_s) are occupied. Indeed, the saturation concentration of adsorbed CO_2 is determined by the chemical potential of the CO_2 and will in general be well below the maximum possible value corresponding to $\theta = 1$. The ratio of C_σ in the stressed state to C in the unstressed state can then be written, from (7) and (9), as

$$\frac{C_\sigma}{C} \approx \exp\left(-\frac{\sigma_e \Omega_0}{kT}\right) \tag{10}$$

The value of Ω_0 can now be estimated from literature on the swelling behaviour and adsorption capacity of the Brzeszcze coal, seam 364. At 40 °C and CO_2 pressures in the range 8-10 MPa, this coal is known to exhibit volumetric swelling strains of 1-3% (van Bergen et al., 2009b) and adsorption capacities of 1-3 mol·kg^{-1} (see Busch et al., 2004, for similar Brzeszcze 315; and Siemons and Busch, 2007, for Breszcze 364). This is equivalent to an adsorption capacity of ~1.34-2.42·10^3 mol·m^{-3}, based on our own measurements of the Brzeszcze coal matrix density (1343 ± 15 kg·m^{-3}). The absolute swelling expected for 1 m^3 of coal matrix under the present conditions is therefore 1→3·10^{-2} m^3, and the associated value of Ω_0 is [(1→3)/(1.34→2.42)]·10^{-5} m^3·mol^{-1}, *i.e.* 0.41·10^{-5} to 2.24·10^{-5} m^3·mol^{-1}. Inserting these values into equation (10), replacing k by the gas constant R, and setting σ_e equal to the maximum effective stress of 35 MPa applied to our samples, now predicts a maximum stress-induced reduction in CO_2 adsorption capacity of C_σ/C = 0.74 to C_σ/C = 0.95. This means a reduction of ~5-26 %, which in view of the crude assumptions made agrees quite well with the reduction of 5-50 % inferred from our experiments.

On this basis, we conclude that the influence of effective stress observed in our experiments is more or less consistent with equation (9), *i.e.* with an adsorption model that takes into account that the free energy change associated with adsorption of a single CO_2 molecule in stressed coal, is increased, relative to the unstressed state, by an amount $\sigma_e \Omega_0$.

To assess the influence of stress-induced desorption on the mechanical properties of our samples, as suggested in section 2.4.1.5, we will now use the reduction in CO_2 adsorption capacity predicted above to estimate the effect on apparent stiffness modulus C_{app}. We start by noting that both a poroelastic strain $e_{He\,\max}$ (obtained from the He control experiment) and a desorption strain e_{des} (to be calculated in our model) will contribute to the apparent stiffness modulus of the samples. Since there is no a priori reason to assume that $e_{He\,\max}$ and e_{des} are dependent on one another, we assume that they occur independently. Because of this composite property, C_{app} takes the form,

$$C_{app} = \frac{\sigma_{e\max}}{e_{\max}} = \frac{\sigma_{e\max}}{\left(e_{He\max} + e_{des}\right)} \tag{11}$$

Here the poroelastic strain $e_{He\,\max}$ has a value of ~0.023 (Fig. 3), and the desorption strain e_{des} is defined as the change in sample volume due to desorption ΔV_{des} over the initial sample volume V in a swollen, stress-free state, so that

$$\varepsilon_{des} = \frac{\Delta V_{des}}{V} = \frac{\Omega_0 m}{V} C\left(1 - C_\sigma \big/ C\right) \tag{12}$$

Following our calculation of the effect of σ_e on desorption using (10), we now assume that the absolute swelling expected under the present conditions is again 1→3 %, which results in a total initial sample volume V of 7.446→7.669·10^{-6} m^3 and an associated value of Ω_0 in the range 0.41→2.24·10^{-5} $m^3 \cdot mol^{-1}$. If we insert these values in (11) and (12), along with the known sample mass m_s of 0.01 kg, the reduction in CO_2 adsorption capacity C_σ/C of 0.74-0.95 already calculated above from (10) for the maximum applied effective stress $\sigma_{e\,max}$ of 35 MPa, and assuming an initial unstressed sorption capacity C of 1-3 mmol·g_{coal}^{-1}, we obtain an apparent stiffness modulus C_{app} of 0.76→1.47 GPa. The lower value of 0.76 GPa corresponds with a sample that has a high initial sorption capacity and experiences high desorption during loading. The upper boundary value (1.47 GPa) corresponds to a low initial sorption capacity and low desorption. The values computed here compare very well to the experimentally determined range in C_{app} of 0.86-1.03 GPa, as presented in Table 3 and Fig. 3. We therefore conclude that the observed stress-induced desorption effect in our samples is the main factor driving the change in mechanical properties, and that any direct effects of CO_2 on elastic modulus (Viete and Ranjith, 2007) or mechanical effects attributed to "plasticisation" or "structural re-arrangement" of the coal structure (Larsen, 2004; White et al., 2005; Goodman et al., 2006) are minor. Indeed, the experimental results and thermodynamic model reported here imply that irreversible processes such as "plasticisation" cannot play a significant role in the reversible mechanical behaviour of coal-CO_2 systems similar to those addressed in the present experiments.

2.4.3. Implications

The above findings have important implications for the CO_2 adsorption capacity of coal under *in situ* conditions. First, the increase in overburden stress with depth will reduce the equilibrium concentration of adsorbed CO_2 (C_σ), *i.e.* it will reduce the sorption capacity to values significantly below those measured in conventional sorption determinations, such as those reported by Fitzgerald et al. (2005), Goodman et al. (2007), Goodman et al. (2004) and Pini et al. (2006). Purely based on this concept, shallow coal seams may be favoured for ECBM operations. Second, under confined *in situ* conditions, self-stressing of coal seams may occur due to the adsorption of CO_2. This, in turn, reduces C_σ *in situ* during the injection procedure itself. To further understand and predict the effects implied by our study, more experimental and modelling work is urgently needed.

2.5. Conclusion

In this study, direct effects of stress on the CO_2 sorption capacity of coal were investigated experimentally. The aim was to demonstrate whether or not the CO_2 sorption capacity of coal is influenced by the application of an effective stress to the solid framework of the coal, and if so to explain the responsible microphysical mechanism. We approached this by conducting experiments on pre-compacted aggregates of crushed matrix material of a high volatile bituminous coal. These aggregates were free of internal cleats and fractures and, because of their substantial intergranular porosity (~20 %), allowed rapid diffusion of fluids into and out of the individual matrix grains. Five experiments were conducted using CO_2, and were performed in two loading cycles at a fixed temperature of 40 °C and at CO_2 pressures of 10.0, 12.5, 15.0, 17.5 and 20.0 MPa. Loading was achieved in a stepwise manner using applied effective stresses of 5, 10, 20, 30 and 35 MPa, while the volume of CO_2 expelled from the samples was monitored. A control test was done on a sample saturated with Helium, at 15.0 MPa He pressure, although only mechanical results were obtained from this test. Our findings can be summarised as follows:

1. The application of a compressive effective stress to our CO_2-saturated samples led to reversible compaction, accompanied by minor reversible creep. Based on the compaction data, an apparent stiffness of the aggregates was calculated, which for the CO_2-saturated samples was 1.7 times lower than the He-saturated samples. The He-saturated sample showed no creep. These comparative results imply that the presence of adsorbed CO_2 has a direct, reversible influence on the mechanical response of the coal matrix material.
2. The application of effective stress caused an expulsion of CO_2 from our samples. Calculations based on two end-member loading scenarios, assuming a constant pore volume during loading as an upper limit (maximum desorption), versus constant solid volume as a lower limit (maximum poroelastic discharge), showed that CO_2 is expelled from the sample in excess of possible poroelastic effects. This unambiguously demonstrates that stress-induced desorption occurs in coal by amounts in the range 0.01-0.11 $mmol \cdot g_{coal}^{-1}$ (at least at CO_2 pressures up to 17.5 MPa).
3. A more realistic upper limit on stress-induced desorption can be set by assuming that the porosity (pore volume fraction) of the aggregates remains constant during loading, due to homogeneous poroelastic deformation of the solid grains and pores. This predicts that about 0.014 $mmol \cdot g_{coal}^{-1} \cdot MPa^{-1}$ was desorbed from our samples during loading. Combined with the lower limit given above, this implies stress-induced desorption in our experiments in the range of 5-50 % of the initial sorption capacity.
4. A thermodynamic model, representing the coal as an adsorbent with a fixed density of adsorption sites, interacting with CO_2 (the adsorbate), is capable of

explaining stress-induced desorption using the principle that the free energy change associated with adsorption of a single CO_2 molecule in stressed coal, is increased, relative to the unstressed state by a work term equal to $\sigma_e \Omega_0$. More specific, this term relates to the work done on the system by one CO_2 molecule that adsorbs in the stressed adsorbent structure. Consequently, the drop in free energy associated with adsorption becomes smaller. Our model predicts desorption of CO_2 and a reduction in apparent axial stiffness of the samples, as observed in our experiments, and within the same order of magnitude.

5. The phenomenon reported here, that the adsorption capacity under a positive effective stress is lower than the sorption capacity of crushed coal under hydrostatic CO_2 pressure only, may have a significant impact on predictions made by thermodynamic and reservoir models at conditions relevant to ECBM. First, the increase in overburden stress with depth will reduce the amount of CO_2 adsorbed by coal. As a consequence, shallow coal seams may be favoured for ECBM operations. Second, self-stressing of coal seams during CO_2-injection may lower the sorption capacity due to swelling associated with adsorption.
6. The urgent need for predictive modelling in the field of ECBM production demands a fundamental understanding of the mechanisms controlling exchange and transport of CO_2 in the pore system of coals. The present results show that both experimental and modelling work is crucial to further understand the effects of stress state on sorption.

3

Competition between adsorption-induced swelling and elastic compression of coal at CO_2 pressures up to 100 MPa

Sander Hol, Christopher J. Spiers

Journal of the Mechanics and Physics of Solids (submitted)

Abstract

Enhanced Coalbed Methane production (ECBM) by CO_2 injection frequently proves ineffective due to rapidly decreasing injectivity. Adsorption-induced swelling of the coal matrix has been identified as the principal factor controlling this reduction. To improve understanding of coal swelling in response to exposure to CO_2 at high pressures, numerous laboratory studies have been performed in the past decades. These studies consistently reveal an increase in swelling with CO_2 pressure. However, it remains unclear what the relative contributions are of adsorption-induced swelling versus elastic compression of the coal framework, and hence what is the true relationship between adsorption-induced swelling and CO_2 uptake. Here, we report the results of dilatometry experiments conducted on unconfined, cylindrical coal matrix samples (~4 mm long and 4 mm in diameter) of high volatile bituminous coal, where we aim to measure the effective volumetric effect of CO_2 and to separate this into a component caused by adsorption-induced swelling and a component caused by elastic compression. The experiments were performed using high pressure eddy current dilatometer that was used to measure one-dimensional sample expansion or contraction (resolution <50 nm). The tests were conducted at a constant temperature of 40 °C, and CO_2 pressures up to 100 MPa. Our results show that the matrix samples reveal anisotropic expansion over the full range of CO_2 pressures used. Expansion perpendicular to the bedding was about 1.4 times the average expansion measured in the bedding plane. Net volumetric strains, which were computed from the net linear strain in all directions measured, reveal that the response of coal is characterised by an expansion-dominated stage below 10-20 MPa of CO_2 pressure and a contraction-dominated stage at higher CO_2 pressures. Our data demonstrate direct competition between adsorption-induced swelling and elastic compression in the coal matrix. We propose a model for coal swelling, which expresses the net volumetric strain as the sum of the adsorption-induced swelling strain and the elastic compression with the adsorption-induced swelling being taken as linearly related to adsorbed CO_2 concentration. A comparison of experimentally determined adsorption-induced swelling strain with the adsorbed concentration of CO_2 (data Gensterblum et al., 2010) confirms the assumed linear dependence. We go on to compare our experimentally determined adsorption-induced swelling strains to those calculated from an adsorbed concentration model. Good agreement was found over the full range of CO_2 pressures up to 100 MPa. This shows that combining this thermodynamically based model for adsorbed concentration with the elastic compression of our samples, obtained from their bulk modulus, provides a good description of the measured volumetric behaviour of our samples, and suggests that the physical basis for the model is also valid. The implications of our results for ECBM operations are that compliant coals (low K), which exhibit little adsorption-induced swelling (hence low dependence C), will show relatively small reductions or even increases in permeability due to competition between swelling and compression when CO_2 pressure increases during ECBM operations. These coals will tend to be more suitable for ECBM operations. Coals exhibiting high stiffness (K) and high adsorption capacity are less suitable for ECBM.

3.1. Introduction

Despite vast global reserves of coalbed methane, Enhance Coalbed Methane production (ECBM) by CO_2 injection frequently proves ineffective due to rapidly decreasing injectivity. Adsorption-induced swelling of the coal matrix has been identified as the principal factor controlling this reduction in injectivity of CO_2 during ECBM (*e.g.* van Bergen et al., 2006). To determine the magnitude of coal swelling, numerous laboratory studies have been performed in which unconfined coal samples are exposed to CO_2 at pressure and temperature conditions relevant to ECBM operations (e.g. Day et al., 2008; Durucan et al., 2009; van Bergen et al., 2009; Day et al., 2010; Majewska et al., 2010). These studies have shown that the observed swelling of coal is directly related to the CO_2 pressure and amount of CO_2 adsorbed, generally in a non-linear manner (Astashov et al., 2008; Day et al., 2008; Kelemen and Kwiatek, 2009; Pini et al., 2009; Day et al., 2010). The relations obtained form key input for interpreting and modelling the progress of adsorption, swelling and permeability/productivity evolution during ECBM operations (Palmer and Mansoori, 1998; Shi and Durucan, 2003; Liu and Rutqvist, 2010).

However, two fundamental problems are associated with the application of the relations found between experimentally determined swelling, CO_2 pressure and absolute adsorption. First, recent thermodynamic/thermo-mechanical models demonstrate that the volumetric response of unconfined coal matrix material with increasing CO_2 pressure is a net effect caused by adsorption-induced swelling combined with elastic compression of the solid matrix framework (Pan and Connell, 2007; Vandamme et al., 2010). Although the latter effect has been demonstrated experimentally by Moffat and Weale (1955) for CH_4-equilibrated coal, it is generally neglected in formulating pressure-swelling-adsorption relations that can be applied to *in situ* conditions. A simple, order-of-magnitude calculation using typical bulk moduli for coal shows that this can result in significant inaccuracies in describing swelling–adsorption data, especially at higher CO_2 pressures or in cases where the sample material exhibits a low or strongly pressure-dependent bulk modulus, K. Second, swelling/adsorption experiments are often carried out on cm-scale coal cores or blocks, which inevitably contain cleats, cracks, and preparation-induced 'core damage' (Harpalani, 1988; Pini et al., 2009). Because of these features, coal cores and blocks display non-linear elastic behaviour at low applied stress, as demonstrated by conventional elastic stiffness tests (Ko and Gerstle, 1976; Gentzis et al., 2007; Deisman et al., 2008). Accordingly, bulk swelling measurements may yield highly variable results that differ significantly from the "true" volumetric response of intact (cleat/damage-free) coal matrix material. To test recent theoretical models linking matrix swelling to CO_2 pressure and adsorbed content, and to obtain reliable swelling-sorption relations that can be coupled with poro-elastic constitutive models, it is therefore necessary for experiments to focus

on "true" (intact, cleat-free) matrix swelling. This requires the use of matrix-scale samples, plus independent investigation of both adsorption-induced swelling and elastic compression effects.

Here, we report the results of detailed dilatometry experiments conducted on three unconfined, cylindrical coal matrix cores (approximately 4 mm in diameter by 4 mm in length) of high volatile bituminous coal (Brzeszcze, Poland). Our aim was to measure the volumetric response of unconfined, cleat-free coal matrix material to exposure to high pressure CO_2, separating this into adsorption-induced swelling and elastic compression components. In each experiment, the sample was equilibrated with CO_2 at a constant temperature of 40 °C, using CO_2 pressures up to 100 MPa. Volumetric strains were computed from the linear strains measured parallel and perpendicular to the bedding of the coal samples. Since we did not subject the samples to an externally applied effective stress, poro-elastic effects in this study reduce to purely elastic volumetric effects of changing fluid pressure. These were measured independently by exposing the samples to high pressure He, yielding the bulk modulus of the samples (*cf.* Wang et al., 2011). Using the volumetric strain and bulk modulus data obtained, we calculate the adsorption-induced swelling for each matrix sample. Together with independent, high-precision determinations of absolute CO_2 adsorption for crushed Brzeszcze coal (<2 mm), reported by Gensterblum et al. (2010), our analysis yields a swelling-adsorption relationship for our coal matrix samples.

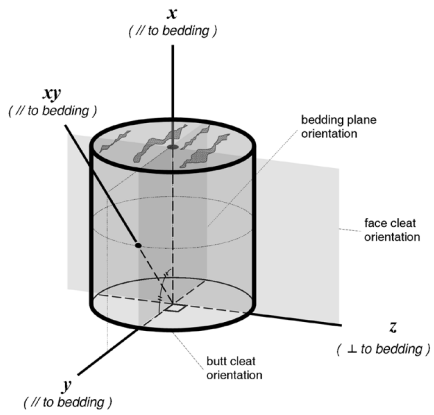

Fig. 1. Schematic diagram of the present coal matrix sample geometry. The sample cylinders were drilled parallel to the coal bedding plane and normal to the butt cleat orientation. Indicated are the x-, y-, and z-directions, in which the linear strains (e_i) occurring in response to CO_2 and He addition were measured in this study. A fourth measurement was made in a direction (xy) intermediate between x and y in the bedding plane, to evaluate swelling any anisotropy in the bedding plane fully.

3.2. Experimental method

3.2.1. Approach

In this study, we used a specially developed, high-pressure eddy-current dilatometer to measure the unconfined dimensional changes of matrix samples of high volatile bituminous coal exposed to CO_2, at pressures up to 100 MPa at a fixed temperature of 40 °C. We aimed to separate the measured strain response into a component caused by adsorption-induced swelling plus a component caused by elastic compression. Millimetre-scale coal samples were used to exclude effects of cleats or cracks on the volumetric response measured *i.e.* to measure true matrix behaviour. Linear expansion measurements were performed as a function of CO_2 pressure in four separate experiments on each sample. These addressed expansion in four different directions, of which three were orientated in the bedding plane (to evaluate fully any anisotropy of swelling in the bedding plane), and one perpendicular to it. We independently measured the elastic compression of the samples, by exposing them to non-adsorbing He at He pressures up to 17 MPa (available bottle pressure).

3.2.2. Samples

The experiments were performed on solid cylindrical samples, measuring approximately 4 mm in length by 4 mm in diameter, taken from a 10 cm scale master block of high volatile bituminous coal, cut from a slab obtained from the Brzeszcze mine (seam 364) in the Upper Silesian Basin of Poland (Nowak, 2004). The Brzeszcze coal has a vitrinite reflectance of 0.77 ±0.05 %, and contains 59.8 % vitrinite, 9.8 % liptinite and 30.0 % inertinite, as shown by petrological analyses performed at the Geochemical Laboratory of the Netherlands Organization for Applied Scientific Research (TNO), in Utrecht.

After identifying the principal bedding and cleat planes bounding the above-mentioned master block, three small cores with a diameter of 4.00 mm and length of ~6 mm were drilled from the same sedimentary layer within it. This was done using a water-cooled pillar drill. The cylinder axis, which we defined as the x-direction of the samples, was drilled parallel to bedding and normal to the butt cleat plane. We defined the y-direction of the samples to coincide with the normal to the face cleat plane, and the z-direction to lie perpendicular to the bedding (Fig. 1).

After drilling, the ends of the cores were ground flat and parallel. Each sample was individually inspected using an optical microscope to guarantee the absence of cleats and damage, other than fine scratches produced by the coring and grinding procedure. The length and diameter of the resulting samples were measured using a digital calliper (resolution 0.01 mm) prior to incorporation in the high pressure vessel. Averaged values obtained from multiple measurements of length and diameter are listed in Table

1, and serve as starting dimensions in all subsequent calculations of strain. Note that the samples used in this study were previously prepared and used as a part of a larger suite in the experiments reported by Hol et al. (2011b) and were exposed to CO_2 up to a maximum CO_2 pressure of 14 MPa during those experiments, *i.e.* before use in the present tests. This means that the present experiments and results exclude any irreversible effects that might occur during first-time exposure of the coal to CO_2, for example of the type reported by Majewska and Ziętek (2007). Note that the starting dimensions and mass of the samples given in Table 1 are values measured immediately prior to the present experiments.

	Initial sample mass (g)	Initial sample length L_{0x} (mm)	Initial sample diameter $L_{0y}=L_{0z}$ (mm)	Initial sample dimension L_{0xy} (mm)
364-1	0.06915	4.08	4.00	5.71
364-2	0.06215	3.79	3.98	5.50
364-3	0.06555	4.00	3.99	5.65

Table 1. Starting dimensions and mass of the cylindrical Brzeszcze 364 coal matrix samples used in this study. The lengths and diameters given serve as the starting dimensions in all strain calculations.

3.2.3. Apparatus and calibration

3.2.3.1. High-pressure eddy-current dilatometer system

Dimensional changes of the samples were measured by means of a purpose-built dilatometer, based on a Micro-Epsilon LS04(03) high-pressure, eddy current sensor, housed in a Remanit 1.4122 stainless steel pressure vessel to allow for the introduction of CO_2 at pressures up to 100 MPa (Fig. 2). In this apparatus, the sensor is mounted in a Grade 5 Titanium support assembly fixed to the top closure nut of the high pressure vessel (inner diameter of 20 mm). This assembly in effect seals the pressure vessel via the Teflon gasket and Viton o-ring located as shown in Fig. 2. The active tip of the eddy current sensor protrudes into the vessel through a sealed bore in the Ti support assembly and acts as a plug in the sealing head assembly (Fig. 2b). The tip is thus exposed to and seals in the CO_2 injected into the vessel at high pressure. The back of the sensor is maintained at atmospheric pressure to allow for routing of signal leads out of the sensor and pressure vessel to an external signal conditioner. Sealing at the contact between the sensor and the Ti support assembly is achieved by means of a 0.2 mm thick PEEK-ring, which is pre-deformed by screwing a backup nut against the back of the sensor to load the ring (Fig. 2b).

Cylindrical samples are located in a Ti sample holder or 'stage' (Fig. 2), mounted opposite the sensor tip by means of a screw connection. The free end of the sample is connected to a Remanit stainless steel target (type 1.4122) via a cap or 'sample hood' assembly supported by a firm but flexible spring steel cross-cantilever. The screw connection between the sample stage and the sensor assembly allow for adjustment of the distance between the steel target and the sensor tip. Three different designs of the sample 'stage' and 'hood' were used to support and measure the sample strain in the four different directions studied, *i.e.* the x, y, xy and z directions (Fig. 1). Expansion or contraction of the sample upon introduction of CO_2 or He into the pressure vessel is transmitted to the Remanit target via the sample 'hood' and spring steel cantilever that holds the sample and hood in place. Displacement of the target alters the eddy current field and thus allows sample expansion and contraction to be measured. The eddy current sensor signal is conditioned using a Micro-Epsilon DT3010-M signal conditioner, which was calibrated for the use of the chosen steel target. In combination with a Micro-Epsilon PS2010 power supply (24 V), a full scale output voltage of 10 V is obtained for a displacement of approximately 500 μm, with zero output voltage corresponding to the position at which the sensor and target are directly in contact.
The pressure vessel plus Ti support assembly and eddy current sensor are maintained

at constant CO_2 pressure using an ISCO 65D servo-mechanical syringe pump coupled to a high pressure NOVA pipe-work system (Fig. 3). This incorporates a CO_2 bottle, a vacuum pump and a Tradinco S441J60/S8199 diaphragm pump connected to the inlet of the syringe pump (Fig. 3). To achieve CO pressures in the range of 0-100 MPa, three different methods of pressure generation are used, each for a specific range of CO_2 pressures. For pressures up to ~6 MPa, CO_2 is introduced into the system directly from the CO_2 bottle through a manually controlled AirProducts R2307 line regulator (Fig. 3). This allows a stepwise increase of the CO_2 pressure up to ~6 MPa (bottle pressure) with an observed maximum stability in applied CO_2 pressure of ±0.01 MPa. To increase the pressure to 10 MPa, the Tradinco diaphragm pump was used, while pressures between 10 and 100 MPa were generated using the ISCO 65D pump. The ISCO 65D pump, which consists of a piston-cylinder assembly with a maximum internal volume of 68.07 ml, was operated in constant pressure mode in the present

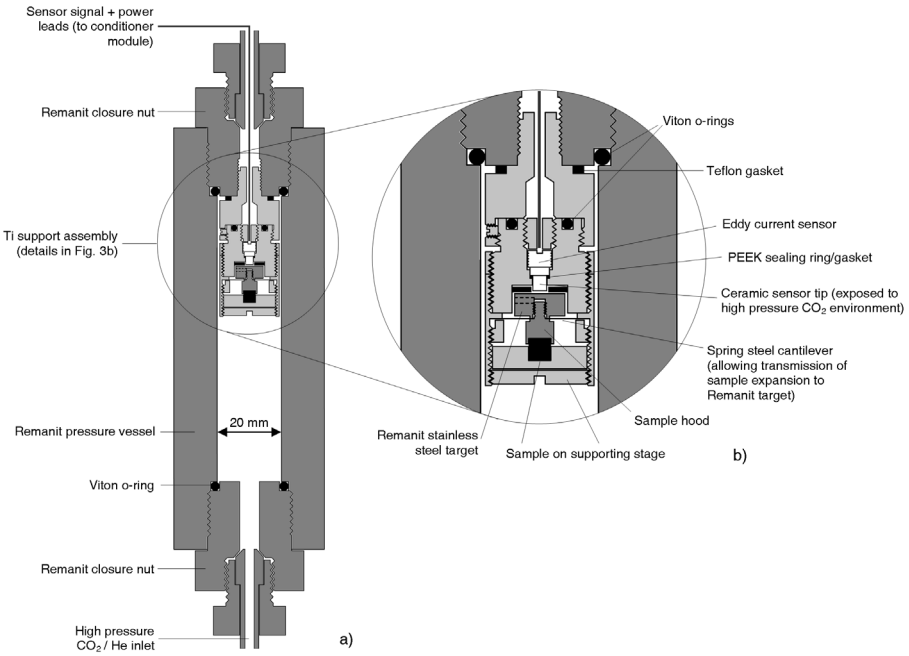

Fig. 2. Semi-schematic diagram of the high-pressure eddy-current dilatometer developed for this study. a) Overview showing the Remanit high pressure vessel (dark grey) holding the Ti support assembly (light grey). CO_2 and He can be admitted to the sample via the fluid inlet on the bottom of the vessel. b) Detail of the Ti support assembly, consisting of the sample, a ferromagnetic target and the eddy current sensor. Expansion or contraction of the sample is transmitted to the Remanit target via the spring steel cross-cantilever that retains the sample in position. Displacement of the target alters the eddy current field and allows sample expansion and contraction to be measured with high resolution.

experiments, enabling pressures to be controlled to within ±0.049 MPa. The CO_2 pressure in the system is measured using a Honeywell TJE 0–137.90 MPa (20,000 psi) pressure transducer (accuracy ±0.6895 MPa), located at the ISCO cylinder head.

To maintain constant temperature in and around the sample, the high pressure dilatometer vessel is placed vertically in a water bath, controlled in the present experiments at 40 °C (±0.05 °C) using a Lauda E200 thermostat (Fig. 3). The temperature of the whole setup is kept constant by placing the water bath plus pressure vessel and sample, the ISCO syringe pump, and much of the high pressure tubing system in a 1 m^3 foam-polystyrene box. In the present experiments, the air temperature within this box was controlled at 38.6 °C (± 0.2 °C) by means of a digital CAL 9900 PID-controller, coupled to a 500 W halogen construction lamp. The air temperature inside the box is homogenised by a powerful fan, operating at constant speed. Temperature is measured using type-K thermocouples located in the water bath, at the pump cylinder head and externally in the laboratory (Fig. 3). The conditioned temperature signals were calibrated using a multifunction reference thermometer (accuracy ±0.3 °C), and were individually scaled using a sixth-order polynomial.

The foregoing describes the system as operated when pressurising the vessel and sample with CO_2. All tests involving He instead of CO_2 were performed at 40 °C using the temperature-controlled water bath but not using the foam-polystyrene box. Because of excessive leakage of the ISCO seals with respect to He, the ISCO syringe pump was not used. Instead the pressure vessel was connected directly to a He bottle, via an AirProducts R2308 line regulator, and to the vacuum pump as shown in Fig. 3, leaving the ISCO pump and diaphragm pump disconnected from the system. In this

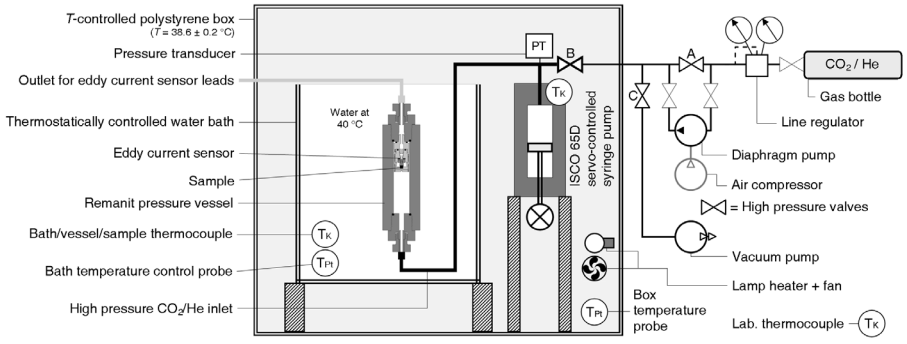

Fig. 3. Full experimental set-up. Note the Remanit pressure vessel containing the eddy current sensor and sample (details see Fig. 2) submerged in a thermostatic bath. Note also the high pressure supply system consisting of an ISCO 65D syringe pump, a Tradinco diaphragm pump, and a CO_2 or He bottle coupled to an AirProducts line regulator. A heated foam-polystyrene box is constructed around the syringe pump and water bath to control the air temperature around the set-up to within ±0.2 °C. T_K = Type K thermocouple; T_{Pt} = Pt100 element.

configuration, a maximum He pressure of 17 MPa (bottle pressure) could be attained. Note that the AirProducts line regular used is only capable of increasing the applied He pressures stepwise to 17 MPa. Thermal control of the vessel was similar in quality to that attained in the CO_2 experiments due to the high efficiency of the Lauda water bath. In the He experiments, however, all high pressure lines were at room temperature (*i.e.* ~20 °C). This had no detectable effect on the performance of the system.

3.2.3.2. Data acquisition

The temperature, CO_2/He pressure and displacement (eddy current sensor) signals obtained from the apparatus were converted at 16-bit resolution using a National Instruments, 16-channel DAQPad-6015 A/D convertor and data acquisition system. The emerging digital data were logged digitally using a PC at a rate of 0.5 Hz using National Instruments VI Logger software. The displacement signal was logged in the form of the raw voltage generated by the eddy current sensing system, whereas the temperature and pressure signals were first scaled to °C and MPa values.

3.2.3.3. Calibrations and apparatus distortion

The change in eddy current sensor voltage with displacement of the sample target was calibrated by translating the target relative to the sensor tip using a Mitutoyo Vernier screw gauge (accuracy ±2 μm). The screw gauge was mounted in the closure nut opposite the sensor body and coupled to the target in the sample holder via a steel rod. To perform the calibration under conditions as close to the experimental conditions as possible, the pressure vessel, plus the attached screw gauge, was placed in the foam-polystyrene box, controlled at 38.6 °C. After allowing the system to settle for approximately 16 h, the target was moved stepwise towards the sensor by rotation of the screw gauge. After each step, the system was allowed to thermally re-equilibrate before recording the sensor output. Linearization of the calibration was achieved by means of fine-tuning of the conditioner unit, and yielded a sensitivity of 25.14 $mV \cdot \mu m^{-1}$ over a distance between the steel target and the sensor of 20 to 140 μm. This range is equivalent to a linear strain of ~2.5 % for a 4 mm long sample. At distances between the target and the sensor greater than 140 μm, the calibration became slightly non-linear, and hence operation of the system at these distances was avoided. To investigate the effect of temperature on sensitivity, a similar calibration procedure was followed at room temperature. This showed a difference in sensitivity of only 1.5 % across the full measuring range (20-140 μm separation between sample and target), which allowed us to confidently apply the calibration obtained at 38.6 °C to all experimental data, which were measured at 40.0 °C. Our calibration experiments further showed that the resolution in measuring sensor-target distance changes was better than 50 nm including effects of minor temperature variation in the Lauda water bath (± 0.05 °C).

In spite of the high accuracy and resolution of the eddy current sensor, the application of CO_2 or He pressure inevitably leads to elastic deformation of the stainless steel vessel and sample assembly. To determine the magnitude of this effect on the measured displacement signal, two different dummy samples, 1 composed of 316 stainless steel (K = 166.7 GPa) and 1 composed of Dural aluminium alloy (K = 74.5 GPa), were incrementally pressurised in the vessel, first up to 100 MPa of CO_2 pressure and then up to 17 MPa of He pressure, at a constant temperature of 40.0 °C. The displacement measured in response to pressurisation was, for each test, corrected for the known compression of the dummy sample and used to yield the apparatus distortion. The data obtained showed two effects, which we developed corrections for. First, an instantaneous shift in the position signal equivalent to between 0 and 1 μm was observed in response to the initial introduction of CO_2 or He, below 1-2 MPa of applied CO_2/He pressure. We attribute this effect to settling of the components in the sensor/sample assembly, and we subtracted this instantaneous effect as an offset on the first data point obtained for both dummy and coal samples. Subsequent values are not affected further. For a standard, 4 mm long sample, the maximum effect on the calculated linear strain of this settling effect was an offset of +0.0125 % strain, which in practice is smaller than the size of the data points plotted for our measurements on coal. Second, the apparatus deformed in a linear elastic manner by 0.02 ±0.001 μm per MPa of applied fluid pressure P. This was measured as an apparent sample expansion, and was independent of dummy sample material or fluid used. A linear correction for this was applied to all data, which, for a standard, 4 mm long sample, had a maximum magnitude of +0.05 % strain at 100 MPa of CO_2 pressure (compared with coal sample strains of 0.6-0.8 % at these conditions). From the observation that the use of CO_2 or He did not influence the apparatus stiffness determined, we further infer that any changes in CO_2 or He permittivity with pressure did not significantly influence the sensitivity of the eddy current sensor.

3.2.4. Experimental procedure

3.2.4.1. Determining linear strain response vs. CO_2 pressure

As indicated earlier, we determined the net swelling strains in of our coal samples in four directions, *i.e.* perpendicular to the bedding (z-direction) and parallel to the bedding in the x-, y- and intermediate or xy-directions (Fig. 1). For each sample, and each different direction, a separate experiment was performed, measuring strain as a function of CO_2 pressure in each case.

In setting up each run, the sample was placed in the sample holder and mounted in the sample/sensor assembly located on the closure nut of the vessel (Fig. 2). The distance between the eddy current sensor tip and the steel target attached to the sample was then set between 100 and 140 μm to ensure that the sensor would operate with the range of linear sensitivity (25.14 $mV \cdot \mu m^{-1}$) as the sample expanded. The closure nut plus sample-sensor assembly were then screwed into the pressure vessel and the complete system was mounted in the water bath, set at a temperature of 40 °C (Fig. 3). The air in the foam-polystyrene box was then heated to 38.6 °C, while continuously homogenising the air inside using the fan. After settling for approximately 2 h to reach thermal equilibrium, the high pressure system was evacuated for 1-2 h. The pressure reading on the ISCO syringe pump controller was then trimmed to zero before commencing testing.

To initiate each run, CO_2 was introduced from the CO_2 bottle via the AirProducts line regulator (Fig. 3), and set at ~1.1 MPa pressure. This caused immediate swelling of the sample. After the sample reached a constant (equilibrium) strain (6-12 h), the CO_2 pressure was increased stepwise to ~3.6 MPa and finally to ~5.4 MPa (bottle CO_2 pressure), allowing equilibration at each stage. To increase the CO_2 pressure to 10.0 MPa, valve A and B (Fig. 3) were first closed, and the CO_2 pressure in the tubing leading to the pump was pressurised to ~12 MPa using the Tradinco diaphragm pump. This CO_2 was then slowly bled into the pressure vessel via valve B (Fig. 3) to increase the pressure to the desired value of 10.0 MPa. The system was subsequently closed using valve B and the ISCO pump used to control the CO_2 pressure.

Again after equilibration, the CO_2 pressure was increased to 20.0 MPa by manually programming the ISCO pump. From this set pressure on, a National Instruments Labview pump control module was used to increment the CO_2 pressure to 100.0 MPa in fixed steps of 10.0-13.7 MPa at pre-set time intervals of 1-1.5 h. After cycling the CO_2 back to 20.0 MPa in the same manner, the ISCO pump was set back to manual programme control at 10.0 MPa CO_2 pressure. The CO_2 was then manually released from the system in a stepwise manner to ~8.5 MPa and ~4.5 MPa, controlling the pressure after each step using the ISCO syringe pump during equilibration. Finally, all CO_2 was released by opening valves B and C (Fig. 3). and the system was evacuated.

Throughout the whole experiment, changes in CO_2 pressure were implemented slowly enough (1-5 min) to avoid temperature changes in the system. Sample dimensional changes were recorded during both upward pressurisation and during depressurisation.

3.2.4.2. Determining bulk elastic response

Elastic compression of the sample due to purely mechanical effects of fluid pressure increase was determined by applying a varying hydrostatic pressure P of He gas. Helium pressure was applied in steps of 1-5 MPa, up to 17 MPa (bottle pressure) by directly bleeding from the He supply bottle, via the AirProducts line regulator and valve A. Under the conventional assumption that He does not interact with the sample in any way (as discussed by Sakurovs et al., 2009), the dimensional change measured by the eddy current sensor can be used to calculate elastic strain in the measurement direction. The samples were tested in three directions, *i.e.* the x-, y- and z-directions (Fig. 1). recording dimensional changes during upward pressurisation only (a consequence of the line regulator used).

3.2.5. Data processing

For each experiment, the raw voltage signal produced by the eddy current sensor as a result of sample expansion/contraction was scaled using the calibration coefficient of 25.14 $mV \cdot \mu m^{-1}$ (Section 2.3.3.3) to yield apparent displacement in μm. After correcting for apparatus distortion, the linear strain e of the sample in the x-, y-, xy- and z-directions (Fig. 1). was calculated as a function of time using the definition $e_i = (\Delta L_i / L_{0i}) \cdot 100\%$, where ΔL_i is the sample expansion in direction i, and L_{0i} is the starting dimension of the sample in the measurement direction i, as determined prior to incorporation in the pressure vessel. Note accordingly that the starting dimension of the sample (L_{0i}) is defined here as the length in the x-direction (L_{0x}), in the y-direction and z-directions (L_{0y} , L_{0z}) and in the diagonal (xy-direction) of the cylinder before testing (L_{0xy} , see Table 1, Fig. 1). Because thermal expansion of the samples during heating of the system was approximately equal to contraction of the samples due to evacuation, and because both are of the order of only 0.01 % strain, we ignore these effects in the calculation of linear strain e_i.

For individual samples and measurement directions, the equilibrium strain response e_i^{eq} to CO_2 pressure change was taken as the asymptotic strain at the end of each CO_2 pressure step. These equilibrium or near-equilibrium strains were ultimately plotted as a function of CO_2 pressure P. The equilibrium strain response of the samples exposed to He as a pore fluid, was defined and treated in an identical manner.

Sample	P	e_x^{eq} (CO_2)	P	e_y^{eq} (CO_2)	P	e_{xy}^{eq} (CO_2)	P	e_z^{eq} (CO_2)
	(MPa)	(%)	(MPa)	(%)	(MPa)	(%)	(MPa)	(%)
364-1	0.0000	0.0000	0.0000	0.0000	0.0000	0.0000	0.0000	0.0000
	1.1384	0.2704	1.2312	0.2424	1.1684	0.3129	1.2254	0.3739
	3.5809	0.4691	3.7227	0.4055	3.5512	0.5168	3.6539	0.6533
	5.3614	0.5506	5.4127	0.4675	5.3830	0.6044	5.3592	0.7568
	9.9929	0.6261	9.9955	0.5296	9.9656	0.6829	10.0043	0.8596
	19.9906	0.6235	19.9775	0.5252	19.9813	0.6752	19.9901	0.8643
	30.0143	0.6097	29.9964	0.5191	29.9769	0.6577	30.0039	0.8571
	40.0074	0.5925	39.9924	0.5066	39.9823	0.6374	40.0182	0.8428
	50.0056	0.5742	49.9885	0.4920	49.9823	0.6154	49.9962	0.8278
	60.0268	0.5557	59.9873	0.4751	59.9775	0.5940	60.0115	0.8120
	70.0133	0.5371	69.9990	0.4567	69.9837	0.5719	70.0073	0.7956
	80.0191	0.5176	79.9893	0.4350	79.9878	0.5488	79.9970	0.7730
	89.9953	0.4978	89.9662	0.4146	89.9820	0.5259	90.0066	0.7486
	100.0074	0.4784	100.0103	0.3947	99.9805	0.5028	100.0280	0.7248
364-2	0.0000	0.0000	0.0000	0.0000	0.0000	0.0000	0.0000	0.0000
	1.1815	0.2946	1.2254	0.3403	1.1564	0.3288	1.1368	0.3629
	3.4933	0.4994	3.6336	0.5557	3.6310	0.5582	3.6727	0.6534
	5.4478	0.5913	5.4063	0.6429	5.4725	0.6522	5.4576	0.7834
	9.9912	0.6609	10.0047	0.7214	9.9834	0.7341	9.9779	0.9064
	19.9907	0.6547	19.9875	0.7147	19.9662	0.7291	19.9569	0.9023
	29.9928	0.6399	29.9857	0.7013	29.9668	0.7131	29.9765	0.8890
	40.0067	0.6228	39.9883	0.6861	39.9841	0.6944	39.9707	0.8718
	50.0085	0.6051	49.9929	0.6691	49.9807	0.6728	49.9790	0.8531
	60.0087	0.5857	59.9938	0.6515	59.9660	0.6512	59.9793	0.8328
	70.0112	0.5658	70.0135	0.6326	69.9790	0.6285	69.9856	0.8116
	79.9948	0.5439	79.9969	0.6128	79.9887	0.6064	79.9791	0.7877
	89.9932	0.5235	89.9982	0.5930	89.9876	0.5829	89.9619	0.7637
	100.0008	0.5019	100.0062	0.5726	99.9801	0.5594	99.9821	0.7412
364-3	0.0000	0.0000	0.0000	0.0000	0.0000	0.0000	0.0000	0.0000
	1.1672	0.2611	1.1239	0.3004	1.1523	0.3397	1.1859	0.3984
	3.5743	0.4481	3.5889	0.5238	3.8652	0.6108	3.6229	0.6694
	5.3463	0.5266	5.3884	0.6046	5.3621	0.6844	5.2793	0.7663
	9.9893	0.5919	9.9873	0.6815	9.9780	0.7786	9.9889	0.8636
	19.9979	0.5859	19.9640	0.6766	19.9657	0.7746	19.9766	0.8640
	31.9987	0.5641	29.9740	0.6631	29.9616	0.7576	33.6910	0.8521
	44.0060	0.5410	39.9836	0.6470	39.9802	0.7387	47.3878	0.8329
	55.9934	0.5169	49.9772	0.6299	49.9810	0.7155	61.0994	0.8090
	67.9798	0.4929	59.9836	0.6120	59.9820	0.6931	74.7753	0.7788
	79.9808	0.4684	69.9674	0.5925	69.9783	0.6682	88.4854	0.7515
	91.9959	0.4432	79.9878	0.5727	79.9869	0.6438		
			89.9835	0.5519	89.9845	0.6196		

Table 2 (opposite page). List of linear strains measured for all samples equilibrated with CO_2 during stepwise increased pressure. The strains given are net linear strains e_x^{eq} (// to bedding), e_y^{eq} (// to bedding), e_{xy}^{eq} (// to bedding) and e_z^{eq} (⊥ to bedding). Note that linear strains measured with decreasing CO_2 pressure are not tabulated but are plotted in Fig. 5.

Sample	P	e_x^{eq} (CO_2)	e_y^{eq} (CO_2)	e_z^{eq} (CO_2)
	(MPa)	(%)	(%)	(%)
364-1	2.10	-0.00934	-0.00830	-0.01837
	4.00	-0.01601	-0.01836	-0.02916
	7.00	-0.02743	-0.03350	-0.04843
	10.00	-0.03969	-0.04398	-0.06176
	12.00	-0.04896	-0.05551	-0.07026
	15.00	-0.05793	-0.06516	-0.08360
	16.80	-0.06421	-0.06996	-0.09411
	0.00	*	*	*
364-2	2.00	0.00970	0.00948	0.01634
	4.00	0.01762	0.01679	0.02664
	7.00	0.02971	0.03147	0.04169
	10.00	0.04067	0.04283	0.05666
	12.00	0.04934	0.05055	0.06852
	15.00	0.05996	0.06287	0.08159
	17.10	0.06674	0.07135	0.09098
	0.00	*	0.00117	0.00827
364-3	2.00	0.00814	0.01328	0.00405
	4.00	0.01661	0.02462	0.01391
	7.00	0.02801	0.03708	0.02788
	10.00	0.04026	0.05112	0.04125
	12.00	0.04878	0.06179	0.05193
	15.00	0.05942	0.07362	0.06730
	17.10	0.06942	0.08368	0.07782
	0.00	0.00013	0.00456	0.00611

Table 3. List of linear strains measured for all samples during stepwise increase and instant release of He pressure. Strains are net linear strains e_x^{eq} (// to bedding), e_y^{eq} (// to bedding) and e_z^{eq} (⊥ to bedding). The asterisk (*) denotes strains not measured after depressurisation.

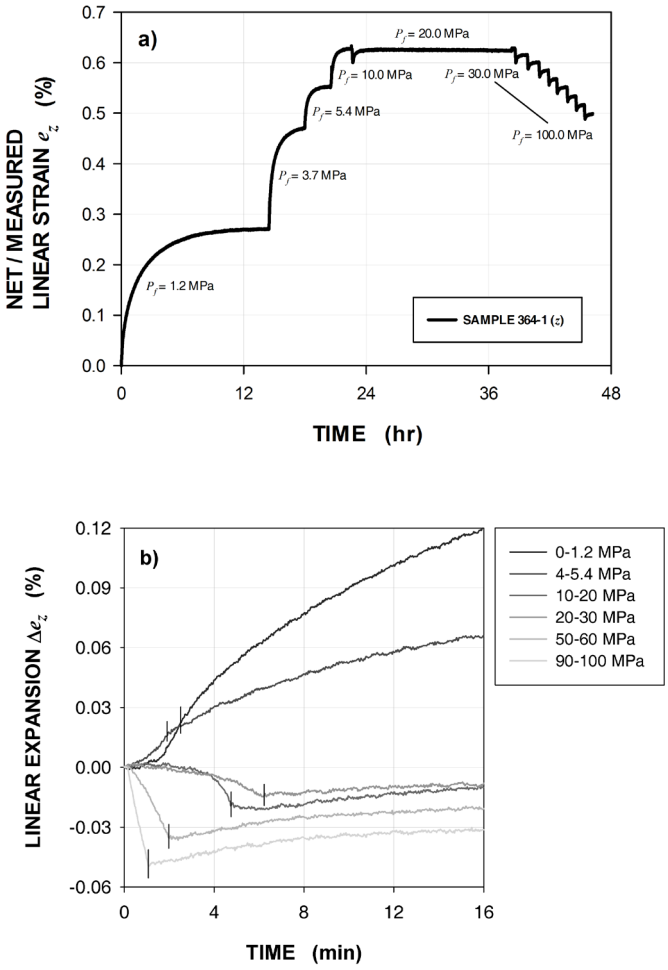

Fig. 4. a) Linear strain in z-direction of sample 364-1 measured in response to stepping CO_2 pressures as a function of time at a constant temperature of 40.0 °C. b) Linear strain change (Δe_z) in the z-direction of sample 364-1 measured in response to stepping CO_2 pressures as a function of the first 16 min in time (t) of each pressure step, at a constant temperature of 40.0 °C. The vertical marks crossing the curves indicate the moment at which the CO_2 pressure step ends (i.e. when P becomes constant). The plots show equilibrium was reached in 1-15 h, and demonstrate a transition from a rapid expansion in the at low CO_2 pressure steps to a combination of initial contraction followed by expansion in high CO_2 pressure steps.

3.3. Results

Dilatometry data obtained for samples of treated with CO_2 are presented in Fig. 4 and Fig. 5. Fig. 4 shows typical data illustrating how the strain evolved with time during individual experiments. Fig. 5 shows the dependence of equilibrium strains e_i^{eq} on CO_2 pressure for all samples tested. The development of equilibrium strain with He pressure for all samples is shown in Fig. 6. All equilibrium data obtained during upwards pressurisation are tabulated in Table 2 (CO_2 experiments) and Table 3 (He experiments). Throughout, we adopt the convention that fluid pressure (*P*), as well as expansion (linear strain e_i) is measured positive. We note that none of the samples failed mechanically, or showed any signs of damage or dimensional change as a result of the application of high CO_2 or He pressure, at least at the scale of visual inspection and micrometer resolution.

3.3.1. Linear expansion due to CO_2 exposure

Fig. 4a shows the total linear strains (e_z) measured in the z-direction for sample 364-1 as a function of time, while Fig. 4b shows changes in strain (Δe_z) versus time elapsed after each increment in CO_2 pressure is initiated during upwards pressurisation. Recall that each pressure increment was implemented in 1-5 min. In a qualitative sense, these data are representative for all experiments performed with CO_2. Two, clearly different pressure-dependent regimes can be recognised in the behaviour shown in Fig. 4b. These were seen in all samples tested. Below 10 MPa CO_2 pressure, the evolution of Δe_z with time due to a stepwise increase in CO_2 pressure is dominated by a continuously increasing change in linear strain with time. Full equilibration of the system takes approximately 6-15 h at these CO_2 pressures (Fig. 4a). Above 20 MPa CO_2 pressure, however, an initial pressure-dependent contraction is observed over the full 1-5 min that the CO_2 pressure stepping operation takes (vertical ticks shown in Fig. 4b). When the target pressure is reached in each step, the sample expands in a time-dependent manner. At these pressures, it takes approximately 1-2 h for equilibrium to be reached after each pressure step (Fig. 4a).

The asymptotic or equilibrium strain values (e_i^{eq}) obtained after 1-12 h of equilibration time (depending on CO_2 pressure) are presented as a function of CO_2 pressure for all samples in Fig. 5a-c. Each graph shows the net expansion curves obtained for all four directions investigated per sample. Contraction data obtained upon depressurisation are also shown, and demonstrate closely reversible behaviour. The data presented in Fig. 5 show that all samples exhibit net expansion in response to saturation with CO_2 over the full pressure range of 0-100 MPa. However, two pressure domains can again be recognised in all equilibrium strain versus CO_2 pressure curves (Fig. 5a-c). Below 10 MPa applied CO_2 pressure, all samples exhibit a sharp increase in linear strain up to a peak strain of approximately 0.9 % measured perpendicular to the coal bedding (e_z^{eq}), and lying between 0.5 % and 0.8 % (e_x^{eq}, e_y^{eq}, e_{xy}^{eq}) for all directions measured in

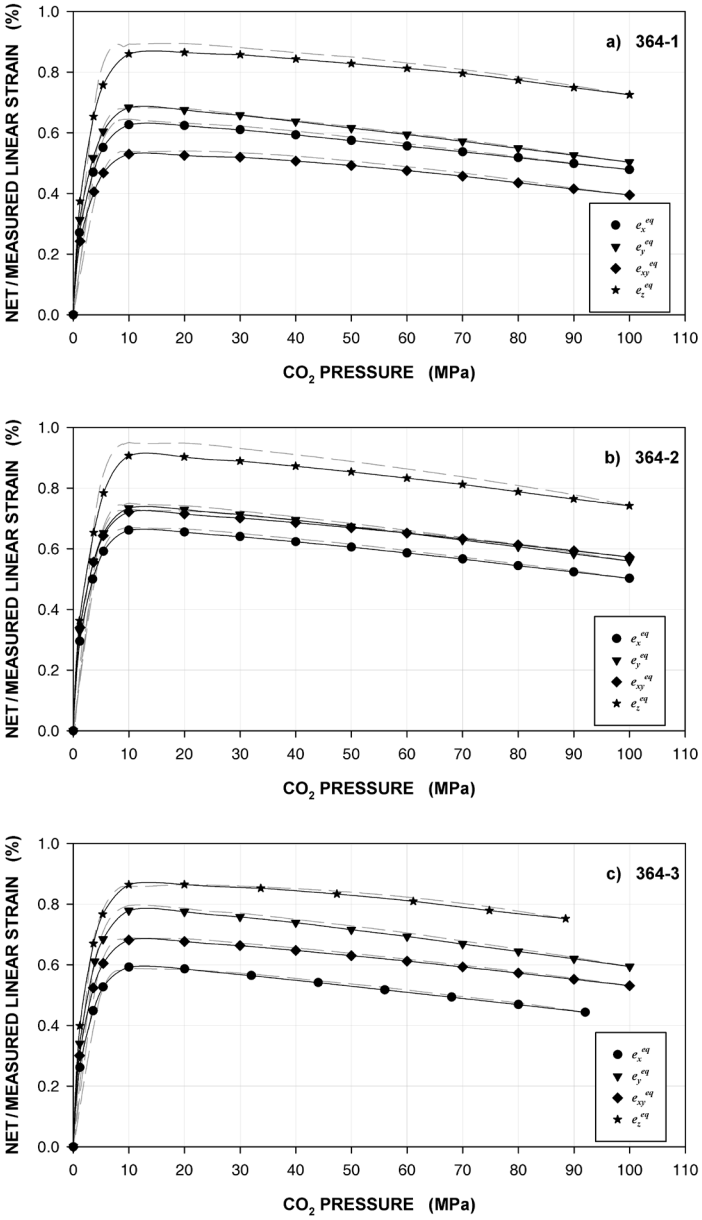

Fig. 5. Linear strain at equilibrium (e_i^{eq}) versus applied CO_2 pressure (P) as measured in 4 directions (x, xy, y and z – see Fig. 1) using the eddy current dilatometer for a) sample 364-1, b) sample 364-2 and c) sample 364-3. The strains were calculated relative to the initial sample lengths as listed in Table 1. All samples show expansion in response to equilibration with CO_2 over the pressure range of 0-100 MPa CO_2 pressure. A transition from expansion-dominated to contraction-dominated behaviour can be observed for all samples at around 10-20 MPa CO_2 pressure. Solid lines show evolution of strains with increasing CO_2 pressure. Dashed lines show evolution with decreasing CO_2 pressure. Note the reversibility of strain response over the full range of CO_2 pressures.

the bedding plane. After attaining these maximum strain values at 10-15 MPa CO_2 pressure, all samples show a gradual decrease in linear equilibrium strain to values between 0.4 % and 0.7 % at 100 MPa CO_2 pressure. Note that the highest CO_2 pressure of 100 MPa was insufficient to return the samples to dimensions similar to those pertaining in the initial evacuated state at 40 °C.

From Fig. 5, each sample tested with CO_2 clearly shows an anisotropic strain response. In samples 364-1 and 364-2, the linear strain responses in the x-, y- and xy-directions fall within a strain band of 0.10-0.15 % of each other, whereas the response in the z-direction is markedly higher (Fig. 5a,b). Sample 364-3, on the other hand, exhibits a smaller difference in expansion in the z-direction compared to the other directions (Fig. 5c). The variability in linear strain in the x-, xy- and y-directions here falls within a band of 0.20 % strain. In addition, the linear strain response in the y-direction of this sample (*i.e.* normal to the face cleat plane) is consistently higher than that in the x- and xy-directions. Also the rate of decrease in linear strain beyond a CO_2 pressure of 20 MPa is slightly less pronounced in the z-direction of sample 364-3 (Fig. 5c) than in the other samples and directions. Overall, for all 3 samples, the linear strains measured perpendicular to bedding (z-direction) were approximately 1.4 times the average linear strains measured in the bedding plane (mean of the strain in the x-, y-, and xy-directions).

3.3.2. Strain data obtained in the He tests

The response of our samples to exposure to non-adsorbing high pressure He was measured up to pressures of 17 MPa (bottle pressure) (Table 3). Recall from section 3.2.3.1 that, because of excessive leakage of the ISCO seals with respect to He, the ISCO syringe pump could not be used to generate higher pressures. The equilibrium strain data obtained for our samples in 3 directions (x-, y- and z-direction) are plotted as a function of He pressure in Fig. 6a-c. In contrast to the CO_2 experiments, all samples show near-linearly increasing compression (compressive strain) with increasing He pressure, in all directions measured. The final strains after instant depressurisation to ambient pressure (measured for sample 364-2 and 364-3) showed no permanent deformation, taking into account uncertainties in correcting for the initial offset caused by the settling effect, as described in section 3.2.3.3. From this, we infer that sample deformation was elastic.

For each sample tested, subtle differences are visible in Fig. 6 in the slope of the data obtained per measurement direction. These are small, however, indicating a more or less isotropic strain response to increasing He pressure. Assuming that the behaviour of all samples is indeed elastic, averaging the slopes of the data over the three directions measured for each sample gives its bulk volumetric stiffness, or bulk modulus *K*. This results in values for the bulk modulus *K* of our samples of 7.651 GPa (sample 364-1), 7.746 GPa (sample 364-2) and 7.413 GPa (sample 364-3). These values, listed in

Table 3, agree well with the bulk moduli reported in the literature for coals of similar rank, *e.g.* by Morcote et al. (2010). These authors determined values of 4-9 GPa for bituminous coal and semi-anthracite by means of sonic velocity measurements made at confining pressures of 0-40 MPa.

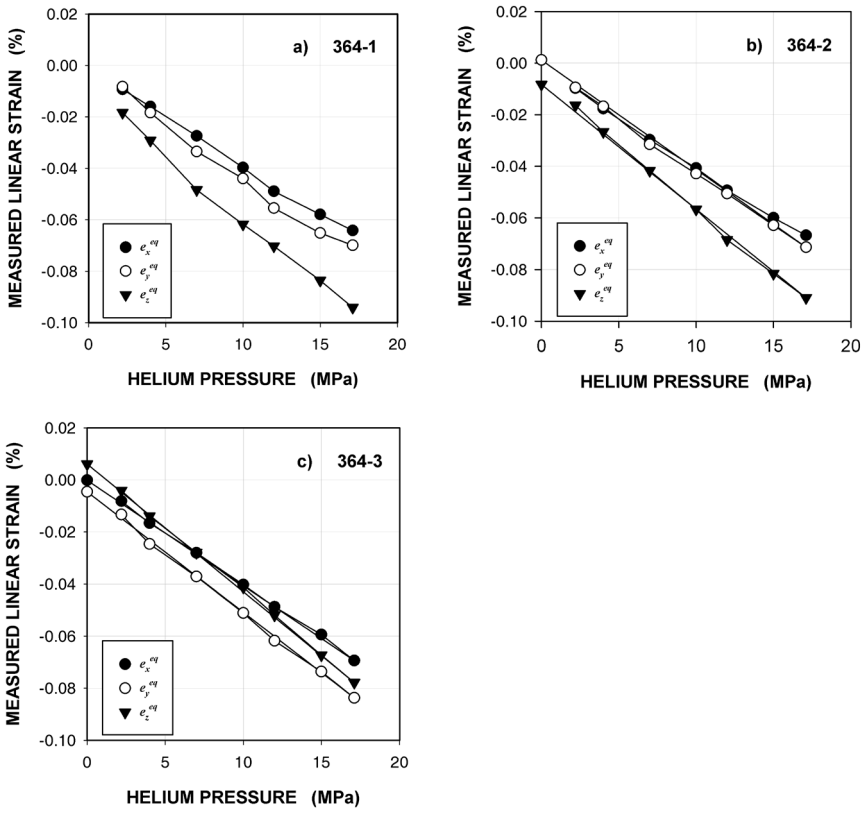

Fig. 6. Linear strain (e_i^{eq}) versus applied He pressure (P) as measured in 3 directions (x, y and z – see Fig. 1) using the eddy current dilatometer for a) sample 364-1, b) sample 364-2 and c) sample 364-3. All strains were calculated relative to the initial sample lengths as listed in Table 1, and show a contraction of -0.08 % at 17 MPa of applied He pressure. Bulk moduli were calculated from the mean strain response of each for each sample, yielding K = 7.651 GPa for sample 364-1, 7.746 GPa for sample 364-2 and 7.413 GPa for sample 364-3.

3.4. Discussion

The present dilatometry experiments have shown that significant net swelling or expansion of matrix-scale coal samples occurs due to interaction with CO_2 at pressures in the range 0 to 100 MPa at a constant temperature of 40.0 °C (Fig. 5a-c). Our data demonstrate a transition from an expansion-dominated to a contraction-dominated strain response that occurs in all samples above ~15 MPa applied CO_2 pressure (Fig. 5a-c). The same samples exhibit reversible linear compression when pressurised with non-adsorbing He (Fig. 6a-c). This strongly suggests that the strain response of our samples is the net result of competition between adsorption-induced swelling versus elastic compression, which would be consistent with the behaviour observed in experiments reported by Moffat and Weale (1955) for coal equilibrated with CH_4, and with the behaviour predicted by recent thermodynamic/thermo-mechanical models for CO_2-induced coal swelling (Pan and Connell, 2007; Vandamme et al., 2010). The present data provide important evidence for the operation of these competing effects in determining the volumetric response of coal exposed to CO_2 because they are the first systematic swelling data reported for CO_2 pressures beyond ~15 MPa, where the transition from net expansion to net contraction occurs.

In the following discussion of our data, we will start by computing the net volumetric strain of our samples from the net linear strains measured in response to the CO_2 pressure applied. We go on to subtract the volumetric compression of the samples calculated from our He-derived bulk modulus data. In this way, we compute the swelling strain response of the coal matrix material due specifically to adsorption of CO_2 by the samples. We subsequently compare this swelling strain response with data on the absolute adsorption of CO_2 by Brzeszcze 364 coal, as reported by Gensterblum et al. (2010) to obtain a relationship between adsorption-induced swelling strain and adsorbed CO_2 concentration, and we propose a model to underpin the relationship found. Finally, we compare our swelling-sorption data with those reported in the literature, and consider the implications of our results for understanding CO_2/CH_4 exchange and transport during ECBM production operations.

3.4.1. Net versus adsorption-induced swelling strain and dependence on CO_2 pressure

In this study, we have determined the elastic compressibility of coal by means of hydrostatic pressurisation of the solid coal structure with non-adsorbing He (Fig. 6). All swelling strain in the coal, which is measured when exposed to CO_2 (Fig. 5), must be attributed to other processes. Since all volumetric effects observed here when CO_2 is added are fully reversible, and because our experiments are conducted at constant temperature, we infer that the expansion effects seen in our samples must be due to physical adsorption of CO_2, which, as mentioned earlier, is well-known to cause swelling in coal (*e.g.* Day et al., 2008; Durucan et al., 2009; van Bergen et al., 2009; Day et al., 2010; Majewska et al., 2010).

Sample	P	e_1^{eq} (CO_2)	e_2^{eq} (CO_2)	e_3^{eq} (CO_2)	e_v^{eq} (CO_2)	e_{el}^{eq} (CO_2)	e_{ads}^{eq} (CO_2)
	(MPa)	(%)	(%)	(%)	(%)	(%)	(%)
364-1	0.00	0.00	0.00	0.00	0.00	0.00	0.00
	1.14	0.37	0.39	0.24	1.00	-0.01	1.02
	3.58	0.65	0.68	0.40	1.74	-0.05	1.78
	5.36	0.76	0.83	0.47	2.06	-0.07	2.13
	9.99	0.86	0.95	0.53	2.34	-0.13	2.47
	19.99	0.87	0.94	0.52	2.33	-0.26	2.60
	30.01	0.86	0.89	0.52	2.27	-0.39	2.66
	40.01	0.85	0.85	0.51	2.20	-0.52	2.73
	50.01	0.84	0.81	0.49	2.14	-0.65	2.79
	60.03	0.82	0.78	0.47	2.08	-0.78	2.87
	70.01	0.81	0.76	0.46	2.03	-0.92	2.94
	80.02	0.79	0.75	0.43	1.98	-1.05	3.02
	90.00	0.77	0.74	0.41	1.92	-1.18	3.10
	100.01	0.75	0.73	0.39	1.87	-1.31	3.17
364-2	0.00	0.00	0.00	0.00	0.00	0.00	0.00
	1.18	0.36	0.35	0.28	0.99	-0.02	1.01
	3.49	0.65	0.57	0.49	1.72	-0.05	1.76
	5.45	0.78	0.66	0.59	2.03	-0.07	2.10
	9.99	0.91	0.74	0.65	2.31	-0.13	2.44
	19.99	0.91	0.74	0.65	2.29	-0.26	2.55
	29.99	0.90	0.72	0.63	2.25	-0.39	2.64
	40.01	0.88	0.71	0.61	2.20	-0.52	2.72
	50.01	0.86	0.69	0.60	2.15	-0.65	2.79
	60.01	0.85	0.67	0.57	2.09	-0.77	2.86
	70.01	0.83	0.65	0.55	2.03	-0.90	2.93
	79.99	0.80	0.63	0.53	1.96	-1.03	2.99
	89.99	0.78	0.61	0.51	1.90	-1.16	3.06
	100.00	0.76	0.58	0.49	1.83	-1.29	3.12
364-3	0.00	0.00	0.00	0.00	0.00	0.00	0.00
	1.15	0.40	0.34	0.26	1.00	-0.02	1.02
	3.68	0.67	0.61	0.45	1.73	-0.05	1.78
	5.37	0.77	0.69	0.53	1.98	-0.07	2.05
	9.98	0.87	0.78	0.59	2.24	-0.13	2.37
	19.98	0.87	0.78	0.59	2.23	-0.27	2.50
	30.00	0.86	0.76	0.57	2.19	-0.40	2.59
	40.00	0.85	0.74	0.55	2.14	-0.54	2.68
	50.00	0.84	0.72	0.53	2.09	-0.67	2.76
	60.00	0.82	0.70	0.51	2.03	-0.81	2.84
	70.00	0.80	0.68	0.48	1.97	-0.94	2.91
	80.00	0.79	0.66	0.46	1.90	-1.08	2.98
	90.00	0.77	0.63	0.44	1.84	-1.21	3.06

Table 4 (opposite page). List of computed principal and volumetric strains for all samples subjected to increasing CO_2 pressure steps, i.e. the principal strains e_1 ($\perp$ to bedding), e_2 (// to bedding) and e_3 (// to bedding), plus the net volumetric strain (e_v). Computed values of the adsorption-induced volumetric swelling strain (e_{ads}) are also listed. Note that the principal strains e_2 and e_3 were obtained by fitting a strain ellipse to the net linear strain data (e_i^{eq}) in the x-, xy- and y-direction (see Table 2) using a Matlab least-squares method algorithm. The elastic volumetric compression (e_{el}) was computed from the applied CO_2 pressure and the bulk modulus K of the samples determined using He as pore fluid after exposure to CO_2 (see Table 3). Adsorption-induced volumetric swelling strains (e_{ads}) were calculated from the relation $e_{ads} = e_v - e_{el}$. All values listed are based on the strain data reported for upward pressure stepping in Table 2.

On this basis, and treating both compressive elastic strains (e_{el}^{eq}) and adsorption-induced swelling strains (e_{ads}^{eq}) as independent and small enough to be additive in determining the net volumetric strain (e_v^{eq}) resulting from exposure of coal matrix material to CO_2, we can write

$$e_v^{eq} = e_{ads}^{eq} + e_{el}^{eq} \tag{1}$$

where the net volumetric strain e_v, is the quantity measured in the experiments reported here. From the theory of small strains, the scalar quantities e_v^{eq}, e_{el}^{eq} and e_{ads}^{eq} are, of course, the sum of the principal components of the corresponding strain tensors. The adsorption-induced swelling strain e_{ads}^{eq} of the coal matrix can accordingly be obtained by re-arranging (1) to yield

$$e_{ads}^{eq} = e_v^{eq} - e_{el}^{eq} = e_v^{eq} + \frac{P}{K} \tag{2}$$

where we recall that K is the elastic bulk modulus of the coal matrix (*cf.* Vandamme et al., 2010).

To obtain e_{ads}^{eq} from (2), we start by calculating the net volumetric strain e_v^{eq} = (e_1^{eq}+e_2^{eq}+e_3^{eq}). As seen from Fig. 5a-c, the net linear strains in our samples are anisotropic, where the strain perpendicular to the bedding is the highest, with smaller, relatively isotropic strains occurring in the bedding. We therefore assume that the maximum principal strain e_1^{eq} is the net linear strain measured perpendicular to the bedding, and that the two remaining principal strains, e_2^{eq} and e_3^{eq}, are orientated in the bedding plane. In the bedding plane, expansion in the y-direction appears to be slightly higher than in the x- or xy-directions, and is presumably related to the orientation of the face cleats, which are normal to the y-direction (Fig. 1). To evaluate the anisotropy of strain in the bedding plane, strain ellipses were fitted to the net linear strain data obtained for the x-, y- and xy-directions at equilibrium (see Table 2), by means of a least-squares method. This yielded the direction and magnitude of the net principal strains e_2^{eq} and e_3^{eq} within the bedding. The fitting procedure was performed for each

sample and each CO_2 pressure at which the samples were equilibrated, to uncover any pressure dependent variations in the directions of the principal axes e_2^{eq} and e_3^{eq}. Table 4 lists the magnitudes of the net principal strains as well as the net volumetric strains obtained from the data given in Table 2. It was found that all samples show a similar net volumetric response to CO_2 (similar e_v^{eq}), although the net principal strains varied slightly in magnitude. The orientation of the principal strains e_2^{eq} and e_3^{eq} in the bedding were relatively unaffected by CO_2 pressure. From inspection of the effect of CO_2 pressure on e_v^{eq} values listed in Table 4 and plotted in Fig. 7, the data consistently reveal a maximum net volumetric strain e_v^{eq} of ~2.3 % occurring at around 10-15 MPa.

We now calculate the elastic volumetric strain e_{el}^{eq} for each sample exposed to CO_2 and for each applied CO_2 pressure P, using the bulk modulus data obtained for the samples from the He experiments (*i.e.* 7.651 GPa for sample 364-1, 7.746 GPa for sample 364-2 and 7.413 GPa for sample 364-3) and employing the second term on the right-hand side of (2), *i.e.* the expression $e_{el}^{eq} = P/K$. The computed elastic volumetric strains e_{el}^{eq} are listed in Table 4 and plotted in Fig. 7. Note that all elastic volumetric strain values obtained for CO_2 pressures higher than 17 MPa are extrapolated from our He strain data, using the bulk moduli determined for the tested samples at He pressures up to 17 MPa. It was thus assumed that the samples were linearly elastic in the range 17-100 MPa, and can be described by the relation on the right-hand side of (2).

Finally, the adsorption-induced swelling strain e_{ads}^{eq} of our samples can be computed from (2). The results are listed in Table 4 and presented in Fig. 7 as a function of CO_2 pressure (P) for all samples exposed to increasing CO_2 pressure. For all samples, the adsorption-induced swelling strain (e_{ads}^{eq}) continuously increases over the full range of CO_2 pressure explored (0-100 MPa). The data clearly illustrate the dominance of elastic compression over adsorption-related swelling as a volumetric straining process in coal above 10-15 MPa CO_2 pressure. Note, however, that the competition is not limited to these higher CO_2 pressures. Our results imply that the strain contributions by the competing-processes of adsorption-induced swelling versus elastic compression are determined at all CO_2 pressures by the concentration of adsorbed species in the coal matrix on the one hand (influencing e_{ads}^{eq}) versus the stiffness of the elastic framework of the coal matrix on the other (influencing e_{el}^{eq}). The balance between the two processes will be markedly different when adsorbate fluids such as Ar, N or CH_4 are used instead of CO_2. Indeed, these fluids typically exhibit lower sorption capacities (*e.g.* Chaback et al., 1996; Fitzgerald et al., 2005) and display a smaller net strain response (*e.g.* van Bergen et al., 2009; Day et al., 2010).

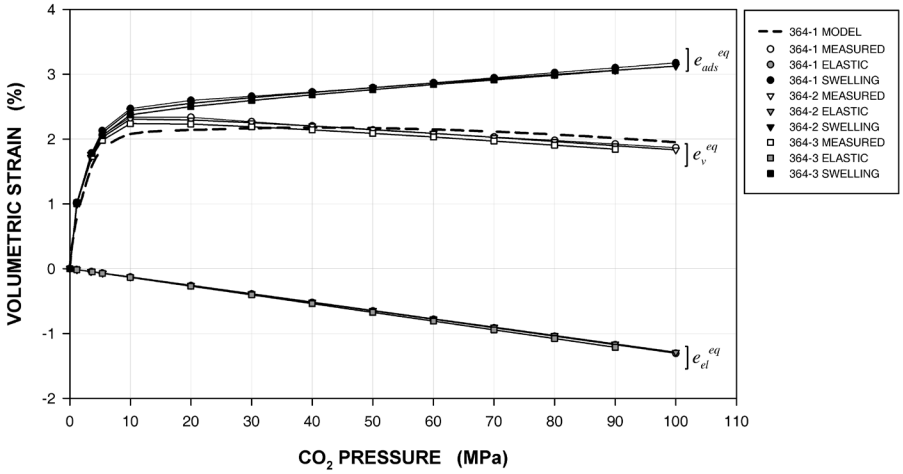

Fig. 7. Net volumetric strain (e_v^{eq}), elastic volumetric compression (e_{el}^{eq}) and adsorption-induced swelling strain (e_{ads}^{eq}) versus applied CO_2 pressure for all three samples exposed to increasing CO_2 pressure. Elastic volumetric compression (e_{el}^{eq}) was calculated from the bulk modulus determined from He injection tests. The adsorption-related swelling strain was calculated for each CO_2 pressure using the relation $e_{ads}^{eq} = e_v^{eq} - e_{el}^{eq}$. Darker line shows model equation (7), applied for $\Omega_0 = 1.36 \rightarrow 1.46 \cdot 10^{-29}$ $m^3 \cdot molecule^{-1}$.

3.4.2. Net versus adsorption-induced swelling strain and dependence on adsorbed CO_2 concentration

In the following, we will consider the dependence of net volumetric strain (e_v^{eq}), and adsorption-related swelling strain e_{ads}^{eq} upon absolute adsorption of CO_2 at equilibrium, *i.e.* on the adsorbed CO_2 concentration *C*. We do this first by comparing our adsorption-induced swelling versus CO_2 pressure data (Table 4, Fig. 7) with the adsorption versus pressure data presented for Brzeszcze coal by Gensterblum et al. (2010), and second by comparing our data with a combined thermodynamic/ thermomechanical model for adsorption plus elastic compression.

3.4.2.1. Adsorption-induced swelling response of coal exposed to CO_2

The relationship between the volumetric swelling strain (e_{ads}^{eq}) resulting from our dilatometry experiments, and the absolute adsorption (*C*) data reported by Gensterblum et al. (2010) is shown in Fig. 8. Gensterblum et al. (2010) report manometric sorption experiments performed on Brzeszcze 364 coal (particles <2 mm) at CO_2 pressures up to 20.5 MPa and at a fixed temperature of 45 °C, which is slightly higher than the 40 °C used here. To construct Fig. 8, volumetric swelling strain data obtained at CO_2 pressures up to 30 MPa were taken from our dataset (CO_2 pressures up to 100

MPa) and plotted against the absolute adsorption *C* as interpolated from the data of Gensterblum et al. (2010). A data point at 30 MPa of CO_2 pressure was added to Fig. 8 by graphically extrapolating the *C* vs. *P* trend obtained by Gensterblum et al. (2010) to complement our e_{ads}^{eq} data at this pressure. We consider extrapolation beyond 30 MPa to be too unreliable to be useful. Note that although Hol et al. (2011b) recently applied a new method to determine the total uptake of CO_2 by the samples tested in this study, the method does not allow discrimination between adsorbed and free CO_2 taken up by the samples, so that the data are not used in Fig. 8.

It is clear from Fig. 8, that the relationship between volumetric swelling strain e_{ads}^{eq} and adsorbed CO_2 concentration *C* is approximately linear at least up to CO_2 pressures of ~20 or 30 MPa. Fitting a linear function to the data in the range 0-30 MPa CO_2 pressure yielded a slope ($\partial e_{ads}^{eq}/\partial C$) of $1.23 \cdot 10^{-2}$ g·mmol^{-1} with a coefficient of determination (R^2) of 0.97. Taking this slope of $1.23 \cdot 10^{-2}$ g·mmol^{-1} (or $1.23 \cdot 10^{-2}$ kg·mol^{-1}) and taking the density of Brzeszcze 364 coal of to lie between 1400→1500 kg·m^{-3} (based on independent determinations of the mass and volume of the cylinders), implies a volumetric expansion of the coal samples of $8.20 \cdot 10^{-6} \rightarrow 8.79 \cdot 10^{-6}$ m^3·mole^{-1} of adsorbed CO_2 in the pressure range 0-30 MPa CO_2 pressure.

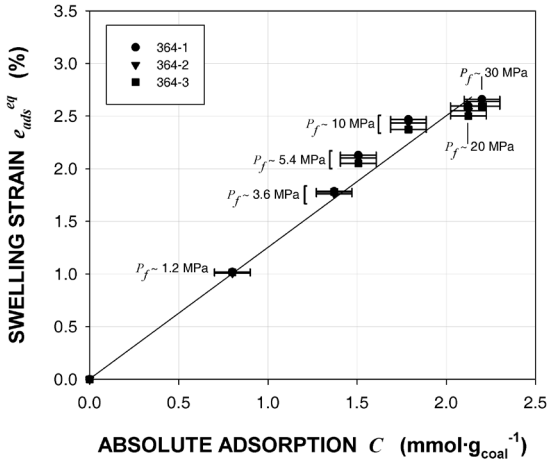

Fig. 8. Relationship between the adsorption-induced swelling strain (e_{ads}^{eq}) and absolute CO_2 adsorption (C) in mmol·g_{coal}^{-1}. The volumetric swelling strain (e_{ads}^{eq}) was determined as a function of CO_2 pressure in this study by subtracting the elastic compressive strain e_{el} from the total measured volumetric strain e_v^{eq}. Absolute adsorption data were adopted from the work of Gensterblum et al. (2010) on Brzeszcze 364 coal with a particle size <2 mm, and were graphically interpolated to match the CO_2 pressures applied in this study. Data are plotted for CO_2 pressures up to 30 MPa. Since the data of Gensterblum et al. (2010) are limited to pressures up to 20.5 MPa, the adsorbed concentration of CO_2 plotted at 30 MPa is estimated by graphical extrapolation of the C vs. P trend obtained by Gensterblum et al. (2010). A linear best-fit of the data yields a slope ($\partial e_{ads}^{eq}/\partial C$) of 1.23 %·$g_{coal}$· mmol^{-1}, or, when using dimensionless units of strain $1.23 \cdot 10^{-2}$ g_{coal}· mmol^{-1}.

3.4.2.2. A model for net volumetric strain versus adsorbed CO_2 content

We shall now consider the relationship between adsorption-induced swelling strain (e_{ads}^{eq}), net strain (e_v^{eq}) and adsorbed CO_2 concentration from a theoretical perspective. We start following Hol et al. (2011a) by assuming that small, cleat-free coal matrix samples consist entirely of nanoporous matrix material. Such samples are thus free of pores that would allow Darcian flow or storage of free (un-adsorbed) CO_2, and only able to take up CO_2 by diffusion and adsorption. In a system so defined, adsorption-induced swelling of the coal against the CO_2 pressure outside the sample means that work must be done as the outer boundaries of the coal framework are displaced. Under conditions of constant temperature T and zero effective stress σ_e (zero stress applied to the solid framework independently of the CO_2 pressure), the net volumetric strain of the coal sample is described by (2), which states that the net strain is the combined effect of elastic deformation of the solid coal skeleton plus adsorption-induced swelling.

Consider now the strain response e_{ads}^{eq} caused by CO_2 adsorption. The concentration $C(P)$ of adsorbed CO_2 molecules present in the coal body, when in equilibrium with CO_2 at a hydrostatic fluid pressure P, is given by the thermodynamic model recently developed by Hol et al. (2011a) as

$$C\left(P_f\right) = C_s\theta = \frac{C_s a_f \exp\left(\frac{\mu_{f0} - \Delta G_a}{kT}\right)}{1 + a_f \exp\left(\frac{\mu_{f0} - \Delta G_a}{kT}\right)} \tag{3}$$

Here, $C(P)$ is the equilibrium concentration of adsorbed CO_2 in mmol·g^{-1} or mol·kg^{-1}, C_s represents the (constant) number of potential adsorption sites per kg of coal, θ is the 'occupancy' (occupied fraction) of the available adsorption sites, a_f is the chemical activity of the free CO_2 at pressure P, and μ_{f0} is its potential in the reference state a_f = 1. The quantity ΔG_a represents the Gibbs energy that must be supplied to remove an adsorbed molecule of CO_2 from an adsorption site into the free CO_2 phase (Hol et al., 2011a), and is given $\Delta G_a = \Delta F_a + P\Delta V_a$, where ΔF_a is the Helmholtz free energy of attachment (which includes any changes in elastic energy stored in coal) and $\Delta V_a = (\Omega_0 - \Omega_f)$ is the difference between the partial or apparent molecular volume (Ω_0) of CO_2 in the adsorbed state and its molecular volume (Ω_f) in the free phase. With Ω_0 defined in this way, Ω_0 represents the volume change (swelling) of the coal per molecule of adsorbed CO_2 and the $P\Delta V_0$ term represents the pressure–volume work associated with adsorption of a single molecule.

This model (equation 3) predicts that, at conditions of constant temperature T and varying fluid pressure P, changes in adsorbed concentration C or site occupancy are a combined effect of two fundamental causes: (1) the changing pressure, density and hence activity and chemical potential of the free fluid phase, and (2) the changing availability of adsorption sites, which is expressed statistically through the pressure

dependence of ΔG_a via the ΔF_a and $P\Delta V_a$ terms (Hol et al., 2011a). For an ideal gas, a_f becomes equal to the gas pressure and (3) reduces to the widely applied Langmuir model (Hol et al., 2011a)

Making use of equation (3) for the adsorbed concentration $C(P)$, the volumetric swelling strain due to adsorption alone can be obtained provided we know the swelling strain associated with the adsorption of one molecule, assuming this is insensitive to C. For the adsorption of one molecule of CO_2 by a coal sample of initial volume V, the associated volumetric strain ${e_{ads}}^{mol}$ at equilibrium can be written

$$ {e_{ads}}^{mol} = \frac{\Omega_0}{V} = \frac{\Omega_0 \rho}{m} \tag{4} $$

where ρ is the initial density of the coal in kg·m^{-3} and m is the initial mass of the coal sample in kg. Multiplying by Avogadro's constant N_A, the volumetric strain (in mol^{-1}) associated with the adsorption of one mole of CO_2 adsorbed ${e_{ads}}^{mole}$ now becomes

$$ {e_{ads}}^{mole} = \frac{N_A \Omega_0 \rho}{m} \tag{5} $$

For a coal sample of mass m containing a concentration of C moles of adsorbed CO_2 per unit mass at equilibrium, the absolute number of moles adsorbed is Cm. Assuming that Ω_0 is constant across a limited range of CO_2 pressures, the volumetric strain response associated with adsorption is consequently given

$$ {e_{ads}}^{eq} = C(P) m {e_{ads}}^{mole} = C(P) N_A \Omega_0 \rho = C(P) V_0 \rho \tag{6} $$

where $V_0 = N_A \Omega_0$ is the apparent molar volume of the adsorbed CO_2 (*i.e.* the absolute change in coal volume when one mole of CO_2 is adsorbed). The net volumetric strain ${e_v}^{eq}$, determined experimentally, which includes both a) the elastic compressional response ${e_{el}}^{eq}$ of the coal sample to the imposed CO_2 pressure P, and b) the adsorption-induced swelling ${e_{ads}}^{eq}$, can thus be expressed using (1) and (2) as

$$ {e_v}^{eq} = {e_{ads}}^{eq} + {e_{el}}^{eq} = C V_0 \rho - \frac{P}{K} \tag{7} $$

This, like the model presented by Vandamme et al. (2010), predicts that the net volumetric response of a coal particle exposed to CO_2 is the result of competition between adsorption-induced swelling (here given explicitly by our thermodynamic model for C and hence ${e_{ads}}^{eq}$) and linear elastic compression of the sample, and is qualitatively in line with our experimental observations.

Moreover, the model presented here predicts a linear dependence of adsorption-induced swelling strain ${e_{ads}}^{eq}$ upon adsorbed concentration (equation 6), provided

that V_0 and ρ are roughly constant. Despite the minor temperature difference between our experimental data and that of Gensterblum et al. (2010), this linear dependence is closely consistent with the results presented in Fig. 8. On this basis, we infer that equation (6) provides a valid description of adsorption-induced swelling in the coal matrix samples used, at least up to 20-30 MPa CO_2 pressure. To examine this further, we calculate the partial molecular volume of CO_2 in the adsorbed state (Ω_0) by comparing (6) to the relationship between volumetric swelling strain e_{ads}^{eq} and adsorbed CO_2 concentration C represented in Fig. 8. Re-arranging (6) to yield Ω_0, gives

$$\Omega_0 = \frac{e_{ads}^{eq}}{C\left(P_f\right)N_A\rho} = \frac{\partial e_{ads}^{eq}}{\partial C}\cdot\frac{1}{N_A\rho} \tag{8}$$

Taking the slope ($\partial e_{ads}^{eq}/\partial C$) of the data in Fig. 8 to be $1.23\cdot10^{-2}$ g·mmol^{-1} for the pressure range 0-30 MPa, and the density of our coal samples to lie in the range 1400→1500 kg·m^{-3}, as described in section 3.4.2.1, we obtain an effective molecular volume of CO_2 in the adsorbed state (Ω_0) of $1.36\rightarrow1.46\cdot10^{-29}$ m^3·molecule^{-1} and a molar equivalent V_0 of $8.20\cdot10^{-6}\rightarrow8.79\cdot10^{-6}$ m^3·mole^{-1}. For comparison, these values of V_0 are one to one half of an order of magnitude smaller than the molar volume of liquid CO_2 ($V_f = 5.1\cdot10^{-5}$ m^3·mole^{-1} at P = 100 bar and T = 20 °C) or of dry ice ($V_s = 2.9\cdot10^{-5}$ m^3·mole^{-1}).

Inserting Ω_0 or V_0 into equation (6), we can now test the validity of (6) by using our thermodynamic model for C (equation 3) to predict e_{ads}^{eq} as a function of P, and by comparing the results obtained to our experimental data for e_{ads}^{eq} versus P (derived by subtracting e_{el}^{eq} from e_v^{eq}). To do this, we start with the assumption that at low CO_2 pressure, the occupancy θ of the available adsorption sites C_s is still low. For such a case, (3) reduces to the expression $C=C_s a_f \exp[(\mu_{f0}-\Delta G_a)/kT]$, and (6) can accordingly be written

$$e_{ads}^{eq} = V_0\rho\cdot a_f C_s \exp\left(\frac{\mu_{f0}-\Delta G_a}{kT}\right) \tag{9}$$

We next plot our measured e_{ads}^{eq} data versus the quantity $V_0\rho\cdot a_f$ determined for corresponding P values using $V_0=8.50\cdot10^{-6}$ m^3·mole^{-1} and ρ=1450 kg·m^{-3}. The CO_2 activity in the term $V_0\rho\cdot a_f$ was computed using the EoS for CO_2 developed by Span and Wagner (1996), taking a thermodynamic reference state defined at P=0.1 MPa and characterised by an e_{ads}^{eq} value interpolated from the data plotted in Fig. 7. In this way, we obtain a value for the slope $C_s\cdot\exp[(\mu_{f0}-\Delta G_a)/kT]$, as shown in Fig. 9a, yielding a value of $7.54\cdot10^{-2}$ mol·kg^{-1}. Substituting for the product $C_s\cdot\exp[(\mu_{f0}-\Delta G_a)/kT]$ in (3), and, in turn, inserting (3) into (6) now allows us to predict e_{ads}^{eq}, provided that the sum s, in the denominator of (6), is known.

Fig. 9b shows a plot of the experimentally derived e_{ads}^{eq} values versus values predicted by equations (3) and (6) using different values of $(\mu_{f0}-\Delta G_a)$ to compute the denominator

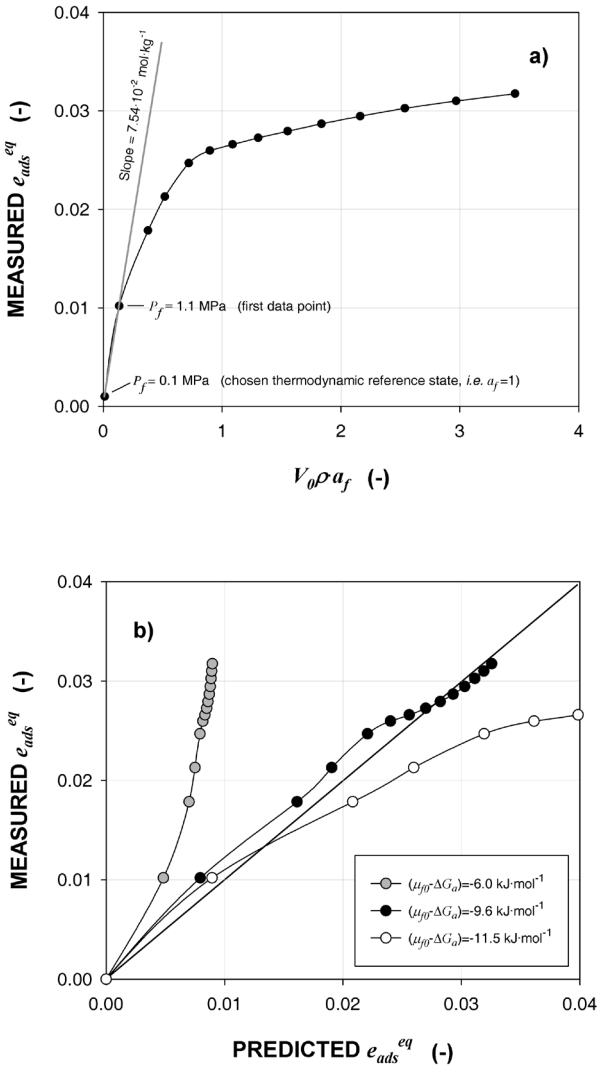

Fig. 9. a) Relationship between experimentally determined volumetric swelling strain (e_{ads}^{eq}) and the term $V_0\rho\cdot a_f$ (calculated taking average V_0=8.50·10^{-6} m^3·mole^{-1}; ρ=1450 kg·m^{-3}). The e_{ads}^{eq} data point at the set reference pressure P=0.1 MPa was interpolated from the data presented in Fig. 7. Assuming low occupancy θ at the first measured data point at 1.1 MPa CO_2 pressure (explained in section 3.4.2.2), the slope of the linear best-fit between this point and the thermodynamic reference state yields a value for the term $C_s\cdot exp[(\mu_{f0}-\Delta G_a)/kT]$ of 7.54·10^{-2} mol·kg^{-1}. b) Experimentally determined volumetric swelling strain (e_{ads}^{eq}) versus volumetric swelling strain (e_{ads}^{eq}) predicted by the thermodynamic/thermomechanical model described by equations (3) and (6). The data were fitted using different values for the term ($\mu_{f0}-\Delta G_a$) of -6.0, -9.6 and -11.5 kJ·mol^{-1}. A best fit to the experimental data was obtained with value for ($\mu_{f0}-\Delta G_a$) of -9.6 kJ·mol^{-1}. On this basis, and in combination with the value obtained for $C_s\cdot exp[(\mu_{f0}-\Delta G_a)/kT]$ (see a)), we determined a value for C_s of 3.01 mol·kg^{-1}.

term in (3). The results demonstrate that a near linear, one-to-one relationship can be obtained between the experimental and predicted values of e_{ads}^{eq} over the full range of CO_2 pressures investigated (up to 100 MPa) when using a constant value for $(\mu_{f0}-\Delta G_a)$ of -9.6 kJ·mol^{-1} (Fig. 9b). Dividing the term $C_s \cdot \exp[(\mu_{f0}-\Delta G_a)/kT]=7.54 \cdot 10^{-2}$ mol·kg^{-1} by the constant term $\exp[(\mu_{f0}-\Delta G_a)/kT]$ calculated on the basis of the fitted value for $(\mu_{f0}-\Delta G_a)$ of -9.6 kJ·mol^{-1}, now yields a value for the (constant) number of potential adsorption sites per kg of coal (C_s) of 3.01 mol·kg^{-1}. Unlike the term $(\mu_{f0}-\Delta G_a)$, C_s is independent of the thermodynamic reference state chosen, and provides us with a measure for the CO_2 adsorption potential of our samples at fully saturated conditions.

The implication of the above is that the adsorption-induced swelling (e_{ads}^{eq}) seen in our experiments is well described by equation (6), where C is given by (3) and where $V_0=8.50 \cdot 10^{-6}$ m^3·mole^{-1} (or $\Omega_0=1.41 \cdot 10^{-29}$ m^3·molecule^{-1}), $\rho=1450$ kg·m^{-3}, $C_s=3.01$ mol·kg$_{coal}^{-1}$, $(\mu_{f0}-\Delta G_a)=-9.6$ kJ·mol^{-1}, and μ_{f0} is defined at 40 °C and $P=0.1$ MPa. Coupling equation (6) and (3) with (7), we can now explicitly compare our model for combined adsorption-induced swelling plus elastic compression, as embodied by (7), with the experimental data for e_v^{eq} versus P plotted in Fig. 7. Good agreement was obtained over the complete range of CO_2 pressures investigated (*i.e.* up to 100 MPa). It accordingly seems likely that our model offers notably not only a good description, but also a physically valid description of the adsorption/volumetric behaviour of coal under hydrostatic conditions.

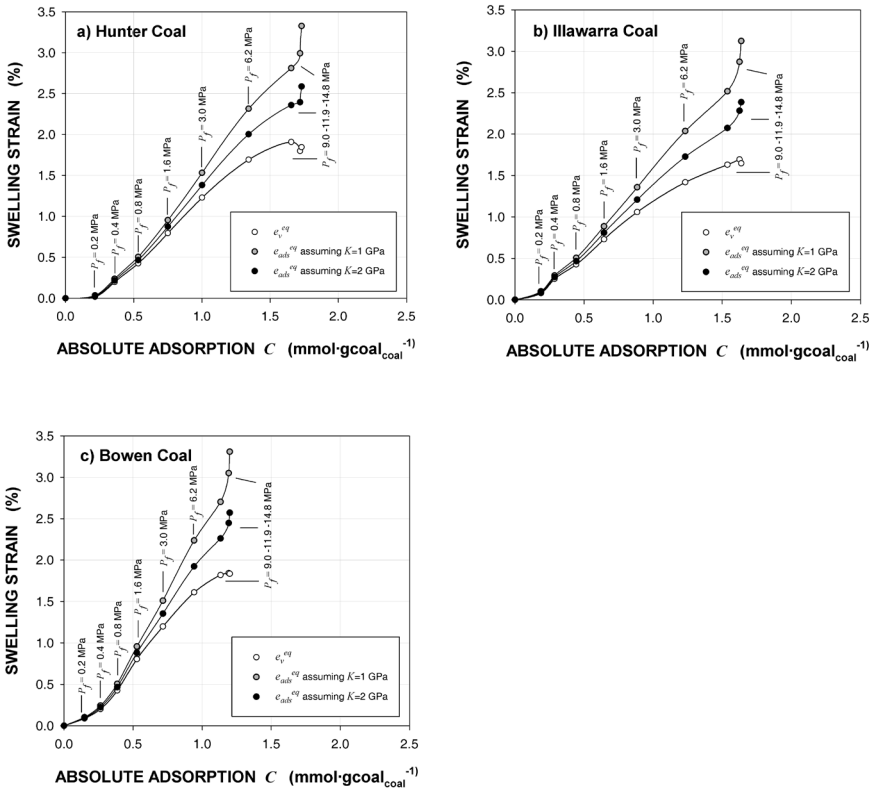

Fig. 10. Relationship between the adsorption-induced swelling strain (e_{ads}) and absolute CO_2 adsorption (C) in mmol·g_{coal}^{-1} for a) Hunter coal, b) Illawarra coal, and c) Bowen coal, as reported by Day et al. (2008). The volumetric swelling strain (e_{ads}^{eq}) was determined as a function of CO_2 pressure by subtracting the elastic compressive strain e_{el}^{eq} from the total measured volumetric strain e_v^{eq} (uncorrected data plotted, determined by Day et al. (2008) at a temperature of 55 °C). Absolute adsorption data were adopted from the work of Sakurovs et al.(2007), who conducted gravimetric sorption tests at a temperature of 53 °C on crushed samples (particle size 0.5-1.0 mm) of all three coals with tested by Day et al. (2008).

3.4.2. Comparison of our data with existing literature

In contrast to the adsorption-induced volumetric swelling strain e_{ads}^{eq} that was determined here, several other studies have determined the dependence of the measured (net) volumetric strain e_v^{eq} upon CO_2 concentration (Ceglarska-Stefanska and Czaplinski, 1991; Ceglarska-Stefanska and Czaplinski, 1993; Levine, 1996; Cui et al., 2007; Astashov et al., 2008; Day et al., 2008; Kelemen and Kwiatek, 2009; Battistutta et al., 2010; Day et al., 2010; Pan and Connell, 2011). These report either an s-shaped (Day et al., 2008), an exponential (Pan and Connell, 2011), or a polynomial (Kelemen and Kwiatek, 2009) dependence of e_v^{eq} on the adsorbed concentration C of CO_2 in coal. Although different strain determination methods were used in these studies, all experiments were conducted on blocks or cores. No corrections were made for the elastic volumetric strain e_{el}^{eq}. We therefore suggest the combination of adsorption-induced swelling and elastic compression may be responsible for the different e_v^{eq}-C trends observed. Even though ECBM involves the injection of CO_2 up to 20 MPa maximum, most e_v^{eq}-C studies have been performed using CO_2 pressures up to 5 MPa. The only exception (known to the authors) is the study of Day et al. (2008), who measure the swelling response of three coals using CO_2 pressures up to 15 MPa. We will consider the effect of the separation of adsorption-induced swelling and elastic compression on the data reported by Day et al. (2008) to assess if the adsorption-induced swelling can be explained by our model for this effect.

The experiments reported by Day et al. (2008) were performed on 30x10x10 mm blocks of coal, which were exposed to CO_2 up to 15 MPa CO_2 pressure, at a temperature of 55 °C using an optical cell. Expansion of the samples was imaged using digital cameras, and 2-D strains computed as function of CO_2 pressure by comparing pixel coordinates of individual images. From the measured 2-D swelling, the net volumetric strain at equilibrium was calculated and directly compared to the absolute adsorption, as measured for their samples by Sakurovs et al. (2007). Fig. 10 shows the relationship found between measured volumetric strains e_v^{eq} and adsorbed CO_2 concentration C for three Australian coals (Hunter coal (a), Illawarra coal (b), and Bowen coal (c)). We first computed the excess adsorption for the CO_2 pressure used by Day et al. (2008) using the modified Dubinin-Radushkevich equation that was fitted to the excess sorption data obtained by Sakurovs et al. (2007) for the three coal samples used by Day et al. (2008). To calculate the absolute adsorbed concentration C from this, we corrected for an adsorbed phase density of 1.5 g·ml^{-1} (following Sakurovs et al., 2007). It can be seen from Fig. 10 that the measured volumetric strain versus absolute adsorption trend is non-linear (s-shaped). In an attempt to obtain the swelling strain e_{ads}^{eq} for these samples, we removed the effect of elastic compression using equation 7, assuming a bulk modulus K of 1.0 and 2.0 (close to value of 1.8 GPa obtained by Pan and Connell, 2011 on the basis of data fitting) and the CO_2 pressures P persisting at each particular e_v^{eq}-C data point. The data in Fig. 10 show that when accounting for elastic compression using a bulk modulus K of 2.0 GPa a nearly linear e_{ads}^{eq}-C

dependence is obtained at CO_2 concentrations above 0.2-0.5 mmol·g_{coal}. The associated slope Ω_0=1.74→2.30→3.29·10^{-29} m^3·$molecule^{-1}$ for the three coals respectively. However, in addition to the linear trend observed 0.2-0.5 mmol·g_{coal}, a substantial non-linearity exists below 0.2-0.5 mmol·g_{coal} (Fig. 10). Careful comparison with the broader shows that this effect is typically observed in adsorption-induced swelling studies performed on samples with a bulk volume larger than approximately 1 cm^3 (e.g. Ceglarska-Stefanska and Czaplinski, 1991; Levine, 1996; Battistutta et al., 2010). A non-linearity at low *C* in the e_{ads}^{eq}-*C* relationship is clearly absent in our data (Fig. 8), suggesting that this effect may be related to internal accommodation of adsorption-induced swelling in larger samples (*i.e.* closure of microfractures/cleats inherent to larger coal samples). This implies that bulk swelling will be observed only when sufficient strain is developed internally. Alternatively, insufficient equilibration with adsorbing CO_2, or accessibility of the coal matrix may play an additional role, in particular in coal cores. The recent findings of Wang et al. (2011), who simultaneously measured permeability, swelling and excess sorption under stressed conditions, support this hypothesis. Of three differently fractured samples tested, only the sample with small, well-distributed fractures present showed a near linear relationship between swelling and adsorption after long equilibration times. The work of Wang et al. (2011) suggest that coal samples, when permeable to CO_2, may not have equilibrated yet. This in turn supports the findings of Siriwardane et al. (2009), who demonstrated that, although coal may be permeable, its permeability drastically reduces in time due to ongoing equilibration between coal and CO_2. We note that the possible interpretations provided here of the frequently observed non-linearity at the onset of e_v^{eq} vs. *C* curves is fundamentally different from the interpretation made by Pan and Connell (2011), who consider the non-linear portion of their e_v^{eq} vs. *C* data to be an adsorption-related effect.

Finally, we note that the e_{ads}^{eq} vs. *C* data obtained by Day et al. (2008) for three different coals, show, in comparison to the data presented here, higher swelling values per adsorbed molecule. Their values derived for Ω_0=1.74→2.30→3.29·10^{-29} m^3·$molecule^{-1}$ are closely similar, but slightly higher than those found in this study for Brzeszcze 364 coal, where Ω_0=1.36→1.46·10^{-29} m^3·$molecule^{-1}$. Possible factor controlling this variability between coals may include a difference in elastic response of the solid coal framework to adsorption, or a different manner of confinement of the adsorbed molecules in the coal structure, such as between tight molecular sheets or in larger pores. Despite the possible role of different coal properties, the overall effect of competition between adsorption-induced swelling and elastic compression processes, as described in our study, is also applicable to other coals.

3.4.3. Implications for ECBM reservoir characterisation

The above findings have significant implications for understanding the volumetric response of coal to CO_2 under pressure and temperature conditions relevant to ECBM. Our results imply that, under conditions of zero effective stress, the net volumetric strain supported by coal matrix material (*i.e.* material residing between cleats) can be separated into a component due to elastic compression under the imposed CO_2 pressure, plus a component due to adsorption-induced swelling. The net effect of CO_2 pressure on the volume of the coal matrix is dependent on the relative contribution of these opposing components. This competition may be particularly important during ECBM operations in deep coal seams, since CO_2 pressures are then expected to be high. Although effects of stress applied to the solid coal framework were not addressed in this study, these have proven to be of major importance too (Karacan, 2007; Pone et al., 2009; Hol et al., 2011a; Wang et al., 2011). We will not consider in detail here the effects of the *in situ* stress state of the coal formation. Instead, we examine two extreme hypothetical scenarios that can occur at hydrostatic fluid pressures relevant to CO_2 injection during ECBM:

1. The most favourable combination of matrix-scale properties for ECBM is one where the coal seam consists of compliant material (low K) that exhibits little adsorption-induced swelling (hence low sensitivity of adsorption-induced swelling to C). From equation 7, the elastic volumetric strain e_{el}^{eq} for such a coal will be relatively high, whereas the volumetric swelling strain e_{ads}^{eq} will be relatively low (since dependence on C is low). During CO_2 injection, elastic compression would therefore tend to dominate, causing an increase or relatively little decrease in permeability and injectivity during ECBM operations. As a consequence, low rank coals, that generally exhibit relatively little adsorption-induced swelling (e.g. Astashov et al., 2008; Durucan et al., 2009), probably possess the best possible combination of properties at matrix scale. This may explain the relatively successful ECBM pilot operation performed in the San Juan Basin (Reeves, 2001) where, for the Fruitland formation, coal rank varies from sub-bituminous to medium volatile bituminous coal.
2. The least favourable combination of matrix-scale properties for ECBM is where the coal seam consists of stiff material (high K) that exhibits large adsorption-induced swelling (hence high swelling sensitivity to C). In this scenario, the volumetric response to changes in CO_2 pressure will be dominated by swelling over compression, and will lead to a strong reduction in injectivity. These properties are typically observed for higher rank coals, and, accordingly, may explain the limited success of ECBM field operations in *e.g.* in Japan (Yamaguchi et al., 2006) GHGT8, Poland (van Bergen et al., 2006) and Canada (Mavor et al., 2004).

On this basis, it is clear that ECBM has the best chance of success when compressibility is high and adsorption-induced swelling low. To assess the magnitude and importance of these effects in a given coal field or seam, measurements of both components of behaviour are needed, as performed here. Since most ECBM operations to date have encountered injectivity problems, we suggest that the inherent volumetric stiffness plus swelling behaviour of most coals is probably not very suitable for ECBM. Only the presence of high cleat density, or the interlyering of coal seams by other, more permeable and/or compressible rock types, may improve the efficiency. However, greater success can probably be achieved by creating space to accommodate coal swelling developed during the CO_2 injection process, hence preventing stress build-up and associated cleat closure. In our view, the required removal of coal mass and volume may be achievable by chemical or mechanical means, *i.e.* by application of solvents/solutes, or by performing active mining of the coal and/or the over- or underlying strata. Further research into the response of ECBM-systems when subject to such approaches is of crucial importance to improve their feasibility.

3.5. Conclusion

This study has addressed the volumetric response of coal matrix material to the application of CO_2 pressures up to 100 MPa, at a constant temperature of 40.0 °C. Our aim was to measure the net volumetric effect of CO_2 on coal and to assess if this can be separated into a component caused by adsorption-induced swelling and a component caused by elastic compression. To do this, we performed dilatometry experiments on three unconfined, cylindrical coal matrix samples (4 mm in diameter and ~4 mm long) of high volatile bituminous coal (Brzeszcze, Poland), using a specially developed, high pressure dilatometer that incorporates an eddy current sensor to measure one-dimensional sample expansion or contraction. Elastic compression of our samples was measured independently in the same dilatometer by subjecting the samples to He at hydrostatic pressures up to 17 MPa. Our findings can be summarised as follows:

1. When subjected to hydrostatic CO_2 pressures up to 100 MPa, Brzeszcze coal exhibits anisotropic expansion over the full range of CO_2 pressures used. Expansion measured perpendicular to the bedding was about 1.4 times the average expansion measured in the bedding plane. Net volumetric strains, computed from the net linear strain in all directions measured, show that the response of the coal is characterised by an expansion-dominated stage below 10-15 MPa CO_2 pressure and by a contraction-dominated stage at higher CO_2 pressures.
2. We explain this behaviour as due to direct additive competition between adsorption-induced swelling and elastic compression of the coal matrix when subjected to hydrostatic CO_2 pressure. These two processes operate independently of one another.
3. We accordingly propose a model for coal swelling, which expresses the net swelling e_v^{eq} as the sum $e_v^{eq}=e_{ads}^{eq}+e_{el}^{eq}$ of the adsorption-induced swelling strain (e_{ads}^{eq}) and the elastic compression (e_{el}^{eq}). In this model e_{ads}^{eq} is assumed to be linearly related to the adsorbed concentration of CO_2, *i.e.* we assume a constant volumetric contribution per adsorbed molecule to the volumetric swelling strain of the sample. By subtracting e_{el}^{eq} from the measured volumetric strain e_v^{eq}, using bulk modulus data for our coal determined by exposure to high pressure He, we calculated the volumetric swelling response e_{ads}^{eq} of coal. This increases continuously with CO_2 pressures up to 100 MPa.
4. A comparison of the experimentally determined volumetric strains e_{ads}^{eq} with independent experimental data on the adsorbed concentration C of CO_2 (data of Gensterblum et al., 2010) reveals a near linear relationship between e_{ads}^{eq} and C at CO_2 pressures up to 20-30 MPa, confirming our model assumption of a linear relation and yielding a volumetric strain per adsorbed molecule Ω_0 of $1.36 \rightarrow 1.46 \cdot 10^{-29}$ $m^3 \cdot molecule^{-1}$ ($V_0=8.20 \cdot 10^{-6} \rightarrow 8.79 \cdot 10^{-6}$ $m^3 \cdot mole^{-1}$). Using this value of Ω_0 (or V_0) for swelling per adsorbed molecule, we compared our e_{ads}^{eq} data for adsorption-induced swelling with e_{ads}^{eq} calculated from the thermodynamic model for adsorbed concentration versus CO_2 pressure presented by Hol et al.

(2011a). Good agreement is obtained for specific parameter values in the model, namely for C_s=3.01 mmol·g_{coal}^{-1}, which represents the (constant) number of potential adsorption sites per kg of coal, and for (μ_{f0}-ΔG_a)=-9.6 kJ·mol^{-1}, which represents the energy of adsorption relative to a thermodynamic reference state taken at 0.1 MPa CO_2 pressure and a temperature of 40 °C. Combining this thermodynamically based model for adsorbed concentration with the inferred value of Ω_0, and with the elastic compression of our samples obtained from their bulk modulus (using the relation $e_v^{eq}=e_{ads}^{eq}+e_{el}^{eq}$), provides a good description of the measured volumetric behaviour of our samples. This suggests that the physical basis for the model is also valid.

5. Our model, expressed through the relationship $e_v^{eq}=e_{ads}^{eq}+e_{el}^{eq}$, also fits the e_v^{eq} versus adsorbed concentration data presented for three Australian coals by Day et al. (2008), for a bulk modulus value of 2.0 GPa and Ω_0 values of 1.74→2.30→3.29·10^{-29} m^3·$molecule^{-1}$.
6. The main implication of our results for ECBM operations is that compliant coals (low *K*) that exhibit relatively little adsorption-induced swelling (hence low sensitivity of swelling strain to *C*) will show relatively small reductions or even increases in permeability due to competition between swelling and compression when CO_2 pressure increases during ECBM operations. Such coals would be relatively favourable for ECBM. By contrast, relatively large reductions in permeability and injectivity can be expected during ECBM operations in coals that exhibit high volumetric stiffness (high *K*) and large amounts of CO_2 adsorption-induced swelling (high sensitivity of swelling strain to *C*). These will be less suitable for ECBM.

4

Direct determination of total CO_2 uptake by coal: A new technique compared to the manometric method

Sander Hol, Yves Gensterblum,
Christopher J. Spiers

Fuel (submitted)

Abstract

The CO_2 adsorption capacity of coal matrix material is generally determined by means of manometric or gravimetric sorption tests performed on powdered coal samples flooded with CO_2 under unconfined, isostatic conditions, in an attempt to obtain the Gibbs Surface Excess (GSE). However, these determinations may be affected by methodological uncertainties related to a) coal swelling, b) the disputed reliability of CO_2 porosity using He-pycnometry, and c) the presence of chemical impurities introducing errors in the required Equation of State (EoS) of CO_2. The present paper reports a newly developed technique that, in principle, directly measures total CO_2 uptake of mm-sized coal matrix cylinders, without the application of the EoS for CO_2 and without the need for swelling corrections or He-pycnometry. The technique makes use of a capsule composed of ductile metals (Au and In), pressure-fitted to the sample, which traps directly both adsorbed and free CO_2 taken up by the sample upon exposure to CO_2. We applied the method to samples of high volatile bituminous coal (Brzeszcze, Seam 364, Poland), saturated with CO_2 at a fixed pressure between 0 and 18 MPa at 40 °C. For comparison, manometric determinations were performed on a combined set of 8 samples, also at 40 °C. The capsule technique yielded a Langmuir-like CO_2 uptake curve showing scatter within a band less than 0.5 mmol·gcoal^{-1} and attaining a CO_2 content of 4.08 mmol·gcoal^{-1} at 18 MPa CO_2 pressure. The manometric method yielded a 3-stage uptake curve showing lower uptake than the capsule-derived curve, showing 20-30 % discrepancy at pressures above ~9 MPa. Allowing for worst case errors, the differences in CO_2 uptake obtained using the two methods are attributed to i) random errors and to uncertainties EoS in the manometric dataset at low CO_2 pressures (3-9 MPa), and ii) systematic errors, due to erroneous trapping of free CO_2, dominating in the capsule dataset high CO_2 pressures (>9 MPa). Taking all error sources into account, the capsule method proved reliable at CO_2 pressures of 0-7 MPa. At pressures higher than 8 or 9 MPa, the manometric method was most reliable. In general, use of the manometric method with sufficiently large samples, or the capsule method at P<9 MPa, provides a reliable means of measuring the CO_2 uptake capacity, yielding errors that are less than the effects of in situ stress on sorption. Although improvement is needed to prevent erroneous trapping of free CO_2 at pressures above 9 MPa, our new encapsulation method has the potential to accurately determine the uptake of any adsorbate by any (swelling) adsorbent, e.g. CO_2 uptake by shale and clay caprocks and is suitable for assessment of the effects of small-scale lithological differences in CO_2 uptake.

4.1. Introduction

Enhanced Coalbed Methane production (ECBM) involves the injection of supercritical CO_2 to desorb CH_4 from coal seams, while trapping CO_2 as a preferentially adsorbed phase (Mazzotti, et al., 2009; White, et al., 2005). For ECBM reservoir simulation purposes, the absolute CO_2 storage potential of the coal matrix under *in situ* conditions forms essential input. This is given by the sum of two contributions, namely the adsorption capacity and the pore-filling capacity. To date, research has focused on the dominant term at low CO_2 pressures, *i.e.* on measuring the adsorption potential of coals. This is done by conducting either manometric or gravimetric sorption tests on powdered coal samples flooded with CO_2 under unconfined, isostatic conditions (Bae and Bhatia, 2006; Gensterblum, et al., 2010; Goodman, et al., 2007; Pini, et al., 2010). These techniques are usually applied to determine the excess sorption, or Gibbs Surface Excess (GSE), *i.e.* the amount of CO_2 adsorbed in the nanoporous coal matrix in excess of any free, bulk phase present at constant pressure and temperature (Sircar, 1999).

However, as recently discussed by Sakurovs et al. (2009), Yu et al. (2008), Ross and Bustin (2007), Condon (2006) and Romanov et al. (2006b), a number of methodological uncertainties are associated with the application of the manometric and gravimetric methods to determine the CO_2 sorption capacity of coal. These all have the potential to lead to underestimation of the storage capacity of coal matrix material. They relate to the fact that, in practice, sorption techniques measure the excess sorption not with respect to the true CO_2-accessible pore volume, but with respect to the He-accessible pore volume plus the empty vessel space around the sample. Any correction required to obtain the true excess sorption, or GSE, may involve errors. First, swelling of the coal upon equilibration with CO_2 can produce a substantial error in corrections made for the volume or mass of free CO_2 present in the sample and measurement system (Ozdemir, et al., 2002; Siemons and Busch, 2007). Second, the reliability of the He-pycnometry method used to determine the free CO_2 volume or mass present in the sample and system may be questioned. This is because He and CO_2 may not always occupy the same pore space in coal (Ross and Bustin, 2007). Third, the *P-V-T* properties of CO_2 near the critical point, as described by the Equation of State (EoS), are extremely sensitive to the presence of chemical impurities (Zhang, et al., 2002), in particular to traces of water or to organic volatiles extracted from coal (Kolak and Burruss, 2006).

Despite attempts made to minimise uncertainties associated with GSE sorption determination methods for coal-CO_2 systems (Ozdemir, et al., 2003; Pini, et al., 2006; Romanov, et al., 2006a; van Hemert, et al., 2009), the above three issues are extremely difficult to resolve, as they are inherent to the assumptions made in the application of the manometric and gravimetric methods to the measurement of physical adsorption

(Condon, 2006). To assess the importance of the accompanying uncertainties, an independent, direct method of determining CO_2 uptake by coal is needed.

Here, we report a new technique developed at the HPT Laboratory at Utrecht University aimed at direct measurement of the total amount of CO_2 taken up by coal matrix material upon equilibration with CO_2, including both the adsorbed and free CO_2 components. The principles involved do not require application of the EoS for CO_2 to determine CO_2 uptake and do not require volumetric corrections for swelling or He-occupied volume. Instead, the method involves direct trapping of the CO_2 taken up by small cylinders of coal matrix material, by means of sealing in a soft, pressure-fitted, ductile metal capsule, after equilibration of the coal matrix sample with CO_2. Using this method, we performed CO_2 uptake experiments on high volatile bituminous coal (Brzeszcze, Poland) at 40 °C and at CO_2 pressures up to 18 MPa. For comparison, a manometric sorption determination was made on the same samples at similar conditions. This was done at Aachen University (RWTH Aachen), following the procedure described by Gensterblum et al. (2009). In addition, our data were compared with the results obtained by Gensterblum et al. (2010)for crushed (<2 mm) Brzeszcze 364 coal. Note that, in comparison to the manometric and gravimetric methods, the encapsulation method relies on entirely different measuring principles, and is therefore fully independent.

The results obtained using the ductile metal capsule technique show CO_2 uptake behaviour resembling a Langmuir isotherm but with significantly higher uptake than measured using the manometric method, notably at pressures above the critical pressure of CO_2. We show that the apparent increase in uptake cannot be explained by storage of free CO_2 in open pores within the coal matrix. We go on to argue that the observed discrepancies instead reflect errors related to application of the EoS for CO_2 when using the manometric method for small samples (especially at CO_2 pressures <9 MPa), plus errors associated with imperfect fitting of our ductile metal capsules (dominating at CO_2 pressures >9 MPa). Finally, we discuss the implications of our results regarding the CO_2 adsorption behaviour of Brzeszcze coal, along with the significance of the inferred errors in comparison with uncertainties stemming from other factors affecting CO_2 adsorption by coal under *in situ* conditions, notably the *in situ* stress state (Hol, et al., 2011; Wang, et al., 2011).

4.2. Experimental methods

4.2.1. Approach – encapsulation versus manometric techniques

The ductile metal encapsulation method described here aims at direct determination of the total CO_2 uptake of single cylinders of coal matrix material at specific conditions of CO_2 pressure and temperature. The method was applied in a series of 18 experiments performed on a set of 7 matrix cylinders, each weighing 36-70 mg. For comparison, a manometric test was subsequently performed at Aachen University (RWTH Aachen) on a set of 8 samples (weighing 0.5 g in total), from which we obtained the total (combined) CO_2 uptake, after correcting for measured swelling behaviour. The eighteen capsule experiments were performed at 40 °C using a specific CO_2 pressure in the range 0-18 MPa for each sample tested, thus obtaining uptake as a function of CO_2 pressure. By contrast, the manometric run was conducted at different pressures using the one combined set of 8 samples.

4.2.2. Samples

4.2.2.1. Origin and preparation

All experiments were performed on small matrix cylinders, prepared from a reference block of high volatile bituminous coal taken from the Brzeszcze mine in the Upper Silesian Basin of Poland (Nowak, 2004). Petrological analysis was performed on a random sample of crushed bulk material at the Geochemical Laboratory at the Netherlands Organization for Applied Scientific Research (TNO), in Utrecht. This showed that the coal has a vitrinite reflectance of 0.77 ± 0.05 % and contains 59.8 % vitrinite, 9.8 % liptinite and 30.0 % inertinite.

Eleven, crack- and cleat-free cores (*i.e.* 11 intact samples) with a diameter of 4 mm and length of ~6 mm were drilled from a single, dense layer within the reference block of Brzeszcze coal, as described in detail by Hol and Spiers (submitted). The samples used for both the capsule experiments and the manometric test are listed in Table 1, per experiment conducted. As already indicated, ductile metal capsule tests were performed on 7 different samples. These were cut and the ends ground flat and square to achieve lengths of 2-4 mm. For experimental CO_2 pressures up to 10 MPa, samples with a length of 4 mm were generally used. At CO_2 pressures above 10 MPa, the volume of CO_2 released by 4 mm long samples was too high to be captured by the capsule method, so that samples of 2-3 mm length were used instead (Table 1, experiments 12-18). Several samples were damaged upon removal from the capsule after testing and could only be used once. Other samples (*e.g.* L1.01 and L1.08) were used multiple times (Table 1), sometimes shortening them in later tests. While the ductile metal capsule technique was applied to individual cylindrical samples, the manometric test was performed using a subset of 8 samples totalling ~0.5 g in mass

Exp. code	Sample code	Sample mass m_0	Sample mass change after testing	Sample length l_0	Sample diameter d_0	Sample volume V_0	Sample density ρ_0
		g	%	mm	mm	ml	kg·m^{-3}
1	L1.07	0.0699	*	4.13	4.00	0.0519	1346.2
2	L1.08	0.0622	*	3.78	3.99	0.0473	1315.0
3	L1.03	0.0684	*	4.10	3.99	0.0513	13340.
4	L1.08	0.0662	*	4.01	3.99	0.0501	1319.9
5	L1.09	0.0657	+0.81	3.93	4.00	0.0494	1330.5
6	L1.10	0.0655	*	4.00	3.97	0.0495	1322.8
7	L1.01	0.0334	*	2.01	3.98	0.0250	1336.7
8	L1.08	0.0657	*	4.01	3.99	0.0501	1309.7
9	L1.08	0.0658	-0.24	4.01	3.99	0.0501	1312.9
10	L1.08	0.0647	*	3.96	3.99	0.0495	1305.7
11	L1.11	0.0653	-2.79	3.92	4.00	0.0493	1325.0
12	L1.01	0.0504	*	3.03	4.00	0.0381	1323.1
13	L1.11	0.0377	*	2.26	4.00	0.0284	1328.9
14	L1.01	0.0502	*	3.03	4.00	0.0381	1317.6
15	L1.11	0.0373	*	2.26	4.00	0.0284	1313.8
16	L1.01	0.0375	*	2.26	3.98	0.0281	1332.9
17	L1.01	0.0360	*	2.16	3.98	0.0269	1338.7
18	L1.11	0.0375	*	2.26	4.00	0.0284	1322.1
Mano-metric test	Random subset of 8 of the 11 cores prepared	0.5079 (before testing) 0.4869 (after testing)	-4.13	30.67	*	0.3854	1317.8 (total mean)

Table 1. List of the cylindrical samples of coal matrix material tested using the capsule method. All samples were uniquely coded, where 'L1.0x' denotes 'layer one, sample x'. Experiment codes are assigned not in chronological order of testing but in order of ascending test pressure (see Table 2). For each experiment performed, the sample mass (m_0), length (l_0) and volume (V_0) are listed as measured at NTP (normal, or room temperature and pressure) immediately before each experiment (=not determined). Sample density before testing was computed following the relation $\rho_0=m_0/V_0$. Note that several samples were used multiple times, in some cases with decreasing length in later experiments.*

(Table 1), selected at random from the 11 intact cores taken. Five of these samples had already been exposed to CO_2 during the capsule tests. Note here, that multiple use of some samples implicitly assumes that both adsorption of CO_2 by the coal matrix material, and filling of accessible pore space, were (near) reversible in our experiments, as reported in previous studies (*e.g.* Goodman, et al., 2005).

4.2.2.2. Sample density and swelling characteristics

Data on sample mass, density and swelling characteristics are essential for processing and interpreting our CO_2 uptake data, especially those obtained using the manometric method.

Prior to each capsule experiment, the sample to be tested was weighed at normal (ambient) temperature and pressure (NTP) in the air-equilibrated condition, using a Mettler AE-163 high precision balance (range 0-30 g, linearity ± 0.00003g). The density of the samples was calculated from their mass and dimensions, the latter being determined using a digital calliper with a resolution of 0.01 mm. The density obtained includes the pore space inherent to the coal matrix structure and will be referred to as the sample density ρ_0. This ranged from 1305 to 1355 kg·m^{-3} with an average of 1328 kg·m^{-3} (Table 1).

Before and after manometric testing, the set of 8 samples used was collectively weighed and the average density of the set (1318 kg·m^{-3}) determined from the combined sample volume determined from the individual sample dimensions (Table 1). He-pycnometry, performed after exposure to CO_2, yielded a mean skeletal matrix density of 1511 kg·m^{-3}. From the difference between the average bulk density and the skeletal density, the He-accessible porosity could be calculated assuming no significant influence of air or water sorption at NTP. This yielded a He-accessible porosity of 16.95 % after exposure to CO_2.

Exposure of coal to CO_2 always results in adsorption-induced swelling. This, combined with the elastic compression of the solid framework, gives rise to a net volumetric strain e_v, which increases as a function of increasing CO_2 pressure at pressures up to ~20 MPa (e.g. Day, et al., 2008; Day, et al., 2010; Durucan, et al., 2009; Majewska, et al., 2010; van Bergen, et al., 2009). Net volumetric strain versus CO_2 pressure data for a subset of the samples used in this study have been reported by Hol and Spiers (submitted), who performed dilatometry tests at 40 °C and at CO_2 pressures up to 100 MPa. These tests showed a consistent increase in sample volume by ~2.2 % at 20 MPa CO_2 pressure. To describe this response, we fitted a 6th order polynomial function $e_v(P)$ to the swelling data of Hol and Spiers for CO_2 pressures (P) up to 20 MPa, achieving a fit within ±0.1 % volumetric strain. The volume (V_{set}) of the sample set, at the P-T conditions pertaining during manometric testing, was accordingly calculated from the volume at NTP ($V_{set\text{-}0}$) using the relation

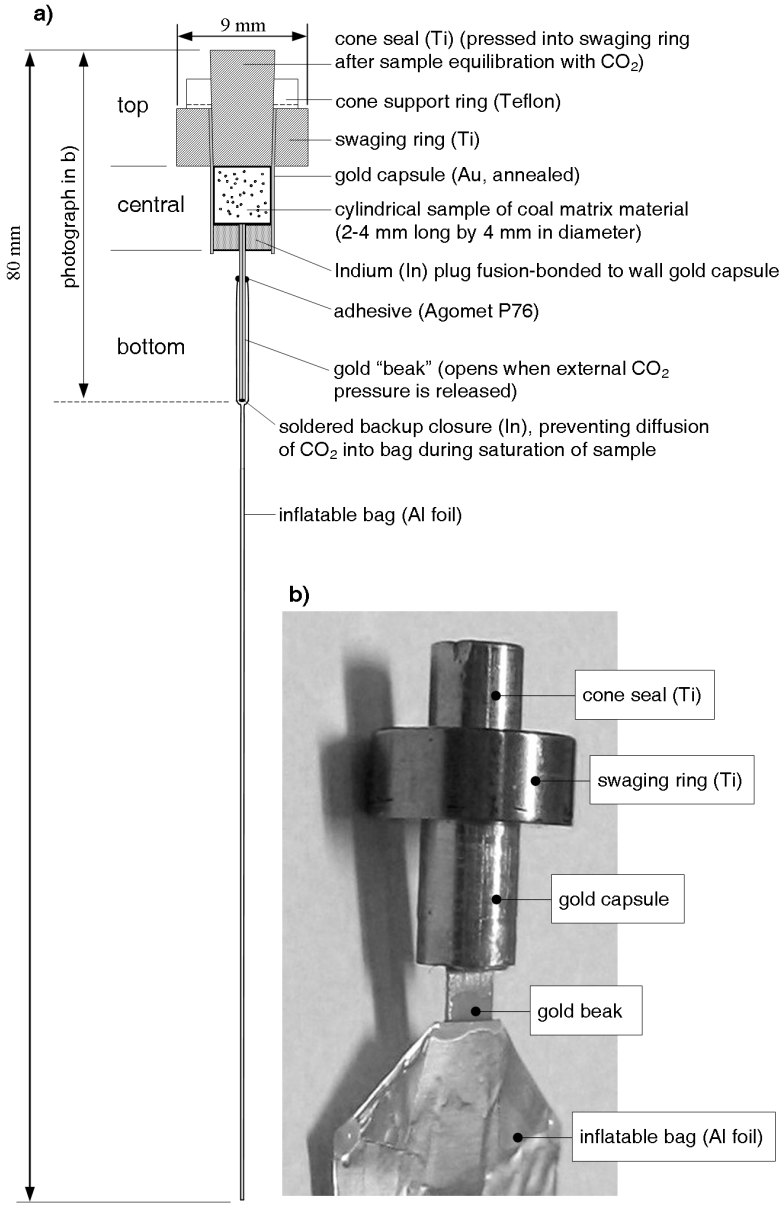

Fig. 1. The ductile metal capsule assembly designed at Utrecht for making direct CO_2 uptake measurements. a) Complete capsule assembly consisting of top, central and bottom elements that respectively serve to seal off CO_2 access, enclose the CO_2-equilibrated coal sample, and capture its CO_2 content in the Al foil bag. The whole assembly has a width of ~9 mm and, including the Al foil bag, a length of 80 mm. b) Photograph of the top, central and bottom elements of the capsule.

$$V_{set} = V_{set-0}\left(1 + e_v\left(P\right)\right) \quad (1)$$

We use this relation to correct for coal swelling when computing the total uptake of CO_2 by our samples during the manometric test. A similar approach was followed by Battistutta et al. (2010), Romanov et al. (2006a) and Ozdemir et al. (2003) in correcting manometric data to obtain excess sorption.

4.2.3. Ductile metal capsule experiments

4.2.3.1. Concept

In this new method, the total uptake of CO_2 by individual samples is determined by equilibrating the sample with CO_2 in a soft, ductile metal capsule (Fig. 1) that is pre-pressed onto the sample to exactly fit it. Equilibration is performed in a large, oedometer-type pressure vessel held at constant temperature (Fig. 2). Swelling of the sample due to the adsorption of CO_2 is accommodated by ductile deformation of the capsule. After equilibration, the sample is sealed in the capsule by means of swage-sealing conducted *in situ* by advancing the upper loading piston into the oedometer vessel (Fig. 2). Upon release of the CO_2 pressure from the vessel, an aluminium foil bag attached to the bottom of the capsule inflates, capturing the CO_2. The volume of the bag is then determined using the Archimedes' method at ambient conditions. Neglecting the very small amount of CO_2 remaining in the sample itself, and using the density of CO_2 at ambient conditions, allows computation of the absolute mass of CO_2 taken up per unit mass of sample material at the conditions of CO_2 pressure and temperature applied during equilibration. The uptake of CO_2 is thus determined without applying the EoS at elevated CO_2 pressure and without any need to correct for swelling.

4.2.3.2. Detailed capsule set-up and CO_2 pressure system

For each experiment, a separate capsule was prepared (Fig. 1). The capsule assembly is 9 mm wide and 80 mm long, including the Al foil bag. It consists of three main elements (top, central and bottom), which serve to enclose the CO_2-equilibrated coal sample, seal the assembly, and capture the CO_2 content of the sample. The central element (Fig. 1) of the capsule consists of a soft, annealed gold (Au) tube (inner diameter 4.00 mm), which encloses the cylindrical coal sample and allows it to swell freely during adsorption of CO_2. The base of the tube is closed with a circular indium plug, which is fusion-bonded to the tube walls. The top element (Fig. 1) consists of a titanium (Ti) swaging ring and cone, constructed to seal the ductile metal capsule by advancing the cone into the ring, after equilibration of the sample with CO_2. The cone

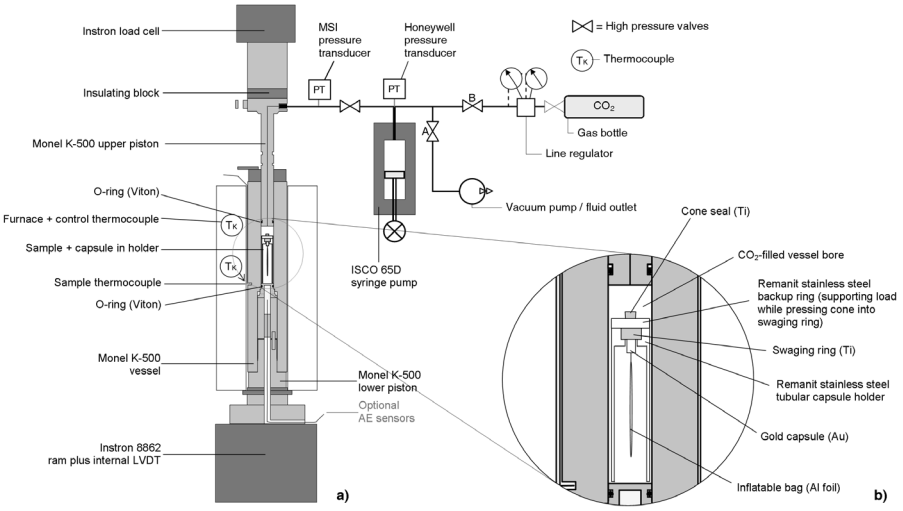

Fig. 2. a) Schematic diagram of the full set-up used during the present capsule tests. The sample is located in the capsule, inside a heated Monel oedometer vessel, which is mounted in an Instron loading frame. CO_2 (or He) can be admitted to the sample via a bore in the upper piston of the Monel vessel, coupled to a CO_2 bottle and an ISCO syringe pump. The whole assembly allows for equilibration of the sample at CO_2 pressures in the range 0-20 MPa, at a temperature of 40 °C. The Monel upper piston serves to press the cone into the swaging ring of the capsule (see Fig. 1). thus achieving sealing of the capsule after the sample has equilibrated with CO_2. b) Enlargement of capsule holder/support positioned inside the Monel pressure vessel.

is supported coaxially on the swaging ring by a thin Teflon support ring, such that the capsule remains open until the cone is advanced into the swaging ring. The bottom element (Fig. 1) collects CO_2 desorbing from the sample when the CO_2 pressure outside the capsule is released at the end of the experiment. This element consists of a completely flattened Au-tube (original diameter 2.00 mm) or "beak", which is fusion-bonded into the indium plug at the base of the capsule. The opposite end of the beak is lightly sealed against diffusion by applying an Indium melt film. Upon release of CO_2 pressure at the end of each experiment the film ruptures, and the CO_2 taken up by the coal cylinder is captured using the flat, aluminium foil bag (Fig. 1). sealed onto the gold beak using a thin film of Agomet P76 epoxy adhesive. The bag foil itself is constructed in the form of an envelope made of ~30 μm Al foil sealed at the edges using a cyanoacrylate adhesive film. Both the adhesives used (cyanoacrylate and Agomet P76) were extensively tested for their performance in sub- and supercritical CO_2, and were shown to be highly resistant to leakage, degradation and CO_2 sorption. Specific control tests will be described in Section 4.2.3.5.

To expose the cylindrical coal sample to high pressure CO_2, within the ductile metal capsule, the oedometer-type, Monel K-500 pressure vessel described by Hol et al. (2011)was used. This was mounted in an Instron 8862 servo-mechanical loading frame to enable loading and sealing of the capsule cone. In the present experiments, the ductile metal capsule was supported in the vessel on a specially designed, tubular capsule holder, constructed out of Remanit 1.4122 stainless steel (Fig. 2). This tubular holder supports the capsule assembly at the swaging ring (top element) and allows the capsule to be closed, after equilibration of the sample with CO_2, by advancing the upper Monel piston to load the Ti capsule.

An ISCO 65D syringe pump was employed to introduce CO_2 into the Monel vessel at pressures of 0-18 MPa (Fig. 2). The CO_2 pressure was measured and controlled using a Honeywell TJE 0-137.90 MPa pressure transducer (absolute accuracy ± 0.6895 MPa), located at the top of the syringe pump cylinder (Fig. 2). In addition, a more sensitive MSI 0-35 MPa pressure transducer was used to attain better resolution and accuracy (± 0.035 MPa). This showed that the CO_2 pressure in the system could be kept constant to within ± 0.049 MPa using the ISCO pump, at least at pressures above 6 MPa. At CO_2 pressures up to ~6 MPa, better control was achieved using an AirProducts R2307 line regulator (Fig. 2). This allowed stepwise increases in CO_2 pressure up to ~6 MPa (bottle pressure), with an observed stability within ±0.01 MPa of the set pressure.

Heating of the Monel pressure vessel and its contents to the test temperature of 40 ±0.3 °C was achieved using an external, PID-controlled furnace (Fig. 2). The temperatures of the sample, the syringe pump, the furnace and the laboratory environment were all measured using type-K thermocouples (Fig. 2). Thermocouple signals were conditioned using a module based on an Analog Devices AD595C cold junction compensator. All temperature signals were calibrated using a multifunction reference thermometer accurate to 0.6 °C, and were individually scaled using a sixth-order polynomial.

4.2.3.3. Capsule conditioning and CO_2 capturing procedure

To ensure that measurements of CO_2 uptake using the capsule method are accurate, all void volume between the capsule walls and the sample must be eliminated or reduced to acceptably small levels. To achieve this, the soft, ductile capsule was intimately pressed onto each coal sample, by means of external hydrostatic pressurisation, so that it exactly fitted the sample. To perform this capsule conditioning procedure, the capsule (with no Al foil bag attached) was first placed in the capsule holder in the Monel pressure vessel, after which the system was evacuated for 1 h. The cone was then pressed into the swaging ring by advancing the upper Monel piston using the Instron's servo-mechanical actuator. While maintaining a constant load on the cone, CO_2 was introduced into the vessel directly from the CO_2 supply bottle (Fig. 2, at pressure of ~5.6 MPa), to press the ductile capsule (Au and In) tightly onto the sample. After

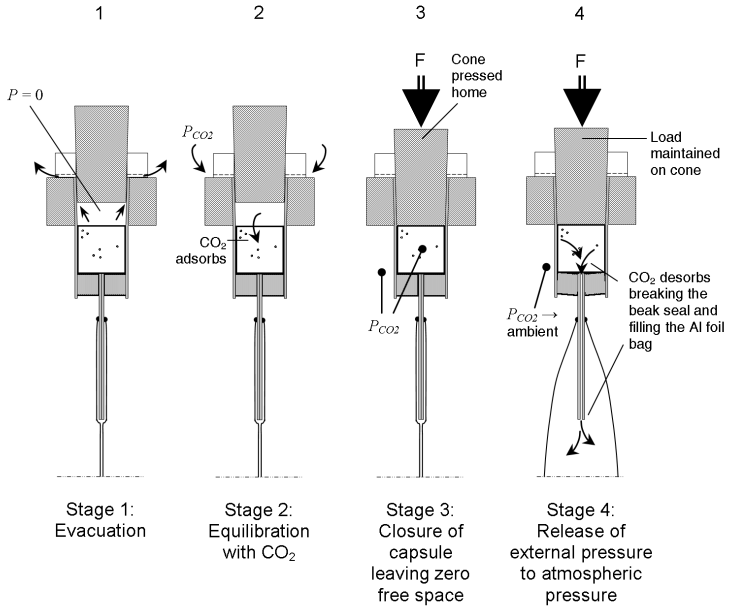

Fig. 3. Schematic overview of the four-stage experimental procedure used to capture CO_2 after pre-pressing the exactly fitting ductile metal capsule onto the sample. Stage 1: the open capsule was heated to 40 °C and evacuated for 1 h in the Monel pressure vessel (Fig. 2). Stage 2: CO_2 was allowed into the open capsule for 24 h at a constant external CO_2 pressure. Stage 3: the equilibrated sample was sealed in the capsule by pressing the cone into the swaging ring. Stage 4: the hydrostatic pressure outside the capsule was released from the Monel vessel. This initiates escape of the CO_2 from sample and capsule through the gold beak into the Al foil bag.

~20 min, the CO_2 was released from the system, the capsule was taken out of the vessel and the cone removed from the swaging ring. The contact between the sample and the capsule wall (inside the capsule) was then inspected for gaps using an optical microscope. Provided no gaps were visible (detection limit ~3 μm), an Al foil bag was attached to the capsule outlet or "beak" and the capsule prepared for further testing.

The CO_2 capture experiments were subsequently conducted in four stages (Fig. 3), employing a CO_2 pressure between 0 and 18 MPa and a constant temperature of 40 °C. In each run, the pre-pressed capsule was placed into the vessel, inside the capsule holder, with the top cone loosely supported above the sample on the Teflon support ring (Fig. 1). In Stage 1 (Fig. 3), the complete system was heated to 40 °C, evacuated for 1 h and then isolated by closing valve A (refer Fig. 2 and Fig. 3). In Stage 2, CO_2 was introduced from the CO_2 bottle via the AirProducts line regulator into the vessel, capsule and sample by opening valve B (Fig. 2). maintaining constant CO_2 pressure using the ISCO syringe pump or line regulator. Swelling of the sample, which occurs due to adsorption, was accommodated by deformation of the ductile metal capsule.

After 24 h, equilibrium was assumed to be reached. This assumption was based on the equilibration time (0.5-2 h) versus particle size data (<0.063-2 mm) reported by Busch et al. (2004). Extrapolation of these data to our sample size (4 mm long by 4 mm in diameter) predicts that our samples should equilibrate in 5-10 h. Moreover, cylindrical samples equilibrated in pilot CO_2 pressurisation experiments, and subsequently placed on a microbalance, reached constant mass in less than 1 h. After equilibration, *i.e.* at Stage 3 (see Fig. 3), the sample was sealed in the capsule by pressing the cone firmly into the swaging ring using the Instron loading frame. The CO_2 present in the coal sample was thereby captured (Fig. 3). While maintaining constant load on the cone, the furnace was then switched off and CO_2 was released from the system by opening valve A – see Stage 4, Fig. 3. This dropped the hydrostatic pressure outside the capsule, allowing free and adsorbed CO_2 in the sample to escape from the sample, breaking through the lightly sealed beak and into the aluminium foil bag, partially inflating the latter to a volume in the range 1-3 ml.

After approximately 1 h, the load was finally removed from the cone by withdrawing the upper Monel piston and the capsule was taken out of the vessel. It was assumed that sufficient void discharge and desorption had occurred after 1 h. The volume of the capsule and inflated aluminium bag containing the trapped CO_2 was then determined at ambient conditions using the Archimedes immersion method (in water). All bags were subsequently inspected for leaks. Each bag was then punctured and fully deflated (*i.e.* compressed), and the volume of the capsule/bag system measured in the empty state. Finally, the sample was retrieved from the capsule to allow re-use where possible.

4.2.3.4. Calculating total CO_2 uptake from volume captured

To calculate the total CO_2 uptake of the samples, we first determined the trapped CO_2 volume by subtracting the empty capsule/bag volume from that measured in the inflated state. The volume of CO_2 trapped in the bag at ambient conditions (V_{bag}, ml) was then multiplied by the density of pure CO_2 (ρ_{CO2}, in mmol·ml^{-1}) at the ambient conditions pertaining during weighing, and the result divided by the mass of the sample m_0 in grams (Table 1), to obtain

$$N = \frac{V_{bag} \cdot \rho_{CO2}}{m_0} \tag{2}$$

where N is the total CO_2 uptake in mmol·g_{coal}^{-1} or mol·kg_{coal}^{-1}. We emphasise that N includes all CO_2 present in the sample and capsule at the experimental conditions employed, without discrimination between free or adsorbed CO_2 phases, and is a measurement for one particular CO_2 pressure and one sample (*i.e.* it is not a cumulative quantity). During our determinations of the capsule plus bag volume at ambient conditions, a small, residual amount of CO_2 likely remains adsorbed and/or stored in the pores of the sample, stored in the opened beak, or stored between the expanded

capsule and sample. This is inherent to the method used. An estimate of these residual amounts, based on the He-accessible porosity of 16.95 %, an opening of the complete gold beak in the order 0.01-0.02 mm over the full length of 20 mm, and a dead space between the expanded capsule and the shrunken sample of 0.001 ml (based on the maximum swelling/shrinkage of the largest sample), shows that they are expected to account for no more than 0.016-0.022 ml of CO_2, compared to a typical (inflated) bag volume V_{bag} in the range 1-4 ml. We therefore neglect the error introduced by such effects.

4.2.3.5. Control tests and errors

To assess the reliability of the new capsule setup and method, we conducted two types of control experiments. These focused on the chemical and mechanical integrity of the individual components of which the capsules are fabricated, as well as on the performance of the capsules in general.

First of all, we specifically tested the performance in supercritical CO_2 of the adhesives and Al foil used to construct and seal the capturing bag. To do this, a standard foil bag was sealed at its open (top) end, in the initial, fully-flattened (zero volume) condition, using an Agomet P76 two-component adhesive film. The fully closed bag was then subjected to supercritical CO_2 at 10.0 MPa CO_2 pressure at 40 °C. After 24 h settling, the system was instantly depressurised and allowed to cool to room temperature. The tested bag did not inflate, showing that CO_2 did not diffuse through the adhesives or through any flaws in the Al foil in detectable amounts. On this basis, we conclude that the sealing performance of the adhesives and Al foil was satisfactory.

Second, a control test was performed using a non-swelling dummy sample, composed of Indium. This was conducted to evaluate any errors associated with a) closure of the capsule before contact was established between the cone and the coal sample during Stage 3 of the experiments (Fig. 3), and/or b) dilation of the flattened gold beak due to sample expansion before sealing and depressurisation of the capsule. Either of these effects could potentially capture extra CO_2 outside the sample during Stage 3. Indium was used as its bulk compressibility ($2.83 \cdot 10^{-2}$ GPa^{-1}) is closer to that of coal ($6.67 \cdot 10^{-2}$-1 GPa^{-1}) than is that of steel ($0.63 \cdot 10^{-2}$ GPa^{-1}). Pressing the capsule onto the sample during the conditioning stage would therefore be more realistic using an Indium rather than steel dummy, but still less intimate than expected when using a coal sample. We performed a test at 4.5 MPa CO_2 pressure and room temperature (duration 24 h), and found that a volume of ~1 µl of pressurised CO_2 had been included in the capsule. Using the density of CO_2 at the conditions of each experiment on coal, we used this volume to estimate the likely systematic error in CO_2 uptake per test (*i.e.* we assume that this volumetric error is representative for all CO_2 pressures used). The density of CO_2 at the conditions of each test was calculated using the Span and Wagner (1996) Equation of State (SWEoS) for pure CO_2.

4.2.4. Manometric test

A single, conventional manometric sorption test was performed at Aachen University (RWTH Aachen). In this determination, 8 of our cylindrical samples were combined together to produce sufficient coal mass (~0.5 g) to enable reasonable accuracy to be achieved in measuring CO_2 sorption.

4.2.4.1. Set-up

The equipment used was essentially identical to that used for the manometric measurements on powdered coal reported by Gensterblum et al. (2009) and Busch et al. (2003). It consists of a stainless steel sample cell connected to a Tecsis P3382 pressure transducer (range 0-25 MPa, accuracy ±0.0125 MPa) via two Valco 3-port switching valves. The internal volume of the pressure transducer, plus that of the high pressure tubing attached to it, is used as a reference cell. The internal volumes of the sample cell (V_{SC}) and reference cell (V_{RC}) were determined by means of He-expansion tests. These yielded a volume of 0.91152 ml (±0.00116 ml) for the sample cell and 1.156225 ml (±0.0003 ml) for the reference cell. Since the mass of the set of 8 cylindrical coal samples studied with this method totalled 0.5 g, which is approximately 10 times less than the sample mass used in the study by Gensterblum et al. (2010), the volume of the sample cell was kept roughly 14 times smaller to yield the largest possible changes in CO_2 pressure in the system during exposure of the samples to CO_2. To maintain constant temperature in the system during experimentation, the entire pressure system was placed in an air-circulating thermostatic oven (control capability ±0.1 °C). Temperature was measured close to the sample cell (to within ±0.0125 °C) using a high-precision (class 1/10 B) Pt100 Resistive Temperature Detector (RTD). The system could be evacuated using a standard, rotary-vane vacuum pump. An ISCO pump was used to charge the reference cell with CO_2 at pressures up to 25 MPa. Helium was introduced directly from the gas bottle. Independent leak tests, performed using He at a pressure of 10 MPa and a temperature of 39.92 °C, revealed that He leak rates did not exceed 0.0017 MPa·h^{-1} over a time span of ~8 h.

4.2.4.2. Manometric measurement procedure

The basic procedure followed for powdered samples has been described in detail by Gensterblum et al. (2009), Busch et al. (2003) and Krooss et al. (2002). The measurements were performed at a constant temperature of 40.32 °C, using sample cell CO_2 pressures up to 25 MPa. First, our set of 8 cylindrical samples totalling approximately 0.5 g in mass was placed in the sample cell, and the entire system was evacuated and heated to 40.32 ±0.2 °C. All CO_2 pressure data were corrected for an offset in initial pressure signal (of 0.9375 MPa) caused by thermal drift of the pressure transducer. It was assumed that this offset was constant over the full pressure range of the sensor (0-25 MPa). After thermal equilibration, the sample cell and reference cell were isolated

from each other by closing the valve separating them. The reference cell was then filled with CO_2 at a fixed pressure and the system allowed to settle for approximately 1 min. The amount of CO_2 present in the reference cell at this point was calculated from the pressure, temperature and known reference cell volume, using the density of CO_2 as obtained from its EoS (Span and Wagner, 1996). Then, CO_2 was admitted to the sample cell from the reference cell, filling the void space in the cell and samples and becoming adsorbed by the samples. The resulting change in CO_2 pressure was sensed by the Tecsis pressure transducer and logged as a function of time. Once the change in measured CO_2 pressure fell below the resolution of the pressure transducer, the CO_2 pressure in the reference cell was increased to a new, higher value, and CO_2 was again admitted to the sample cell. This procedure was repeated stepwise until the CO_2 pressure in the sample cell had reached approximately 25 MPa. To return to the initial evacuated state of the system, the reference cell was isolated, vented and evacuated. Then, CO_2 was allowed to flow from the sample cell into the reference cell by opening the valve between them. The resulting change in CO_2 pressure in the sample cell, due to void discharge and desorption, was sensed by the pressure transducer and again logged as a function of time. This procedure was repeated several times until the whole system approached the fully evacuated state. After the experiment, a He-expansion or pycnometry test was performed to determine the void volume accessed in the sample cell, *i.e.* the free volume present around the sample plus the pore volume accessible to He ($V_{void\text{-}He}$) within the sample.

4.2.4.3. Calculating total CO_2 uptake versus pressure in the manometric runs

Conventional use of manometric data, in combination with He-pycnometry, yields the Gibbs surface excess (Sircar, 1999), or 'excess sorption' (*cf.* Busch, et al., 2003 for crushed coal equilibrated with CO_2). In the present study, we use the manometric data obtained to compute the total uptake of CO_2 by our coal sample set. This represents the amount of CO_2 residing in the pores as a free phase, plus the amount of CO_2 adsorbed by the coal samples. In calculating the total CO_2 uptake, we assume that, at manometric equilibrium, the volume of free CO_2 within the sample cell is that contained in the void space present both inside and outside the samples. A complicating factor, however, is the volumetric swelling of the sample material as a function of CO_2 pressure. We apply equation (1), based on the swelling data reported by Hol and Spiers (submitted) to correct for this.

To calculate the total uptake of CO_2 at equilibrium at a given CO_2 pressure and temperature, we represent our sample set as a porous adsorbing body, of which we know the bulk volume at all CO_2 pressures. By choosing this approach, the total number of moles of CO_2 present in the sample set (n_{set}) at a particular equilibrium pressure can be obtained by subtracting the number of moles of CO_2 outside the sample set ($n_{non\text{-}set}$) from the total number of moles of CO_2 present in the sample cell (n_{SC}). This procedure is independent of He-porosity, and hence avoids problems related to the reliability of He-pycnometry data (*i.e.* it avoids the second problem stated in the Introduction).

Partly using the notation adopted by Van Hemert et al. (2009) for the manometric method, we accordingly write,

$$n_{set} = n_{SC} - n_{non-set} \tag{3}$$

To investigate the pressure-dependence of the partitioning of CO_2 expressed by equation (3), and hence to construct a CO_2 uptake isotherm for the present sample set, the CO_2 pressure in the system is increased stepwise (in steps *i*). To apply each pressure increment, a certain amount of CO_2 is first admitted to the reference cell at pressure P_i^f (where superscript *f* denotes the filling stage). By allowing CO_2 to flow from the reference cell (RC, with volume V_{RC}), CO_2 is "added" to the sample cell (SC, with volume V_{SC}), to equilibrate with the samples. At the point where pressure equilibrium is reached, CO_2 is present around the coal samples as a free phase and in the coal as both a free and an adsorbed phase. The equilibrium pressure P_i^e (where superscript *e* denotes equilibrium with the sample) measured in the reference cell in step *i* allows us to calculate the number of moles of CO_2 added to the sample cell from the reference cell, using the density of CO_2 predicted by the SWEoS (*i.e.* using P_i^f and P_i^e to calculate the CO_2 densities ρ_i^f and ρ_i^e, measured in mol·m^{-3}). This is done under the assumption that the SWEoS accurately describes the density of the CO_2. The result is given (*cf.* van Hemert, et al., 2009)

$$n_{SC} = n^{start} + n_i^{added} = n^{start} + \sum_{i=1}^{N} V_{RC}\left(\rho_i^f - \rho_i^e\right) \tag{4}$$

Note that in the present experiments, the first CO_2 pressure increment begins from an initially evacuated system, so that n^{start}=0. For $n_{non\text{-}set}$ in equation (3), we now write

$$n_{non-set} = \sum_{i=1}^{N}\left(V_{SC} - V_{set}\right)\rho_i^e \tag{5}$$

where V_{set} at each pressure equilibrium is given by equation (1), *i.e.* the expression $V_{set}=V_{set\text{-}0}(1+e_v(P))$, in which $V_{set\text{-}0}=m_0/\rho_0$ is the volume occupied by the bulk coal samples (including pores) at NTP, the pressure P is given by P_i^e, and where m_0 and ρ_0 are the pre-measured mass and mean density of the sample set used. Because our procedure to calculate the total CO_2 uptake uses the absolute bulk volume V_{set} at given *P*-*T* conditions, swelling is fully corrected for and, as such, the first problem stated in the Introduction is avoided. Combining equations 3-5, the expression for n_{set} finally becomes,

$$n_{set} = \sum_{i=1}^{N}\left[V_{RC}\left(\rho_i^f - \rho_i^e\right) - \left(V_{SC} - V_{set}\right)\rho_i^e\right] \tag{6}$$

To obtain the cumulative CO_2 uptake (N_{set}) per unit mass of coal in mmol·g_{coal}^{-1}, or mol·kg_{coal}^{-1}, we simply divide by the initial mass of the samples, using

$$N_{set} = \frac{n_{set}}{m_0} \tag{7}$$

It can easily be shown that the procedure followed here is exactly equivalent to obtaining the total CO_2 uptake from the sum of a) excess sorption acquired following the conventional manometric procedure (*e.g.* Condon, 2006; Sircar, 1999), b) the amount of CO_2 filling the He-accessible pore space, and c) the amount of CO_2 displaced by volumetric expansion of the sample (*i.e.* a swelling correction on the determined excess sorption). The latter calculation route assumes that the free porosity of the sample (which is usually determined by performing He-pycnometry), and the swelling response as a function of CO_2 pressure are both known. However, the He-porosity term cancels out because the free CO_2 contained in the pore space of the sample is required in calculating both the excess sorption term (term subtracted), as well as the pore filling capacity (term subtracted). This calculation route consequently leads to a total CO_2 uptake that is equivalent to that obtained from equations 3-7. Nonetheless, we choose not to use the excess sorption plus He-pycnometry route in our calculation of total CO_2 uptake, but to use the more direct approach (*i.e.* equations 3-7). Using this procedure it follows that by calculating the total CO_2 uptake, instead of excess sorption, the three problems mentioned in the introduction (*i.e.* coal swelling, He-accessibility and an inaccurate EoS) reduce to problems in the applicability of the EoS only.

Since the manometric test reported here involves a stepwise introduction of CO_2 at variable pressure increments, the uncertainties in measured CO_2 pressure and temperature, as well as the sample and reference cell volume determinations, have a cumulative effect on the data. A random error analysis was therefore performed following the Gaussian error propagation method, described by Gensterblum et al. (2010). In addition, we considered the sensitivity of the CO_2 uptake data to sample density (ρ_0), allowing for approximately 1 % variation in ρ_0 (upper values of 1300 kg·m^{-3} and lower values of 1325 kg·m^{-3}). This enabled to our final CO_2 uptake data to be plotted with random error bars and with a band showing the upper and lower bound effects of an approximately 1 % variation in ρ_0 on our da
Aside from applying the above calculation method (equations 3-7) and error/sensitivity analysis to the present manometric run performed on our set of 8 cylindrical samples, we also applied them to the manometric data set reported by Gensterblum et al. (2010) for a large, crushed sample (grain size <2 mm, mass 8.36 g) of the same Brzeszcze coal. This was done to enable comparison of our capsule data with manometric data both for our own (small) sample set, and with the conventional results of Gensterblum et al. (2010)for a large powdered Brzeszcze 364 coal sample. In the procedure of calculating the total uptake of the powdered sample, we assumed that the sample density ρ_0 for crushed coal was similar to the density of the cylindrical samples used in this study (*i.e.* ρ_0=1318 kg·m^{-3}, with upper and lower bound values of 1300 kg·m^{-3} and 1325 kg·m^{-3} respectively).

4.3. Results

The total CO_2 uptake data obtained for our samples using the capsule method ($N(P)$ data) and using the conventional manometric method ($N_{set}(P_i^e)$ data) are presented in Fig. 4. The values plotted represent the sum of pore filling and adsorption capacity in both cases. Both sets of data show an increase in total uptake of CO_2 by the samples with increasing CO_2 pressure. The detailed data obtained using the two methods are tabulated in Table 2 and Table 3, along with the corresponding systematic and/or random errors (as calculated from the uncertainty in CO_2 pressure, temperature and volume determinations). For later comparison, data on total CO_2 uptake by crushed Brzeszcze coal (particle size <2 mm), as derived from the manometric data reported by Gensterblum et al. (2010), are also plotted in Fig. 4.

4.3.1. Capsule data

All of the samples tested using the capsule method showed inflation of the Al foil bag after the experiment (Fig. 5). Those exposed to CO_2 at pressures >3 MPa also showed expansion of the Au jacket as a result of sample swelling (inset, Fig. 5).

The total uptake of CO_2 measured using the capsule method continuously increases as a function of increasing CO_2 pressure, up to a value of 4.08 mmol·g_{coal}^{-1} at 18.10 MPa CO_2 pressure (Fig. 4). Below ~5.5 MPa CO_2 pressure, the mean rate of CO_2 uptake with increasing pressure is ~0.5 mmol·g_{coal}^{-1}·MPa^{-1}, decreasing steadily to a mean rate of ~0.1 mmol·g_{coal}^{-1}·MPa^{-1} at CO_2 pressures in the range 7-13 MPa, and to 3.5-4 mmol·g_{coal}^{-1} at 13-18 MPa.

Even though the experiments were conducted on separate samples, the data show a smooth Langmuir-shaped trend within a band of scatter less than 0.5 mmol·g_{coal}^{-1} in amplitude. Measurement errors estimated as discussed in section 4.2.3.5 are represented by the error bars shown in Fig. 4 and are listed in Table 2. These include the random error due to inaccuracies in the determination of the volume of CO_2 in the bag after the experiment (arising from inaccuracies in the measurement of ambient pressure and temperature), as well as the larger systematic error due to CO_2 captured in voids between the sample and capsule. Note that, when samples could be removed from their capsules without chipping or breakage, their mass measured before and after testing varied by less than -2.79 to +0.81 % (Table 1).

Exp. code	CO_2 pressure	Volume change of inflated Al foil bag	Total CO_2 uptake N	Max. expected systematic error due to possible CO_2 trapping above sample (A)	Max. expected systematic error due to possible CO_2 trapping around sample (B)	Random error due to uncertainty in measurement of P and T at NTP (R)	Total positive uncertainty = (R)	Total negative uncertainty = (A)+(B)+(R)
	MPa	ml	$mmol \cdot g_{coal}^{-1}$	$mmol \cdot g_{coal}^{-1}$	$mmol \cdot g_{coal}^{-1}$	$mmol \cdot g_{coal}^{-1}$	$mmol \cdot g_{coal}^{-1}$	$mmol \cdot g_{coal}^{-1}$
1	0.69	0.44612	0.2651	0.02	0.01	0.00037	0.00037	0.03
2	1.75	0.79362	0.5258	0.06	0.03	0.00077	0.00077	0.09
3	1.88	1.48447	0.8874	0.06	0.03	0.00124	0.00124	0.09
4	2.59	2.24723	1.4174	0.09	0.04	0.00201	0.00201	0.13
5	3.01	1.65026	1.0405	0.02	0.05	0.00148	0.00148	0.07
6	4.19	3.01928	1.9168	0.02	0.00	0.00273	0.00273	0.03
7	4.45	2.00242	2.5059	0.05	0.00	0.00547	0.00547	0.06
8	6.13	3.88311	2.4030	0.04	0.00	0.00341	0.00341	0.05
9	7.00	4.06003	2.5650	0.05	0.00	0.00364	0.00364	0.06
10	7.00	3.88305	2.5284	0.05	0.00	0.00361	0.00361	0.06
11	7.64	4.20858	2.6714	0.07	0.00	0.00382	0.00382	0.07
12	10.00	3.69134	3.0375	0.22	0.00	0.00498	0.00498	0.23
13	10.00	3.16901	3.4584	0.30	0.00	0.00688	0.00688	0.30
14	12.00	4.11485	3.4047	0.25	0.00	0.00558	0.00558	0.26
15	13.80	3.48726	3.8505	0.36	0.00	0.00767	0.00767	0.37
16	15.60	3.46837	3.8980	0.37	0.00	0.00780	0.00780	0.38
17	15.60	3.25907	3.8230	0.39	0.00	0.00791	0.00791	0.40
18	18.10	3.67715	4.0812	0.39	0.00	0.00812	0.00812	0.40

Table 2. Total CO_2 uptake measured using the capsule method for samples equilibrated with CO_2 at a fixed CO_2 pressure and at 40 °C. Systematic (A, B) and random errors (R) are estimated on the basis of control tests (as described in section 4.2.3.5) and summed as total positive and negative uncertainties. Note that the possibility of trapping of CO_2 in the space between the sample and the cone dominates the total uncertainty in the method.

Initial CO_2 pressure in reference cell	Initial CO_2 density (SWEoS)	Total amount of CO_2 in reference + sample cell	Total amount of CO_2 in the sample cell	Equilibrium CO_2 pressure in system	Equilibrium CO_2 density (SWEoS)	True non-coal volume in sample cell	Absolute CO_2 uptake by the sample set	Total CO_2 uptake by the sample set	Random error due to uncertainty in measurement
P_i^f	ρ_i^f	n_{sys}	n_{SC}	P_i^e	ρ_i^e	$(V_{SC} - V_{set})$	n_{set}	N_{set}	of P_i, T_i, V_{SC}, V_{RC}
MPa	kg·m^{-3}	mmol	mmol	MPa	kg·m^{-3}	ml	mmol	mmol·g$_{coal}^{-1}$	mmol·g$_{coal}^{-1}$
1.21	21.63	0.28	0.29	0.00	0.00	0.5261	0.00	0.00	0.00
2.82	54.61	0.97	0.75	0.61	10.54	0.5240	0.17	0.34	0.01
3.63	74.05	1.58	1.12	2.00	37.10	0.5208	0.31	0.64	0.01
6.50	170.82	3.48	2.12	3.06	60.17	0.5195	0.41	0.83	0.02
6.50	170.82	4.14	2.47	5.58	132.56	0.5180	0.56	1.15	0.03
8.46	341.50	7.33	4.11	6.21	157.72	0.5178	0.61	1.25	0.04
12.33	725.07	15.20	7.96	8.03	278.92	0.5174	0.83	1.70	0.11
15.31	783.77	18.86	9.69	9.53	578.60	0.5171	1.16	2.38	0.12
15.37	784.67	20.04	10.27	12.07	717.84	0.5166	1.26	2.59	0.14
20.30	841.68	21.43	10.95	14.04	762.61	0.5164	1.32	2.71	0.16
25.47	880.56	22.58	11.51	17.77	815.85	0.5162	1.38	2.83	0.17
25.31	880.85	22.95	11.69	22.37	859.30	0.5159	1.43	2.94	0.19
0.01	-	7.53	4.17	24.28	873.66	0.5158	1.46	2.99	0.20
0.01	-	2.54	1.63	8.09	286.53	0.5174	0.80	1.64	0.19
0.01	-	0.90	0.73	4.47	96.74	0.5185	0.49	1.00	0.20
0.01	-	0.35	0.38	1.85	34.10	0.5211	0.33	0.67	0.20
0.01	-	0.16	0.22	0.76	13.27	0.5236	0.22	0.46	0.21
0.01	-	0.09	0.13	0.36	6.18	0.5248	0.15	0.30	0.21
0.01	-	0.05	0.08	0.19	3.28	0.5254	0.09	0.19	0.21
0.01	-	0.03	0.05	0.12	1.95	0.5257	0.06	0.12	0.22
0.01	-	0.02	0.03	0.08	1.27	0.5258	0.03	0.07	0.22

Table 3. Total CO_2 uptake measured using the manometric method applied for CO_2 pressures stepped up to 25 MPa at a temperature of 40 °C. The measurements were performed on a combined set of 8 cylindrical samples with a total mass of ~0.5 g. All data were computed using the Span and Wagner EoS (Span and Wagner, 1996) and corrected for swelling of the samples following the measured expansion reported by Hol and Spiers (submitted). Random errors were calculated on the basis of the effect of pressure, temperature and volumetric measurement inaccuracies on the densities predicted by the SWEoS. Note that random errors cumulatively increase with each pressure step employed in the single experiment performed.

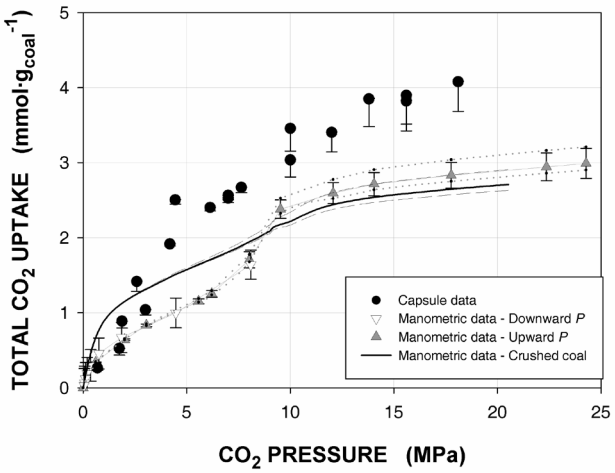

Fig. 4. Total CO_2 uptake as a function of CO_2 pressure for Brzeszcze 364 cylindrical samples of coal matrix material, as determined using the capsule method (18 separate experiments on 7 samples) and the manometric method (single experiment on a set of 8 samples). Upper and lower bound values for the manometric data points reported in this study (dotted) and for the results obtained by Gensterblum et al. (2010) (dashed) were calculated using ρ_0=1300 kg·m^{-3} (upper) and ρ_0=1325 kg·m^{-3} (lower). Note the two CO_2 pressure intervals where significant differences in total CO_2 uptake (in mmol·g_{coal}^{-1}) are visible between the data generated by the two methods, i.e. at 3-9 MPa CO_2 pressure (max. difference ~1 mmol·g_{coal}^{-1} around 6 MPa) and at CO_2 pressures >9 MPa (difference consistently 0.8-1.0 mmol·g_{coal}^{-1}).

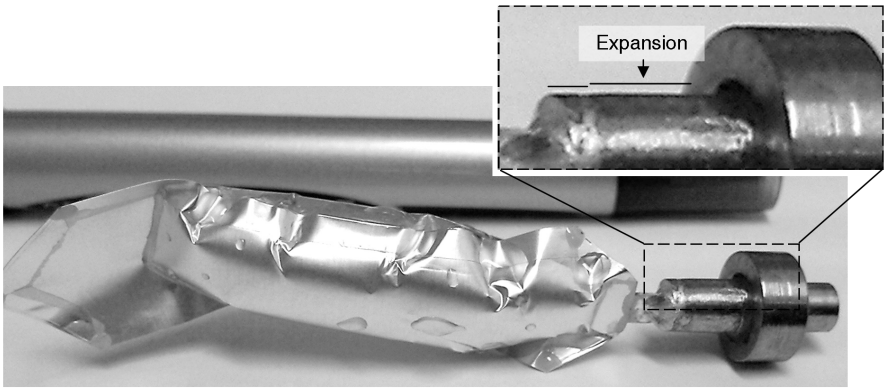

Fig. 5. Photograph of ductile metal capsule assembly after a successful experiment (note pen for scale). The Al foil bag is strongly inflated showing the captured CO_2 volume. Note the radial expansion of the ductile Au jacket due to adsorption-induced swelling of the coal sample. Deformation of the Au jacket was visible with the naked eye after all experiments conducted at CO_2 pressures higher than ~3 MPa. Droplets of water are visible at various points on the side of the bag, as its volume had just been determined using the Archimedes method (in water).

4.3.2. Manometric data

At each CO_2 pressure step implemented in the manometric test, the samples required 10-12 h to attain pressure equilibrium within the accuracy of the Tecsis P3382 pressure transducer. This implies that during both the manometric and the capsule tests (run time 24h) equilibrium between the samples and the CO_2 was sufficiently approached. In contrast to the capsule tests, we note that the mass of the sample set decreased significantly, by 4.13 %, after manometric testing. Since this mass loss is most probably due to loss of water or hydrocarbons, the measured uptake was normalised with respect to sample mass after testing (following equation 5). Taking the mass of the samples before testing would yield 4.31 % lower uptake values. We did not plot these slightly lower values in Fig. 4.

The manometric data (Fig. 4) indicate that the total uptake of CO_2 by our set of 8 samples, corrected for sample swelling, increases continuously as a function of increasing CO_2 pressure, up to a value of 2.99 mmol·g_{coal}^{-1} at 24.28 MPa CO_2 pressure. Random errors are indicated using error bars in Fig. 4 and are listed in Table 3. The upper and lower bounds calculated to illustrate the sensitivity of the manometric data to variations in sample density ρ_0 (upper values of 1300 kg·m^{-3} and lower values of 1325 kg·m^{-3}) show similar deviation from the plotted data point as do the random measurement errors calculated for the CO_2 uptake (Fig. 4). In contrast to the smooth Langmuir-shaped curve obtained from the capsule test, three stages can be observed in the total CO_2 uptake versus CO_2 pressure curve obtained manometrically. Below ~7 MPa CO_2 pressure, the CO_2 uptake first increases sharply (up to 1 MPa CO_2 pressure) and then more gradually at a rate of ~0.14 mmol·g_{coal}^{-1}·MPa^{-1}. In the range 7-9 MPa CO_2 pressure (*i.e.* in the neighbourhood of the critical pressure of CO_2), the uptake data show an abrupt increase at a rate of ~0.4 mmol·g_{coal}^{-1}·MPa^{-1}. Beyond ~10 MPa CO_2 pressure, the CO_2 uptake continues at a mean rate of only ~0.04 mmol·g_{coal}^{-1}·MPa^{-1} up to the maximum CO_2 pressure applied of 24.28 MPa.

4.4. Discussion

The two measurement methods applied here rely on fundamentally different and independent principles and assumptions, and it is for this reason that the capsule method was developed. In the discussion that follows, we will compare in detail the CO_2 uptake trends obtained using both methods, quantifying the main differences. We will go on to explain these differences in relation to the sensitivity of the methods to both systematic and random errors. Finally, we discuss the implications of our findings in the context of applying CO_2 uptake measurements to assess the CO_2 storage capacity of coal seams under *in situ* conditions.

4.4.1. Comparison of the methods – role of systematic and random errors

From Fig. 4 it is evident that, besides the reasonable agreement seen below 3 MPa CO_2 pressure, our two data sets show three main ranges of CO_2 pressure, in which significant differences in total CO_2 uptake (in mmol·g_{coal}^{-1}) exist between the data sets. First, uptake in the range of 3-8 MPa CO_2 pressure shows consistently lower values (30-50 %) for the manometric results. This difference is the largest at around 6 MPa, with a magnitude of ~1 mmol·g_{coal}^{-1} (50 %). At 7-9 MPa CO_2 pressure, the manometric data show a sharp jump toward the capsule data, reducing the discrepancy by 0.1-0.5 mmol·g_{coal}^{-1} to 25 %. Beyond 9 MPa, the difference in CO_2 uptake again increases as the capsule data show a faster increase with CO_2 pressure than the manometric data, reaching a maximum difference of ~1 mmol·g_{coal}^{-1} (30 %) at the maximum CO_2 pressure of 18 MPa investigated in the capsule tests. We will first consider the reliability of our error calculations based on the uncertainties in pressure and temperature sensing, as well as the systematic errors expected in the capsule method (section 4.2.3.5). We then go on to consider the maximum errors that might be possible for the two measurement approaches used, taking a worst case approach.

4.4.1.1. Expected magnitude of random and systematic errors

The scatter seen from point to point in the capsule dataset could potentially reflect sample heterogeneity. Nonetheless, the limited amplitude of this scatter suggests that any major errors in determinations must be systematic. Table 2 lists the systematic errors inferred on the basis of the control tests reported in section 4.2.3.5. These strongly dominate over random errors. For the manometric data, on the other hand, only random measurement errors were considered, and these only become significant in the downward CO_2 pressure cycle (Table 3). Cumulative, total error bars are indicated on all data plotted in Fig. 4. Four important observations can be made on the basis of these error bars plotted for the measurements made on our cylindrical samples. First, the random and systematic errors considered are smaller than the difference between the capsule and manometric results for total CO_2 uptake in the CO_2 pressure range 3-8 MPa or at pressures >9 MPa. Second, the substantial systematic

errors inferred from the control tests performed using the capsule method only affect the values plotted for CO_2 pressures in excess of 9 MPa. Third, the jump in uptake observed in the manometric data at 7-9 MPa is larger than the magnitude of the error bars shown. Fourth, the propagation of random errors in the manometric results seems to be very sensitive to its cumulative character, as observed from the size of the 'adsorption' versus 'desorption' error bars at CO_2 pressures of 0-4 MPa.

We infer that the discrepancy between the two data sets cannot be explained in terms of the expected systematic errors in the capsule method, or in terms of the random errors caused by uncertainties in CO_2 pressure, temperature and volume determinations as calculated for the manometric method following Gensterblum et al. (2010). This implies that the discrepancy is either real, pointing to uncertainty in describing the *P-V-T* properties of CO_2, or that our capsule or manometric errors are underestimated. In addition, we note that substantial differences exist (up to 0.5 $mmol \cdot g_{coal}^{-1}$) between the manometric data derived for the present cylindrical samples (total sample mass ~0.5 g) and the data reported by Gensterblum et al. (2010) for crushed coal (total sample mass ~8.4 g) in the CO_2 pressure range 0-7 MPa (Fig. 4). The data reported by Gensterblum et al. (2010) show a sharper increase in CO_2 uptake versus pressure in the range 0-2 MPa, while, in the CO_2 pressure range 2-7 MPa, the increase is about the same for both data sets. This indicates either a high variability in adsorption potential at low CO_2 pressure, between samples of the same Brzeszcze coal (seam 364), or methodological problems in the manometric method that underlie the data sets.

4.4.1.2. Worst case scenario for random and systematic errors

To gain further insight into the difference seen between our two data sets, we now investigate the effect of unexpectedly extreme but physically possible uncertainties in both datasets (*i.e.* a worst case error scenario).

We start by allowing for higher systematic errors in the capsule method. Since the sealing cone and swaging ring were machined to within 0.1 mm, sealing of the capsule (Fig. 3) could, in the worst case, have occurred with the cone positioned 0.1 mm above the sample, trapping an undesired volume of CO_2 (at conditions of *P* and *T*) inside the capsule, between the cone and the sample. In addition, we assume that the magnitude of the random errors is increased to include major inaccuracies in a) ambient temperature (±4.0 °C) and pressure values (±0.006 MPa – max. variability ever recorded in meteorological office records for Utrecht), and b) sample mass determination using the balance (±0.0005 g, which is 10x balance resolution). The sum of these errors constitutes a full worst case error scenario for the capsule method. The computed worst case errors are listed in Table 4 and the total CO_2 uptake data, including the worst case error bars, are shown as a function of CO_2 pressure in Fig. 6. It is clear from Fig. 4 and Fig. 6 that below ~8 MPa CO_2 pressure, the magnitude of

Exp. code	CO_2 pressure	Total CO_2 uptake N	Max. expected systematic error due to possible CO_2 trapping above sample (A)	Max. expected systematic error due to possible CO_2 trapping around sample (B)	Max. expected systematic error due to possible CO_2 trapping in flattened Au-tube (C)	Random error due to uncertainty in measurement of P and T at NTP (R)	Total positive uncertainty = (R)	Total negative uncertainty = (A)+(B) +(C)+(R)
	MPa	mmol·g_{coal}^{-1}	mmol·g_{coal}^{-1}	mmol·g_{coal}^{-1}	mmol·g_{coal}^{-1}	mmol·g_{coal}^{-1}	mmol·g_{coal}^{-1}	mmol·g_{coal}^{-1}
1	0.69	0.2651	0.00	0.01	0.00	0.02	0.02	0.03
2	1.75	0.5258	0.01	0.03	0.01	0.03	0.03	0.08
3	1.88	0.8874	0.01	0.03	0.01	0.06	0.06	0.11
4	2.59	1.4174	0.02	0.04	0.01	0.09	0.09	0.16
5	3.01	1.0405	0.03	0.05	0.01	0.07	0.07	0.15
6	4.19	1.9168	0.04	0.00	0.02	0.12	0.12	0.18
7	4.45	2.5059	0.08	0.00	0.03	0.17	0.17	0.29
8	6.13	2.4030	0.07	0.00	0.03	0.15	0.15	0.25
9	7.00	2.5650	0.09	0.00	0.03	0.16	0.16	0.28
10	7.00	2.5284	0.09	0.00	0.03	0.16	0.16	0.28
11	7.64	2.6714	0.11	0.00	0.04	0.17	0.17	0.32
12	10.00	3.0375	0.36	0.00	0.14	0.20	0.20	0.70
13	10.00	3.4584	0.48	0.00	0.19	0.24	0.24	0.90
14	12.00	3.4047	0.41	0.00	0.16	0.22	0.22	0.79
15	13.80	3.8595	0.58	0.00	0.23	0.26	0.26	1.07
16	15.60	3.8980	0.60	0.00	0.24	0.27	0.27	1.11
17	15.60	3.8230	0.63	0.00	0.25	0.26	0.26	1.14
18	18.10	4.0812	0.62	0.00	0.25	0.28	0.28	1.15

Table 4. Worst case errors in total CO_2 uptake measured using the capsule method. Worst case systematic errors were computed assuming limited accuracy of machining of the capsule components (within 0.1 mm). Worst case random errors were computed by assuming a) extreme uncertainties in ambient temperature (±4.0 °C) and pressure (±0.006 MPa), and b) inaccurate mass determination using the balance (±0.0005 g).

the error bars associated with the capsule data is relatively insensitive to the worst case errors allowed for here, whereas above ~8 MPa the length of the error bars increases drastically. Indeed, at high CO_2 pressures, the magnitude of the negative errors, reflecting mainly free CO_2 assumed to be trapped in the capsule, is about ⅓ of the uptake values plotted. This is because above the critical point of CO_2, the density of the free phase increases dramatically. At least part of the discrepancy between our capsule and manometric data above 8 MPa CO_2 pressure could therefore be due to erroneous trapping of small but still unexpectedly high amounts of free CO_2. We conclude that care should be taken in the application of the capsule method at CO_2 pressures higher than 8-9 MPa, making every effort to check for, and to eliminate, dead-volume trapping.

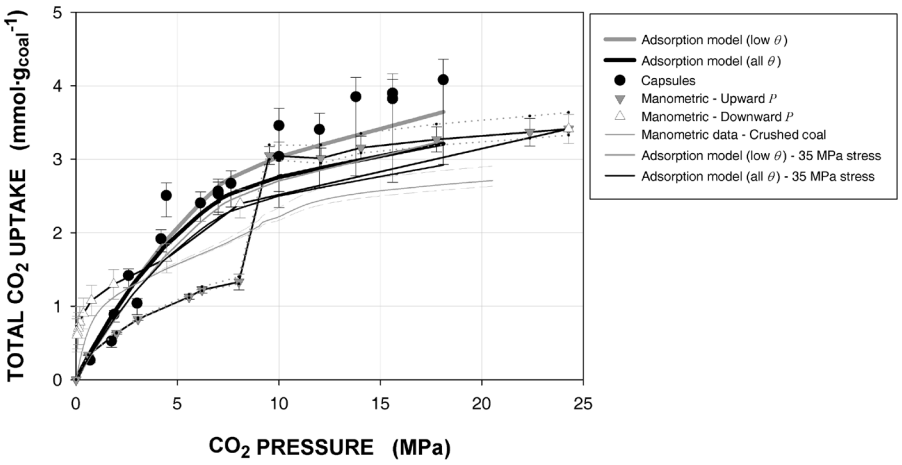

Fig. 6. Total CO_2 uptake as a function of CO_2 pressure for our cylindrical samples of Brzeszcze 364 coal matrix material, as determined using the capsule method and the manometric method, and considering worst case errors. Manometric data reported by Gensterblum et al. (2010) for crushed Brzeszcze 364 coal (particle size <2 mm) are also included for comparison. The capsule method is most sensitive to systematic errors above ~8 MPa of CO_2 pressure, while below that it is insensitive. Manometric data for the cylindrical samples were plotted on the basis of CO_2 densities derived as a function of CO_2 pressure from the data reported by Bae and Bhatia (2006). Upper and lower bound values for the manometric data points reported in this study (dotted line) and for the results obtained by Gensterblum et al. (2010) (dashed line) were calculated using ρ_0=1300 kg·m^{-3} (upper) and ρ_0=1325 kg·m^{-3} (lower). Note the difference compared with Fig. 4 for the manometric method, demonstrating the high sensitivity of the method to the EoS. The thermodynamic model in equation (7 – all θ) and (8 – low θ) was fitted to the capsule data in CO_2 pressure range 0-7 MPa, and extrapolated to the CO_2 pressure range 7-18 MPa.

Initial CO_2 pressure in reference cell	Initial CO_2 density (SWEoS)	Total amount of CO_2 in reference + sample cell	Total amount of CO_2 in the sample cell	Equilibrium CO_2 pressure in system	Equilibrium CO_2 density (B&B)	True non-coal volume in sample cell	Absolute CO_2 uptake by the sample set	Total CO_2 uptake by the sample set	Random error due to uncertainty in measurement
P_i^f	ρ_i^f	n_{sys}	n_{SC}	P_i^e	ρ_i^e	$(V_{SC} - V_{set})$	n_{set}	N_{set}	of $P_i T_i V_{SC} V_{RC}$
MPa	kg·m^{-3}	mmol	mmol	MPa	kg·m^{-3}	ml	mmol	mmol·g$_{coal}^{-1}$	mmol·g$_{coal}^{-1}$
1.21	21.84	0.28	0.29	0.00	0.00	0.5261	0.00	0.00	0.00
2.82	54.83	0.98	0.75	0.61	10.75	0.5240	0.16	0.34	0.01
3.63	74.20	1.59	1.11	2.00	37.36	0.5208	0.31	0.63	0.01
6.50	169.96	3.47	2.11	3.06	60.35	0.5195	0.40	0.83	0.02
6.50	169.96	4.13	2.44	5.58	132.23	0.5180	0.55	1.13	0.03
8.46	328.52	7.20	3.87	6.21	157.09	0.5178	0.60	1.22	0.04
12.33	721.45	14.74	8.08	8.03	274.18	0.5174	0.65	1.33	0.11
15.31	780.63	18.75	9.84	9.53	561.24	0.5171	1.49	3.05	0.12
15.37	781.53	19.94	10.44	12.07	713.53	0.5166	1.47	3.01	0.14
20.30	839.74	21.37	11.13	14.04	758.80	0.5164	1.54	3.16	0.16
25.27	878.54	22.52	11.69	17.77	813.40	0.5162	1.59	3.27	0.17
25.31	878.82	22.90	11.88	22.37	857.32	0.5159	1.64	3.37	0.19
0.01	-	7.40	4.48	24.28	871.66	0.5158	1.66	3.41	0.20
0.01	-	2.54	1.94	8.09	281.66	0.5174	1.17	2.40	0.19
0.01	-	0.90	1.04	4.47	96.55	0.5185	0.80	1.65	0.20
0.01	-	0.35	0.69	1.85	34.36	0.5211	0.63	1.30	0.20
0.01	-	0.17	0.52	0.76	13.47	0.5236	0.53	1.08	0.21
0.01	-	0.09	0.42	0.36	6.45	0.5248	0.44	0.90	0.21
0.01	-	0.06	0.37	0.19	3.54	0.5254	0.38	0.78	0.21
0.01	-	0.04	0.33	0.12	2.15	0.5257	0.34	0.70	0.22
0.01	-	0.02	0.31	0.08	1.40	0.5258	0.31	0.64	0.22

Table 5. Total CO_2 uptake measured using the manometric method for present samples. All data are computed on the basis of CO_2 densities derived from data reported by Bae and Bhatia (2006), and corrected for swelling of the samples following the measured expansion reported by Hol and Spiers (submitted). Random errors were calculated on the basis of the effect of pressure, temperature and volumetric inaccuracies on the densities predicted by the SWEoS, and are exactly equivalent to those calculated for the expected error scenario. Note that random errors cumulatively increase with each pressure step employed in the single experiment performed.

With respect to the manometric method, it is well-known that, aside from random error propagation, more fundamental errors may be associated with the underlying methodological assumptions (Condon, 2006; Ross and Bustin, 2007; Sakurovs, et al., 2009) – see Introduction. However, two of the three sources of methodological error have been eliminated in the present application of the manometric method. The remaining possibility is that inaccuracies in the EoS used for the free CO_2 phase have a substantial impact on the data, particularly when a small quantity of sample material is used, as in this study. In the present case, the aggregate mass of the 8 cylinders used for the manometric measurements was ~0.5 g, increasing errors by about an order of magnitude compared to the standard sample mass of several grams (*e.g.* Gensterblum, et al., 2010; Goodman, et al., 2004). Such errors can occur either when the thermophysical properties of the pure CO_2 phase are not accurately described by the available EoS, or when the CO_2 is impure, *e.g.* contaminated by water or hydrocarbon molecules derived from the samples, producing different *P-V-T* behaviour. Kolak and Burruss (2006) reported that both water and hydrocarbons are extracted from coal matrix material as a result of exposure to CO_2. Although it is recognized that such impurities strongly influence the thermophysical behaviour of pure CO_2 near the critical point (Zhang, et al., 2002), the effect of this on our manometric results cannot be assessed as the concentration of any impurities is unknown. Recall, however, that our samples lost 4.13 % of their combined mass during the full course of the manometric experiment (including both evacuation and saturation). Therefore, an effect of impurities on the manometric data obtained near the critical point can not be excluded, especially noting the step in the manometric data at 7-9 MPa (Fig. 4). Finally, we note that the swelling correction applied to the manometric result for the cores was derived for samples that have been exposed to CO_2 in earlier tests (Hol and Spiers, submitted). However, three out of the 8 samples tested manometrically were not exposed to CO_2 in preceding experiments, which may have given rise to inaccuracies in the swelling correction, for example if there are any irreversible effects associated with initial exposure of virgin samples (Goodman, et al., 2006). Even so, these inaccuracies are expected to be negligible at CO_2 pressures below the critical pressure (*i.e.* below 7.3 MPa) where the density of CO_2 is relatively low and the swelling correction (equation 1) is small.

Consider now the effect of uncertainties in the EOS for pure CO_2 on the manometric method. This can have particularly large effects for the small sample set used. Measurements of the change in density of CO_2 with increasing CO_2 pressures up to 20 MPa, at a fixed temperature of 40 °C, have recently been performed by Bae and Bhatia (2006), who used a gravimetric method to yield data on the density of CO_2 independently of the SWEoS. For most of the range of CO_2 pressures investigated, the CO_2 densities derived from their measurements were within 1 % of those predicted by the SWEoS (see Fig. 7 – data kindly provided by J.-S. Bae). However, the data demonstrate that small differences can exist between SWEoS-derived densities and densities actually measured in experiments. We used CO_2 densities interpolated from the data reported by Bae and Bhatia (2006) to calculate the total uptake of CO_2 that

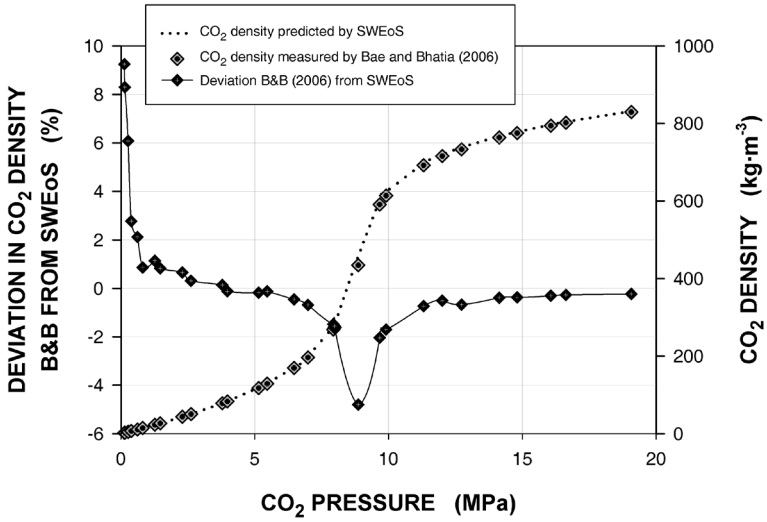

Fig. 7. CO_2 density as a function of CO_2 pressure (grey, solid line; referring to the right hand axis). Data are taken from experiments performed by Bae and Bhatia (2006). These experiments were conducted at CO_2 pressures up to 20 MPa, at a fixed temperature of 40 °C. The data were fitted using the Span and Wagner EoS (Span and Wagner, 1996). The deviation (in %) of the measured CO_2 densities (Bae and Bhatia, 2006) from the expected CO_2 densities (Span and Wagner, 1996) is calculated using the expression $((\rho_{B\&B}-\rho_{SWEoS})/\rho_{SWEoS})x100\%$, and is plotted in black as a function of CO_2 pressure (black, dotted line; referring to the left hand axis).

occurred in our manometric experiment (Table 5). The resulting uptake versus CO_2 pressure data and random error bars are plotted in Fig. 6. From Fig. 6, it is clear that the total CO_2 uptake as determined using the manometric method, in combination with the CO_2 densities measured by Bae and Bhatia (2006), shows significant hysteresis between the upward and downward pressure cycles. The upward trend shows low uptake (0-1.3 $mmol \cdot g_{coal}^{-1}$) in the CO_2 pressure range of 0-7 MPa, increasing sharply to ~3.0-3.2 $mmol \cdot g_{coal}^{-1}$ above 7 MPa CO_2 pressure. Desorption follows a continuously decreasing trend, without interruptions or sharp changes, and is similar to the trend observed in the CO_2 uptake data versus pressure data obtained for powdered samples by Gensterblum et al. (2010). All data plotted in Fig. 6 for the present manometric experiment, except those falling in the low CO_2 pressure range of the upward-going cycle, fall within the worst case experimental error range for the capsule method. The capsule and manometric data thus agree within the worst case experimental error when the *P-V* (*i.e.* density) data of Bae and Bhatia (2006) are used instead of the SWEoS. The remaining discrepancy in the CO_2 pressure range 3-9 MPa, and hence the hysteresis observed in the manometric pressurisation cycle, may reflect an additional possible influence of impurities on the *P-V-T* behaviour of CO_2, or perhaps an effect of water on the affinity of CO_2 for coal (at low CO_2 pressures) of the type inferred by Busch et

al. (2006). In any case, the use of the CO_2 densities obtained from the data of Bae and Bhatia (2006) demonstrates that the results of the present manometric experiment are extremely sensitive to inaccuracies in the EoS of CO_2. This applies in particular to the low pressure range, *i.e.* to CO_2 pressures in the range 0 to 9 MPa.

Summarising the above considerations, we attribute the differences between the capsule and manometric methods (*i.e.* the difference in total CO_2 uptake seen in the CO_2 pressure range 3-9 MPa and above 8-9 MPa (Fig. 4 and/or Fig. 6) to a) a combination of random errors and EoS problems dominating in the manometric dataset in the CO_2 pressure interval 3-9 MPa, and b) systematic errors dominating in the capsule dataset at CO_2 pressures higher than 9 MPa. At low CO_2 pressures (*i.e.* in the range 0-7 MPa), our analysis shows that the capsule method is reliable. By contrast, the manometric method shows high sensitivity to small errors in the densities predicted by the EoS, at these CO_2 pressures. On the other hand, when significantly large quantities of sample material are used (*e.g.* >5 g depending on system characteristics), the effect of such errors will be relatively small, since the absolute errors are then normalised over a larger coal mass. At high CO_2 pressures (*i.e.* above 8 or 9 MPa, where CO_2 is in the supercritical phase), at least part of the discrepancy seen between our capsule and manometric data is likely due to erroneous trapping of small amounts of free CO_2 residing outside the sample. This means that caution should be exercised in the application of the capsule method at CO_2 pressures higher than 8-9 MPa.

4.4.1.3. Final remarks on the applicability of the capsule and manometric methods

Storage of CO_2 in coal beds and expulsion of CH_4 involves adsorption trapping of, and pore filling by CO_2. The total storage capacity can therefore be obtained by adding the absolute adsorption potential obtained from the manometric or gravimetric data (*i.e.* from excess sorption determinations), under the assumption that a fixed density of the adsorbed phase exists, to the filling capacity of the pore space by CO_2. To determine the total CO_2 content of coal samples at conditions of fixed temperature, zero effective stress and CO_2 pressures in the range 0-20 MPa, we have developed a new method in this study (capsule method) and compared this to the conventional manometric method, which we used without making the distinction between an adsorbed and a free phase (*i.e.* without calculating the total CO_2 uptake from excess sorption data).

Although the capsule method is highly sensitive to systematic errors introduced at CO_2 pressures higher than 9 MPa, it has been shown here to be a reliable method at low CO_2 pressures (*i.e.* 0-7 MPa). In addition, this method is suitable for the assessment of the local (mm-scale) CO_2 storage properties of coal layers, and can hence give insight into the layer-dependent, or even maceral-dependent variability of the CO_2 storage potential of coal seams. Moreover, when uptake of mixed fluids needs evaluation, the capsule method allows chemical analysis of the captured fluid,

and hence study of preferential adsorption processes or chemical reactions. Clearly, additional experiments must be performed to assess the broader applicability of the capsule method and to improve its reliability especially above the critical pressure of CO_2, in particular to remove undesired trapping of CO_2 outside the sample. However, the method does have the potential to accurately determine the uptake of any adsorbate by any (swelling) adsorbent, and can be applied to investigate CO_2 uptake by small cores of shale and clay caprocks in the context of CO_2 storage in depleted oil and gas reservoirs, again allowing the assessment of spatial differences in CO_2 uptake due to small-scale lithological variations. We note, however, that the preparation of the capsules is elaborate, time-consuming and costly.

The manometric method was applied here to an extremely small amount of sample material –only ~0.5 g. Hence, associated random errors due to measurement inaccuracy and fluctuation in CO_2 behaviour were relatively high. However, these errors constitute small relative errors for the large quantities of sample material that are typically used (*i.e.* >5 g). The manometric method applied for total uptake is accordingly the most suitable for testing the CO_2 storage potential of large amounts of (homogenised) granular material under unconfined, isostatic exposure conditions. Nonetheless, improvements in volume, temperature and fluid chemistry control may be valuable, especially when applied for determining excess sorption where possible uncertainties related to H-pycnometry and swelling cannot be entirely eliminated (*cf.* equations 1 plus 3-7). Finally, we note that the manometric method, in contrast to the capsule method, offers a means of investigating the relative contributions of adsorbed and free CO_2 to the total CO_2 uptake of coal, and that the method is cost-efficient and relatively easy to perform. It will therefore remain the principal method for CO_2 uptake determinations by coal under unconfined, isostatic test conditions.

4.4.2. Implications of capsule data for CO_2 storage capacity of Brzeszcze coal matrix material

The CO_2 uptake versus CO_2 pressure trend, as determined by the capsule method (Fig. 4 and Fig. 6), has been shown to be reliable at low CO_2 pressures (*i.e.* in the range 0-9 MPa). Moreover, its smooth, Langmuir-like form (Fig. 4 and Fig. 6) demonstrates that adsorption is the dominant uptake process in our samples at CO_2 pressures below 10 MPa. This is because any major contribution of free CO_2 to the total CO_2 uptake measured would give rise to a sudden "jump" in uptake at 7-10 MPa CO_2 pressure, due to the drastic increase in CO_2 density near the critical pressure (~7.3 MPa), which is not seen. Having inferred the dominance of adsorption at CO_2 pressures below 10 MPa, we will now compare our capsule data with the site adsorption model recently developed by Hol et al. (2011), in order to obtain a parameterised description of the observed sorption behaviour for this pressure range at 40 °C. We go on to consider not only adsorption under unconfined conditions as in our experiments, but also the

effects of a positive effective stress or overburden pressure on sorbed CO_2 amount. The magnitude of these effects is in turn compared with the errors found in the capsule and manometric data.

4.4.2.1. Thermodynamic model for adsorption of CO_2 by coal under unconfined conditions

The model developed recently by Hol et al. (2011) considers adsorption by small samples or particles of cleat-free, nanoporous coal matrix material. The matrix material is assumed free of pores allowing Darcian flow or storage of free (un-adsorbed) CO_2 and can take up CO_2 only by diffusion and adsorption. In a system so defined, Hol et al. (2011) showed that the concentration C of adsorbed CO_2 molecules present in the coal body, when in equilibrium with CO_2 at a hydrostatic fluid pressure P under unconfined conditions (zero effective stress), is given

$$C(P) = C_s\theta = \frac{C_s a_f \exp\left(\frac{\mu_0 - \Delta G_a}{kT}\right)}{1 + a_f \exp\left(\frac{\mu_0 - \Delta G_a}{kT}\right)} \tag{6}$$

Here, $C(P)$ is the equilibrium concentration of adsorbed CO_2 in mmol·g^{-1} or mol·kg^{-1}, C_s represents the (constant) number of potential adsorption sites per kg of coal and θ is the 'occupancy' (occupied fraction) of the available adsorption sites. In addition, a_f is the chemical activity of the free CO_2 at pressure P, μ_0 is its potential in the reference state $a_f = 1$, and ΔG_a represents the Gibbs energy that must be supplied to remove an adsorbed molecule of CO_2 from an adsorption site into the free CO_2 phase (Hol, et al., 2011). Note that ΔG_a is given $\Delta G_a = \Delta F_a + P\Delta V_a$, where the term ΔF_a is the Helmholtz free energy of attachment (which includes any changes in elastic energy stored in coal) and $\Delta V_a = (\Omega_0 - \Omega_f)$ is the difference between the partial molecular volume (Ω_0) of CO_2 in the adsorbed state and its molecular volume (Ω_f) in the free phase. With Ω_0 defined in this way, Ω_0 represents the volume change (swelling) of the coal per molecule of adsorbed CO_2 and the $P\Delta V_a$ term represents the pressure–volume work associated with swelling due to adsorption of a single molecule.

This model predicts that, at conditions of constant temperature T and a varying fluid pressure P, changes in adsorbed concentration C or site occupancy are a combined effect of two fundamental causes: (1) the changing pressure, density and hence activity and chemical potential of the free fluid phase, and (2) the changing availability of adsorption sites, which is expressed statistically through the pressure dependence of ΔG_a in (3) via the ΔF_a and $P\Delta V_a$ terms (Hol, et al., 2011; Tuin and Stein, 1995). For an ideal gas, a_f becomes equal to the gas pressure and (3) reduces to the widely applied Langmuir model (cf. Hol, et al., 2011). However, for non-ideal and supercritical CO_2, the activity a_f must be retained and is given by the ratio between the fugacity of CO_2

(f, in MPa) at pressure P and the fugacity of CO_2 (f_0) defined at the thermodynamic reference state, characterised by CO_2 pressure P_0 and potential μ_{f0}. Accordingly, equation (6) then modifies to

$$C(P) = \frac{C_s \frac{f}{f_0} \exp\left(\frac{\mu_0 - \Delta G_a}{kT}\right)}{1 + \frac{f}{f_0} \exp\left(\frac{\mu_0 - \Delta G_a}{kT}\right)} \tag{7}$$

for present purposes. To investigate the applicability of this model to the (reliable) CO_2 uptake data obtained in the capsule tests at CO_2 pressures below 10 MPa, we fit equation (6) to these data. We do this in a similar manner to that reported by Hol and Spiers (submitted), who included (6) in a theoretical model for coal swelling, taking the reference state of free CO_2 to correspond to P_0=0.1 MPa and T=40 °C.

We start by simplifying the full model, using the assumption that at low CO_2 pressures the occupancy θ of the available adsorption sites is low, and, that the change in activity a_f (determined by the change in fugacity f) dominates over the statistical effect of filling of adsorption sites as a function of CO_2 pressure. Under these conditions of low occupancy, the denominator in (6) and (7) asymptotically approaches 1, so that the adsorbed concentration C is then given by

$$C(P) \approx \frac{f(P) C_s}{f_0} \exp\left(\frac{\mu_0 - \Delta G_a}{kT}\right) \tag{8}$$

defined relative to the thermodynamic reference state at 0.1 MPa CO_2 pressure. Best-fitting of equation (8) to our C versus P data points (Fig. 6) in the low pressure range of 0-5 MPa, using f and f_0 as given by the EoS of CO_2 (Span and Wagner, 1996), yields the result $C_s \exp[(\Delta\mu_0 - \Delta G_a)/kT]$=0.052 mmol·$g_{coal}^{-1}$ and the fit shown in Fig. 6 for CO_2 pressures up to 18 MPa.

We now go on to consider the most reliable part of the capsule data set (0-9 MPa CO_2 pressure), including the large systematic errors (as in Fig. 6), fitting equation (6) for large θ to the lower limit of the error bars on our capsule data. In doing this, we assume that our data points overestimate the actual CO_2 uptake by a worst case amount indicated by the lower error bar. We take $C_s \exp[(\Delta\mu_0 - \Delta G_a)/kT]$=0.052 mmol·$g_{coal}^{-1}$ as determined from the low P fit. Adding an interpolated C data point of 0.1 mmol·g_{coal}^{-1}, the model was fit successfully to the data relative to the thermodynamic reference state defined at 0.1 MPa CO_2 pressure (reference for f_0 and μ_0) by using values for C_s in the range 9 to 20 mmol·g_{coal}^{-1} and for $(\Delta\mu_0 - \Delta G_a)$ in the range -13 to -16 kJ·mol^{-1}. Fig. 6 shows the data fit for the values C_s=18 mmol·g_{coal}^{-1} and $(\Delta\mu_0 - \Delta G_a)$=-15 kJ·$mol^{-1}$, plotted for CO_2 pressures up to 18 MPa. Note that the value for term $(\mu_0 - \Delta G_a)$ is dependent on the thermodynamic reference state chosen, *i.e.* the absolute value for μ_0 is unknown.

Note also that these values for C_s and ($\Delta\mu_0$-ΔG_a) are different than the values of C_s=3.01 mmol·g_{coal}^{-1} and ($\Delta\mu_0$-ΔG_a)=-9.6 kJ·mol^{-1} reported by Hol et al. (submitted), who compared (6) with the absolute adsorption data reported by Gensterblum et al. (2010). These values are, however of the same order and provide first constraints on C_s and ($\Delta\mu_0$-ΔG_a).

The reasonable fit to our capsule data obtained using the thermodynamic model of Hol et al. (2011) supports our inference that adsorbed CO_2 dominates the total uptake of CO_2 by our coal samples, and that pore filling by free, un-adsorbed CO_2 forms only a minor contribution. Moreover, with reference Fig. 6, the small difference in quality of the fit obtained using the full model (equation 7) versus the low θ model (equation 8), across the pressure range 0-18 MPa, may suggest that the driving force for adsorption reflects both the changing activity of the free fluid phase (dominating in (8)), and the changing availability of adsorption sites (dominating in (7)), *i.e.* that the samples are not yet saturated with CO_2 ($C<C_s$) at the highest pressures reached.

4.4.2.2. Effects of *in situ* stress state versus measurement errors

In contrast to the experimental conditions of zero effective stress used in sorption tests, coal seams experience a state of effective stress due to the overburden overlying the formation, and due to the effect of self-stressing during adsorption-induced swelling processes when CO_2 is injected (Harpalani and Mitra, 2010). Besides the poroelastic response of the bulk coal formation to such stresses (Biot, 1941; Wang, 2000), it has recently been demonstrated experimentally that the application of an effective stress directly influences the equilibrium sorption capacity of coal (Hol, et al., 2011; Wang, et al., 2011). Application of CO_2 storage capacities determined in the laboratory to *in situ* conditions of fluid pressure, temperature and stress requires these effects to be accounted for. The model developed by Hol et al. (2011) states that when a solid coal particle is subjected to a hydrostatic stress σ which exceeds the CO_2 pressure P by an effective stress $\sigma_e=\sigma-P$, then expansion of the coal by the amount Ω_0 accompanying adsorption of a single CO_2 molecule, will require an extra amount of work to be done on the system of magnitude $\sigma_e\Omega_0$. The free energy change ΔG_σ associated with adsorption in the stressed case must accordingly be written as $\Delta G_\sigma=\Delta G_a+\sigma_e\Omega_0$, so that (7) modifies to (*cf.* Hol, et al., 2011)

$$C(P)=\frac{C_s\frac{f}{f_0}\exp\left(\frac{\mu_0-\Delta G_a}{kT}\right)\exp\left(-\frac{\sigma_e\Omega_0}{kT}\right)}{1+C_s\frac{f}{f_0}\exp\left(\frac{\mu_0-\Delta G_a}{kT}\right)\exp\left(-\frac{\sigma_e\Omega_0}{kT}\right)} \tag{9}$$

and (8) modifies to

$$C(P)\approx C_s\frac{f}{f_0}\exp\left(\frac{\mu_0-\Delta G_a}{kT}\right)\exp\left(-\frac{\sigma_e\Omega_0}{kT}\right) \tag{10}$$

Here, the term $\exp[-(\sigma_e\Omega_0)/(kT)]$ can be treated as an uptake reduction factor reflecting the adsorption-inhibiting effect of σ_e, the (hydrostatic) effective stress applied to the samples. If we now insert into equation (10) a value for the effective hydrostatic overburden stress σ_e of 35 MPa, corresponding to a coal seam burial depth of 1.5-2.5 km, and take from Hol and Spiers (submitted) a partial molecular volume (Ω_0) of CO_2 in the adsorbed state of the order of $8.5\cdot10^{-6}$ $m^3\cdot mol^{-1}$, then we obtain an uptake reduction factor of 0.89. This implies that the application of an effective hydrostatic stress σ_e of 35 MPa reduces the adsorbed CO_2 concentration by 11 %, compared to unstressed conditions at fixed temperature. Inserting the same values for σ_e and Ω_0 into equation (9), *i.e.* using the high θ model, we can calculate the adsorbed CO_2 concentration (again assuming T=40 °C and σ_e=35 MPa) using the values C_s=18 $mmol\cdot g_{coal}^{-1}$ and $(\Delta\mu_0-\Delta G_a)$=-15 $kJ\cdot mol^{-1}$, obtained in section 4.4.2.1. For CO_2 pressures up to 18 MPa, this yields a reduction in C of 9-11 % relative to the unstressed state, where the highest reduction is obtained below the critical CO_2 pressure of 7.3 MPa. Note that the reduction of 11 % found using the low θ model (equation 10), compares closely with that found using the high θ model (equation 9). If we retain the assumption that adsorption is dominant over pore filling, then the obtained values represent the reduction in total storage capacity under *in situ* conditions corresponding to 35 MPa effective hydrostatic stress (~2 km depth and 40 °C). Note however, that the effective (overburden) stress in coal seams varies with depth, will not generally be hydrostatic, increases in magnitude due to constrained swelling when CO_2 is injected, and increases when CH_4 and water are produced. Of course, temperature increases with depth according to the geothermal gradient and influences the sorption capacity via the fugacity f, as well as via the exponential terms in (9). A detailed treatment of the effects of *in situ* stress and temperature require detailed modelling and will be considered in a later paper.

For present purposes, on the basis of the calculations above, we conclude that the effect of *in situ* stress on CO_2 adsorption under ECBM or CO_2 storage conditions will typically be of the order of 10 %. Elaborate discussions of errors in hydrostatic sorption experiments are therefore only justified when they are of this order. In practice, when using the conventional manometric method to determine CO_2 sorption capacity (and certainly CO_2 uptake capacity) of large crushed samples (*e.g.* Battistutta, et al., 2010; Gensterblum, et al., 2010; van Hemert, et al., 2009), or when using the capsule method at CO_2 pressures <7 MPa, the effects of stress on sorption will often be much more significant than any measurement errors, and need to be evaluated carefully.

4.5. Conclusions

In this study, we have developed a new method for measuring the total uptake of CO_2 by small (4x4 mm) cylindrical samples of coal matrix material. This has been applied at CO_2 pressures up to 18 MPa and at 40 °C to Brzeszcze 364 coal. The method involves enclosing a CO_2-saturated sample in a ductile metal capsule, and capturing its CO_2 content in an attached aluminium foil bag. The method does not discriminate between adsorbed and free CO_2. For comparison, a manometric experiment was performed on the same samples to assess the total uptake following a conventional, but slightly adapted, approach. The main findings were as follows:

1. The capsule technique yielded a CO_2 uptake versus pressure curve for the cylindrical samples (~0.05 g) of coal matrix material, which showed that the total CO_2 content of the samples at the experimental conditions reached 4.08 $mmol \cdot g_{coal}^{-1}$ at the maximum pressure investigated of 18 MPa. The data show a smooth Langmuir-shaped trend to within a band of scatter less than 0.5 $mmol \cdot g_{coal}^{-1}$ in amplitude. Taking into account systematic errors evaluated on the basis of control experiments, the measured uptake data were inferred to overestimate the actual uptake by 1.5-17 % at P<9 MPa, and 7-10 % at P>9 MPa.
2. A manometric experiment was conducted on a 0.5 g subset of the same samples set, yielding a three-stage CO_2 uptake versus pressure curve attaining an uptake of ~2.95 $mmol \cdot g_{coal}^{-1}$ at the CO_2 pressure of 18 MPa applied in the capsule experiments. Uptake values were up to 20-30 % lower than obtained in the capsule tests, at P>9 MPa. Random errors expected on the basis of pressure, temperature and volumetric measurement inaccuracies fell in the range 0.00-0.22 $mmol \cdot g_{coal}^{-1}$. Unlike the smooth, Langmuir-shaped curve obtained from the capsule tests, in the range 7-9 MPa CO_2 pressure (*i.e.* in the neighbourhood of the critical pressure of CO_2), the manometric uptake data show an abrupt increase at a rate of ~0.4 $mmol \cdot g_{coal}^{-1} \cdot MPa^{-1}$.
3. Reasonable agreement between the capsule and manometric CO_2 uptake data versus pressure data is seen below 3 MPa CO_2 pressure. However, the differently shaped curved show significant differences in uptake a) in the range of 3-8 MPa CO_2 pressure, where the manometric results consistently show 30-50 % lower values, b) in the range 7-9 MPa CO_2 pressure, where the manometric data show a sharp jump, reducing the discrepancy to 25 %, and c) beyond 9 MPa, where the capsule data show a faster increase with CO_2 pressure than the manometric data, such that the difference in CO_2 uptake again increases.
4. The differences in CO_2 uptake curves obtained using the two methods (*i.e.* at pressures in the range 3-9 MPa and above 8 or 9 MPa) cannot be explained in terms of the systematic errors expected in the capsule method, or in terms of random errors in either method caused by uncertainties in CO_2 pressure, in temperature or in volumetric determinations. Instead, various discrepancies are best explained in terms of a combination of random errors and EoS problems dominating in the manometric dataset (in the CO_2 pressure interval 3-9 MPa),

and systematic errors dominating in the capsule dataset (at CO_2 pressures higher than 9 MPa). The latter were likely caused by erroneous trapping of small amounts of free CO_2.

5. At CO_2 pressures of 0-7 MPa, the capsule method proved a reliable method. A good fit was found between our data for this range and the adsorption model recently developed by Hol et al. (2011), for adsorption site concentrations C_s in the range 9 to 20 mmol·g_{coal}^{-1} and for adsorption energy values ($\Delta\mu_0$-ΔG_a) in the range -13 to -16 kJ·mol^{-1} relative to a thermodynamic reference taken at 0.1 MPa CO_2 pressure. The reasonable fit of the thermodynamic model of Hol et al. (2011) to our capsule data (*i.e.* the observed Langmuir-type uptake curve), suggests that adsorbed CO_2 dominates the total uptake of CO_2 by our coal samples, with only a minor contribution from pore filling by free, un-adsorbed CO_2.
6. At CO_2 pressures above 8 or 9 MPa, the manometric method proved the most reliable method, although substantial random errors and EoS uncertainties remained. However, when large quantities of sample material are used, the effect of such errors will be relatively small, since the absolute errors are then normalised over a larger coal mass. In the same pressure range, errors in the capsule method were up to 30 % due to erroneous trapping of small amounts of free CO_2. This means that caution should be exercised in the application of the capsule method at CO_2 pressures higher than 8-9 MPa.
7. An extension of the adsorption model developed by Hol et al. (2011), accounting for stressed conditions, predicts that the application of an effective hydrostatic stress up to 35 MPa to coal matrix material reduces the total uptake of CO_2 in the pressure range 0-10 MPa by up to 11 % at fixed temperature. Adsorption measurement errors in the present methods therefore become significant for evaluating *in situ* adsorption only when they approach 10 % of the measured equilibrium CO_2 uptake. In practice, when using the conventional manometric method to determine sorption and/ot toal uptake capacity of large crushed samples, or when using the capsule method at CO_2 pressures <7 MPa, the effects of stress on sorption will be much more significant than any measurement errors, and need to be evaluated carefully.
8. Improvement of the capsule technique is needed to prevent erroneous trapping of free CO_2 at pressures above 9 MPa. Nonetheless, our new encapsulation method has the potential to accurately determine the uptake of any adsorbate by any (swelling) adsorbent, *e.g.* CO_2 uptake by shale and clay caprocks and is suitable for assessment of the effects of small-scale lithological differences in CO_2 uptake.

5

Effect of 3-D stress state on adsorption of CO_2 by coal

Sander Hol, Colin J. Peach,
Christopher J. Spiers

International Journal of Coal Geology (submitted)

Abstract

Though several models have been developed to describe unconfined swelling of coal exposed to adsorbing fluids such as CH_4 or CO_2 at elevated pressure, no models exist that include the role of stress supported by the solid framework (*i.e.* and effective stress in excess of the fluid pressure). Considering that *in situ* stress may substantially influence the uptake, swelling and permeability of coal reservoirs to the injection of CO_2 and recovery of CH_4 during Enhanced Coalbed Methane (ECBM) production, there is a clear need for improved understanding of the coupling between stress, strain and adsorption. To do this, we developed a thermodynamic model for the equilibrium concentration of CO_2 adsorbed by stressed coal. For unconfined (zero effective stress) conditions, the model describes the change in adsorbed concentration as a combined effect of the changing chemical activity of the fluid, and the changing availability of adsorption sites in the solid. For an ideal gas and an adsorbate under unconfined conditions, this model reduces to the widely applied Langmuir model. When the solid framework of the coal matrix material in subjected to a general stress state σ_{ij} the adsorption energy of a single molecule is increased by a general stress-strain work term. The effect of this in the adsorption model is that the adsorbed concentration is reduced by several percent to several tens of percent for effective stress magnitudes similar to those expected *in situ* during (E)CBM production. This prediction was confirmed by a preliminary experiment, performed on a sample of Brzeszcze 364 high volatile bituminous coal at 15 MPa fluid pressure, a temperature of 40 °C, and an effective hydrostatic stress or confining pressure of 1-25 MPa. This showed that the equilibrated adsorption capacity at 1 MPa effective stress of 1.38 $mmol \cdot g_{coal}^{-1}$ was reduced by almost 10 % at 25 MPa effective stress. Finally, a full constitutive equation was derived, which describes the competitive relation between adsorption-induced swelling strain and poroelastic compression, as a function of adsorbed concentration, fluid pressure and state of stress. Our equations offer a basis for full coupled modelling of the problem of injecting or producing a (single) fluid phase such as CO_2 into or from a coal seam under *in situ* (E)CBM conditions. Moreover, the model provides a means to estimate the effect of "self-stressing" as a result of adsorption of CO_2 by coal under confined *in situ* conditions. A first analysis of this effect for coal initially at 25 MPa effective stress, with CO_2 injection at 15 MPa, showed an increase in effective stress to 35-105 MPa, which would lower CO_2 uptake at equilibrium by a total amount of ~13-30 % compared to conventional adsorption measurements made at 15 MPa CO_2 pressure.

5.1. Introduction

The elastic behaviour of reservoir rocks containing a pore fluid phase is classically described by the theory of linear poroelasticity, first formulated by Biot (1941). This theory, and extensions of it to include both non-linear and anisotropic elastic effects (Biot, 1973; Thompson and Willis, 1991; Cheng, 1997), has been widely applied in geomechanical modelling of reservoir and other rock systems (Boone et al., 1991; Pride and Berryman, 1998; Wang, 2000; Du and Olson, 2001; Zhang et al., 2003). The theory is highly successful when there is no interaction between the solid rock matrix material and the pore fluid phase, *i.e.* when the rock matrix behaves as an inert elastic solid (Detournay and Cheng, 1993; Wang, 2000). However, in the case of coals and clay-rich rocks, exposure to fluids such as CO_2 and H_2O leads to a variety of reversible sorption effects that cause significant swelling/shrinkage of the rock matrix (Briggs and Sinha, 1932; Israelachvili and Pashley, 1983; Cases et al., 1992; Karacan, 2003; Day et al., 2008; Durucan et al., 2009; Fry et al., 2009; van Bergen et al., 2009; Hol and Spiers, submitted). In such cases, a general constitutive theory clearly requires extension of poroelasticity to include not only the reversible coupling between stress, strain and fluid pressure, but also the effects of the chemical potential of the pore fluid phase, which is the force responsible for driving sorption by, and swelling of the solid rock matrix material (Heidug and Wong, 1996).

Focusing now on coal, it is well-established that exposure to CH_4, H_2O, N_2, CO_2, under unconfined conditions, leads to significant adsorption-induced swelling, with CO_2 producing the largest swelling effects (Briggs and Sinha, 1932; Chikatamarla et al., 2004; Robertson and Christiansen, 2005; Cui et al., 2007; Kelemen and Kwiatek, 2009; van Bergen et al., 2009; Day et al., 2010). This behaviour is of key importance for understanding and modelling coal seam response during methane production from coal, in particular by means of Enhanced Coalbed Methane (ECBM) production, where CH_4 is displaced by preferentially adsorbing CO_2 (Puri and Yee, 1990; White et al., 2005). In order to predict coal reservoir behaviour and system performance during (E)CBM operations, in a physically realistic way, a constitutive model is needed which couples CO_2 and CH_4 sorption behaviour (*i.e.* uptake versus fluid pressure) to swelling and stress state, and which in turn can be linked to a poroelastic description of bulk, cleat-bearing coal. Also needed are, a relationship between stress/strain state and cleat permeability (Durucan and Edwards, 1986; Harpalani and Schraufnagel, 1990; Harpalani and Chen, 1997; Li et al., 2004; Pini et al., 2009; Siriwardane et al., 2009), a description of matrix diffusion/equilibration rates, and realistic assumptions about *in situ* stress and displacement boundary conditions.

At present, one of the least well-understood links in the above modelling chain is the coupling between stress, strain and sorption behaviour, under general boundary conditions. Several models exist for the unconfined (zero stress) swelling response of

coal material exposed to adsorbing fluids such as CH_4 or CO_2 (Pan and Connell, 2007; Vandamme et al., 2010). In these models, coal matrix material is treated as a porous, elastic adsorbent, which takes up the adsorbate phase by reversible physical adsorption on the internal surface of the nanoscale pore network of coal. The model developed by Pan and Connell (2007) is based on the theory developed by Meyers (2002) and Scherer (1986) for the reversible dilation of porous glass, caused by adsorption on the pore walls, while free fluid remains in the cores of the pore. In this approach, adsorption-related changes in surface energy at the interface between the solid and fluid phases lead to swelling as surface free energy is converted into elastic strain energy of the glass matrix under the assumption of isothermal equilibrium and zero external work. Vandamme et al. (2010) also consider adsorption-related changes in surface energy to produce unconfined swelling, but in their model relate the changes in surface energy to changes in surface stress, *i.e.* changes in the force that opposes the elastic deformation of the interface between the adsorbent and adsorbate (*cf.* Kramer and Weissmüller, 2007). These models (Pan and Connell, 2007; Vandamme et al., 2010) have been successfully fitted to quantitatively describe laboratory measurements of coal swelling during exposure to CO_2 at varying pressure, under isothermal, unconfined conditions. Other authors (Clarkson et al., 2010; Pan et al., 2010) have used the unconfined swelling models proposed by Pan and Connell (2007), or else purely empirical relations linking swelling strain to Langmuir-type adsorption isotherms (Palmer and Mansoori, 1998; Cui and Bustin, 2005; Shi and Durucan, 2005; Liu and Rutqvist, 2010), to compute cleat opening/closure and associated changes in reservoir permeability under *in situ* (E)CBM conditions.

In all of the above modelling studies, it is assumed that adsorption of fluid species such as CO_2 causes swelling of coal, hence leading to changes in stress state and cleat permeability under *in situ* conditions where displacements are constrained. No attention has been given in these models, or in the literature as a whole, to the possible (feedback) effects of stress and strain on adsorption capacity. However, recent experiments performed by Hol et al. (2011) have shown that the application of positive effective stress to coal samples in equilibrium with supercritical CO_2 at a pressure P leads to stress-induced expulsion of adsorbed CO_2, *i.e.* to desorption or a reduction in adsorption capacity. In view of the fact that coals swell significantly when CO_2 is adsorbed, this effect is not surprising and would appear to be a simple expression of Le Chatelier's principle. It is nonetheless a potentially very important effect as it means that the sorption capacity of coal for CO_2, CH_4 and possibly H_2O, under *in situ* stress conditions, may be substantially reduced compared with measurements made under unconfined conditions in experiments. Indeed, the preliminary data produced by Hol et al. (2011) suggest that an effective lithostatic stress of 35 MPa, equivalent to a burial depth of 2-2.5 km, can be expected to reduce CO_2 sorption capacity by 5-50 % compared with unconfined conditions.

In the present paper, we aim to explain and quantify this effect more rigorously. We therefore develop a thermodynamic model of adsorption of CO_2 by coal matrix material, first under unconfined conditions, where the coal is exposed to CO_2 at pressure P with no additional stress added to the solid framework, and then under stressed conditions, where a general 3-D stress state σ_{ij} is applied to the solid framework while CO_2 still has access at applied pressure P. The analysis presented applies not only to adsorption of CO_2 by coal, but to the adsorption of any fluid molecules by any stress-supporting solid phase. To evaluate our whole approach, we make a comparison of the model with a single experiment performed on a dense sample of Brzeszcze high volatile bituminous coal, the aim being to determine the dependence of adsorbed CO_2 concentration on applied hydrostatic stress at fixed temperature and fixed CO_2 injection pressure. The results support the model. We then combine our thermodynamic model of adsorption in a stress-supporting solid with the poroelastic equation to obtain a stress-strain-sorption relation describing the constitutive behaviour of coal, under general conditions, including *in situ* coalbed conditions. An application of our constitutive equations to CO_2 injection into coal, under confined, *in situ* conditions, reveals stress-related reductions in sorption capacity by amounts up to 30 % compared to standard sorption measurements.

5.2. Adsorption under stress-free conditions

We start our analysis, following Hol et al. (2011), by considering a small cubic particle of coal matrix material of mass m and side l, and containing n_s localised adsorption sites. The cube is chosen to be so small ($l \leq 1$ mm) that it is free of cleats and consists entirely of nanoporous coal matrix material. The particle is thus free of pores allowing Darcian flow or storage of free (un-adsorbed) CO_2 and can take up CO_2 only by diffusion and adsorption. The particle is assumed homogeneous in structure and composition at the length scale l, but is allowed to be anisotropic in properties like natural coal.

The coal particle is now exposed to CO_2 at constant pressure P and at constant temperature T (Fig. 1). In line with numerous previous treatments of sorption processes (Everett and Powl, 1976; Hill, 1986), adsorption of CO_2 molecules within the coal structure is assumed to occur at specific, localised sites where interaction with the macromolecular structure of the coal produces potential wells that dynamically trap CO_2 (Tambach et al., 2009). To obtain an expression for the amount of CO_2 that is absorbed at equilibrium, we consider the thermodynamic changes associated with reversible adsorption first of a single CO_2 molecule and then of a population of n molecules. The approach adopted is identical to that used to evaluate the uptake of point defects by crystalline solids (Pourier, 1985; Kelly et al., 2000) and is fully consistent with the partition function approach used in statistical thermodynamic treatments of adsorption (*e.g.* Hill, 1986; Tuin and Stein, 1995), yielding an identical result.

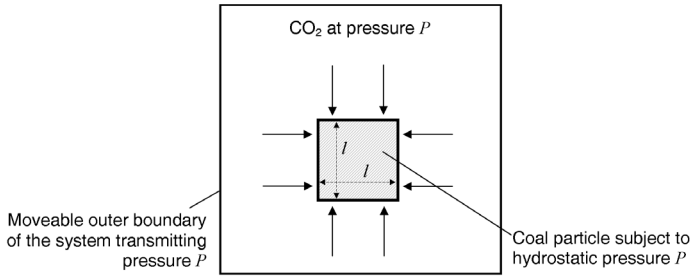

Fig. 1. Representative volume of coal matrix material in the analysis of adsorption under stress-free conditions. The volume consists of a small, cubic particle of coal matrix material of mass m and side l, containing n_s localised adsorption sites. The cube is free of cleats and consists entirely of nanoporous coal matrix material. Once the coal particle is exposed to CO_2 at constant pressure P and at constant temperature T, it takes up CO_2 only by diffusion and adsorption.

5.2.1. Adsorption of a single molecule – the attachment energy

Adsorption of a single CO_2 molecule under the hydrostatic conditions described above, where the stress in the solid equals the hydrostatic pressure in the surrounding CO_2, leads to changes in energy and entropy in the solid and fluid phases, and to swelling of the coal particle. The total energy change occurring can be viewed as the energy released when a single molecule is captured from the free fluid phase into the potential well associated with an adsorption site, or alternatively as an energy that must be supplied to remove the adsorbed molecule from the adsorption site into the free fluid (Tuin and Stein, 1995).

Focusing first on the solid phase, the swelling associated with adsorption of a single CO_2 molecule will, in general, be anisotropic, producing a very small but finite strain $\Delta\varepsilon_{ij}^{ads}$ and an associated volumetric strain $\Delta\varepsilon_v^{ads} = \Delta\varepsilon_{11}^{ads} + \Delta\varepsilon_{22}^{ads} + \Delta\varepsilon_{33}^{ads} = \Delta\varepsilon_{ii}^{ads} = \Omega_0/l^3$, where Ω_0 is the partial molecular volume of CO_2 in the adsorbed state, *i.e.* the volume change exhibited by the particle upon adsorption of a single CO_2 molecule. Adsorption of a single molecule is therefore associated with a PV work term of magnitude $P\Omega_0$. For the solid phase (subscript s), and using standard thermodynamic notation, the very small yet finite internal energy change accompanying adsorption is now given by the first law as

$$\Delta U_s = W_s + Q_s = -P\Omega_0 + Q_s \tag{1}$$

which, on applying the second law for a reversible process ($Q = T\Delta S_s$), yields the Gibbs equation

$$\Delta U_s = -P\Omega_0 + T\Delta S_s \tag{2}$$

Taking into account the energy carried by the added CO_2 molecule now yields the Gibbs equations:

$$\Delta U_s = -P\Omega_0 + T\Delta S_s + \mu_s \tag{3a}$$

or

$$\Delta F_s = \Delta U_s - T\Delta S_s = \mu_s - P\Omega_0 \tag{3b}$$

where μ_s is the chemical potential of the adsorbed molecule and ΔF_s is the change in Helmholtz free energy. Note that since these relations contain state variables only, they must apply for small irreversible as well as small reversible changes.

In the case of the fluid phase (subscript f), the internal energy change that occurs when a CO_2 molecule is adsorbed is given, via an identical route, as

$$\Delta U_f = W_f + Q_f = P\Omega_f + T\Delta S_f \tag{4}$$

where Ω_f is the molecular volume of the free CO_2 and where $P\Omega_f$ is the PV work done on the fluid as the outer boundary of the fluid moves inward to accommodate the removal of the adsorbed CO_2 molecule at constant pressure. Taking into account the energy carried out of the fluid by the adsorbed molecule now yields

$$\Delta U_f = P\Omega_f + T\Delta S_f - \mu_f \tag{5a}$$

or

$$\Delta F_f = \Delta U_f - T\Delta S_f = P\Omega_f - \mu_f \tag{5b}$$

where μ_f is the chemical potential of the free CO_2 molecules.

For the combined solid-fluid system (subscript a), we hence obtain, from (3a) plus (5a), the result

$$\Delta U_a = P\left(\Omega_f - \Omega_0\right) + T\Delta S_a + \mu_s - \mu_f \tag{6a}$$

giving

$$\Delta\mu_a = \mu_s - \mu_f = \Delta U_a + P\left(\Omega_f - \Omega_0\right) - T\Delta S_a \tag{6b}$$

or

$$\Delta\mu_a = \Delta F_a + P\Delta V_a \tag{6c}$$

Here, $\Delta\mu_a$ is simultaneously the change in potential associated with the adsorbed molecule and the change in the energy of the system due to the attachment of the adsorbed molecule. The term $\Delta V_a = (\Omega_f - \Omega_0)$ is the associated volume change of the system.

Like equations (3) and (5), this result (equation 6) contains state variables only and is therefore valid for both reversible and irreversible changes. Note that the quantity $\Delta\mu_a$ represents the energy released when a single CO_2 molecule is adsorbed, or, conversely, the energy that must be supplied to a single adsorbed molecule to remove it reversibly from its adsorption site (potential well) into the free fluid phase (*cf.* $\mu^{\square}$ of Tuin and Stein, 1995).

Compare now equation (6c) with the Gibbs potential defined $G = U + PV - TS$ and written in difference form as

$$\Delta G = \Delta U - T\Delta S - S\Delta T + P\Delta V + V\Delta P \tag{7}$$

From this it is evident that, under the present hydrostatic conditions where both P and T are constant, (6c) can be rewritten as

$$\Delta G_a = \Delta F_a + P\Delta V_a \tag{8}$$

where $\Delta G_a = \Delta \mu_a$ is the Gibbs energy of attachment of a single adsorbed molecule.

5.2.2. Adsorption energy for *n* molecules

From the definition of entropy in statistical thermodynamics (Hill, 1986), if n molecules of CO_2 are adsorbed rather than just one, the total change in potential or free energy contributes by the adsorbed phase is given

$$\Delta G = n\Delta G_a - kT \ln W \tag{9}$$

where k is the Boltzmann constant and $\Delta S_c = k\ln W$ is the confugurational entropy change associated with the W different ways that the n molecules of CO_2 can be distributed over the n_s adsorption sites present in the coal particle (*cf.* Tuin and Stein, 1995). Taking $W = n_s! / n!(n_s\text{-}n)!$ from combination theory now yields

$$\Delta G = n\Delta G_a - kT \ln \frac{n_s!}{n!(n_s - n)!} \tag{10}$$

This is the adsorption energy or "energy of adsorption" for n molecules (*e.g.* 1 mole) and is equivalent to ΔG_R for the Langmuir-type reaction.

$$CO_2 + C^* \rightleftarrows CO_2{:}\,C^* \tag{11}$$

where C* represents an adsorption site and CO_2:C* represents the complex formed when a CO_2 molecule is bound to the adsorption site (Masel, 1996; Butt et al., 2003). The equivalence of ΔG and ΔG_R is easily seen by expressing ΔG_R in terms of the free energies associated with each species involved in the reaction, *i.e.* by writing

$$\Delta G_R = G_{CO2:C^*} - G_{CO2} - G_{C^*} = G_{C^*} + \mu_{CO2}{}^{ads} - \mu_{CO2}{}^{free} - G_{C^*} \tag{12}$$

or

$$\Delta G_R = \mu_{CO2}{}^{ads} - \mu_{CO2}{}^{free} = \Delta G \quad (cf. \text{ equations 6-8}) \tag{13}$$

5.2.3. Chemical potential per molecule for *n* adsorbed molecules

Equation 10 shows that ΔG depends on n in a highly non-linear way, so that the chemical potential per molecule cannot be derived by simply dividing ΔG by n. To obtain the molecule-specific chemical potential for n adsorbed molecules, the Gibbs equations (*i.e.* equations 3 and 5) for the solid and fluid phases must be considered, applying them now in infinitesimal form as opposed to the finite difference form appropriate for adsorption of a single molecule, to allow differentiation of ΔG with respect to n. Rewriting equations (3a) and (5a) in infinitesimal form accordingly yields

$$d\mu_s = -PdV_s + TdS_s + \mu_s dn \tag{14}$$

and

$$d\mu_f = PdV_f + TdS_f - \mu_f dn \tag{15}$$

for the solid and fluid phases respectively, where μ_s and μ_f are the molecule-specific chemical potentials of CO_2 in the adsorbed and free states. For the system, adding these yields (*cf.* equation 6)

$$dU = -P\left(dV_s - dV_f\right) + TdS + \mu_s dn - \mu_f dn \tag{16a}$$

or

$$\left(dG\right)_{P,T} = dU + PdV - TdS = \left(\mu_s - \mu_f\right)dn \tag{16b}$$

for the present constant P-T conditions (*cf.* equation 7).

Now, G for the system can be written as

$$G = G_s + G_f + \Delta G - n\mu_f \tag{17}$$

where G_s and G_f are the total free energies of the solid and free phases before adsorption of n molecules of CO_2 (*i.e.* constants), ΔG is of course the change in free energy contributed by the adsorbed molecules, and $n\mu_f$ is the change in the free energy of the fluid phase due to the transfer of n molecules into the adsorbent. Equations (16b) and (17) thus lead to the derivative

$$\left(\frac{\partial G}{\partial n}\right)_{P,T} = \left(\frac{\partial \Delta G}{\partial n}\right)_{P,T} - \mu_f = \mu_s - \mu_f \tag{18}$$

demonstrating that

$$\mu_s = \left(\frac{\partial \Delta G}{\partial n}\right)_{P,T} \tag{19}$$

Inserting the expression for ΔG given in (10) into this formula, applying Stirling's approximation that $x! = x\ln x - 1$, and differentiating ΔG with respect to n now yields the result

$$\mu_s = \Delta G_a + kT \ln\left(\frac{\theta}{1-\theta}\right) \tag{20}$$

where $\theta = n/n_s$ is the concentration of adsorbed molecules per available site.

5.2.4. Equilibrium concentration of adsorbed CO_2 under stress-free conditions

If adsorption is allowed to proceed until equilibrium is reached with the free CO_2 surrounding the coal particle, then the potential of the adsorbed CO_2 will become equal to the potential of the free CO_2 phase, *i.e.* $\mu_s = \mu_f$. From the thermodynamics of fluid systems

$$\mu_f = \mu_{f0} + kT \ln a_f \tag{21}$$

where $a_f = a_f(P)$ is the chemical activity of the free CO_2 at pressure P and μ_{f0} is its potential in the reference state $a_f = 1$ (Prausnitz et al., 1986; Israelachvili, 1992). Combining this with the equilibrium condition $\mu_s = \mu_f$ and with (20), we can therefore write

$$\Delta G_a + kT \ln\left(\frac{\theta}{1-\theta}\right) = \mu_{f0} + kT \ln a_f \tag{22}$$

or

$$\theta = \frac{a_f \exp\left(\frac{\mu_{f0} - \Delta G_a}{kT}\right)}{1 + a_f \exp\left(\frac{\mu_{f0} - \Delta G_a}{kT}\right)} \tag{23}$$

This gives the concentration θ of adsorbed CO_2 molecules as a fraction of the number of adsorption sites n_s present in the coal particle. Writing the forward rate of the adsorption reaction (11) as $r_+ = k_+(1-\theta)a_f$ and the reverse rate as $r_- = k_-\theta$, following the basic approach of Langmuir (see Masel, 1996), now allows us to write the equilibrium constant for the reaction as

$$K = \frac{k_+}{k_-} = \frac{\theta}{(1-\theta)a_f} \tag{24}$$

which, using the equilibrium condition embodied in (22), modifies to

$$K = \exp\left(\frac{\mu_{f0} - \Delta G_a}{kT}\right) \tag{25}$$

Substituting this into (23) now gives

$$\theta = \frac{Ka_f}{1 + Ka_f} \tag{26}$$

If the free fluid phase outside the coal particle behaves as an ideal gas, with a reference state taken at P_0=1, then $a_f = P$ and (26) reduces to the Langmuir isotherm (Langmuir, 1918). However, CO_2 is highly non-ideal in its behaviour and the concentration of CO_2 adsorbed by coal is usually measured in mmol·g_{coal}^{-1} or mol·kg^{-1}. Therefore, for present purposes, equations (23) and (26) are best written in the form

$$C = C_s\theta = \frac{C_s a_f \exp\left(\dfrac{\mu_{f0} - \Delta G_a}{kT}\right)}{1 + a_f \exp\left(\dfrac{\mu_{f0} - \Delta G_a}{kT}\right)} \tag{27}$$

where C is the equilibrium concentration of adsorbed CO_2 in mol·kg^{-1} and $C_s = n_s/m$ is the (constant) number of adsorption sites present per kg of coal.

In summary, our key relations for the equilibrium concentration of CO_2 adsorbed by stress-free coal matrix material at fixed pressure (P) and temperature (T) are

$$\theta = \frac{a_f \exp\left(\dfrac{\mu_{f0} - \Delta G_a}{kT}\right)}{1 + a_f \exp\left(\dfrac{\mu_{f0} - \Delta G_a}{kT}\right)} \qquad [(23)]$$

and

$$C = C_s\theta = \frac{C_s a_f \exp\left(\dfrac{\mu_{f0} - \Delta G_a}{kT}\right)}{1 + a_f \exp\left(\dfrac{\mu_{f0} - \Delta G_a}{kT}\right)} \qquad [(27)]$$

For small equilibrium concentrations of CO_2, achieved at low values of a_f (low pressures P), we have $\theta << 1$. Under these conditions, it follows from (22) that

$$\theta \approx a_f \exp\left(\frac{\mu_{f0} - \Delta G_a}{kT}\right) \tag{28}$$

and

$$C \approx C_s a_f \exp\left(\frac{\mu_{f0} - \Delta G_a}{kT}\right) \tag{29}$$

However, from (21) $\mu_f = \mu_{f0} + kT\ln a_f$, so that

$$a_f = \exp\left(\frac{\mu_f - \mu_{f0}}{kT}\right) \tag{30}$$

Hence, equation (28) and (29) for low values of a_f, P and θ (and the corresponding terms in 23 and 27) can be written

$$\theta \approx \exp\left(\frac{\mu_f - \Delta G_a}{kT}\right) \tag{31}$$

and

$$C \approx C_s \exp\left(\frac{\mu_f - \Delta G_a}{kT}\right) \tag{32}$$

or

$$C \approx C_s \exp\left(\frac{\mu_f}{kT}\right)\exp\left(\frac{-\Delta G_a}{kT}\right) \tag{33}$$

Comparing these relations with the equation for the potential of a dissolved species in an ideal solution, written $\mu = \mu_0 + RT\ln C/C_0$, it is clear that (32) and (33) are equivalent in form to an ideal solution model for adsorption. Examination of the various results shows that the dependence of adsorbed concentration C or site occupancy θ is a combined effect of two fundamental causes: (1) the changing pressure, density ρ_f and hence activity a_f and chemical potential μ_f of the free fluid phase, and (2) the changing availability of adsorption sites, which is expressed statistically through the pressure dependence of the Gibbs energy of attachment ΔG_a. For an ideal gas, the activity a_f becomes equal to the gas pressure P and the model reduces to the widely applied Langmuir model.

5.3. Adsorption under stressed conditions

Having obtained an expression for the concentration of CO_2 that adsorbs in a coal matrix particle surrounded by CO_2 at pressure P, we now consider the effect of applying a general stress state σ_{ij} to the coal particle, while still allowing access of CO_2 to the particle at pressure P (for example, by transport through surrounding permeable, load-transmitting material). Throughout this paper, we adopt the convention that compressive pressure and stresses, and external (swelling) strains are measured positive.

The general situation envisaged is illustrated in Fig. 2. The size (l) and mass (m) of the particle are as already defined in our analysis of the unstressed case. In the stressed scenario, the coal particle experiences an excess stress, over and above the CO_2 pressure acting on its surfaces, described by the effective stress tensor

$$\sigma_{ij}^{\ e} = \sigma_{ij} - P\delta_{ij} \tag{34}$$

where δ_{ij} is Kronecker delta defined

$$\delta_{ij} = \begin{pmatrix} 1 & 0 & 0 \\ 0 & 1 & 0 \\ 0 & 0 & 1 \end{pmatrix} \tag{35}$$

The effective stress tensor thus differs from σ_{ij} in that its normal (diagonal) components are reduced by an amount P and are thus effective normal stresses.

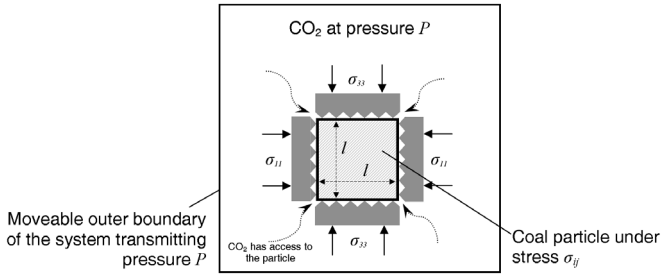

Fig. 2. Representative, cubic particle of coal matrix material as depicted in Fig. 1, but in this case equilibrated with CO_2 while a general 3-D stress state σ_{ij} is applied to the solid framework (via surrounding load-transmitting but permeable material).

We now assume that σ_{ij} and P, hence σ_{ij}^{e}, are held constant, just as P and T were held constant in our previous analysis of the stress-free case. To obtain an expression for the amount of CO_2 that is adsorbed at equilibrium in the stressed case, we once again consider the thermodynamic changes associated with adsorption of a single molecule and then of a population of n molecules.

5.3.1. Attachment energy for adsorption of a single molecule

In the stressed case, adsorption of a single CO_2 molecule by the solid phase, and the ensuing anisotropic swelling of the coal described by the strain tensor $\Delta\varepsilon_{ij}^{ads}$, will be associated not with a PV work term but with a general stress-strain work term of magnitude $\sigma_{ij}\Delta\varepsilon_{ij}^{ads}$ per unit solid volume. The first law for the solid (volume l^3) accordingly yields

$$\Delta U_s = W_s + Q_s = -\sigma_{ij}\Delta\varepsilon_{ij}^{ads} l^3 + Q_s \tag{36}$$

On applying the second law for a reversible process ($Q_s = T\Delta S_s$), and taking into account the energy carried into the solid by the added CO_2 molecule (μ_s) gives the Gibbs equation

$$\Delta U_s = -\sigma_{ij}\Delta\varepsilon_{ij}^{ads} l^3 + T\Delta S_s + \mu_s \tag{37a}$$

or

$$\Delta F_s = \Delta U_s - T\Delta S_s = \mu_s - \sigma_{ij}\Delta\varepsilon_{ij}^{ads} l^3 \tag{37b}$$

for the change in Helmholtz free energy. Once again, these contain only state variables so must apply for both reversible and irreversible changes.

Referring the molecule-specific strain tensor $\Delta\varepsilon_{ij}^{ads}$ now to its principal axes, which will generally lie parallel and perpendicular to the bedding of the coal, we can write

$$\Delta\varepsilon_{ij}^{ads} = \begin{pmatrix} \Delta\varepsilon_1^{ads} & 0 & 0 \\ 0 & \Delta\varepsilon_2^{ads} & 0 \\ 0 & 0 & \Delta\varepsilon_3^{ads} \end{pmatrix} \tag{38}$$

where $\Delta\varepsilon_1^{ads}$, $\Delta\varepsilon_2^{ads}$, and $\Delta\varepsilon_3^{ads}$ are the principal strains accompanying adsorption of a single molecule. Assuming that the effective molecular volume Ω_0 of CO_2 in the adsorbed state is a constant that is independent of stress state, the volumetric strain $\Delta\varepsilon_v^{ads}$ accompanying adsorption of a single CO_2 molecule is now given

$$\Delta\varepsilon_v^{ads} = \Delta\varepsilon_{ii}^{ads} = \Delta\varepsilon_1^{ads} + \Delta\varepsilon_2^{ads} + \Delta\varepsilon_3^{ads} = \frac{\Omega_0}{l^3} \tag{39}$$

On this basis, we can define a mean extensional or isotropic strain $\Delta\bar{\varepsilon}^{ads}$ given

$$\Delta\bar{\varepsilon}^{ads} = \frac{\left(\Delta\varepsilon_{11}{}^{ads} + \Delta\varepsilon_{22}{}^{ads} + \Delta\varepsilon_{33}{}^{ads}\right)}{3} = \frac{\Delta\varepsilon_{v}{}^{ads}}{3} = \frac{\Omega_0}{3l^3} \tag{40}$$

which is an invariant of $\Delta\varepsilon_{ij}{}^{ads}$ and therefore holds for all coordinate reference frames. Referring $\Delta\varepsilon_{ij}{}^{ads}$ once again to its principal axes, this tensor can now be written in the form

$$\Delta\varepsilon_{ij}{}^{ads} = \begin{pmatrix} a\Delta\bar{\varepsilon}^{ads} & 0 & 0 \\ 0 & b\Delta\bar{\varepsilon}^{ads} & 0 \\ 0 & 0 & c\Delta\bar{\varepsilon}^{ads} \end{pmatrix} \tag{41}$$

where a, b, and c describe the magnitude of the principal swelling strains, and where $a+b+c = 3$ since $\Delta\bar{\varepsilon}^{ads} = \Delta\varepsilon_{v}{}^{ads}/3$. Splitting this into deviatoric and isotropic components, $\Delta\varepsilon'_{ij}{}^{ads}$ and $\Delta\bar{\varepsilon}^{ads}\delta_{ij}$ respectively, now leads to the result

$$\Delta\varepsilon_{ij}{}^{ads} = \underbrace{\overbrace{\begin{pmatrix} a-1 & 0 & 0 \\ 0 & b-1 & 0 \\ 0 & 0 & c-1 \end{pmatrix}}^{A_{ij}}\Delta\bar{\varepsilon}^{ads}}_{\Delta\varepsilon'_{ij}{}^{ads} = \Delta\bar{\varepsilon}^{ads}A_{ij}} + \underbrace{\begin{pmatrix} \Delta\bar{\varepsilon}^{ads} & 0 & 0 \\ 0 & \Delta\bar{\varepsilon}^{ads} & 0 \\ 0 & 0 & \Delta\bar{\varepsilon}^{ads} \end{pmatrix}}_{\Delta\bar{\varepsilon}^{ads}\delta_{ij}} \tag{42}$$

or

$$\Delta\varepsilon_{ij}{}^{ads} = \Delta\bar{\varepsilon}^{ads}A_{ij} + \Delta\bar{\varepsilon}^{ads}\delta_{ij} \tag{43}$$

where the tensor A_{ij} represents the anisotropy of swelling of the coal particle. This will be referred to henceforth as the "swelling anisotropy tensor", having principal components $A_1=(a-1) > A_2=(b-1) > A_3=(c-1)$, whereby in the isotropic case $A_1=A_2=A_3=0$, as $a=b=c=1$. Note that the swelling anisotropy tensor A_{ij} is referred to the same Cartesian reference frame x_1, x_2 and x_3 as used for the stress tensor σ_{ij} and strain tensor $\Delta\varepsilon_{ij}{}^{ads}$. In general, of course the principal axes of A_{ij} need not coincide with x_i, though a reference frame tied to bedding symmetry and hence tot the principal axes of A_{ij} will be convenient in many practical cases.

Returning to the Gibbs equation (37a) for the solid, and rewriting this in terms of the conventional deviatoric and mean stress components σ'_{ij} and $\bar{\sigma}$, now yields

$$\Delta U_s = T\Delta S_s + \mu_s - l^3\left(\sigma'_{ij}\,\Delta\varepsilon_{ij}{}^{ads,} + \bar{\sigma}\Delta\varepsilon_{v}{}^{ads}\right) \tag{44}$$

since $\sigma_{ij}\Delta\varepsilon_{ij}{}^{ads} = (\sigma'_{ij}\Delta\varepsilon'_{ij}{}^{ads} + \bar{\sigma}\Delta\varepsilon_{v}{}^{ads})$. Substituting into this for $\Delta\varepsilon'_{ij}{}^{ads}$ and $\Delta\varepsilon_{v}{}^{ads}$ from (42) and (39), and using (40), hence produces

$$\Delta U_s = T\Delta S_s + \mu_s - l^3\left(\sigma'_{ij}\, A_{ij}\Delta\bar{\varepsilon}^{ads} + \bar{\sigma}3\Delta\bar{\varepsilon}^{ads}\right) \tag{45}$$

yielding

$$\Delta U_s = T\Delta S_s + \mu_s - \left(\tfrac{1}{3}\sigma'_{ij}\, A_{ij}\Omega_0 + \bar{\sigma}\Omega_0\right) \tag{46a}$$

or

$$\Delta F_s = \mu_s - \left(\tfrac{1}{3}\sigma'_{ij}\, A_{ij}\Omega_0 + \bar{\sigma}\Omega_0\right) \tag{46b}$$

For the free CO_2 fluid, the same Gibbs equation (5) applies as in the case of unstressed coal. Thus, for the combined solid-fluid system, addition of (46a) to (5a) gives for the stressed case

$$\Delta U_a = T\Delta S_a + \mu_s - \mu_f + P\Omega_f - \bar{\sigma}\Omega_0 - \tfrac{1}{3}\sigma'_{ij}\, A_{ij}\Omega_0 \tag{47}$$

or

$$\Delta\mu_\sigma = \mu_s - \mu_f = \Delta U_a - T\Delta S_a - P\Omega_f + \bar{\sigma}\Omega_0 + \tfrac{1}{3}\sigma'_{ij}\, A_{ij}\Omega_0 \tag{48}$$

Defining the effective mean stress as $\bar{\sigma}_e = \bar{\sigma} - P$, now leads to the result

$$\Delta\mu_\sigma = \Delta U_a - T\Delta S_a + P\left(\Omega_0 - \Omega_f\right) + \bar{\sigma}_e\Omega_0 + \tfrac{1}{3}\sigma'_{ij}\, A_{ij}\Omega_0 \tag{49}$$

hence

$$\Delta\mu_\sigma = \Delta U_a - T\Delta S_a + P\Delta V_a + \bar{\sigma}_e\Omega_0 + \tfrac{1}{3}\sigma'_{ij}\, A_{ij}\Omega_0 \tag{50a}$$

or

$$\Delta\mu_\sigma = \Delta F_a + P\Delta V_a + \bar{\sigma}_e\Omega_0 + \tfrac{1}{3}\sigma'_{ij}\, A_{ij}\Omega_0 \tag{50b}$$

$$= \Delta G_a + \bar{\sigma}_e\Omega_0 + \tfrac{1}{3}\sigma'_{ij}\, A_{ij}\Omega_0 \tag{50c}$$

Here, $\Delta\mu_\sigma$ represents the change in chemical potential associated with a single CO_2 molecule when adsorbed by our stress coal particle. It hence corresponds to the energy released when a single CO_2 molecule is adsorbed by stressed coal, or, conversely, the energy that must be supplied to a single adsorbed molecule to remove it reversibly from its adsorption site (potential well) into the free CO_2 phase.

By comparison with the Gibbs potential $G = U + PV - TS$ defined for unstressed coal (see 7), (48) and (50) imply the existence of a potential function, for the stressed case, of the type

$$\Phi = U - TS + PV + \sigma_{ij}\varepsilon_{ij} \tag{51}$$

or in difference form

$$\Delta\Phi = \Delta U - T\Delta S - S\Delta T + P\Delta V + V\Delta P + \sigma_{ij}\Delta\varepsilon_{ij} + \varepsilon_{ij}\Delta\sigma_{ij} \tag{52}$$

Since under the present conditions T, P, and σ_{ij} are constant, we can rewrite (50) as

$$\Delta\Phi_{\sigma} = \Delta F_a + P\Delta V_a + \bar{\sigma}_e\Omega_0 + \tfrac{1}{3}\sigma'_{ij}A_{ij}\Omega_0 \tag{53}$$

where $\Delta\Phi_a = \Delta\mu_{\sigma}$ is the attachment energy of a single adsorbed molecule in the stressed state. Here, $\Delta\Phi_a$ occupies a position analogous to ΔG_a, the Gibbs energy of attachment, derived for the unstressed case. Note that we avoid referring to $\Delta\Phi_a$ as "a generalised Gibbs energy" (*cf.* Landau and Lifshitz, 1986), however, as strictly speaking the Gibbs function is defined for hydrostatic stress/pressure states only (Lehner, 1990; Heidug and Wong, 1996) and because our analysis is restricted to stressed systems so is not truly general.

5.3.2. Adsorption energy for *n* molecules by stressed coal

By analogy with our considerations for unstressed coal (see equation 9), if n molecules are adsorbed then the total change in potential contributing by the adsorbed phase will be given

$$\Delta\Phi = n\Delta\Phi_a - kT\ln W \tag{54}$$

or

$$\Delta\Phi = n\Delta\Phi_a - kT\ln\frac{n_s!}{n!(n_s - n)!} \tag{55}$$

This is the energy of adsorption for n molecules (*e.g.* 1 mole) adsorbing within stressed coal via the Langmuir reaction of equation (11).

5.3.3. Chemical potential per molecule for *n* adsorbed molecules – stressed coal

Following the approach adopted for the unstressed case, the molecule-specific chemical potential of the adsorbed phase, when n molecules are adsorbed, can be obtained from the Gibbs equation for the stressed solid-plus-fluid system (equation 47) written in infinitesimal form as

$$dU = TdS + \mu_s dn - \mu_f dn + PdV_f - \bar{\sigma} dV_s - \tfrac{1}{3}\sigma'_{ij} A_{ij} dV_s \tag{56a}$$

or

$$\left(d\Phi\right)_{\sigma_{ij},P,T} = dU - TdS + PdV_f + \bar{\sigma} dV_s + \tfrac{1}{3}\sigma'_{ij} A_{ij} dV_s \tag{56b}$$

$$= \left(\mu_s - \mu_f\right) dn$$

for the present conditions of constant stress state σ_{ij}, CO_2 pressure P, and temperature T (*cf.* 51-53).

As in the case of the potential function G in the unstressed case, the thermodynamic potential or equivalent free energy of the system in the unstressed case, after adsorption of n CO_2 molecules, is given

$$\Phi = \Phi_s + \Phi_f + \Delta\Phi - n\mu_f \tag{57}$$

where Φ_s and Φ_f are the (constant) total energies of the solid and fluid phases before adsorption, $\Delta\Phi$ is the change in potential contributed by the n adsorbed molecules (53), and $n\mu_f$ is the change in the potential of the fluid phase due to transfer of n molecules of CO_2 into the coal. Equations (56b) and (57) hence lead to the derivative

$$\left(\frac{\partial\Phi}{\partial n}\right)_{\sigma_{ij},P,T} = \left(\frac{\partial\Delta\Phi}{\partial n}\right)_{\sigma_{ij},P,T} - \mu_f = \mu_s - \mu_f \tag{58}$$

proving that

$$\mu_s = \left(\frac{\partial\Delta\Phi}{\partial n}\right)_{\sigma_{ij},P,T} \tag{59}$$

Repeating the procedure employed for the stress-free case, by putting $\Delta\Phi$ from (54) in (59), applying Stirling's approximation, and differentiating now gives

$$\mu_s = \Delta\Phi_a + kT\ln\left(\frac{\theta_\sigma}{1-\theta_\sigma}\right) \tag{60}$$

for the molecule-specific chemical potential of the adsorbed CO_2 phase, where $\theta_\sigma = n/n_s$ is the concentration of adsorbed CO_2 in the stressed condition.

5.3.4. Equilibrium concentration of adsorbed CO_2 in stressed coal

At equilibrium, the chemical potential of the adsorbed CO_2 must be equal to that of the free CO_2, so that $\mu_s = \mu_f$. Using (60) plus the expression for μ_f given in (21) accordingly gives

$$\Delta\Phi_a + kT\ln\left(\frac{\theta_\sigma}{1-\theta_\sigma}\right) = \mu_{f0} + kT\ln a_f \tag{61}$$

and hence

$$\theta_\sigma = \frac{a_f \exp\left(\frac{\mu_{f0} - \Delta\Phi_a}{kT}\right)}{1 + a_f \exp\left(\frac{\mu_{f0} - \Delta\Phi_a}{kT}\right)} \tag{62}$$

Using the expression for the attachment energy $\Delta\Phi_a = \Delta\mu_\sigma = \Delta G_a + \bar{\sigma}_e\,\Omega_0 + \tfrac{1}{3}\sigma'_{ij}A_{ij}\,\Omega_0$ from (50c) now yields

$$\theta_\sigma = \frac{a_f \exp\left(\frac{\mu_{f0} - \Delta G_a}{kT}\right)\exp\left(\frac{-\bar{\sigma}_e\Omega_0}{kT}\right)\exp\left(\frac{-\sigma'_{ij}A_{ij}\Omega_0}{3kT}\right)}{1 + a_f \exp\left(\frac{\mu_{f0} - \Delta G_a}{kT}\right)\exp\left(\frac{-\bar{\sigma}_e\Omega_0}{kT}\right)\exp\left(\frac{-\sigma'_{ij}A_{ij}\Omega_0}{3kT}\right)} \tag{63}$$

which, using the equilibrium constant K for reaction (11) given in (25), reduces to

$$\theta_\sigma = \frac{a_f K \exp\left(\frac{-\bar{\sigma}_e\Omega_0}{kT}\right)\exp\left(\frac{-\sigma'_{ij}A_{ij}\Omega_0}{3kT}\right)}{1 + a_f K \exp\left(\frac{-\bar{\sigma}_e\Omega_0}{kT}\right)\exp\left(\frac{-\sigma'_{ij}A_{ij}\Omega_0}{3kT}\right)} \tag{64}$$

Under the assumption that the number of adsorption sites C_s is a constant, and is not altered by the application of a state of stress, the adsorbed concentration of CO_2 in mmol·g^{-1} or mol·kg^{-1} now of course becomes

$$C_\sigma = C_s\theta_\sigma \tag{65}$$

In this case, at low equilibrium concentration of adsorbed CO_2, *i.e.* at low CO_2 pressures (low a_f) or at high stresses in the solid (high $\bar{\sigma}_e$ and/or high σ'_{ij} values), θ_σ will take values << 1. It then follows from (61) that

$$\theta_\sigma \approx a_f \exp\left(\frac{\mu_{f0} - \Delta G_a}{kT}\right)\exp\left(\frac{-\bar{\sigma}_e\Omega_0}{kT}\right)\exp\left(\frac{-\sigma'_{ij}A_{ij}\Omega_0}{3kT}\right) \tag{66}$$

and using $\mu_f = \mu_{f0} + kT\ln a_f$ from (21) that

$$\theta_\sigma \approx \exp\left(\frac{\mu_f - \Delta G_a}{kT}\right)\exp\left(\frac{-\bar{\sigma}_e\Omega_0}{kT}\right)\exp\left(\frac{-\sigma'_{ij}\,A_{ij}\Omega_0}{3kT}\right) \tag{67}$$

or

$$\theta_\sigma \approx \theta\exp\left(\frac{-\bar{\sigma}_e\Omega_0}{kT}\right)\exp\left(\frac{-\sigma'_{ij}\,A_{ij}\Omega_0}{3kT}\right) \tag{68}$$

and

$$C_\sigma \approx C\exp\left(\frac{-\bar{\sigma}_e\Omega_0}{kT}\right)\exp\left(\frac{-\sigma'_{ij}\,A_{ij}\Omega_0}{3kT}\right) \tag{69}$$

where, θ and C are the adsorbed CO_2 concentrations in the stress-free case at low CO_2 pressures (see 28-33).

The above relations in (64)-(69) predict that the adsorbed concentration C, at unconfined conditions, is lowered as a result of the application of a positive stress state σ_{ij} expressed in terms of the effective mean stress and the deviatoric stress components. To predict the magnitude of this reduction in adsorption capacity, the partial molecular volume Ω_0 of the adsorbed phase must be known. This can be obtained from unconfined swelling-sorption experiments, and typically yields values in the range $1\rightarrow 2\cdot 10^{-5}$ $m^3\cdot mol^{-1}$ (Hol et al., 2011; Hol and Spiers, submitted). Using these values, plus a version of the model applicable to hydrostatically stressed coal (i.e. applying equation 69 for $\sigma'_{ij}=0$; see below), Hol et al. (2011) have recently estimated that this effect is of the order of tens of percent at *in situ* effective hydrostatic stresses of the order of 35 MPa (*cf.* coal buried at ~2 km depth). When the coal is anisotropic, both hydrostatic and deviatoric components on *in situ* stress can accordingly be expected to have significant effects on the sorption capacity of coal for CO_2. Note also, that the model provides a basis for investigating the effects of self-stressing developed by constrained swelling of coal. Finally, we note that the present analysis applies not only to adsorption of CO_2 by coal, but to the adsorption of any fluid molecules by any stress-supporting solid phase.

5.3.5. Special Case I: Adsorption under hydrostatic applied stress

The above results for θ_σ and C_σ apply for a general 3-D stress σ_{ij} applied to a coal matrix particle. For the special case of a hydrostatic (*i.e.* isotropic) stress state in the solid, the deviatoric components of stress disappear, so that $\sigma'_{ij}=0$ for all i and j. In this case, our expressions (63 and 65) for the adsorbed concentration of CO_2 at equilibrium reduce to

$$\theta_\sigma = \frac{C_\sigma}{C_s} = \frac{a_f \exp\left(\frac{\mu_{f0} - \Delta G_a}{kT}\right)\exp\left(\frac{-\bar{\sigma}_e \Omega_0}{kT}\right)}{1 + a_f \exp\left(\frac{\mu_{f0} - \Delta G_a}{kT}\right)\exp\left(\frac{-\bar{\sigma}_e \Omega_0}{kT}\right)} \tag{70a}$$

or

$$\theta_\sigma = \frac{a_f K \exp\left(\frac{-\bar{\sigma}_e \Omega_0}{kT}\right)}{1 + a_f K \exp\left(\frac{-\bar{\sigma}_e \Omega_0}{kT}\right)} \tag{70b}$$

at high CO_2 pressures and low effective stress (where $\theta \to 1$), and to

$$\theta_\sigma = \frac{C_\sigma}{C_s} = a_f \exp\left(\frac{\mu_{f0} - \Delta G_a}{kT}\right)\exp\left(\frac{-\bar{\sigma}_e \Omega_0}{kT}\right) \tag{71a}$$

or

$$\theta_\sigma = \theta \exp\left(\frac{-\bar{\sigma}_e \Omega_0}{kT}\right) \tag{71b}$$

at low CO_2 pressures and high effective stress $\bar{\sigma}_e$. Recall here that $\bar{\sigma}_e$ is the mean effective stress defined $\bar{\sigma}_e = \bar{\sigma} - P = \sigma - P$ for an isotropic applied stress σ. Note also that these results (70 and 71) apply regardless of whether swelling properties of coal are isotropic or anisotropic (*i.e.* independently of A_{ij}). They are identical to the results obtained by Hol et al. (2011) who considered adsorption of CO_2 by coal the special case of hydrostatic loading only. Interestingly, the same results apply for isotropic coal subjected to an anisotropic stress, since then $A_{ij}=0$.

5.3.6. Special Case II: Adsorption in horizontally bedded coal at *in situ* stress state $\sigma_1>\sigma_2>\sigma_3$

The special case considered here is directly relevant to ECBM operations in horizontally bedded coal buried at a depth z, under stress conditions whereby the vertical stress σ_1 is greater than the horizontal stresses $\sigma_2 \geq \sigma_3$. We will assume that the coal is first isotropic ($A_1=A_2=A_3=0$) and then anisotropic with different swelling properties normal to bedding compared with in the bedding ($A_1>A_2=A_3$).

For isotropically swelling coal, the term $\sigma'_{ij}A_{ij}\,\Omega_0$ in (63) equals zero, and the full stress term in (63) reduces to $\overline{\sigma}_e\,\Omega_0$, which is written as

$$\overline{\sigma}_e\Omega_0 = \frac{(\sigma_1+\sigma_2+\sigma_3)}{3}\Omega_0 - P\Omega_0 \tag{72}$$

Inserting (72) in (63), under the assumption of $A_1=A_2=A_3=0$, gives the adsorbed concentration θ_σ for isotropic coal

$$\theta_\sigma = \frac{C_\sigma}{C_s} = \frac{a_f K \exp\left(\frac{P\Omega_0}{kT}\right)\exp\left(\frac{-[\sigma_1+\sigma_2+\sigma_3]\Omega_0}{3kT}\right)}{1+a_f K \exp\left(\frac{P\Omega_0}{kT}\right)\exp\left(\frac{-[\sigma_1+\sigma_2+\sigma_3]\Omega_0}{3kT}\right)} \tag{73}$$

Extending the result obtained in (73) for the case of an anisotropic coal, first requires the expression

$$\sigma'_{ij} = \begin{pmatrix} \frac{2}{3}\sigma_1 - \frac{1}{3}\sigma_2 - \frac{1}{3}\sigma_3 & 0 & 0 \\ 0 & -\frac{1}{3}\sigma_1 + \frac{2}{3}\sigma_2 - \frac{1}{3}\sigma_3 & 0 \\ 0 & 0 & -\frac{1}{3}\sigma_1 - \frac{1}{3}\sigma_2 + \frac{2}{3}\sigma_3 \end{pmatrix} \tag{74}$$

which, combined with $A_1>A_2=A_3$ for the swelling anisotropy tensor, can be inserted in the term $\sigma'_{ij}A_{ij}\,\Omega_0$ in (63). This finally yields

$$\theta_\sigma = \frac{a_f K \exp\left(\frac{P\Omega_0}{kT}\right)\exp\left(\frac{-[\sigma_1+\sigma_2+\sigma_3]\Omega_0}{3kT}\right)\exp\left(\frac{[2\sigma_1-\sigma_2-\sigma_3][A_1-A_2]\Omega_0}{9kT}\right)}{1+a_f K \exp\left(\frac{P\Omega_0}{kT}\right)\exp\left(\frac{-[\sigma_1+\sigma_2+\sigma_3]\Omega_0}{3kT}\right)\exp\left(\frac{[2\sigma_1-\sigma_2-\sigma_3][A_1-A_2]\Omega_0}{9kT}\right)} \tag{75}$$

5.4. Experimental test of the effect of hydrostatic stress on adsorption of CO_2 by coal

The thermodynamic model developed in this study for adsorption under a 3-D stress state σ_{ij} (equations 63-65) provides a starting point for describing the adsorption behaviour of CO_2 in coal, under *in situ* conditions of stress, and predicts a reduction in adsorbed concentration due to the application of a positive effective stress. To test the validity of our thermodynamic model approach, we conducted a single experiment on a dense coal sample with the aim of determining the dependence of adsorbed CO_2 concentration on applied hydrostatic stress at fixed temperature and fixed CO_2 pressure. We explicitly compare the model describing adsorption under hydrostatic applied stress (Special Case I, section 5.3.5.) to our experimental results. Several previous experimental studies suggest that the application of positive effective stress to coal samples leads to a reduction in CO_2 sorption capacity (Pone et al., 2009; Hol et al., 2011; Wang et al., 2011). In particular, Hol et al. (2011) showed that this effect can be attributed to a direct of stress on adsorption, independently of other effects such as reduced accessibility of the coal matrix due to pore/cleat closure. However, the experiments reported by Hol et al. (2011) were done on powdered coal. To more rigorously test our themodynamic model, the present experiment was performed on solid coal matrix material.

5.4.1. Method

We performed a single, isothermal dilatometric sorption experiment on a virgin sample of high volatile bituminous coal (Brzeszcze 364, Poland), at a constant CO_2 pressure P of 15 MPa, a temperature of 40 °C, and using a varying effective confining stress $\overline{\sigma}_e$ of 1-35 MPa. The sample consisted of a cylindrical stack of 15, flat ground coal matrix discs of 25 mm in diameter and 3.0-6.2 mm thick. A cylindrical hole of 1 mm in diameter was drilled though the centre of each disc. The use of perforated discs allowed rapid and easy access of CO_2 into the coal matrix material via the centre of the stack and the planar openings between the individual discs. This allowed rapid enough access of CO_2 to achieve equilibration in a reasonable time (~2-3 weeks), while minimising the free CO_2 volume in the sample. The mass and bulk volume of the composite sample, measured before the experiment, were 40.59 g and 32.39 ml respectively. A Helium pycnometry test performed under 1 MPa confinement showed that the sample contained 0.95 ml of He-accessible pore space, which included 0.05 ml for the drilled holes. This is equivalent to a He-accessible porosity of 2.93 %, including 0.15 % for the drilled holes. For testing at elevated pressure, the sample was sealed in a 0.5 mm thick, annealed lead (Pb) jacket, which was welded onto brass end-cups. This assembly was then attached to a high pressure CO_2 line passing through the closure nut of a hydrostatic, steel pressure vessel (30 mm inner diameter), and the vessel was closed and sealed. Hydrostatic confining pressure was applied outside the jacketed sample using H_2O, while CO_2 pressure was applied to the inside. The external confining

pressure and internal CO_2 pressure were controlled by independently operated ISCO 65D syringe pumps. The volume change measured by these pumps was taken as a measure for the bulk volumetric strain of the sample (H_2O pump), and the volume of CO_2 injected into, or expelled from the sample (CO_2 pump). No measurable leak rates could be detected. The pressure vessel was placed in a water bath, controlled at 40 °C. The water bath (containing the pressure vessel) and the CO_2 pump were placed inside a foam-polystyrene box controlled at 38.6 °C.

The experiment first involved isothermal equilibration (40 °C) of the virgin coal sample at 15 MPa CO_2 pressure and at a fixed confining pressure of 16 MPa. At these conditions, the density of CO_2 is 17.73 mmol·ml^{-1} (Span and Wagner, 1996), and hence 16.84 mmol can potentially fill the He-accessible pore space of 0.95 ml. This is equivalent to maximum 0.41 mmol·g_{coal}^{-1} of free CO_2 if all He-accessible pores would be filled with free CO_2. Equilibration took ~15 days. Once the sample was sufficiently equilibrated, the hydrostatic effective (confining) stress $\overline{\sigma}_e$ was increased stepwise from the initial 1 MPa during equilibration to 6, 15, and 25 MPa, controlled by increasing the pressure in the H_2O pump. Each step was applied in less than 60 s. Unfortunately the Pb jacket failed in our attempt to increase the pressure from 25 to 35 MPa. Re-equilibration after each stress increment took approximately 3-6 h only, in line with more rapid re-equilibration effects reported elsewhere (Goodman et al., 2006; Majewska and Ziętek, 2007).

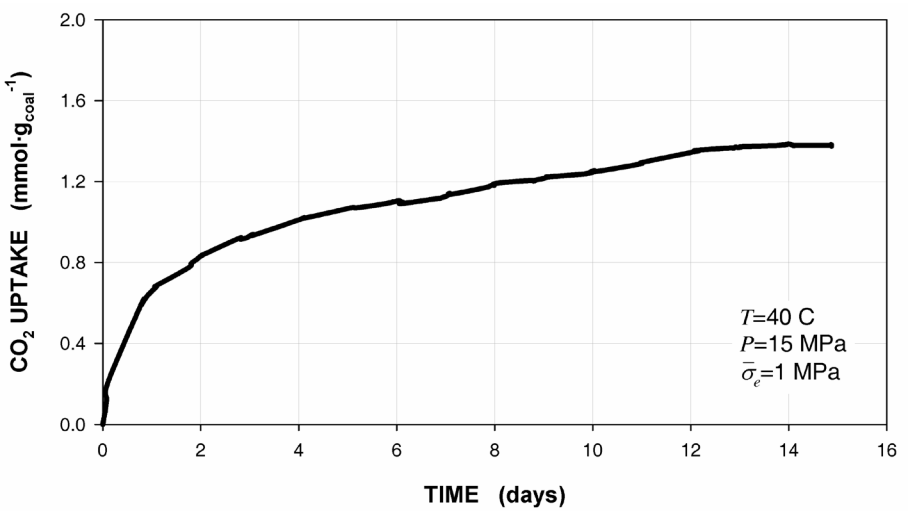

Fig. 3. CO_2 uptake versus time during initial isothermal equilibration of the virgin Brzeszcze coal sample (disc stack) with CO_2 at P=15 MPa, a confining pressure of 16 MPa, and hence an effective stress $\overline{\sigma}_e$ of 1 MPa.

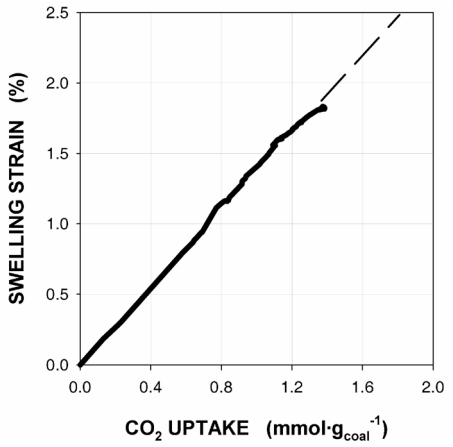

Fig. 4. Total swelling strain versus total CO_2 uptake measured for the virgin Brzeszcze sample (disc stack) during initial equilibration (see Fig. 3). Note that the strain and uptake plotted are developed in time, where the origin of plot thus represents the onset of equilibration with CO_2 at t=0.

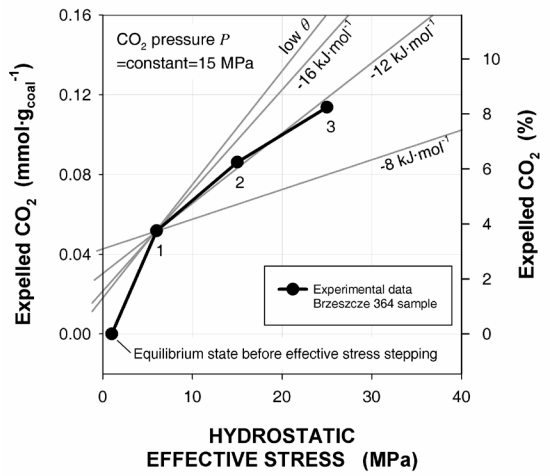

Fig. 5. CO2 expelled from the Brzeszcze coal sample (disc stack) at equilibrium, as a function of effective stress applied after initial equilibration of the sample with CO2 at P=15 MPa and a confining pressure of 16 MPa (effective stress 1 MPa). Left hand axis shows cumulative absolute amount of CO2 expelled per applied stress step (Steps 1-3) expressed in mmol·gcoal-1. Right hand axis shows the expelled amount of CO2 as a percentage (%) of the uptake at equilibrium before increasing the effective stress (1.38 mmol·gcoal-1). Fits of the thermodynamic model in (70) and (71), using values for (μf0-ΔGa) of -8, -12 and -16 kJ·mol-1, are indicated using grey lines relative to the first stress step (Step 1, at 6 MPa).

5.4.2. Results

The uptake of CO_2 during equilibration of the sample is plotted as a function of time in (Fig. 3), and plotted against the measured volumetric swelling strain e_v in (Fig. 4). Equilibration after approximately 15 days yielded a final, asymptotic CO_2 uptake value of 1.38 mmol·g_{coal}^{-1}, and a volumetric strain e_v^{eq} of 1.83 %. Note that, during equilibration at constant confining and CO_2 pressures, the volumetric expansion strain developed linearly with CO_2 uptake (Fig. 4). We infer that the time-dependent uptake must have been caused by adsorption. The slope of the linear e_v versus C trend is $1.13 \cdot 10^{-5}$ $m^3 \cdot mol^{-1}$. This is closely similar to the (V_0) value of $8.20 \cdot 10^{-6} \rightarrow 8.79 \cdot 10^{-6}$ $m^3 \cdot mol^{-1}$ obtained by Hol and Spiers (submitted) for the adsorption-induced swelling strain accumulated per mole of CO_2 adsorbed by Brzeszcze coal at equilibrium, supporting the idea that equilibration in the present experiment reflects the progress of adsorption.

Fig. *5* shows the expelled amount of CO_2 measured at equilibrium expressed in mmol·g_{coal}^{-1} versus applied hydrostatic effective stress $\overline{\sigma}_e$. An increase in expulsion is clearly seen as a result of upward stress stepping. At 25 MPa of hydrostatic effective stress, about 0.11 mmol·g_{coal}^{-1} of CO_2 is expelled from the sample, which corresponds to ~8.5 % of the initial uptake of 1.38 mmol·g_{coal}^{-1} (right-hand vertical axis in Fig. *5*). The data trend is near-linear in the interval 6-25 MPa, but shows a non-linear onset in the interval 1-6 MPa.

5.4.3. Analysis

Our CO_2 uptake/expulsion and volumetric strain data represent the combined effects of poroelastic compression expulsion and any stress-induced desorption/shrinkage. To assess the role of stress-induced desorption in our experiment, we first need to estimate the likely poroelastic strain expulsion. To do this, we assume that the coal behaves as a homogeneously deforming isotropic elastic solid, and that the poroelastic expulsion of CO_2 by the application of a hydrostatic effective stress $\overline{\sigma}_e$ can be calculated from the poroelastic relation for drained pore compression, *i.e.* from the relation $\Delta V_{pore} = V_{pore} \cdot \overline{\varepsilon}^{poroel} = V_{pore} \cdot \overline{\sigma}_e / K$, where ΔV_{pore} is the change in pore volume, V_{pore} is the initial pore volume, $\overline{\varepsilon}^{poroel}$ is the mean poroelastic strain, and K is the bulk modulus of the coal sample. For values of K in the range 0.5-7.5 GPa and the pycnometrically determined (maximum) porosity of 2.93 %, it follows that the expulsion of free CO_2 from our sample was of the order of 0.003-0.048 ml at 25 MPa of hydrostatic effective stress $_e$. This is equivalent to an amount in the range 0.001-0.021 mmol·g_{coal}^{-1}, or 1-19 % of the total expulsion measured at 25 MPa effective stress. Due to stiffening of the sample upon loading, as a result of closure of cracks and the gaps between the discs, poroelastic expulsion may account for the slight non-linearity seen $\overline{\sigma}_e$ below 6 MPa in Fig. *5*. However, above 6 MPa, the total expulsion effect is linear with increasing hydrostatic effective stress, and reaches a value of 0.09 mmol·g_{coal}^{-1} at 25 MPa. This is

significantly higher than expected from the poroelastic response. On this basis, we conclude that the total, measured amount of CO_2 expelled reflects mainly desorption of CO_2. Desorption in the present experiment thus approaches ~9 % at 25 MPa hydrostatic effective stress, or extrapolated slightly, around 10 % at 30 MPa effective stress.

5.4.4. Comparison with model

We now compare our thermodynamic model as written in (70) and (71) with the present data. First, we fit the model to the data points at 6, 15 and 25 MPa hydrostatic effective stress $\overline{\sigma}_e$, to avoid the non-linearity at the onset of the curve. Isothermal desorption in excess of that measured at 6 MPa effective stress was predicted from the consideration that the fractional, or percental change in adsorption ΔC_σ can be expressed by the relation $\Delta C_\sigma = 1-(C_\sigma / C_{\sigma=6MPa})$, where C_σ was calculated using (71a) for low site occupancy θ, and using (70a) for the full model. Fits were made under the assumption that the value of $V_0 = 1.13 \cdot 10^{-5}$ m^3·mol^{-1} is constant. In the case of the full model, values for the term $(\mu_{f0}-\Delta G_a)$ of -8, -12 and -16 kJ·mol^{-1} were taken, close to the value of -9.6 kJ·mol^{-1} obtained by Hol and Spiers (submitted) from a fit of the model for stress-free swelling-adsorption relationships for the same coal. All data were computed using a thermodynamic reference state taken at P=0.1 MPa. Fig. *5* shows the fits of the low θ model and the full model relative to the data point at 6 MPa. The full model is plotted for the three values of the term $(\mu_{f0}-\Delta G_a)$. It is clear from Fig. *5* that the trend of the whole dataset would be best fit by the low θ model, or by the full model using $(\mu_{f0}-\Delta G_a)$=-16 kJ·mol^{-1}. The data above 6 MPa are most successfully fitted using a value for $(\mu_{f0}-\Delta G_a)$ of -12 kJ·mol^{-1}. In that case, the remaining expelled amount of 0.03 mmol·g$_{coal}^{-1}$ seen at the onset of the curve, would be a reflection of the poroelastic effect (which was predicted to be of the order of 0.001-0.021 mmol·g$_{coal}^{-1}$ at 25 MPa hydrostatic effective stress ($\overline{\sigma}_e$) as speculated above.

Inserting into our thermodynamic model in (70a) the values C=1.38 mmol·g$_{coal}^{-1}$ at a_f=68.88, which is based on P=15 MPa and T=40 °C, and using the fitted value for $(\mu_{f0}-\Delta G_a)$ of -12 kJ·mol^{-1}, we obtain a value for the concentration of available adsorption sites C_s of 3.40 mmol·g$_{coal}^{-1}$. This is closely similar to the value obtained by Hol and Spiers (submitted), who determined a value of C_s=3.01 mmol·g$_{coal}^{-1}$, based on isothermal adsorption data of Gensterblum et al. (2010) for the same coal, and suggests that our model successfully captures the physical process operating, *i.e.* it is successful in describing adsorption both under stress-free, and under stressed conditions.

5.4.5. Magnitude of the effect of stress

The experiment reported here has shown an almost 10 % reduction in CO_2 sorption capacity of Brzeszcze coal due to the application of 25 MPa effective stress for a CO_2 pressure of 15 MPa at 40 °C. A significant effect is therefore implied, *in situ*, at a depth

of approximately 2 km, where similar conditions can be expected. In addition, the effect of stress on adsorption strongly depends on the partial molar volume V_0 of the adsorbed phase. In this context, the Australian coals tested by Day et al. (2008), for which Hol and Spiers (submitted) calculated a value for V_0 in range $1.05 \rightarrow 1.98 \cdot 10^{-5}$ $m^3 \cdot mol^{-1}$, can be expected from equation (70a) to be up to twice as sensitive to stress-induced desorption, *i.e.* these coals should show ~20 % reduction in sorption capacity at 25 MPa effective stress. Finally, we note that it cannot be ruled out that desorbed CO_2 was not able to diffuse out of the coal matrix in the present experiment, which implies that the almost 10 % reduction in sorption capacity at 25 MPa may even be an underestimate of the real effect. Also, we have not considered the effect of self-stressing due to laterally constrained swelling. This will increase the *in situ* stress when CO_2 is injected into a coal seam, because displacements are restricted. However, to assess this effect realistically, a fully coupled constitutive description of the isothermal stress-strain-adsorption behaviour of the coal-CO_2 system is needed.

5.5. Constitutive equation for stress-strain-sorption behaviour of coal

Several authors have recently presented models in which the volumetric strain (e_v^{eq}) developed in unconfined coal matrix material in equilibrium with an adsorbing fluid at pressure P is described by the sum

$$\varepsilon_v^{eq} = \varepsilon_{ads}^{eq} + \varepsilon_{el}^{eq} \tag{76}$$

where the volumetric strain ε_{el}^{eq} represents elastic compression of the matrix under the applied fluid pressure P and ε_{ads}^{eq} represents the adsorption-induced swelling strain (Pan and Connell, 2007; Vandamme et al., 2010; Hol and Spiers, submitted). In this approach, it is assumed that the strains are independent and small enough to be simply added, and that ε_{el}^{eq} is given by the ratio P/K_s, where K_s is the bulk modulus of the matrix skeleton. The adsorption-induced swelling strain ε_{ads}^{eq} is defined from a) the adsorbed fluid molecule concentration (C) and for fluid pressure, through either a Langmuir isotherm (Pan and Connell, 2007; Vandamme et al., 2010) or through the hydrostatic adsorption model given in equation (27) (Hol et al., 2011), and b) the swelling per adsorbed molecule, which is treated in the simplest case as a constant (*e.g.* Ω_0 in the model of Hol et al. (2011), or α_ε in that of Vandamme et al. (2010)).

These models provide a good description of the swelling versus pressure data obtained in unconfined sorption-swelling experiments performed on coal using both CH_4, (see Pan and Connell, 2007; Vandamme et al., 2010, plus data provided by Levine, 1996; Moffat and Weale, 1955) and CO_2 (Hol and Spiers, submitted). Agreement up to high pressures, in particular, indicates that net swelling (ε_v^{eq}) is indeed determined by competition between adsorption-induced swelling and elastic compression of the matrix, as described by (76) (Pan and Connell, 2007; Vandamme et al., 2010; Hol and Spiers, submitted). For CO_2, the swelling versus pressure data presented by Hol and Spiers (submitted) for pressures up to 100 MPa are well described by the model developed by these authors, taking $\varepsilon_{el}^{eq}=P/K_s$ and $\varepsilon_{ads}^{eq}=C\Omega_0$, where C is the adsorbed CO_2 concentration at equilibrium given by equation (27), and clearly demonstrate the validity of (76).

Equation (76) applied in the manner followed by Hol and Spiers (submitted), or by Pan and Connell (2007) or Vandamme et al. (2010), can be regarded as a constitutive equation linking swelling strain to fluid pressure under unconfined hydrostatic conditions. In the following, we extend the approach of Hol and Spiers (submitted) to obtain a full 3-D constitutive model for coal describing the complete coupling between stress state σ_{ij}, strain ε_{ij} and stress-dependent adsorption, under equilibrium conditions.

To do this, we assume that 1) the solid framework of the coal matrix deforms in a linear elastic manner, as described by the poroelastic equation (Biot, 1941; Wang,

2000), 2) the linear relation between the adsorption-induced swelling strain ε_{ads}^{eq} of the coal matrix and adsorbate concentration C (assumed by Hol and Spiers, submitted) still holds (*i.e.* that $\varepsilon_{ads}^{eq}=C(P)N_A\Omega_0\rho$, where ρ is the bulk density of the coal matrix), and 3) equations (63) and (65) adequately describe the adsorbed concentration C_σ as a function of P and σ_{ij}. In assuming thermodynamic equilibrium, we implicitly assume that access of the adsorbing species to the particle at a potential in equilibrium with the free fluid at pressure P is independent of the state of stress σ_{ij}. A full constitutive equation for a coal matrix-CO_2 system (at equilibrium) can accordingly be written

$$\varepsilon_{ij}^{eq} = \varepsilon_{ij}^{poroel} + \varepsilon_{ij}^{ads} \tag{77}$$

where the poroelastic equation (Biot, 1941; Wang, 2000) describes the elastic strain components $\varepsilon_{ij}^{poroel}$, and ε_{ij}^{ads} represents the strains due to adsorption.

Employing the poroelastic equation to describe the elastic strains $\varepsilon_{ij}^{poroel}$ allows (77) to be applied to representative coal volumes large enough to contain macroscopic pores and cleats containing the free fluid phase at pore pressure P. The matrix strains ε_{ij}^{ads} induced by adsorption within the representative volume can then be obtained from a consideration of (43). This shows that the matrix strain due to adsorption of a single molecule by a volume of coal V having mass M and density $\rho=M/V$ can be written as

$$\Delta\varepsilon_{ij}^{ads} = \Delta\bar{\varepsilon}^{ads}\left(A_{ij}+\delta_{ij}\right) \tag{78}$$

where from (40)

$$\Delta\bar{\varepsilon}^{ads} = \frac{\Omega_0}{3V} = \frac{\Omega_0\rho}{3M} \tag{79}$$

Now, for a concentration of adsorbed molecules of C_σ moles per unit mass, established at equilibrium under the stress state σ_{ij}, the total number of molecules adsorbed per unit mass is $N_A C_\sigma$ and the total number of molecules adsorbed in the mass M is $M\cdot N_A C_\sigma$, where N_A is the Avogadro constant. Assuming that $\Delta\varepsilon_{ij}^{ads}$, the strain due to adsorption of a single molecule is a constant (*i.e.* insensitive to adsorbed concentration C_σ), then the strain associated with the adsorbed concentration C_σ is accordingly given as

$$\varepsilon_{ij}^{ads} = \left(MN_A C_\sigma\right)\Delta\varepsilon_{ij}^{ads} \tag{80}$$

which using (78) and (79) becomes

$$\varepsilon_{ij}^{ads} = \frac{V_0\rho\left(A_{ij}+\delta_{ij}\right)}{3}\cdot C_\sigma \tag{81}$$

where the concentration of the adsorbed phase C_σ in the stressed coal in given by (63) and (65) and where $V_0=N_A\Omega_0$ is the partial molar volume of the adsorbed phase (*i.e.* the absolute change in coal volume when one mole of adsorbate is adsorbed).

For a representative elementary volume (REV) of coal displaying anisotropic elastic properties on the scale of the REV as well as anisotropic swelling properties within the matrix, equations (77) and (81) now yield the final 3-D constitutive equation for stress-strain-adsorption behaviour. This is written

$$\varepsilon_{ij}^{\,eq} = \varepsilon_{ij}^{\,poroel} + \frac{V_0 \rho \left(A_{ij} + \delta_{ij} \right)}{3} \cdot C_\sigma \left(\sigma_{ij}, P \right) \tag{82}$$

where $\varepsilon_{ij}^{\,poroel}$ is the strain tensor given by the full anisotropic form of the poroelastic equation (Biot, 1973) and where the equilibrium concentration of the adsorbed species $C_\sigma(\sigma_{ij},P)$ depends on stress state σ_{ij} and pore fluid pressure P within the coal according to (63) and (65), *i.e.* where

$$C_\sigma = \frac{C_s \cdot a_f \cdot K \exp\left(\dfrac{P\Omega_0}{kT} \right) \exp\left(\dfrac{-\sigma_{ij}\left[A_{ij} + \delta_{ij} \right]\Omega_0}{3kT} \right)}{1 + a_f \cdot K \exp\left(\dfrac{P\Omega_0}{kT} \right) \exp\left(\dfrac{-\sigma_{ij}\left[A_{ij} + \delta_{ij} \right]\Omega_0}{3kT} \right)} \tag{83}$$

For coal with more or less isotropic elastic properties but showing anisotropic swelling, $\varepsilon_{ij}^{\,poroel}$ in (82) can be replaced by the poroelastic equation for an isotropic elastic material (Biot, 1941; Wang, 2000). When both the elastic and swelling properties of the coal are isotropic, or can be approximated as such, then A_{ij}=0 for all i and j, and inserting the isotropic form of the poroelastic equation for $\varepsilon_{ij}^{\,poroel}$ into (82) yields

$$\varepsilon_{ij}^{\,eq} = \frac{-1}{2\mathrm{G}} \left[\sigma_{ij} - \left(\frac{3\mathrm{K} - 2\mathrm{G}}{9\mathrm{G}} \right) \sigma_{kk} \delta_{kk} - \frac{2\mathrm{G}}{3\mathrm{K}} \alpha P \delta_{ij} \right]$$
$$+ \frac{V_0 \rho \delta_{ij}}{3} \cdot \frac{C_s \cdot a_f \cdot K \exp\left(\dfrac{PV_0}{RT} \right) \exp\left(\dfrac{-\sigma_{kk} V_0}{3RT} \right)}{1 + a_f \cdot K \exp\left(\dfrac{PV_0}{RT} \right) \exp\left(\dfrac{-\sigma_{kk} V_0}{3RT} \right)} \tag{84}$$

where K is the elastic bulk modulus, G is the shear modulus of the coal matrix, and α is the Biot-Willis coefficient.

These constitutive equations (82-84) apply to any adsorbing, single fluid phase, such as CO_2, CH_4, H_2O or N_2, each fluid being characterised by its own specific values of Ω_0, V_0 and equation of state giving $a_f(P,T)$. The constitutive equations predict, for isothermal conditions, how the total strain response $\varepsilon_{ij}^{\,eq}$ of an REV of coal in equilibrium with an adsorbing pore fluid phase at pressure P depends not only on P but also on σ_{ij}, the state of stress in the coal. They clearly show that only σ_{ij} not reduces the degree of adsorption by the coal but also the adsorption-related swelling strain. The constitutive equations derived thus predict the full coupling governing the stress-strain-adsorption behaviour of coal. Note, that such a coupling also affects derived properties such as

measured stiffness moduli. For example, the 26 % and 33 % reduction of apparent elastic modulus of coal upon adsorption of CO_2, as reported by Viete and Ranjith (2006) and Hol et al. (2011), can be explained by the combined effect of reversible, stress-induced adsorption/desorption superimposed upon the truly elastic response of solid framework (as proposed by Hol et al., 2011).

An interesting and important feature of the constitutive equations derived here is that they can be applied to REV's of any scale within a coal seam, for example at the true matrix or sub-cleat scale, at a scale containing tertiary cleats, or at a scale containing primary or secondary cleats (scales *cf.* Laubach et al., 1998). To do this, it is simply necessary to use poroelastic parameters in the expression for $\varepsilon_{ij}^{poroel}$ which describe the poroelastic response of the material at the appropriate scale. The mechanical effects of pores and cleats are then entirely accounted for via $\varepsilon_{ij}^{poroel}$, while the matrix swelling response is given by the second (ε_{ij}^{ads}) term on the right of (82) applied for coal-specific parameters (ρ, C_s, and the coal-fluid dependent parameter V_0) that represent an average for the matrix material over the REV. This "scalable" property of the present constitutive equations means that they can be coupled to stress-permeability relations (e.g. Palmer and Mansoori, 1998; Cui and Bustin, 2005; Shi and Durucan, 2005; Liu and Rutqvist, 2010) defined for the same REV scale and describing cleat closure with increasing (mean) normal stress. Our equations therefore offer a basis for full coupled modelling of the problem of injecting or producing a fluid such as CO_2 into or from a coal seam under *in situ* (E)CBM conditions, allowing for the coupling between stress state, pore pressure, poroelastic response, adsorption/swelling response and evolving permeability. The limitation of the present equations, however, is that they are derived only for a single fluid phase.

An outstanding issue is the feedback effect of self-stressing of coal by adsorption-induced swelling under the constrained-displacement conditions that exist *in situ*. A detailed treatment of this issue is beyond the scope of this paper. However, a first-order estimate of the effect of equilibration of isotropic coal with CO_2, at P=15 MPa, an initial *in situ* effective stress $\overline{\sigma}_e$=25 MPa and at T=40 °C, was obtained by numerical solution of equation (84). This was done for the condition that the coal is volumetrically fully constrained, so that swelling by adsorption of CO_2 is accommodated by elastic compression associated with a self-stress developed by the swelling process. We obtained the numerical solution under the assumption that the bulk modulus K of the coal ranges from 0.5 to 5.0 GPa, that $(\mu_{f0}-\Delta G_a)$=-12 kJ·mol^{-1}, V_0=1.13 m^3·mol^{-1} and C_s=3.40 mmol·g$_{coal}^{-1}$, as determined from our experiment on Brzeszcze coal (Section 5.4). The results showed that, due to the swelling process, the *in situ* effective stress $\overline{\sigma}_e$ increases from the initial value of 25 MPa to values in the range 35-105 MPa at equilibrium. These estimates appear to be consistent with stresses reported by Harpalani and Mitra (2010), who performed swelling-sorption experiments on stressed coal cores using CO_2 and CH_4. The authors inferred from their data the stress required to recover the adsorption-induced swelling at 2.1

MPa CO_2 pressure (*i.e.* the "excess stress" *cf.* Harpalani and Mitra, 2010) could be as much as four times the fluid pressure. Inserting the stresses of 35-105 MPa, predicted here for 15 MPa CO_2 pressure, back into equation (70a), yields a 3-20 % reduction of adsorbed concentration in addition to the reduction of ~9 % at 25 MPa effective stress. This suggests the development of high stresses under the constrained (*i.e.* limited displacement) conditions expected under *in situ* conditions relevant to (E)CBM. This self-stressing effect leads to significantly lower CO_2 uptake than expected from conventional (unconfined) sorption measurements. Our constitutive relations thus allow realistic modelling of the coupling between stress, strain and adsorption in (E)CBM reservoirs, including self stressing effects and the dependence of CO_2 and CH_4 sorption capacity of coals on depth. They also provide a basis for obtaining realistic predictions of the change in permeability during CH_4 extraction from and CO_2 storage in coalbeds. These applications will be attempted in future papers.

5.6. Conclusions

A thermodynamic model has been derived for the adsorption of CO_2 by unconfined (unstressed), and for stressed coal. The model was developed for the equilibrium between coal matrix material and the adsorbing CO_2, at any CO_2 pressure P and applied stress state σ_{ij}, assuming that CO_2 has homogeneous access to coal matrix volume considered. To test the model, we conducted a single experiment on a hydrostatically stressed coal sample, which was equilibrated with CO_2 at 15 MPa and at a temperature of 40 °C. We then developed a full constitutive model that describes the coupling between stress state, strain and adsorption. The models can be applied to any solid adsorbent and any adsorbate, thought the focus here is on the coal-CO_2 system. Here, we summarise our main findings and conclusions:

1. For unconfined coal matrix material, the thermodynamic model derived here predicts the amount of CO_2 adsorbed by coal, at conditions of varying temperature T and fluid pressure P. The adsorbed concentration C or site occupancy θ vary with temperature and pressure due to the combined effect of two fundamental causes: (1) the changing pressure, density ρ_f and hence activity a_f and chemical potential μ_f of the free fluid phase, and (2) the changing availability of adsorption sites, which is expressed statistically through the pressure dependence of the Gibbs energy of attachment ΔG_a. For an ideal gas, the activity a_f becomes equal to the gas pressure P and the model reduces to the widely applied Langmuir model.
2. For the case where a general stress state σ_{ij} is applied to the solid framework of the coal matrix material, the adsorption of a single CO_2 molecule by the solid phase, and the ensuing anisotropic swelling of the coal described by the strain tensor $\Delta\varepsilon_{ij}^{ads}$, are associated not with a PV work term but with a general stress-strain work term of magnitude $\sigma_{ij}\Delta\varepsilon_{ij}^{ads}$ per unit solid volume. For effective stress magnitudes similar to lithostatic *in situ* values during (E)CBM, the model developed to account for this work term predicts that the adsorbed concentration C, or site occupancy θ, is reduced by several percent to several tens of percent.
3. A first experiment, performed on a sample of Brzeszcze 364 high volatile bituminous coal at a pressure of 15 MPa, a temperature of 40 °C, and using a varying effective hydrostatic confining stresses $\overline{\sigma}_e$ of 1-35 MPa, showed that the initially equilibrated adsorption capacity of 1.38 mmol·g_{coal}^{-1} was reduced by almost 10 % at 25 MPa effective stress. This sensitivity to stress is also predicted by the model for adsorption under stress taking a value for the parameter (μ_{f0}-ΔG_a) of -12 kJ·mol^{-1} and a partial molar volume of the adsorbed phase V_0 of $1.13\cdot10^{-5}$ $m^3\cdot mol^{-1}$ in line with independent estimates of these parameters. Fitting the model to the absolute adsorption value measured during initial equilibration yielded value for the concentration of available adsorption sites C_s in Brzeszcze coal of 3.40 mmol·g_{coal}^{-1}.

4. A constitutive equation was further developed relating the general stress state σ_{ij} to net (total) strain ε_{ij}^{eq} and the adsorbed concentration *C*. The net (total) strain ε_{ij}^{eq} was formulated as the sum of the adsorption-induced strain ε_{ij}^{ads} and the poroelastic strain $\varepsilon_{ij}^{poroel}$, where ε_{ij}^{ads} is the strain tensor due to adsorption, and $\varepsilon_{ij}^{poroel}$ is the strain tensor given by the full (an)isotropic form of the poroelastic equation. Competition between the adsorption and poroelastic components of strain at fixed fluid pressure is affected by the state of stress σ_{ij}. Compressive stresses produce compressive strains via stress-induced desorption i the case of ε_{ij}^{ads}, as well as by direct elastic compression in the case of $\varepsilon_{ij}^{poroel}$. Our equations therefore offer a basis for full coupled modelling of the problem of injecting or producing a (single) fluid phase such as CO_2 into or from a coal seam under *in situ* (E)CBM conditions, allowing for the coupling between stress state, pore pressure, poroelastic response, adsorption/swelling response and evolving permeability at different scales.
5. The model also provides a means to estimate the effect of "self-stressing" as a result of adsorption of CO_2 by coal under the condition of zero strain (*i.e.* fully constraint conditions). A first estimate of this effect on the basis of our constitutive model was made using model parameter values $(\mu_{f0}\text{-}\Delta G_a)$=-12 kJ·mol^{-1}, V_0=1.13 m^3·mol^{-1} and C_s=3.40 mmol·g$_{coal}^{-1}$, consistent with our experiment on Brzeszcze coal. For coal material having a bulk modulus K of 0.5-5.0 GPa, equilibrated under conditions of 15 MPa fluid pressure *P* and 25 MPa effective stress, a reduction of adsorbed concentration, in addition to the reduction of almost 10 % at 25 MPa effective stress, is predicted to be of the order of 3-20 %, *i.e.* a total reduction in the range 13-30%. This suggests the development of high stresses under constrained conditions, such those expected under *in situ* conditions relevant to (E)CBM. This will lead to significantly reduced CO_2 uptake. Our constitutive relations allows realistic modelling of the coupling between stress, strain and adsorption in (E) CBM reservoirs, including self stressing effects, and provide a basis for obtaining realistic predictions of the change in permeability during CH_4 extraction from and CO_2 storage in coalbeds.

6

Microfracturing of coal due to interaction with CO_2 under unconfined conditions

Sander Hol, Christopher J. Spiers,
Colin J. Peach

Fuel (submitted)

Abstract

It is well-established that exposure of coal to CO_2 under unconfined, hydrostatic conditions leads to reversible adsorption and swelling. However, several authors also report irreversible changes in sorption capacity, sample volume, equilibration time and brittle failure strength. Some relate these effects to the formation of microfractures, while others consider "structural rearrangements" in the macromolecular structure of coal to be responsible. In this study, we investigate the magnitude of irreversible swelling effects and changes in equilibration time in high volatile bituminous coal (Brzeszcze, Seam 364, Poland), and attempt to explain the results in terms of the operative microphysical processes. We also assess the implications for Enhanced Coalbed Methane (ECBM) operations. Our approach involves detailed dilatometry experiments conducted on fresh, unconfined, mm-scale coal matrix cylinders at CO_2 pressures up to 100 MPa, and at 40.0 °C. Exposure of our samples to CO_2 produced reversible and irreversible strains resulting predominantly from competition between adsorption-induced swelling and elastic compression. During the first or second cycle of exposure, substantial hysteresis was observed in volumetric behaviour, notably at CO_2 pressures above 35-40 MPa. After two or three upward and downward CO_2 pressure cycles, the measured strain response became fully reversible. Equilibration with CO_2 took about four times longer during the first CO_2 pressurisation cycle than in subsequent CO_2 pressurisation cycles. Microstructural analysis and comparison showed that microfractures formed in the coal during first exposure to CO_2. From the microstructural and mechanical data, we infer that microfracturing was responsible for enhanced CO_2 penetration into the present samples. This, in turn allowed more homogeneous access of CO_2, and caused adsorption-induced swelling of matrix material not previously accessed by CO_2. We further infer that the enhanced penetration, sorption and swelling, in turn, resulted in the observed hysteresis in dimensional response and in the decrease in equilibration time seen in subsequent exposure cycles. Since most microfractures developed parallel to the bedding, roughly following maceral-maceral and bedding/layer interfaces, and because the largest permanent strains and strain hysteresis were measured perpendicular to the bedding, we infer that the formation of microfractures was caused by heterogeneous swelling, in combination with differential accessibility of the coal microstructure. No evidence was found that CO_2-induced plasticisation of the macromolecular structure of the coal matrix played any role in the behaviour observed. Simple mechanical considerations indicate that at *in situ* stresses corresponding to a depth of 1000-1500 m, *i.e.* effective stresses in the range 25-35 MPa, adsorption-induced microfractures are unlikely to form. This means that improved access of CO_2 to coal matrix material for ECBM production can probably be achieved only by inducing damage into coal seams, either by injection of solvents/solutes, or by performing active mining of the coal and/or the over- or underlying strata.

6.1. Introduction

In the past few decades, many studies have been conducted to assess the effects of H_2O, CH_4, N_2 and CO_2 on coal. The chief aim of these has been to quantify the uptake and release of these fluids under conditions pertaining to the production of coalbed methane (CBM) and to Enhanced Coalbed Methane production (ECBM). Much work has also been done on the volumetric response and permeability changes that occur in coal when these fluids are extracted or injected.

In the case of CO_2, the principal interaction with coal is that of reversible, physical adsorption by the coal matrix (Goodman et al., 2005). Numerous coal-CO_2 equilibration experiments have demonstrated that, compared to other fluids naturally occurring in coal, CO_2 has the highest adsorption potential (Hall et al., 1994; Cui et al., 2004; Ottiger et al., 2008; Kelemen and Kwiatek, 2009; Mares et al., 2009) and causes the largest volumetric (swelling) response (Briggs and Sinha, 1932; Chikatamarla et al., 2004; Robertson and Christiansen, 2005; Cui et al., 2007; Kelemen and Kwiatek, 2009; van Bergen et al., 2009; Day et al., 2010). Despite the fact that the stress supported by the coal matrix under *in situ* conditions plays a significant role in controlling adsorption (Pone et al., 2009a; Hol et al., 2011; Wang et al., 2011), most such experiments have been performed under unconfined conditions, whereby coal samples are simply "immersed" in CO_2 at hydrostatic pressure with no additional stress applied to the solid.

Where detailed measurements have been made, exposure of coal to CO_2 (or CH_4) under unstressed, hydrostatic conditions has been shown to give rise not only to the well-known reversible effects of adsorption and swelling, but also to irreversible changes in sorption capacity (Goodman et al., 2006) and sample volume (Moffat and Weale, 1955; Khan and Jenkins, 1985). These irreversible changes are accompanied by a major reduction in equilibration time and in inferred permeability upon repeated exposure to CO_2 (Goodman et al., 2006). Interaction of CO_2 with coal has also been shown to lead to irreversible reductions in yield strength (*i.e.* the stress supported at the onset of brittle failure) under conditions of uniaxial loading (Viete and Ranjith, 2006; Ranjith et al., 2010).

Several authors have concluded that the irreversible changes observed in experiments on coal, and in pilot ECBM operations, are due to the formation of microfractures, as a result of adsorption-induced differential swelling of coal macerals or drying and shrinkage of the coal (Durucan and Edwards, 1986; Sakurovs et al., 2007; Gathitu et al., 2009; van Wageningen et al., 2009; Harpalani and Mitra, 2010). Others attribute the observed permanent changes to "structural rearrangements" that affect the macromolecular structure or intermolecular bonding of the coal matrix, and that are facilitated by the "plasticising properties" of CO_2 (Larsen, 2004; Goodman et al.,

2006; Majewska and Ziętek, 2007), *i.e.* by weakening of cross-linking bonds in the macromolecular structure of coal. Determining the mechanism responsible for the permanent changes seen in experiments, especially the reduction of equilibration time and in the increase in permeability or accessibility to CO_2, is important for explaining and predicting the changes in permeability, accessibility and equilibration time that occur in coal during ECBM operations, and hence for predicting ECBM reservoir performance.

In this paper, we investigate the magnitude and ongoing irreversible effects such as permanent swelling and changes in equilibration time in virgin coal matrix material, namely a high volatile bituminous coal from the Brzeszcze mine, Poland. The aim was to establish if such effects indeed occur in this type of material, and if so, to explain the microphysical processes responsible. We performed dilatometry experiments, combined with microstructural analyses of Brzeszcze 364 coal samples before and after exposure to CO_2. Dilatometry was performed under unconfined conditions on two fresh, cylindrical samples of cleat-free, coal matrix material exposed to CO_2 at pressures up to 100 MPa at a constant temperature of 40 °C. Our results show a number of reversible and irreversible effects that are best explained in terms of competition between (reversible) adsorption-induced swelling and elastic compression (*cf.* Hol and Spiers, submitted), accompanied by (irreversible) microfracturing, improved CO_2 access and hence hysteresis in swelling behaviour. We argue that microfracturing is caused by differential swelling related to differences in the properties and accessibility of different coal macerals and different compositional layers, and that plasticisation plays little or no role. Finally, we consider the issue of whether the microfracturing and associated permanent effects observed in our unconfined experiments will occur under *in situ* stress conditions, and whether they can be expected to significantly influence ECBM reservoir behaviour.

6.2. Experimental methods

6.2.1. Basic approach

In this study, three samples of Brzeszcze high volatile bituminous coal were exposed to and equilibrated with CO_2 at 40 °C and at CO_2 pressures up to 100 MPa to assess their swelling and microstructural response. This was done in multiple cycles of pressure increase and decrease. High-precision dilatometry was performed during these pressure cycles on two samples, and the microstructure of one of them studied using SEM after CO_2 treatment. The microstructure of a third sample was studied before and after one complete CO_2 pressure cycle, executed without performing accurate dilatometry.

6.2.2. Sample selection and preparation

The experiments were performed on mm-scale samples of high volatile bituminous coal from the Upper Silesian Basin in Poland (Nowak, 2004), namely from Seam 364, exposed in the Brzeszcze mine. Petrological and chemical analyses reported earlier by Hol et al. (2011) revealed that the sample material consisted on average of 60.1 % vitrinite, 9.8 % liptinite and 30.1% inertinite (all vol.%). It was further characterised by a vitrinite reflectance (R_0) of 0.77 ±0.05 %, and contained 2.93% of moisture, 31.21% of volatile matter, 5.16% of ash and 60.70% of fixed carbon.

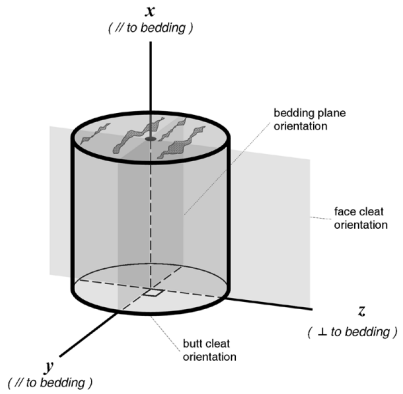

Fig. 1. Schematic diagram of the cylindrical, sample geometry used in the present experiments on coal matrix material. The sample cylinders were drilled parallel to the coal bedding plane and normal to the butt cleat orientation. Indicated are the x-, y-, and z-directions. Linear strains (e_l) occurring in response to CO_2 addition were measured in the x- and z- directions in this study, i.e. parallel and perpendicular to the bedding plane.

Two cylindrical samples measuring 4.00 mm in diameter by 4.75 mm (Sample 1) and 3.75 mm (Sample 2) in length were prepared from a 10 cm block of the Brzeszcze coal material following the procedure described by Hol and Spiers (submitted). The cylindrical samples were cored from a single sedimentary layer of coal matrix material, and were free of cleats and cracks. The cylinder axis, which we define as the x-direction of the samples, was drilled parallel to bedding and normal to the butt cleat plane (Fig. 1). We define the y-direction of the samples to coincide with the normal to the face

Sample N°	Initial sample mass (g)	Final sample mass (g)	Sample shape	Initial sample length L_{0x} (mm)	Initial sample diameter or width L_{0y}=L_{0z} (mm)
1	0.07974	0.07916	cylinder	4.75	4.02
2	0.06034	0.05948	cylinder	3.75	3.96
3	0.09649	*	rough-cut block	~6	~4

Table 1. Starting dimensions and mass of the Brzeszcze 364 coal matrix samples used in this study. The dimensions were measured using a digital calliper at NTP and serve as the starting dimensions in all strain calculations. Starting mass was determined using a microbalance, also at NTP.

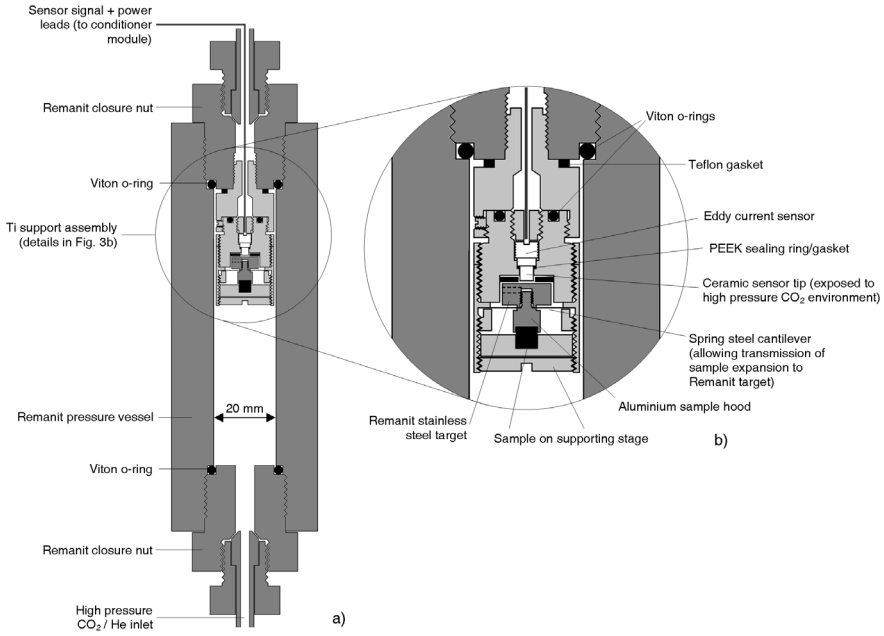

Fig. 2. Semi-schematic diagram of the high-pressure eddy-current dilatometer developed for this study. a) Overview showing the Remanit high pressure vessel (dark grey) holding the Ti support assembly (light grey). CO_2 and He can be admitted to the sample via the fluid inlet at the bottom of the vessel. b) Detail of the Ti support assembly, consisting of the sample, a ferromagnetic target and the eddy current sensor. Expansion or contraction of the sample is transmitted to the Remanit target via the spring steel cross-cantilever that retains the sample in position. Displacement of the target alters the eddy current field and allows sample expansion and contraction to be measured with high resolution.

cleat plane, and the z-direction to lie perpendicular to the bedding (Fig. 1). In addition to the two cylindrical samples, a small, rough-cut block of coal matrix (Sample 3), measuring approximately 6 mm x 4 mm x 4 mm parallel to the x, y, and z directions respectively, was taken from the same matrix layer within the 10 cm block. The sample dimensions and mass measured at normal (ambient) temperature and pressure (NTP) in the virgin state, *i.e.* before exposure to CO_2, are listed in Table 1.

6.2.3. Dilatometry experiments

6.2.3.1. High pressure eddy current dilatometer

Dimensional changes of Samples 1 and 2 were measured using an eddy current dilatometer (Fig. 2), which was specially developed to measure displacements in a high pressure environment with a resolution better than 50 nm. The apparatus is described in detail by Hol and Spiers (submitted), but for clarity, a description of the essential components of the system is repeated here.

The dilatometer is housed in a Remanit (1.4122) stainless steel pressure vessel with an inner diameter of 20 mm (Fig. 2). Sealing of the vessel is achieved by means of high pressure o-ring seals composed of Viton, plus a series of PEEK and Teflon gaskets (Fig. 2). The measurement of displacement due to expansion or contraction of the samples is based on changes in the inductive coupling between a coil in the stationary eddy current sensor (Micro-Epsilon LS04(03)) and currents induced in a target fixed to the sample. Displacement of the target alters the eddy current field, producing a DC signal, which is scaled to give an output of 10 V per 398 μm of displacement, *i.e.* of 25.14 $mV \cdot \mu m^{-1}$. The sensor is mounted in a grade 5 titanium body fixed onto the closure nut of the high pressure vessel (Fig. 2). The cylindrical coal samples are mounted opposite the sensor tip in a Ti sample holder, fixed to the sensor body by means of a screw connection (Fig. 2). The free end of the sample is connected to a Remanit stainless steel target via an aluminium cap or 'sample hood' assembly, supported by a firm but flexible spring steel cross-cantilever. Expansion or contraction of the sample upon introduction of CO_2 into the pressure vessel is transmitted to the Remanit target via the sample 'hood' and cantilever, and measured by the eddy current sensor as indicated above. The eddy current signal is conditioned using a Micro-Epsilon DT3010-M signal conditioner, adjusted specifically for the use of the ferromagnetic (Remanit) steel target.

To achieve CO_2 pressures in the range 0-100 MPa, three different types of pressure generation and/or control system were used, for specific ranges of CO_2 pressure (see also Hol and Spiers, submitted). First, CO_2 was introduced into the system from a CO_2 bottle via a manually controlled AirProducts line regulator. This allowed stepwise increases in CO_2 pressure up to ~6 MPa (bottle pressure) with a control capability of ±0.01 MPa. To increase the pressure to 10 MPa, a Tradinco diaphragm pump was used. Pressures above 10 MPa were generated by means of an ISCO 65D syringe pump.

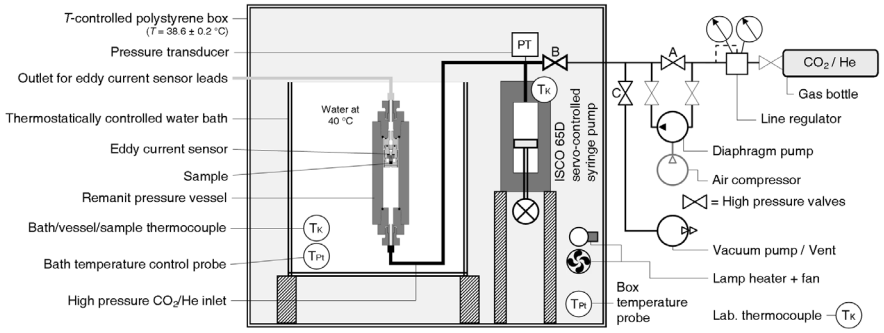

Fig. 3. Full experimental set-up. Note the Remanit pressure vessel containing the eddy current sensor and sample (for details see Fig. 2) submerged in the thermostatic bath. Note also the high pressure supply system consisting of an ISCO 65D syringe pump, a Tradinco diaphragm pump, and a CO_2 bottle coupled to an AirProducts line regulator. A heated foam-polystyrene box encloses the syringe pump and water bath, controlling the air temperature around the set-up to within ±0.2 °C. T_K = Type K thermocouple; T_{Pt} = Pt100 element; A, B, C = high pressure valves.

This was used to control the pressure at all values investigated between 10 and 100 MPa (pressure control accuracy ±0.6895 MPa). The pressure of CO_2 experienced by the sample was measured using a Honeywell TJE 0–137.90 MPa (20,000 psi) pressure transducer (accuracy ±0.6895 MPa), located at the ISCO cylinder-head (Fig. 3).

To maintain constant temperature in and around the sample, the Remanit pressure vessel was placed in a thermostatic water bath controlled at 40.0±0.05 °C. The temperature of the whole set-up was kept constant by placing the water bath, ISCO syringe pump, high pressure tubing, and the temperature-sensitive, eddy-current signal conditioner in a 1 m^3 foam-polystyrene box, the temperature of which was controlled at 38.6±0.2 °C using a digital controller, lamp heater and fan (Fig. 3). The thermostatic bath and foam box temperatures were measured and controlled using a Pt-100 element (Fig. 3). Temperature was also measured with an accuracy of ±0.3 °C using type-K thermocouples located in the water bath, on the ISCO pump cylinder-head and outside the box (*i.e.* in the laboratory).

The temperature, CO_2 pressure and displacement (eddy-current sensor) signals were converted at 16-bit resolution using a National Instruments, 16-channel DAQPad-6015 data acquisition system and were logged digitally by a computer at a rate of 0.5 Hz using National Instruments VI Logger software. The displacement signal was logged in the form of the raw voltage generated by the eddy current sensing system, whereas the temperature and CO_2 pressure signals were first appropriately scaled.

6.2.3.2. Testing procedure: Samples 1 and 2

We measured swelling strain as a function of CO_2 pressure and time for Samples 1 and 2 parallel to the bedding (x-direction, Sample 1) and perpendicular to the bedding (z-direction, Sample 2) (Fig. 1). This was done during multiple CO_2 pressure cycles, where one "cycle" refers to a complete upward-download pressurisation sequence. The experimental procedure followed for each sample was similar to that described by Hol and Spiers (submitted) for one pressure cycle. In the present study, however, this procedure was repeated once in the case of Sample 1 and twice in the case of Sample 2.

In setting up each experiment, the sample was placed in the sample holder and mounted in the sample/sensor assembly attached to the (upper) closure nut of the vessel (refer Fig. 2). The distance between the eddy current sensor tip and the steel target attached to the sample was then set between 100 and 140 μm, to ensure that the sensor would operate within the linear range of the sensor. The upper and lower closure nuts (Fig. 2) were then screwed into the pressure vessel and the complete system placed vertically in the water bath, set at a temperature of 40 °C. The air in the foam polystyrene box was then heated to a temperature of 38.6 °C. After heating up and settling for approximately 2 h to reach thermal equilibrium, the high pressure system was evacuated for 1-2 h via valves B and C (Fig. 3).

To initiate each dilatometry run on Samples 1 and 2, valve C was closed and CO_2 was introduced from the CO_2 bottle, via the AirProducts line regulator plus valves A and B (Fig. 3), and set at ~1.1 MPa pressure. This caused immediate swelling of the sample. After the sample reached a constant (equilibrium) strain (6-12 h), the CO_2 pressure was increased in a single step to ~3.6 MPa and then to ~5.4 MPa (CO_2 bottle pressure), allowing equilibration at each stage. To increase the CO_2 pressure further to 10.0 MPa, valves A and B were first closed, and the CO_2 pressure in the A-B section of the tubing was pressurised to ~12 MPa using the Tradinco diaphragm pump (Fig. 3). This CO_2 was then slowly bled into the pressure vessel via valve B to increase the CO_2 pressure on the sample to 10.0 MPa. Valve B was subsequently closed and the ISCO pump used to control the CO_2 pressure in the main part of the system. Again after equilibration, the CO_2 pressure was increased to 20.0 MPa by manually programming the ISCO pump. From this set pressure on, the ISCO pump was programmed (using a National Instruments Labview control module) to increment the CO_2 pressure to 100.0 MPa in fixed steps of 10.0-15.0 MPa at pre-set time intervals of 1-3 h. After cycling the CO_2 back to 20.0 MPa in fixed steps of 10.0-15.0 MPa, the ISCO pump was set back to manual programme control at 10.0 MPa CO_2 pressure. The CO_2 was then manually released from the system in a stepwise manner to ~8.5 MPa and ~4.5 MPa, controlling the pressure after each step using the ISCO pump until equilibration. Finally, all CO_2 was released by opening valves B and C, and the system was evacuated. Throughout the whole experiment, changes in CO_2 pressure were implemented slowly enough (1-5 min) to avoid temperature changes in the system. Sample dimensional changes

were recorded during both upward pressurisation and during depressurisation. The pressure-cycling procedure was repeated for each sample (Sample 1 and 2) until a dimensional response without major hysteresis was obtained. After the last cycle of exposure to CO_2, the sample was recovered from the dilatometry system, and stored for further analysis by means of SEM.

For each experiment, the linear strain e_i of the sample in the x- (Sample 1) and z-directions (Sample 2), was calculated as a function of time using the definition $e_i = (\Delta L_i/L_{0i})\cdot 100\%$, where ΔL_i is the sample expansion measured in direction i, and L_{0i} is the starting dimension of the sample in that direction, as determined at NTP prior to incorporation in the pressure vessel (see Table 1). Thermal expansion of the samples during heating of the system was minor and approximately equal to contraction of the samples due to evacuation (~0.01 % strain). Therefore, we ignored both effects in the calculation of linear strain e_i.

6.2.4. Exposure of Sample 3 to CO_2

Sample 3 (6x4x4 mm block) was exposed to CO_2 in a manner similar to Samples 1 and 2 (cylinders). To do this, the sample was placed in the dilatometer sample holder, between the supporting stage and sample hood, and mounted in the sample/sensor assembly attached to the upper closure nut of the Remanit high-pressure vessel (Fig. 2). The sample was mounted such that its long axis (x-direction) was aligned parallel to the axis of the eddy current sensor.

A CO_2 pressurisation procedure similar to that employed for Samples 1 and 2 was then followed, in this case exposing the sample to only one CO_2 pressure cycle. This was closely similar in step history and duration to the cycles employed for Samples 1 and 2. Reliable dilatometric measurements could not be made, due to the irregular shape of the sample (block of ~6x4x4 mm), and hence unstable positioning in the sample holder. Instead, the change in output voltage of the eddy current sensor with CO_2 pressure was used simply to monitor the equilibration of the sample with CO_2 after each pressure increment.

6.2.5. Microstructural methods

Of the three samples studied, Sample 1 (cylinder) and Sample 3 (block) were selected for analysis using the SEM operated in backscatter imaging mode. Sample 1 was imaged after two cycles of dilatometry exposure to CO_2 at pressures up to 100 MPa. Its initial microstructure was not investigated. Sample 3 was analysed both before and after a single cycle of CO_2 pressurisation and depressurisation. The area observed in Sample 3 before CO_2 treatment was relocated after CO_2 treatment in order to examine changes occurring in the initially observed microstructural features.

In preparing Sample 1 (cylinder) for observation after CO_2 treatment, special attention was paid to observing the microstructure within the centre of the sample rather than at the outer sample surface, to avoid any effects related to core preparation. Sample 1 was therefore ground and polished after dilatometry to reduce its length by about 50%. This was done using fine, then ultrafine, SiC polishing paper, blasting with compressed air to remove debris from the sample surface at different stages in the procedure. The freshly exposed surface, which effectively formed a section though the middle of the original cylinder, was then cleaned and polished at 3 spots, measuring approximately 1 mm^2, using a Gatan 691 Argon Ion Precision Polishing System (two Ar^+ beams orientated at 3° relative to the slowly rotating sample surface). The sample surface was ion-milled for 30 min per spot, after which the sample was attached to an aluminium SEM stub using a standard SEM carbon sticker.

Sample 3 (block) was prepared for SEM analysis before CO_2 treatment by dry polishing the end to be placed in contact with the Al sample hood in the dilatometer. Polishing was again done using fine, and then ultrafine SiC polishing paper, in combination with compressed air to remove debris. No ion-milling was directly on Sample 3, because it was too large to fit in the polishing system. Instead, the sample was subsequently attached to an aluminium SEM stub using a highly viscous graphite-methanol dag. The use of this dag allowed the sample to be studied in the SEM, then taken off and placed into the dilatometer for exposure to CO_2. Finally, it was reattached to the SEM stub with the graphite dag to allow SEM examination after exposure to CO_2.

The samples were studied by means of backscatter electron microscopy (BSE) performed using a Philips XL30SFEG field emission scanning electron microscope, equipped with an energy-dispersive x-ray detector (EDX). A relatively low accelerating voltage of 6 keV was used to distinguish more clearly between the internal microstructure and surface scratches remaining from the grinding and polishing procedure applied to the samples, notably Sample 3 which was not subsequently ion-milled. EDX spectroscopy was conducted at an accelerating voltage of 6 keV (and once at 10 keV), at selected spots on the sample surfaces, to assess the chemical composition of a variety of surface features.

Sample	P (MPa)	e_i^{eq} (CO_2) (%)	P (MPa)	e_i^{eq} (CO_2) (%)	P (MPa)	e_i^{eq} (CO_2) (%)	P (MPa)	e_i^{eq} (CO_2) (%)	P (MPa)	e_i^{eq} (CO_2) (%)	P (MPa)	e_i^{eq} (CO_2) (%)
1 (x-dir)	0.0000	0.0000	100.0536	0.4060	-0.0297	-0.1496	100.0385	0.4289				
	1.2177	0.2280	85.0452	0.4493	1.2086	0.1765	90.0298	0.4511				
	3.5788	0.4110	70.0535	0.4846	3.7428	0.3988	80.0468	0.4703				
	5.6291	0.5105	55.0629	0.5115	5.6976	0.4824	70.0293	0.4867				
	10.0385	0.5486	40.0402	0.5314	10.0229	0.5572	60.0478	0.5050				
	25.0463	0.5199	25.0530	0.5491	20.0307	0.5550	50.0286	0.5251				
	40.0260	0.4712	10.0487	0.5369	30.0239	0.5433	40.0324	0.5400				
	55.0372	0.5026	8.5682	0.5399	40.0348	0.5298	30.0433	0.5547				
	70.0379	0.4688	4.5454	0.4436	50.0439	0.5151	20.0418	0.5693				
	85.0411	0.4380	-0.0297	-0.1496	60.0417	0.4999	10.0517	0.5744				
	100.0536	0.4060			70.0195	0.4824	8.5692	0.5690				
					80.0378	0.4652	4.5395	0.4570				
					90.0436	0.4473	-0.0136	-0.1278				
					100.0385	0.4289						
Duration (h)	190 (UP)		140 (DOWN)		43 (UP)		35 (DOWN)					
2 (z-dir)	0.0000	0.0000	95.0450	0.5604	-0.0457	0.0662	95.0425	0.8422	0.0000	0.0647	95.0438	0.7782
	1.0180	0.2441	80.0245	0.5966	1.1530	0.4535	80.0522	0.8972	1.2135	0.4121	80.0289	0.8236
	3.5161	0.4976	65.0379	0.6317	3.5904	0.6172	65.0480	0.9358	3.5441	0.6629	65.0464	0.8611
	5.8694	0.5758	50.0400	0.6519	5.7893	0.6873	50.0242	0.9715	5.7506	0.8029	50.0232	0.8951
	10.0277	0.6199	35.0409	0.6704	10.0229	0.7185	35.0329	1.0018	10.0364	0.9167	35.0278	0.9271
	20.0138	0.6170	20.0321	0.6916	20.0473	0.7157	20.0516	1.0223	20.0300	0.9212	20.0259	0.9505
	35.0103	0.6061	10.0248	0.7080	35.0120	0.6958	10.0303	1.0259	35.0248	0.9013	10.0496	0.9539
	50.0629	0.5889	8.5374	0.7054	50.0458	0.6947	8.5522	1.0258	50.0362	0.8739	8.5557	0.9373
	65.0372	0.5675	4.5472	0.6899	65.0170	0.7377	4.5543	0.8791	65.0379	0.8427	4.5373	0.7695
	80.0087	0.5514	-0.0457	-0.02 (extr.)	80.0595	0.8312	-0.0127	0.0647	80.0431	0.8116	-0.0008	0.0029
	95.0450	0.5604			95.0425	0.8422			95.0438	0.7782		
Duration (h)	205 (UP)		129 (DOWN)		33 (UP)		23 (DOWN)		37 (UP)		29 (DOWN)	

Table 2. Linear strains e_i^{eq} measured for Samples 1 and 2 at equilibrium during CO_2 pressure cycling. P represents the CO_2 pressure applied in each step of the pressure cycling procedure. The corresponding strains are the linear strains e_x^{eq} measured for Sample 1 (// to bedding) and e_z^{eq} measured for Sample 2 ($\perp$ to bedding). Note that Sample 1 was subjected to two pressurisation cycles, whereas Sample 2 was subjected to three cycles. Durations are as shown per cycle. Note that the final strain in Cycle 1 of Sample 2 was obtained by extrapolated by following the trends seen in Fig. 4b, at the same stage in other cycles.

6.3. Results

6.3.1. Dilatometry data: Samples 1 and 2

For the dilatometry data, we adopt the convention that fluid pressure P, as well as linear expansion strains e_i are measured positive. Our data on strain development as a function of time (e_i versus t) at fixed CO_2 pressure, and on strain achieved at equilibrium as a function of applied CO_2 pressure (e_i^{eq} versus P), are plotted in Fig. 4 and Fig. 5. The data on the strain measured at equilibrium versus applied CO_2 pressure are listed in Table 2.

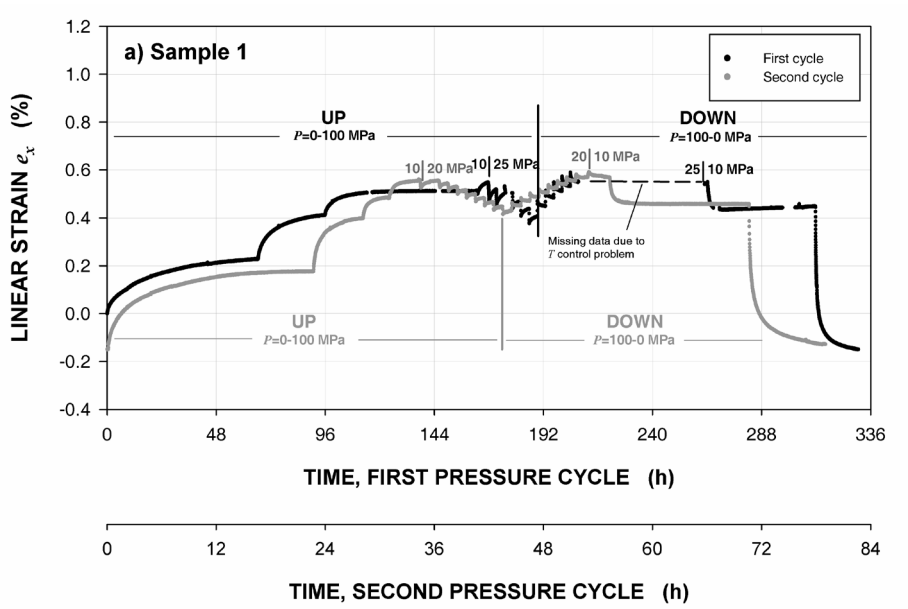

Fig. 4. Linear strain (e_i) development in a) the x-direction of Sample 1 and b) the z-direction of Sample 2 measured in response to stepping the CO_2 pressure at a constant temperature of 40.0 °C. The pressures corresponding to each step are listed in Table 2. Upward and downward step sequences are labelled "UP" and "DOWN". The plots show equilibrium was reached in 1-60 h, and demonstrate a transition from a rapid expansion in the low CO_2 pressure steps (< 10 MPa) to a combination of initial contraction followed by expansion in the high CO_2 pressure steps. These transitions are indicated by labelling the corresponding 10-20 MPa or 10-25 MPa pressure steps. Note, the hysteresis in the pressurisation versus depressurisation portions of the e_i^{eq}-P data during the first (Sample 1) or second (Sample 2) CO_2 pressure cycles. Note also the three to five times faster equilibration during the second and third exposure cycles compared to the first cycles.

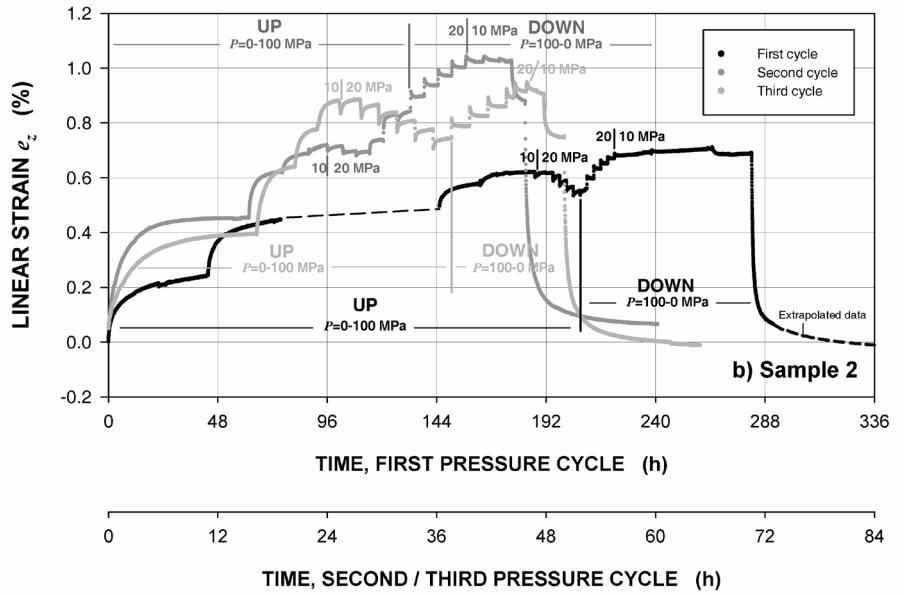

Fig. 5. Linear strain at equilibrium (e_i^{eq}) versus applied CO_2 pressure (P) as measured in a) the x-direction of Sample 1 and b) the z-direction of Sample 2 (for x, y and z directions – see Fig. 1). Strains were calculated relative to the initial sample lengths as listed in Table 1. Solid lines show evolution of strain with increasing CO_2 pressure, dashed lines with decreasing CO_2 pressure.

6.3.1.1. Development of strain versus time

The development of the linear strains (e_i) measured for Sample 1 (x-direction) and Sample 2 (z-direction) as a function of time per CO_2 pressure cycle is shown in Fig. 4. In this figure, the elapsed time was re-set to zero at the onset of each CO_2 pressure cycle.

Broadly speaking, after each CO_2 pressure increment, the samples expanded in a time-dependent manner, approaching an equilibrium linear expansion in 1-70 h. Similar behaviour was observed after pressure decrements but then involving contraction. From Fig. 4a and Fig. 4b, it is clear that the equilibration time strongly depends on both the magnitude of the set CO_2 pressure step, and on the exposure history. For most CO_2 pressure cycles, two clearly different, pressure-dependent domains can be recognised in the behaviour shown in Fig. 4. Below 10 MPa of CO_2 pressure, the e_i-t trend due to a stepwise increase in CO_2 pressure, is dominated by a rapid, time-dependent increase in linear strain, *i.e.* by swelling. Above 20-30 MPa of CO_2 pressure, however, further pressure increments cause immediate contraction determined by the magnitude of the upward pressure step, *i.e.* contraction that directly tracks the CO_2 pressure as it

is increased during each pressure step. When the target pressure is reached and held fixed in each step above 20-30 MPa, the sample then re-expands in a time-dependent manner, taking approximately 1-2 h to equilibrate after each pressure step. The net strain in each step above 20-30 MPa is nonetheless contractional. These low pressure expansion and high pressure contraction regimes are most clearly recognised in the strain development seen during the last pressure cycle of each experiment, *i.e.* the second cycle of Sample 1 (e_x – Fig. 4a) and the third cycle of Sample 2 (e_z – Fig. 4b). During the pressure release cycles, the same expansion-compaction domains are seen, but in reverse (Fig. 4).

We now examine the behaviour exhibited in each cycle and sample in more detail. The first, complete up-and-down CO_2 pressure cycle applied to the samples took approximately 320 h for Sample 1 (Fig. 4a) and 270 h for Sample 2 (Fig. 4b). The longest equilibration time occurred in response to the first CO_2 pressure increment (1.2 MPa), taking approximately 50-70 h in both samples. In all subsequent CO_2 pressure increments and decrements, equilibrium was approached in 3-30 h.

In the case of Sample 1, this continuously expanded as a function of increasing applied CO_2 pressure up to 20 MPa (at equilibrium), and then contracted slightly as the CO_2 pressure was increased further to 100 MPa. Both expansion and contraction occurred in approximately equal amounts of + and -0.02 % per 15 MPa pressure increase (Fig. 4a). Decreasing the CO_2 pressure stepwise, first resulted in a stepwise expansion in the interval 100-30 MPa, and then in strong contraction upon further depressurisation, final release of the CO_2 and evacuation. No deviation from this trend was observed as a function of CO_2 pressure during either pressurisation or depressurisation, although data are missing between 200 and 260 h due to failure of temperature control in the foam-polystyrene box in this interval. The maximum linear strain exhibited by Sample 1 in the first pressure cycle was 0.55 %, reached at P=10 MPa in the upward and downward portions of the cycle. Deformation during this cycle was recoverable to within -0.2 % linear strain (Fig. 4a), *i.e.* Sample 1 showed a permanent shrinkage of 0.2 % after completion of the first pressure cycle.

Sample 2 showed similar expansion/contraction behaviour in its first pressurisation-depressurisation cycle, although it reached a higher maximum linear strain of 0.7 % (Fig. 4b). In this sample, however, a slight expansion of 0.01 % was observed in response to the highest pressurisation step (*i.e.* the step from 90-100 MPa CO_2 pressure) in contrast to the contractions of -0.02 % that occurred during pressurisation steps in the range 20-90 MPa. Because we did not wait long enough in the final step in the depressurisation part of the first cycle, the strain reached at equilibrium in the evacuated state was estimated by extrapolation following the trend seen at the same stage in other cycles. This indicated that deformation of Sample 2 in the first pressurisation-depressurisation cycle was recoverable to within -0.02 % linear strain (Fig. 4b), *i.e.* the sample showed a minor permanent shrinkage of ~0.02 %.

During the second CO_2 pressure cycle applied to the samples, equilibration was approximately three to five times faster than in the first pressurisation-depressurisation cycle (see Fig. 4a and Fig. 4b; note scaling of the x-axes). Again, the longest equilibration time was obtained in response to the first CO_2 pressure increment of 1.2 MPa, in this case taking approximately 6-16 h in both samples. Focusing first on Sample 1, relative to the final strain attained after the first pressure cycle (*i.e.* in the evacuated state), this sample exhibited perfectly recoverable behaviour. Linear strains developed during pressurisation were all recovered during depressurisation (no permanent expansion or shrinkage). The low pressure expansion and high pressure contraction regimes were clearly displayed by the sample. A maximum strain similar to that attained during the first exposure cycle (approx. 0.55 %) was attained in the pressurisation and depressurisation portions of the second cycle, at a CO_2 pressure of 10 MPa (Fig. 4a).

By contrast, Sample 2 in its second cycle showed behaviour that strongly deviates from the pressure-dependent expansion/contraction domains exhibited by Sample 1 and seen in the first exposure cycle applied to Sample 2. This deviation is observed, in particular, during the upward CO_2 pressure step from 50 to 65 MPa (Fig. 4b, Table 2), where marked expansion (~0.05 % strain) was observed instead of the expected contraction. This expansion continued to occur at each following CO_2 pressure increment, totalling 0.9 % linear strain (e_z) at 80-95 MPa. Note, that the change in linear strain per upward pressure step was 0.05 % strain per 15 MPa. This is 2.5 times larger than the change observed in upward steps throughout the first cycle, and throughout both cycles applied to Sample 1. Depressurisation from 100-10 MPa resulted in further expansion up to 1.05 % linear strain, after which the sample strongly contracted in the descent to the evacuated state. However, the hysteresis in e_i-t / e_i-P behaviour observed in the second pressurisation-depressurisation cycle of Sample 2 did not lead to significant permanent strain. In this cycle, the deformation of Sample 2 was recoverable to within +0.05 % linear strain (Fig. 4b).

The third pressure cycle, applied to Sample 2 only (Fig. 4b), exhibited behaviour similar to the first and second pressure cycles of Sample 1 (Fig. 4a), *i.e.* it demonstrated well-defined low pressure expansion and high pressure contraction regimes. However the maximum strain measured in Sample 2 (perpendicular to the bedding plane) at 10 MPa CO_2 pressure was 0.9 % in the third cycle, which is approximately 1.6 times the maximum linear strain measured in Sample 1 (parallel to the bedding plane) in the first and second cycle. As in the preceding cycles, the deformation of Sample 2 during the third cycle was again recoverable to within +0.05 % linear strain (Fig. 4b).

6.3.1.2. Equilibrium strain data

Asymptotic or equilibrium strain values obtained after 1-70 h of equilibration time depending on CO_2 pressure and exposure history, are plotted as a function of CO_2 pressure in Fig. 5. Fig. 5a shows the linear strain (e_x^{eq}) measured at equilibrium in the x-direction of Sample 1 for the two pressure-cycles applied. Fig. 5b shows the strains (e_z^{eq}) measured at equilibrium in the z-direction of Sample 2 for the three cycles applied in this case. Clearly, all samples show net expansion in response to saturation with CO_2 over the full pressure range of 0-100 MPa. Broadly speaking, two pressure domains can be recognised, as seen in the data of Fig. 4 and as reported by Hol and Spiers (submitted). Below 10 MPa of applied CO_2 pressure, both samples exhibit sharp swelling up to a peak strain of ~0.6 to ~1.0 %. Beyond 10-20 MPa, the equilibrium strain mostly decreases.

Sample 1 shows more or less reversible behaviour in the two pressure-cycles applied. In detail, however, minor hysteresis can be observed in the strain (e_x^{eq}) versus CO_2 pressure (P) curves obtained for the upward and downward portions of the first pressurisation cycle (Fig. 5). During the first CO_2 pressure cycle, Sample 1 expands almost by ~0.6% during upward pressurisation to ~10 MPa, *i.e.* in the initial swelling domain. It then contracts by almost 0.1 % strain in the range 10-40 MPa CO_2 pressure, expands by 0.03 % in the range 40-55 MPa and then resumes steady contraction between 55 and 100 MPa CO_2 pressure. This produces a downward dip in the strain versus pressure curve at 20-55 MPa during upward pressurisation (Fig. 5). During the depressurisation stage of Cycle 1, however, no such dip occurs (Fig. 5). Instead, Sample 1 expanded steadily as the CO_2 pressure was decreased from 100 to 10 MPa, then contracting sharply below 10 MPa. In the second pressure cycle applied to Sample 1, closely reversible behaviour was obtained, almost exactly following the depressurisation curve produced in Cycle 1 (Fig. 5c).

The equilibrium linear strains measured perpendicular to the bedding (*i.e.* in the z-direction) for Sample 2 were significantly (1.1-1.9 times) greater than the average linear strains measured in the bedding plane (x-direction) for Sample 1 (Fig. 5). Moreover, Sample 2 shows strong hysteresis in the strain (e_z^{eq}) versus CO_2 pressure (P) curves obtained in both cycles 1 and 2 (Fig. 5b). This is most clearly observed in the second CO_2 pressure cycle (Fig. 5b), where the linear strain at equilibrium increases strongly from ~0.7 % to ~0.85 %, during upward pressurisation from 50 to 80 MPa CO_2 pressure, while depressurisation follows a smooth expansion-contraction curve parallel to that obtained in Cycle 1. In the depressurisation stage of Cycles 1 and 2, Sample 2 shows the two pressure domains of swelling and contraction observed in Sample 1 (Fig. 5a) and seen. In Cycle 3, the observed strain versus CO_2 pressure data are almost exactly reversible, and lie close to the depressurisation curve obtained in Cycle 2.

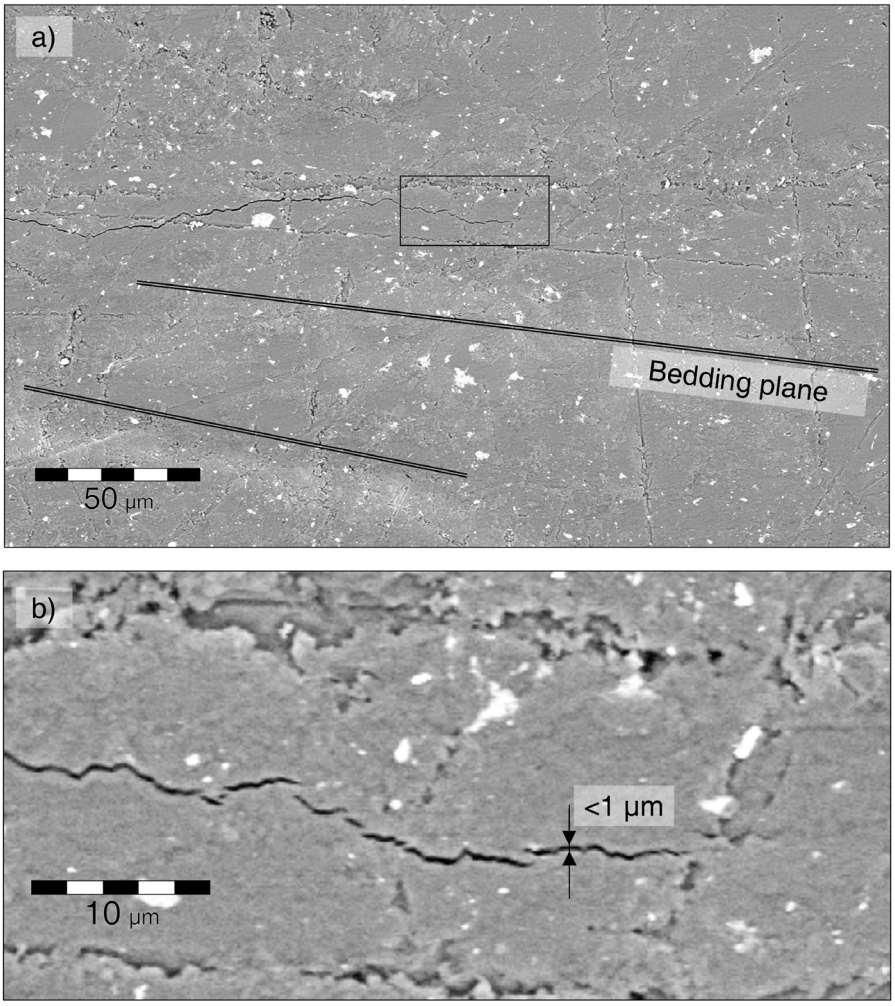

Fig. 6. SEM/BSE micrographs of the dry-polished surface of Sample 3 of Brzeszcze 364 high volatile bituminous coal in the virgin state, i.e. before exposure to CO_2. a) Overview of a representative area measuring approx. 250x150 µm, b) detail of crack tip within box shown in (a).

6.3.2. Microstructural observations

Representative microstructural data obtained using SEM in backscatter mode are presented in Fig. 6 (for Sample 3 before exposure to CO_2), in Fig. 7 (for Sample 3 after exposure to CO_2) and in Fig. 8 (for Sample 2 after exposure to CO_2). Note that no significant changes were measured in the mass of either sample after exposure to CO_2 (Table 1).

6.3.2.1. Sample 3: microstructure before exposure to CO_2

The microstructure observed within the outer (dry-polished) surface of Sample 3 before exposure to CO_2 is illustrated in Fig. 6a and Fig. 6b. These micrographs show that the starting material is characterised by dense coal matrix material, with few pore spaces or cavities being visible at the scale of imaging (Fig. 6a). Compositional and/or density differences can be recognised from the contrast between the dark grey, lighter grey and bright areas (scale <10 μm) distributed over the sample surface, with the lighter and darker grey bands visible in the bottom left and middle right portion of Fig. 6a defining the coal bedding. These variations contrast likely reflect variations in maceral composition and/or structure (Gamson et al., 1993). However, due to insufficient contrast in the grey areas, no information could be obtained regarding maceral content of these areas. Nonetheless, the bright phases observed in Fig. 6 (~5 vol%) appeared structurally similar to inertinites (van Krevelen, 1993), and, taking into account the absence of a mineral signature in EDX analysis, are believed to correspond to such macerals.

Aside from the above microstructural features, the surface of Sample 3 before exposure to CO_2 showed a variety of scratches and microcrack features (Fig. 6). The scratches are preparation-induced, and are easily identified as they are perfectly straight, show little topographic contrast in BSE imaging mode (diagnostic for scratches - *cf.* Howell and Boyde, 1999), and bear no special relationship to the bedding orientation (*e.g.* see Fig. 6a, right hand side, sub-vertical scratches). By contrast, microfractures are seen as open, irregular fractures often running sub-parallel to bedding. One typical microfracture is illustrated in Fig. 6a. This is aligned horizontally, *i.e.* sub-parallel to the bedding, and extends over ~200 μm from the left edge of the micrograph to the centre (Fig. 6a and Fig. 6b). The crack aperture is <1 μm, which is consistent with previous observations of microfractures in virgin coals (Karacan and Okandan, 2001; Solano-Acosta et al., 2007). The crack tip, seen in the centre of the micrograph (Fig. 6a and Fig. 6b), appears as an en-echelon sequence of microfractures with individual lengths often less than 10 μm (Fig. 6b). Elsewhere short fractures of similar aperture are occasionally found running almost perpendicular to bedding.

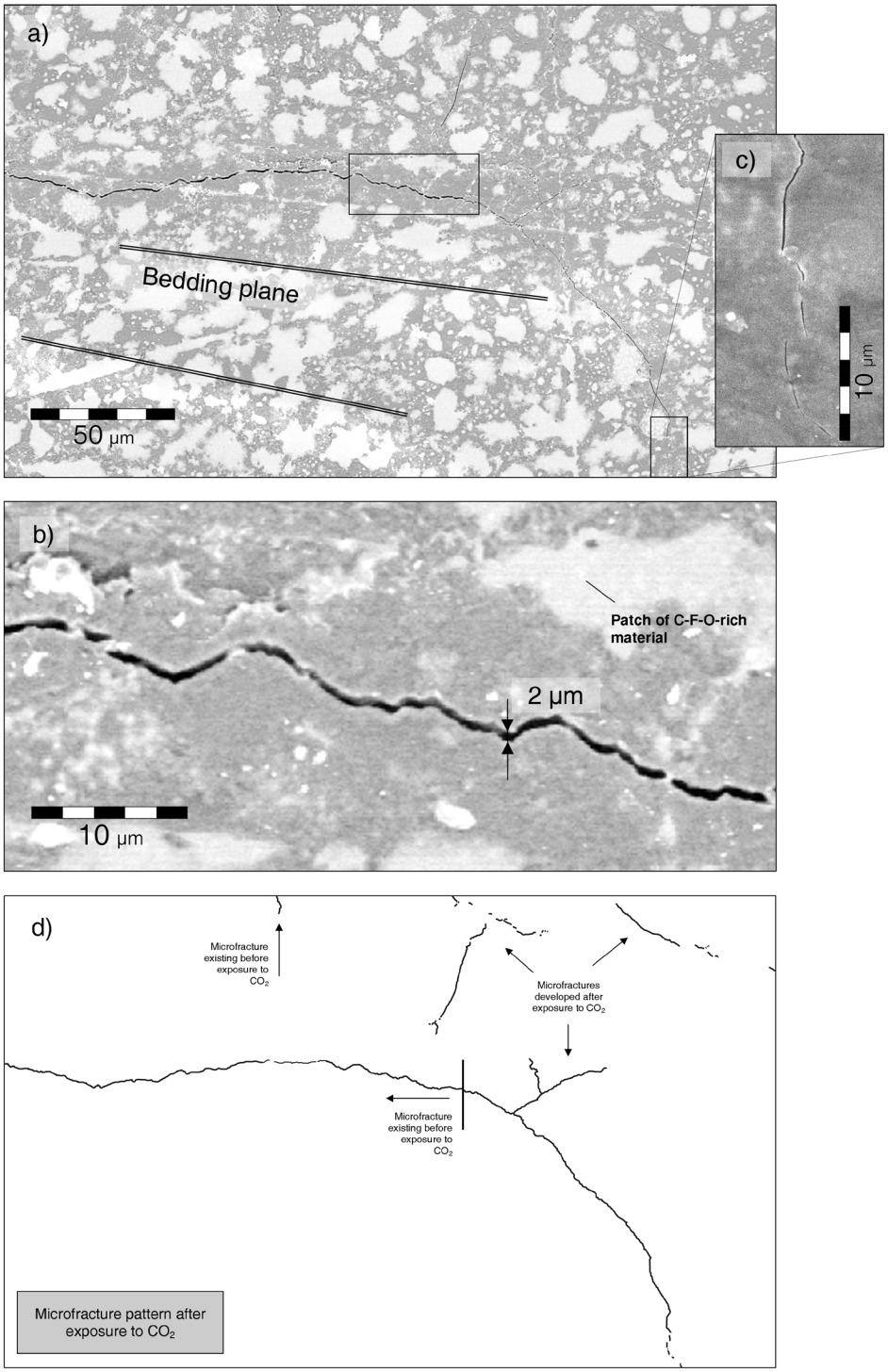
a)
Bedding plane
50 µm
c)
10 µm
b)
Patch of C-F-O-rich material
2 µm
10 µm
d)
Microfracture existing before exposure to CO_2
Microfractures developed after exposure to CO_2
Microfracture existing before exposure to CO_2
Microfracture pattern after exposure to CO_2

6.3.2.2. Samples 2 and 3: microstructure after exposure to CO_2

Fig. 7 shows micrographs of the same region of the outer (dry polished) surface of Sample 3 shown in Fig. 6, but after exposure to CO_2 during the single pressure cycle applied to this sample (total duration 300 h, maximum CO_2 pressure 100 MPa, temperature 40 °C). The following changes can be observed due to exposure to CO_2. These typify the microstructural changes seen throughout the sample.

The most obvious change is the appearance of 10-20 μm size patches of surface deposit, appearing white using the BSE detector, and distributed more or less uniformly over the entire sample surface (Fig. 7a). These patches often fill or cover the scratches recognised in the sample before exposure to CO_2. We note that the patches do not obscure the crack seen in Fig. 6a. Nor did they occur at locations where the Al sample hood had covered the surface of the sample. EDX spectroscopy of the patches revealed enrichment in carbon, fluorine and oxygen, suggesting they represent material leached from the Viton o-rings present in the dilatometry apparatus used to expose Sample 3 to CO_2.

After CO_2 exposure, the microfracture pattern seen in Fig. 6 was significantly modified, and new microfractures had appeared (Fig. 7a, Fig. 7b and Fig. 7c). All fractures were traced manually, and are shown in the "overlay" presented in Fig. 7d. In detail, the fracture pattern observed in Sample 3 after exposure to CO_2 consists of an array of new 5-50 μm long fractures in the top right of the micrograph, orientated roughly perpendicular to each other. In addition, the horizontal microfracture represented in Fig. 6 (before exposure to CO_2) has extended to the bottom right of the sample, and has forked in the centre-right of the micrograph (Fig. 7a). Fig. 7b shows the original location of the crack tip represented in Fig. 7b. Here, the original en-echelon sequence of microfracture segments has become connected into a continuous fracture, which has opened slightly at this location to ~2 μm. The new crack tip, located in the bottom right of Fig. 7a after exposure to CO_2, is shown in Fig. 7c, and exhibits a new, en-echelon sequence of microfracture segments, now running perpendicular rather than parallel to the bedding plane.

In contrast to Sample 3, dilatometry was performed on Sample 2 during exposure to CO_2 and the sample was sectioned and ion-milled to yield a fresh, clean surface for SEM observation. Representative portions of the ion-milled regions studied

Fig. 7 (opposite page). SEM/BSE micrographs of Sample 3 after exposure to CO_2 at a pressure of 100 MPa and a temperature of 40 °C. a) Overview of same selected area as in Fig. 6a,b). Detail of the part of the surface where the crack tip was located before exposure to CO_2 (cf. Fig 6b). Note the propagation and opening of the fracture compared with the situation before exposure to CO_2 (Fig. 6b), as well as the patch of C-F-O-rich material (determined using EDX spectroscopy). c) Crack tip after propagation of the fracture. d) Manually-traced microfracture pattern.

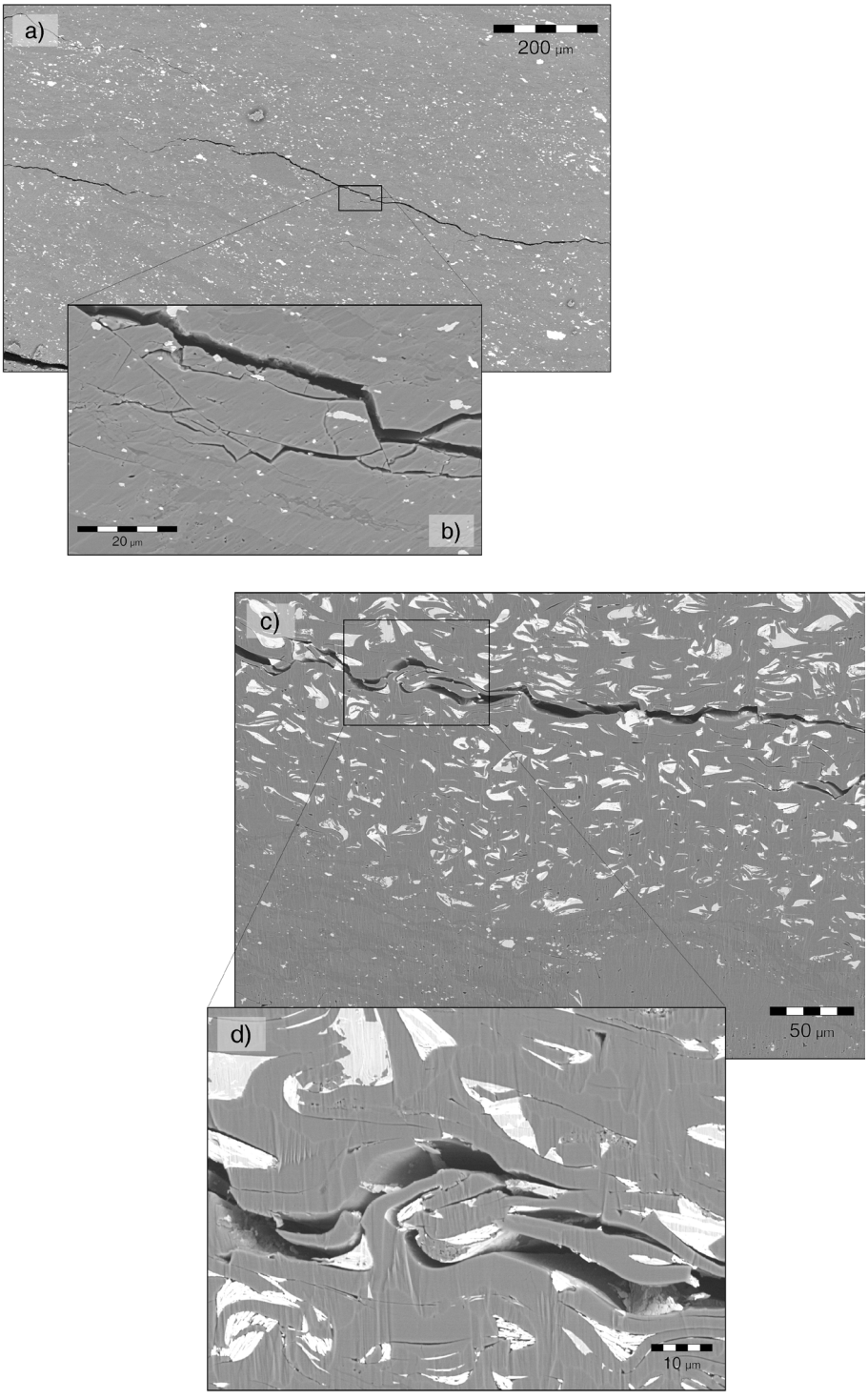
a)
200 µm
20 µm
b)
c)
50 µm
d)
10 µm

are shown in Fig. 8. The BSE micrographs obtained show the microstructure of the samples much more clearly, due to the better sample preparation. Indeed, different macerals present in the coal now seem to be visible by virtue of both composition and structure. Note, for example, the bright domains showing an internal structure similar to that displayed by inertinite (Fig. 8d) (*cf.* Bustin et al., 1985). Note also the lamellar structures visible between the bright domains, which presumably also reflect (compressed) maceral fragments. Compositional banding marking the coal bedding, which runs at approximately 25° to the base of the micrographs, is also clearly visible. In addition, microfractures are widespread. These run parallel to the bedding plane (Fig. 8), and occur both as straight (Fig. 8a and Fig. 8b) and as wavy fractures (Fig. 8c and Fig. 8d). The enlargements presented in Fig. 8b and Fig. 8d clearly demonstrate that the fractures predominantly disjoin the bedding planes, often following the lamellar maceral structure (Fig. 8d), *i.e.* disjoining the contacts between different macerals and between similar lamellar (Fig. 8b).

To investigate whether or not the C-F-O rich material was present at the maceral contacts and within the microfractures observed in Sample 2 (Fig. 8), and hence to assess if the C-F-O rich material seen on the surface of Sample 3 after CO_2 treatment was present inside Sample 2, we conducted EDX spectroscopy on the pore surfaces visible in Fig. 8b and Fig. 8d. The analyses revealed no enrichment in C, F, or O inside Sample 2. We therefore infer that while the surface of Sample 3, and probably of all samples, had indeed become coated with deposits of C-F-O rich material from an external source, probably by the Viton o-rings used to seal the high pressure vessel, the samples were not penetrated by this contaminant.

Fig. 8 (opposite page). SEM/BSE micrograph of the dry-polished and ion-milled (Ar^+) section of Brzeszcze coal Sample 2, after exposure to CO_2 at a pressure of 100 MPa and a temperature of 40 °C. a) and b) give overviews. Note the preferential fracture orientation parallel to the bedding plane. c) and d) show disjoining of the bedding planes at inferred maceral-maceral contacts.

6.4. Discussion

The present experiments, performed on virgin samples of coal matrix material (Samples 1 and 2) have shown that significant linear strain, or expansion (1.1 % maximum), occurs during repeated exposure to CO_2 at pressures in the range 0 to 100 MPa at a constant temperature of 40.0 °C (Fig. 4 and Fig. 5). The behaviour observed is broadly consistent with competition between reversible adsorption-induced swelling and elastic compression, as reported for multiply exposed coal by Hol and Spiers (submitted), with compression dominating over swelling at CO_2 pressures above 10 MPa. However, our data show significant hysteresis in the strain versus CO_2 pressure data obtained during first or sometimes second exposure of our samples to CO_2, as well as the accumulation of minor permanent strains. Moreover, equilibration of the samples in the second and third CO_2 pressure cycles occurred much faster than during first exposure to CO_2 (Fig. 4). In addition, SEM study (Sample 3) demonstrated increased microfracturing of the coal matrix after first exposure to CO_2 (Fig. 6 and Fig. 7).

In the following, we will discuss the possible mechanisms responsible for these effects. We go on to discuss the effect of the application of an effective stress to coal matrix material on the processes inferred to operate, and hence consider the implications of our results for the exposure of coal to CO_2 under *in situ* conditions, *i.e.* during ECBM operations.

6.4.1. Mechanisms driving mechanical evolution during exposure to CO_2

Physical adsorption of CO_2 is well-known to cause reversible swelling in coal (e.g. Day et al., 2008; Durucan et al., 2009; van Bergen et al., 2009; Day et al., 2010; Majewska et al., 2010). The fully reversible expansion and contraction effects seen in the later pressure cycles applied to our samples can accordingly be inferred to be due to physical adsorption of CO_2, operating in competition with reversible elastic compression – as recently demonstrated by Hol et al. (submitted) for identical samples of Brzeszcze coal that had been pre-exposed to CO_2. However, the hysteresis in equilibrium expansion/contraction behaviour (Fig. 5), and the longer equilibration times seen in the first (and, for Sample 2, the second) cycle of CO_2 pressurisation applied to the present samples (Fig. 4), clearly indicate the operation of additional, irreversible processes during early exposure to CO_2.

The microstructural work conducted on our samples has shown that the various irreversible effects seen in the first pressurisation cycle are accompanied by an increase in microfracture density relative to untreated coal, involving both propagation of pre-existing microfractures, but also formation of new microfractures (Fig. 7 versus Fig. 6). The microfractures developed show a strong tendency to lie in the orientation of the bedding plane (Sample 2, Fig. 8) but also develop and propagate at high angles to the

bedding (Sample 3, Fig. 7). Recently, Majewska and Ziętek (2007) performed similar unconfined swelling experiments on medium-rank coal obtained from the Upper Silesian Basin (Seam 358), exposing the coal to CO_2 and CH_4 at pressures in the range 0-4 MPa and room temperature. As well as measuring the expansion of the samples, acoustic emissions (AE) were monitored, revealing four times higher cumulative AE counts upon first exposure of their samples to CO_2 than in the final, third run. As in our experiments, first exposure to CO_2 was accompanied by approximately four times slower equilibration compared to subsequent runs (Majewska and Ziętek, 2007). This effect of exposure on equilibration time has also been observed by Goodman et al. (2006), who conducted cyclic CO_2 sorption tests on Argonne Premium coal samples. Since high acoustic rates were recorded by Majewska and Ziętek (2007) during the first upward CO_2 pressurisation run only, the microfracturing events that likely caused the AE activity seen in their samples could not have been generated by rapid depressurisation. On this basis, we infer that processes occurring during the first or second exposure to increasing CO_2 pressure caused the formation of the new microfractures seen in our samples.

Alongside this, the present data on equilibrium strain (e_i^{eq}) versus applied pressure (Fig. 5) show that the hysteresis seen in the first and second cycles of exposure to CO_2 also originated during upward pressurisation. This is evident from the "kinks" in the upward portion of the e_i^{eq}-P curves obtained for Sample 1 in Cycle 1 and for Sample 2 in Cycles 1 and 2 (refer Fig. 5). The implication is that the observed hysteresis, i.e. the development of these kinks, is directly associated with microfracture development during upward pressurisation of our samples in the first or second exposure cycles.

The following hypotheses can be put forward to explain the association between microfracturing and the onset of hysteresis in e_i^{eq}-P behaviour during upward pressurisation:

1. After each upward pressure increment, CO_2 homogeneously penetrated and equilibrated with the samples, with microfracture development causing dilatation of the samples (*i.e.* the kinks in the e_i^{eq}-P curves) in specific pressure increments applied beyond a total pressure of 35-40 MPa (Fig. 5).
2. At pressures below 35-40 MPa, CO_2 penetration into the samples, and hence equilibration with the samples, was incomplete and non-uniform. At higher pressures, pressure-dependent microfracturing, occurring in specific pressure increments, allowed more uniform CO_2 access to the samples and hence additional adsorption-induced swelling of regions not previously accessed by CO_2. This too would produce kinks in the e_i^{eq}-P curves of the type seen in the early exposure cycles shown in Fig. 5.

The behaviour embedded by Hypothesis 1 above, would be expected to lead to a permanent component of microfracture-related dilatancy roughly equal in magnitude to the amplitude of the microfracturing-induced hysteresis loop. Alternatively, part of the microfracture-related dilatation might be recovered on depressurisation, if coupled to reversible swelling effects within the coal matrix, leading to reduced, but still positive dilatancy. However, our samples showed 0.05-0.2 % permanent shrinkage after the first cycle of exposure to CO_2 (Fig. 4). Moreover, the much larger expansion and larger hysteresis (kink) amplitude exhibited by Sample 2, in the second pressure cycle compared with the first (see Fig. 5b), is inconsistent with Hypothesis 1, as the observed behaviour would require more microfracturing in the second pressurisation cycle than in the first. Hypothesis 1, however, implies uniform CO_2 penetration and equilibration in both cycles.

Hypothesis 2, on the other hand, fits better with our experimental data. Increased penetration of the samples with CO_2, as microfractures develop in specific pressure steps applied above 35-40 MPa, coupled with competition between adsorption-induced swelling and elastic compression of the bulk samples as described by Hol and Spiers (submitted), would lead to hysteresis of the type seen in Fig. 5. In addition, progressive microfracturing and increased CO_2 penetration from cycle to cycle offers an explanation for a) the increase in maximum swelling exhibited by Sample 2 in Cycle 2 versus Cycle 1 (Fig. 5), b) the convergence towards reversible e_i^{eq}-P behaviour with almost zero hysteresis seen in the last pressure cycles applied to Samples 1 and 2 (Fig. 5), and c) the decrease in equilibration time exhibited by both samples in successive pressurisation cycles (Fig. 4; see also the similar behaviour reported by Goodman et al. (2006) and by Majewska and Ziętek (2007)). We accordingly infer that the behaviour of our samples is determined by Hypothesis 2 behaviour superimposed on adsorption-induced swelling and elastic compression of the samples (*cf.* Hol and Spiers, submitted). Microfracture dilatation presumably also contributed to the observed e_i^{eq}-P behaviour, but to a relatively minor extent in view of the lack of marked permanent swelling strain.

An outstanding observation that remains unexplained by Hypothesis 2 is the small permanent shrinkage exhibited by Samples 1 and 2 after the first CO_2 exposure cycle. We suggest that this might reflect small contractional strains caused by extraction of residual, adsorbed water, present in the samples after initial evacuation, through preferential adsorption of CO_2 during the first pressure cycle (*cf.* Iwai et al., 1998). An alternative possibility is that incomplete access of CO_2 to our samples, during initial pressurisation, led to permanent compaction of CO_2-poor regions within the coal matrix under the confining action of the high applied CO_2 pressures (up to 100 MPa).

6.4.2. Cause of microfracturing

We have argued above that microfracturing of our samples occurred progressively with increasing applied CO_2 pressure, allowing more homogeneous access of CO_2 to the samples in pressure increments applied above 35-40 MPa, and causing adsorption-induced swelling of matrix material not previously accessed by CO_2. However, the cause of this microfracturing has not yet been addressed.

The micrographs presented in Fig. 8 demonstrate that microfracturing of our sample material is related to the structure of the material. Clearly, the microfractures seen in the material exposed to CO_2 often disjoin the bedding plane (Fig. 8b), follow the wavy interfaces between lamellar maceral structures (Fig. 8c), and disrupt contacts between what we infer to be different maceral types (Fig. 8d). Some microfractures cross-cut the bedding or fork in directions perpendicular to bedding (Fig. 7). This all suggests that the anisotropic orientation distribution of macerals (*i.e.* their preferred alignment parallel to bedding), plus the compositional layering of the material, lead to anisotropic strength and heterogeneous swelling properties that not only allow easy microfracturing parallel to bedding, but also produce differential displacements within neighbouring layers, hence generating bedding-normal cracks. The notion of easy microfracturing parallel to the bedding fabric is strongly supported by the dilatometry data presented in Fig. 4 and Fig. 5, which show that the amplitude of hysteresis in e_i^{eq}-P behaviour measured perpendicular to the bedding (e_z) in Sample 2 is some 5 to 6 times larger than measured parallel to bedding (e_x) in Sample 1. At the same time, the absolute magnitude of expansion measured perpendicular to bedding in Sample 2 was ~1.5 times that measured parallel to bedding in Sample 1.

On this basis, we infer that the cause of microfracturing during pressurisation of the present samples with CO_2 is heterogeneous swelling, caused by adsorption-induced differential expansion of macerals and compositional layers/zones with different swelling properties (*cf.* Karacan, 2003), combined with differential accessibility of the different macerals and compositional layers or zones present in the coal. This provides a mechanism of producing stress-strain gradients at both maceral and bedding/layer interfaces, thus causing microfracturing during upward pressurisation. The cracks thus formed may of course have become subsequently widened during depressurisation and associated CO_2 release.

Although differential swelling within the coal upon exposure to CO_2 could not be directly observed in our experiments, it has been studied using CT-scanning under both unconfined conditions (Karacan and Mitchell, 2003) and under conditions of positive effective confining pressure (Karacan, 2007). These studies show that vitrinite-rich layers in coal exhibit preferential swelling when exposed to CO_2 (*cf.* Shibaoka et al., 1979). On this basis of He-pycnometry required to determine excess sorption, Sakurovs et al. (2007) have inferred that the small increase in He-accessibility of coal

after exposure to CO_2, as well as accelerated equilibration seen upon re-exposure to CO_2, are caused by microfracturing. Microfracturing, in turn, has been related to stresses induced by differential swelling (Harpalani and Mitra, 2010), as observed in polymers exposed to water vapour, for example by Pegoraro et al. (1977). On the other hand, in some previous studies, differential swelling and compression appears to be related to the orientation of pre-existing fractures (Pone et al., 2009a), which provide preferential access to CO_2 and cause local swelling. We concur with the broad picture put forward by Harpalani and Mitra (2010) that microfracturing and the associated hysteresis and equilibrium effects are caused by differential adsorption-induced swelling and the related development of internal stresses. However, our data show that this is due not only to differences in the sorption and swelling response of different macerals and compositional layers, but also to differences in the accessibility of these different microstructural elements within the coal matrix.

For the present sample material, it has been shown that the magnitude of reversible swelling is directly (and linearly) related to the adsorbed concentration of CO_2, and hence to the activity or chemical potential of CO_2 (Hol and Spiers, submitted). Since the hysteresis observed in the various e_i^{eq}-P curves shown in Fig. 5 occurs at different applied CO_2 pressures, it must be controlled by factors that are independent of, or not wholly determined by, CO_2 activity. Note that this is fully consistent with the hypothesis (Hypothesis 2) that the microfractures observed in our samples are related to heterogeneous adsorption-induced swelling associated with varying maceral types and with compositional layering, and to the related heterogeneity and anisotropy of strength and transport properties.

Finally, we note that the present concept of microfracturing caused by a differential and heterogeneous response of the layering and maceral structure in unconfined coal exposed to CO_2 is also consistent with observations reported in the literature for coal exposed to organic solvents. For example, Brenner (1983) observed that the further solvent-driven swelling is allowed to proceed, the less reversible it becomes. Brenner attributed this irreversibility to the development of fractures and distortions within the coal matrix, resulting from uneven swelling. In addition, it is well-known that the swelling of coal exposed to pyridine produces visible cracking (French et al., 1993). In this case, analyses of NMR data have shown that regions with varying pyridine-accessibility produce differential swelling, which in turn is accompanied by microfracturing (French et al., 1993).

6.4.3. Role of plasticisation

In contrast to the explanation given here and put forward by Harpalani and Mitra (2010), several authors have proposed CO_2-induced plasticisation to be responsible for irreversible behaviour observed in coal-CO_2 systems. The term "plasticisation" refers here to a softening effect brought about by an enhanced degree of chain and segmental mobility that develops within the structure of many polymers due to dissolution of CO_2. In this process, the CO_2 becomes reversibly incorporated, and weakens cross-linking bonds in the polymer structure. After release of the CO_2 pressure, these effects may result in permanent morphological alterations in the polymeric structure, referred to as "crystallisation" in polymer science (Kemmere and Meyer, 2005). With respect to coal, Majewska and Ziętek (2007), for example, proposed plasticisation processes as the cause of the CO_2-induced acoustic emission events observed in their experiments on medium volatile bituminous coal (Upper Silesian Basin, Poland). The decrease in equilibration time seen upon repeated exposure of Argonne coal samples to CO_2 has also been attributed to plasticisation (Goodman et al., 2006). In this context, it is important to emphasise that plasticisation of polymers by CO_2 is a fully reversible process (Kemmere and Meyer, 2005). Direct effects of plasticisation, such as modified rheological and/or transport properties seen in polymer-CO_2 systems as a result of polymer restructuring, must therefore be reversible as well. It is precisely this principle that is applied in the field of polymer reaction engineering in order to reversibly restructure polymers (Kemmere and Meyer, 2005). If plasticisation is involved in modifying the behaviour of coal exposed to CO_2, all permanent effects and hysteresis observed in our samples, and reported by others, could therefore occur only as a side-effect of the plasticisation process. Consistent with this, previous applications of plasticisation concepts to explain the effects of CO_2 on coal assume that the driving force for permanent changes in coal properties, such as the hysteresis, permanent strain, equilibration effects and microfracturing observed in our experiments, is already present in coal before exposure to CO_2, in the form of internal or residual stresses related to burial and exhumation. The proposed explanation for the observed irreversible effects of CO_2 on coal is that these stresses are "released" by means of the plasticisation process, producing associated strains and changes in transport properties (Larsen, 2004).

Although several other studies claim to have demonstrated the occurrence of plasticisation in coal-CO_2 systems, through the application of dilatometric techniques during heating (Khan and Jenkins, 1985) and through the application of calorimetric methods (Mirzaeian and Hall, 2006), these studies do not consider the possible role that residual water (Allardice et al., 2003) or other natural volatiles (Alexeev et al., 2006) present in coal might have played in determining the properties of bulk coal that were measured. For example, Larsen et al. (1997) observed that the exposure of coal to pyridine resulted in a loss of water, which was accompanied by a reduction in heat capacity. Moreover, plasticisation processes are unable to explain several other

important observations. First of all, the e_i-t data presented in Fig. 4 show that our coal matrix samples exhibit a permanent shrinkage after first exposure to CO_2, whereas a "release" of internal strain energy (cf. Larsen et al., 1997; Larsen, 2004), due to plasticisation, would lead to permanent expansion. Other observations are reported in the literature. For example, significant hysteresis is observed in the e_i^{eq}-P behaviour of coal-CH_4 systems (Moffat and Weale, 1955) despite the fact that CH_4 does not cause substantial plasticisation of polymers. Also, dilatometry data provided by Khan and Jenkins (1985) suggest that coal samples plasticise only at CO_2 pressures higher than ~3 MPa, whereas unconfined coal swelling data exhibit continuous swelling over the CO_2 pressure range 0-15 MPa (*e.g.* Day et al., 2008; Hol and Spiers, submitted), and acoustic emissions are sensed well below 3 MPa CO_2 pressure (Majewska and Ziętek, 2007). We believe that plasticisation is therefore unlikely to play a significant role in relation to the formation of microfractures in coal samples exposed to CO_2, or in relation to the associated hysteresis, equilibration time and permanent strain effects. Note that a similar conclusion concerning the role of plasticisation of coal by CO_2 was drawn recently by Mastalerz et al. (2010) on the basis of sorption tests, FTIR spectroscopy and Gieseler fluidity measurements performed on specific coal lithotypes before and after CO_2 equilibration. These authors concluded that the molecular interactions between CO_2 and their samples only involve physical adsorption (Mastalerz et al., 2010).

6.4.4. Likely implications for ECBM under *in situ* conditions of stress

We have inferred that a mechanism of heterogeneous adsorption-induced swelling and differential accessibility of coal matrix material offers the best explanation for the formation of microfractures in our samples upon first or second exposure to CO_2. The associated hysteresis in expansion/contraction behaviour and shorter equilibration times observed upon subsequent exposure (Fig. 4, Fig. 5) are caused by microfracture-enhanced accessibility of the coal structure leading to increased adsorption and more pronounced swelling. However, all of our measurements were performed under condition of zero effective stress. We will now go on to discuss likely implications of our results for the mechanical and sorption behaviour of coal under ECBM conditions, *i.e.* taking into account the effects of *in situ* stress state. For conditions relevant to ECBM production at a depth of 1000-1500 m, the effective lithostatic stress will likely be of the order of 25-35 MPa.

Our data show that hysteresis in e_i^{eq}-P behaviour of up to maximum 0.3 % strain occurred in our samples in the direction perpendicular to the bedding, due to the formation of microfractures, and increased CO_2 penetration. As a consequence of the enhanced penetration, adsorbed CO_2 concentrations increased gradually per cycle. This suggests a coupling between the amount of CO_2 taken up by the coal matrix versus the progress of microfracturing, which, in turn, means that the extent of microfracturing can play a role in controlling the effective *in situ* uptake capacity of the coal matrix for CO_2. A key question remaining is whether or not these fractures will open under *in*

situ stress conditions. Our experiments were performed under unconfined conditions, so that the results cannot be used to directly assess the occurrence microfracturing in stressed coal. However, since the fractures formed in our samples generally had a very high length-to-width aspect ratio (>100, Fig. 7, Fig. 8), and since this type of crack damage, like pores, drastically reduces the elastic stiffness of bulk rock materials (Walsh, 1965), it is highly unlikely that such cracks will open under confining stresses in excess of a few MPa.

In addition, recent work on the effect of confining pressure on the CO_2 uptake provides indirect evidence that adsorption-induced microfracturing of the type reported here is strongly inhibited under conditions of elevated normal stress. Specifically, recent experiments addressing the effect of applied stress on the CO_2 uptake by coal (Pone et al., 2009b; Hol et al., 2011; Wang et al., 2011), have led to the conclusion that the sorption capacity of coal under confined conditions is lower than that under unconfined conditions. However, substantial differences are observed in the reductions estimated. Notably, Wang et al. (2011) and Pone et al. (2009b), who attempted to inject CO_2 into large, virgin coal cores subjected to a hydrostatic confining pressures of up to 12 and 13.8 MPa respectively, found that the sorbed CO_2 concentration was reduced by 59 % (Wang et al., 2011) and 64 % (Pone et al., 2009b) compared to the sorbed concentration measured in the unconfined state. Methane uptake was reduced by 91 % (Pone et al., 2009b). Less dramatic reductions in sorption capacity were found by Hol et al. (2011), who subjected crushed coal samples to an applied effective stress after equilibration with CO_2, and found a reduction in adsorption of 5-50 % at 35 MPa applied effective stress, which they showed was due to a direct thermodynamic effect of stress on sorption capacity. The higher reductions observed by Wang et al. (2011) and Pone et al. (2009b) at lower confining stresses suggest that the samples used in their study could not be completely accessed due to the pre-confinement. From this we infer that in the experiments by Wang et al. (2011) and Pone et al. (2009b) limited penetration of the coal matrix by CO_2 occurred due to the pre-confinement. This implies that any pre-existing cracks were probably closed by the applied confining pressure of 3-9 MPa, and more importantly, that adsorption-induced microfractures, which would facilitate the enhanced penetration, likely did not open under the applied stress. This suggests that under *in situ* conditions, adsorption will not cause cracking or any increase in permeability. As suggested earlier by Hol and Spiers (submitted), improved access of the coal matrix by CO_2 can probably only be achieved by creating space to accommodate coal swelling developed during the CO2 injection process and the resulting formation and opening of microfractures. The required removal of coal mass and volume may be achievable either by application of solvents/solutes, or by performing active mining of the coal and/or the over- or underlying strata. To improve the feasibility of ECBM operations, such approaches require further research.

6.5. Conclusions

This study has focused on detailed dilatometry experiments performed on fresh, unconfined coal matrix samples (cylinders of 4 mm in diameter and ~4 mm long) of high volatile bituminous coal (Brzeszcze, Poland), at CO_2 pressures up to 100 MPa, and at 40.0 °C. This was combined with microstructural analyses of the sample material before and after exposure to CO_2. The aim was to establish the magnitude of irreversible effects such as permanent swelling and changes in equilibration time in the coal studied, to explain these effects in terms of the operative microphysical processes, and in turn to evaluate whether these effects are likely to have any significant effects under *in situ* ECBM conditions of stress. Our findings can be summarised as follows:

1. Exposure of our samples to CO_2 at pressures up to 100 MPa produced strains resulting predominantly from competition between adsorption-induced swelling and elastic compression, as recently reported for multiply exposed samples by Hol and Spiers (submitted) and as implied by the data of Moffat and Weale (1955) for coal-CH_4 systems. The measured strain response was reversible after two or three upward and downward CO_2 pressure cycles, in close agreement with expectations for adsorption-induced swelling and elastic compression. However, during the first or second cycle of exposure of our samples to CO_2, substantial hysteresis was observed in volumetric behaviour at CO_2 pressures above 35-40 MPa, accompanied by minor permanent strain, was observed in the expansion behaviour measured. Moreover, equilibration with CO_2 took about four times longer during the first CO_2 pressurisation cycle than in subsequent CO_2 pressurisation cycles.
2. Microfractures formed in or propagated though the coal samples as a result of the cyclic exposure to CO_2. This is consistent with the recording of acoustic emissions (AE) during swelling versus CO_2 adsorption tests on virgin samples of medium rank coals reported by Majewska and Ziętek (2007), who recorded significantly higher acoustic rates during initial upward pressurisation compared to subsequent cycles. From these observations, we infer that the formation of microfractures is responsible for enhanced CO_2 penetration into the present samples, allowing more homogeneous access of CO_2 in pressure increments applied above 35-40 MPa, and causing adsorption-induced swelling of matrix material not previously accessed by CO_2. We further infer that the enhanced penetration, sorption and swelling, in turn, resulted in the observed hysteresis in dimensional response and in the decrease in equilibration time seen in subsequent exposure cycles.
3. Most microfractures developed parallel to the bedding fabric of the coal, roughly following maceral-maceral and bedding/layer interfaces. Moreover, the largest permanent strains and strain hysteresis were measured perpendicular to the bedding. We infer that the formation of microfractures in our samples was caused by a mechanism of heterogeneous adsorption-induced swelling at the maceral and compositional layering scale, accompanied by differential accessibility of the coal microstructure.

4. No evidence was found that CO_2-induced plasticisation of the macromolecular structure of the coal matrix caused the observed microfracturing, and related hysteresis in swelling behaviour and decrease in equilibration time. Plasticisation is unlikely to play a significant role during ECBM operations.
5. Under *in situ* conditions of stress at a depth of 1000-1500 m, *i.e.* effective stresses in the range 25-35 MPa, adsorption-induced microfractures are unlikely to open or propagate. This is implied by simple stiffness considerations and by the effects of confining pressure on CO_2 uptake of coal observed in previous experiments. This indicates that under *in situ* conditions adsorption will not cause any auto-cracking effects or any increase in permeability. Improved access of the coal matrix by CO_2 can probably only be achieved by creating space to accommodate coal swelling developed during the CO_2 injection process and the resulting formation and opening of microfractures. The required removal of coal mass and volume may be achievable either by application of solvents/solutes, or by performing active mining of the coal and/or the over- or underlying strata.

7

Conclusions and suggestions for future research

Sander Hol, Christopher J. Spiers

7. Conclusions and suggestions for future research

This thesis presents the results of a fundamental experimental and theoretical study of the response of dry coal matrix material to injected CO_2 under conditions relevant to the recovery of methane from coal seams by means of Enhanced Coalbed Methane (ECBM) production employing CO_2. The study focused primarily on quantifying and understanding the physical phenomena and processes associated with CO_2 adsorption and swelling under both unconfined and confined conditions. In particular, the study addressed the coupling, at thermodynamic equilibrium, between stress, strain, CO_2 pressure and adsorption in coal-CO_2 systems under isothermal conditions. The work was motivated by a need for an improved understanding of the response of coal seam reservoirs to CO_2 injection, in order to help advance existing ECBM reservoir "simulators" towards predictive reservoir models.

The specific aims of this research were:

1. to determine whether stress applied to the solid framework of coal matrix material significantly affects the CO_2 sorption capacity,
2. to quantify the relative contributions of adsorption-induced swelling versus elastic compression of coal matrix exposed to CO_2 at high pressures, and hence to determine the true relationship between purely adsorption-induced swelling and CO_2 uptake under unconfined conditions,
3. to determine the total uptake of CO_2 by coal matrix material, *i.e.* the sum of pore filling and adsorption capacity, in a manner avoiding the need for swelling corrections, He-porosity determinations, and uncertainties related to the EoS for CO_2,
4. to describe the fundamental thermodynamic relationship between stress, strain and sorption and to develop a full 3-D constitutive equation coupling adsorption-related mechanical effects and poroelastic response and, finally,
5. to determine whether the expansion of coal matrix material is accompanied by irreversible deformation and to explain any observed effects in terms of microscale processes responsible.

These aims were addressed by means of one-dimensional (*i.e.* laterally constrained) compression experiments, hydrostatic loading tests, and unconfined dilatometry experiments, combined with determinations of CO_2 uptake – and by means of thermodynamic analysis of adsorption under stress. All experiments were performed on crushed or intact coal matrix samples of high volatile bituminous coal from the Brzeszcze mine in Poland. The main conclusions drawn are summarised below, along with a brief evaluation of their implications for ECBM production, and with recommendations for future research.

7.1. Main conclusions

(1) Effect of an applied compressive stress on the CO_2 sorption capacity of coal.

One-dimensional (oedometric) compression experiments performed on pre-compacted, porous aggregates of crushed coal matrix material (grain size 63-212 μm), performed at 40 °C and at CO_2 pressures between 10 and 20 MPa have indicated that the application of an effective stress of 35 MPa results in a reduction of the CO_2 sorption capacity by an amount in the range between 0.0014 to 0.014 $mmol \cdot g_{coal}^{-1} \cdot MPa^{-1}$. The temperature, CO_2 pressure, and stress conditions investigated are roughly applicable to *in situ* conditions during ECBM operations, and the results suggest that the sorption capacity of coal under such stresses is about 5-50 % lower than the sorption capacity at zero applied effective stress. The desorption observed in the experiments during the application of an effective stress was accompanied by a reduction in apparent axial stiffness of the samples by about 33 % from 1.52 to 0.95 GPa. The processes responsible for desorption and the change in apparent axial stiffness were investigated by deriving a standard thermodynamic model for adsorption but, in contrast to previous studies, taking into account the *PV*-type work term associated with swelling against a hydrostatic effective stress. This predicted a reduction in CO_2 sorption capacity and in apparent axial stiffness of the samples of similar magnitude to the effects observed in the experiments. The conclusion is that the predicted effect of a compressive stress applied to coal matrix material, in excess of the stress applied to coal matrix material, in excess of the applied CO_2 pressure, does indeed reduce adsorption capacity, and by a significant amount.

(2) Competition between adsorption-induced swelling and elastic compression in coal under unconfined conditions.

Dilatometry experiments performed using a high pressure eddy current sensor were conducted on pre-exposed, unconfined, cylindrical coal matrix samples at a constant temperature of 40 °C and CO_2 pressures up to 100 MPa, and have demonstrated that pre-exposed coal matrix exhibits reversible, but anisotropic expansion over the full range of CO_2 pressures used. Expansion perpendicular to the bedding was about 1.4 times the more or less isotropic expansion measured in the bedding plane. Net volumetric strains were characterised by expansion below 10-20 MPa of CO_2 pressure and contraction at higher CO_2 pressures, and demonstrated that direct competition exists between purely adsorption-induced swelling, dominating at low pressures, versus elastic compression of the coal matrix, which dominates at high pressures. A combined thermodynamic swelling plus elastic compression model for coal swelling was developed that included this competitive behaviour. In the model, the adsorption-induced swelling was taken as linearly related to adsorbed CO_2 concentration. This linear relationship was confirmed by a comparison of the experimentally determined adsorption-induced swelling strain with the adsorbed concentration of CO_2 measured

independently. We compared our experimentally determined adsorption-induced swelling strains to those calculated from an adsorbed concentration model. Good agreement was found, which showed that combining the thermodynamically based model for adsorbed concentration with the elastic compression of our samples, obtained from their bulk modulus, provides a good description of the measured volumetric behaviour of our samples. The conclusion is that adsorption-induced swelling is more or less linearly related to adsorbed CO_2 concentration, at least in the Brzeszcze coal, and that total volumetric strain occurring under unconfined conditions can be realistically modelled as the sum of an adsorption-related and an elastic compression term.

(3) Direct determination of total CO_2 uptake by coal.

Motivated in particular by the effects that volumetric strain due to swelling might have on the accuracy of conventional manometric and gravimetric methods of measuring CO_2 adsorption (excess sorption), a new, independent method was developed to measure the total uptake of CO_2 by small cylindrical samples of coal matrix material (mass ~0.05 g). The method was conceived with the aim of avoiding the use of the Equation of State (EoS) of CO_2 and of avoiding volumetric corrections of any kind. No distinction between adsorbed and free CO_2 was made. Using this method, samples were individually exposed to CO_2 at 40 °C and CO_2 pressures up to 18 MPa. This method involved enclosing each small, CO_2-saturated sample in a ductile metal capsule and capturing its CO_2 content directly in an attached aluminium foil bag. This new capsule technique yielded Langmuir-like CO_2 uptake curves for the total CO_2 content of the coal matrix material tested, reaching 4.08 $mmol \cdot g_{coal}^{-1}$ at the maximum applied CO_2 pressure of 18 MPa. Control experiments showed that at CO_2 pressures above 9 MPa small amounts of free CO_2, trapped unwantedly in the capsule assembly, led to systematic errors in CO_2 uptake measurements estimated at 0.40 $mmol \cdot g_{coal}^{-1}$ maximum. For comparison, manometric experiments were performed on a set of the same samples (combined mass ~0.5 g) to determine the total uptake. This was done following a conventional excess sorption approach, modified to obtain total CO_2 uptake. These manometric experiments produced an uptake curve with a significant jump at 7-9 MPa CO_2 pressure. This showed a total CO_2 uptake of ~2.95 ±0.17 $mmol \cdot g_{coal}^{-1}$ at the maximum CO_2 pressure of 18 MPa used in the capsule experiments (*i.e.* 20-30 % lower mean values). The errors quoted here for the manometric method take into account random errors expected on the basis of pressure, temperature and volumetric measurement inaccuracies.

The differences between the two methods could not be explained by the expected systematic and random errors for the two methods. Allowing for worst case errors, the differences in CO2 uptake obtained using the two methods are attributed to i) random errors and to uncertainties EoS in the manometric dataset at low CO2 pressures (3-9 MPa), and ii) systematic errors, due to erroneous trapping of free CO2, dominating

in the capsule dataset high CO2 pressures (>9 MPa). Taking all error sources into account, the capsule method proved reliable at CO2 pressures of 0-7 MPa. At pressures higher than 8 or 9 MPa, the manometric method was most reliable. In general, use of the manometric method with sufficiently large samples, or the capsule method at P<9 MPa, provides a reliable means of measuring the CO2 uptake capacity, yielding errors that are less than the effects of in situ stress on sorption. In practice, when using the conventional manometric method to determine sorption and/or uptake capacity of large crushed samples, or when using the capsule method at CO_2 pressures <7 MPa, the effects of stress on sorption will generally be much more significant than any measurement errors, and need to be evaluated carefully. Improvement of the capsule technique is needed to prevent erroneous trapping of free CO_2 at pressures above 9 MPa. Nonetheless, our new encapsulation method has the potential to accurately determine the uptake of any adsorbate by any (swelling) adsorbent, *e.g.* CO_2 uptake by shale and clay caprocks and is suitable for assessment of the effects of small-scale lithological differences in CO_2 uptake.

(4) Effect of σ_{ij} on adsorption of CO_2 by coal: Thermodynamic model and constitutive equation for stress-strain-sorption behaviour.

A thermodynamic model was developed for site adsorption by coal under a general 3-D stress state σ_{ij}, predicting the effect of σ_{ij} on adsorbate concentration at equilibrium between the coal and the adsorbing fluid phase. The model was developed for CO_2, but is applicable to any adsorbing fluid having homogeneous access to a representative volume of coal matrix material. The new feature of the model is the inclusion of of the stress-strain work term, associated with adsorption-induced swelling under the general stress state σ_{ij}, in the formulation of an expression for adsorption energy. The model predicts that application of a general compressive stress state to the solid framework of the coal matrix material, over and above the fluid pressure *P*, generates a reduction in the site occupancy, and therefore in adsorbed concentration. This prediction was confirmed by a preliminary experiment performed on a 25 mm cylindrical sample of Brzeszcze 364 high volatile bituminous coal at 15 MPa fluid pressure, a temperature of 40 °C, and an effective stress of 1-35 MPa. This showed that the initial equilibrated adsorption capacity of 1.38 $mmol \cdot g_{coal}^{-1}$ was reduced by almost 10 % at 25 MPa effective stress.

A general constitutive equation was further developed to relate the stress state σ_{ij} to the fluid pressure *P*, net (total) strain ε_{ij}^{eq}, and the adsorbed concentration, taking into account both the adsorption-induced strain and poroelastic deformation of the coal. The model includes full coupling between stress, strain and sorption at given fluid pressure and temperature, including the inhibited effect of compressive stresses on sorbed concentration at equilibrium. The constitutive model can be coupled permeability-stress relations to provide a realistic basis for modelling stress-strain-sorption-permeability evolution and CO_2 movement under confined ECBM

conditions. A first analysis of this effect for coal initially at 25 MPa effective stress, with CO_2 injection at 15 MPa, showed an increase in effective stress to 35-105 MPa, which would lower CO_2 uptake at equilibrium by a total amount of ~13-30 % compared to conventional adsorption measurements made at 15 MPa CO_2 pressure. The principal conclusion drawn is that while *in situ* stress in coal seams will significantly reduce the sorption capacity of coal for CO_2, that self-stressing accompanying swelling upon CO_2 injection leads to an even greater effect which needs to be taken into account in ECBM reservoir modelling.

(5) Irreversible behaviour and microfracturing of coal due to interaction with CO_2 under unconfined conditions.

In addition to the above experimental and modelling work on reversible stress-strain-sorption behaviour of coal, dilatometry experiments were performed on fresh, unconfined Brzeszcze coal matrix samples, at a constant temperature of 40 °C and at CO_2 pressures up to 100 MPa, to investigate the magnitude and origin of any irreversible effects of the type reported in the literature. Multiple exposure runs were performed. Substantial hysteresis was observed in expansion versus CO_2 pressure behaviour measured during the first (or second) exposure of the samples to CO_2, accompanied by minor permanent shrinkage, with the largest permanent strain and largest strain hysteresis occurring in the direction perpendicular to the bedding. Moreover, dilatometric equilibration of the samples took three to five times longer in the first than in subsequent CO_2 pressurisation cycles. Microstructural analysis of the coal samples before and after CO_2 exposure showed that exposure resulted in the formation and propagation of microfractures, mostly delaminating the bedding planes and roughly following maceral interfaces or the maceral fabric. From the dilatometry and microstructural data, it was inferred that non-uniform access of CO_2, hence non-uniform swelling, plus a differential response of different coal macerals caused the hysteresis, permanent strain and microfracturing in first or second exposure cycles. The subsequently improved accessibility to CO_2 caused the observed decrease in equilibration rate. No evidence was found that CO_2-induced plasticisation of the coal structure played any role in the behaviour observed. Simple mechanical considerations imply that at *in situ* stresses corresponding to a depth of 1000-1500 m, i.e. effective stresses in the range 25-35 MPa, adsorption-induced microfractures will not form. It is concluded that, at *in situ* stresses, injection of CO_2 into coal, while leading to differential swelling strains within the material, can not generate significant microfracture permeability, and that full penetration by, and equilibration of the coal matrix with CO_2 will generally be prevented.

7.2. Implications for ECBM production

The theoretical models and experimental work reported in this thesis have shown that the CO_2 adsorption capacity of crushed and matrix-scale coal under a positive effective stress is markedly lower than under hydrostatic CO_2 pressure only. For *in situ* stress magnitudes, the effect is much larger than typical errors in measurements of CO_2 uptake. The present results therefore have significant implications for the potential for methane production from coal seams by ECBM methods, as considered below.

A constitutive equation was developed here, which describes the coupling between stress state, pore pressure, adsorption, poroelastic response, and adsorption-induced swelling response. The model predicts a reduction of expected CO_2 sorption capacity of coal seams by 3-10% during CO_2-injection due to the effective *in situ* stresses in the range 25-35 MPa. The model also provides a means to calculate the effect of "self-stressing" as a result of adsorption of CO_2 by coal under the conditions of restricted or zero strain (*i.e.* fully constrained conditions). High stresses are predicted to develop under fully constrained conditions, more than doubling the expected *in situ* stresses under typical (E)CBM reservoir conditions. This effect leads to an additional reduction in CO_2 uptake. A first estimate of this reduction on the basis of our constitutive model was made using model parameter values determined experimentally for Brzeszcze 364 high volatile bituminous coal. For this coal, equilibrated at 40 °C under conditions of 15 MPa fluid pressure *P* and 25 MPa effective stress (equivalent to ~2 km burial depth), and having a bulk modulus K of 0.5-5.0 GPa, the reduction of adsorbed concentration, in addition to the reduction of almost 10 % at 25 MPa effective stress, is predicted to be of the order of 3-20 %, implying a total reduction in the range 13-30%. the amount of methane that can be displaced by ECBM operations will be correspondingly reduced.

Under unconfined conditions, the exposure of coal matrix material to CO_2 at 40 °C and up to 100 MPa CO_2 pressure, also resulted in the formation of microfractures, caused by heterogeneous swelling and differential access. However, it has been argued here that such microfractures will not open or propagate under *in situ* conditions of stress, certainly at a depth of 1000-1500 m. As a consequence, permeability will remain low and access of the coal matrix to CO_2 will be limited. Also, present results have shown that effects of CO_2-induced plasticisation will be insignificant. Moreover, once access is gained by CO_2, the adsorption-induced swelling response of coal under *in situ* fluid pressures is accommodated by elastic compression and the self-stressing effect described above. The main implication of this for ECBM operations is that highly compliant coals (low K) that exhibit relatively little adsorption-induced swelling (hence low sensitivity of swelling strain to adsorbed concentration *C*) will show relatively small reductions or possibly even increases in permeability due to competition between swelling and poroelastic compression when CO_2 pressure increases during ECBM operations. Such coals would be relatively favourable for ECBM. By contrast, large reductions in permeability and injectivity can be expected

during ECBM operations in coals that exhibit high volumetric stiffness (high K) and large amounts of CO_2 adsorption-induced swelling (high sensitivity of swelling strain to *C*). These will be less suitable for ECBM. The suitability of given coals for ECBM production can thus be assessed from laboratory measurements of K and of sorption behaviour, coupled with application of the present constitutive model and a suitable stress-permeability relation.

In practice, the results of this study show that the CO_2 access problem remains a major one for ECBM operations, especially in the case of stiff, highly swelling coals situated at (unmineable) depth. Major improvements in access to the coal matrix by CO_2 can probably only be achieved by creating space to accommodate coal swelling and the associated opening of microfractures that have been shown to occur at maceral scale under zero confinement. The required removal of coal mass and volume, or creation of void volume, may be achievable either by hydrofracturing and injection of solvents to remove either organic or mineral rock components, by performing active mining of the coal and/or the over- or underlying strata, or possibly by pore pressure depletion of porous sediments enclosing the target coal seams.

The urgent need for predictive modelling in the field of ECBM production, with or without the additional stimulation measures suggested above, demands a fundamental understanding of the mechanisms controlling exchange and transport of CO_2 in the pore system of coals. The present results show that both experimental and modelling work is crucial to understand the effects of stress state on sorption. Our constitutive relations allows realistic modelling of the coupling between stress, strain and adsorption in (E)CBM reservoirs, including self stressing effects, and provide a basis for obtaining realistic predictions of the change in permeability during CH_4 extraction from and CO_2 storage in coalbeds. Nonetheless, the theory needs to be extended to account for the coupled response multi-fluid phase/coal systems.

7.3. Suggestions for future research

The results of the experimental and theoretical work described in this thesis have improved understanding of the response of the coal matrix to CO_2 under confined/stressed *in situ* conditions, and provide a basis for improved (E)CBM reservoir modelling and hence assessment of the feasibility of (E)CBM operations. Nonetheless, the study has involved several assumptions, as well as shortcomings in experimental methods or equipment. Moreover, new problems were identified, and several questions remain unsolved or still to be addressed. These issues are discussed briefly below and suggestions made for future research:

1. All experiments reported in this study were performed on high volatile bituminous coal, taken from the Upper Silesian Basin in Poland, and extracted from Seam 364, as exposed in the Brzeszcze Mine. This material was in part chosen because CO_2 was injected into this layer in 2004 at a distance of 5 km from the mine, as a part of the ECBM pilot project 'RECOPOL'. The use of Brzeszcze coal provides new data relevant to evaluating the response of a coal seam into which CO_2 has actually been injected, and relevant to high volatile bituminous coal in general. However, the applicability of the present results to coals of other rank and different geological settings is only qualitative. Future experimental studies of stress-strain-sorption effects, and especially of the coupling between stress and adsorption, should address a wider variety of coal types.
2. The choice of particular sample structure or dimensions, *i.e.* using powder (Chapter 2), small cylinders (Chapters 3 and 6) or cylinders composed of discs (Chapter 5), was motivated by the nature and scale of the physical processes investigated. Because of our focus on matrix-scale processes, the effects of cleats, cracks and large pores were intentionally eliminated from our experiments. In addition, relatively small samples were preferred because of the shorter equilibration times involved (*e.g.* in Chapters 2 and 5). However, our use of small matrix scale samples limits direct application of our results to the core-scale, and above. The role of cleats, cracks and large pores in determining bulk stress-strain-sorption behaviour needs to be further investigated in future research on large coal samples, paying careful attention to effects of scale on elastic and transport effects, alongside the phenomena reported here. It would be useful to compare systematically the swelling-sorption behaviour of coal samples of different size. Similarly, the thermodynamic and constitutive models developed here (Chapter 5) need to be compared with the behaviour seen in samples of different scales for extending or verifying rationales for upscaling to the coal seam scale.
3. While a useful constitutive modelling framework has been established for modelling stress-strain-sorption behaviour of coal under *in situ* conditions, and the magnitude of the effects of *in situ* stress development due to CO_2 injection estimated in a preliminary way, the model needs to be rigorously applied to investigate a) CO_2 and CH_4 storage potential in coal as a function of seam depth,

and b) the evolution of CO_2 injection in the framework of and ECBM reservoir model, making use of an appropriate relation coupling stress-strain-sorption to cleat permeability evolution.

4. To accurately determine CO_2 uptake or expulsion in several of our experiments on the effect of stress on coal (Chapters 2 and 5), a linear leak rate correction was applied to the raw ISCO pump volume data obtained. Leaks are a problem in all experimental studies of adsorption, especially using CO_2, He or CH_4. In future, leakage can possibly be reduced by including either a bellows in-between the ISCO pumps usually used in such work, filling the pump and bellows with a stiff fluid.
5. In Chapters 3 and 6, a new method to precisely measure the dilation of mm-scale cores by means of an eddy current sensor was described. In the configuration used, only one such sensor could be embedded in the vessel, so that the 3-D anisotropic strain response of the sample to CO_2 could only be determined by making sequential measurements of the dilation of our samples in four directions, relying on reversible swelling and compression of the samples. It was shown in Chapter 6, that reversibility was attained only after two or three exposure cycles. Hence, the assessment of permanent strain could only be performed in one direction per sample. A multidirectional eddy current dilatometer therefore needs to be designed.
6. In Chapter 3 experiments using a newly developed ductile metal encapsulation technique were reported. More control tests are needed to improve the applicability and accuracy of the ductile metal encapsulation technique, *i.e.* to firmly establish the errors involved in this technique. Moreover, improvements are needed in minimising unwanted void space in the capsule for useful application above fluid pressures of 9 MPa.
7. The present thermodynamic model for the effect of a general applied stress σ_{ij} on the adsorption capacity has so far been tested only in a single hydrostatic loading experiment performed on a matrix coal sample (disc stack). Triaxial loading experiments are needed to test the model rigorously and to establish firmly whether the CO_2 induced reduction in apparent Young's modulus reported in the literature is indeed due to stress-induced desorption as predicted here.
8. In all of the present experiments, the fluid phase was restricted solely to CO_2. Of all fluids naturally occurring in coal, CO_2 is expected to affect the mechanical state of coal the most strongly. Nevertheless, the interplay between CO_2 and other fluids/gases naturally present in coal, such as CH_4, H_2O and N_2, and their combined role in determining the stress-strain-sorption behaviour of coal should be addressed in future experiments.
9. The present thermodynamic models addressing the effects of stress applied to coal matrix material are quite general in that the behaviour of different coals and of different (single) adsorbing fluids is embodied in the values of the various model parameters (such as the concentration of available adsorption sites C_s, the

partial molecular volume of the adsorbed phase Ω_0, or the attachment energy ΔG_a). However, for application to other coals, and to other fluids besides CO_2, appropriate experiments must be done in future to determine the necessary sorption-specific parameter values (for so far as not available or inferable from the literature). Perhaps more important for the future is an attempt to derive (and calibrate) thermodynamic models addressing stress-strain-sorption behaviour of coal exposed to several fluids, such as CO_2, CH_4 and H_2O. Combined with experiments involving multiple fluids (see point 3), this is needed for more realistic application to the *in situ* environment of ECBM operations.

10. A practical implication of the interplay between stress state, strain and CO_2 adsorption capacity emerging from the present work is that CO_2 uptake and associated self-stressing reduces the efficiency hence feasibility of ECBM operations. Future research should therefore focus on creating space to accommodate coal swelling developed during the CO_2 injection process, hence preventing stress build-up and associated cleat closure or on causing active shrinkage of the coal. As discussed in section 7.2, possibilities that may be considered include hydraulic fracturing and removal of coal mass or of adjacent or included inorganic rock material by chemical or mechanical means, *e.g.* by application of solvents. Other option for fracturing coal seams and "creating space" for swelling include active mining and possibly poroelastic deformation of enclosing strata.

Bibliography

Abou Najm, M., Mohtar, R.H., Weiss, J. and Braudeau, E., 2009. Assessing internal stress evolution in unsaturated soils. Water Resour. Res., 45.

Alexeev, A.D., Ulyanova, E.V., Kalugina, N.A. and Degtyar, S.E., 2006. Phase transitions in the coal-water-methane system. Condensed Matter Physics, 9(1(45)): 109-114.

Allardice, D.J. et al., 2003. The characterisation of different forms of water in low rank coals and some hydrothermally dried products. Fuel, 82: 661-667.

Astashov, A.V., Belyi, A.A. and Bunin, A.V., 2008. Quasi-equilibrium swelling and structural parameters of coals. Fuel, 87(15-16): 3455-3461.

Ates, Y. and Barron, K., 1988. The effect of gas sorption on the strength of coal. Mining Science and Technology, 6: 291-300.

Aziz, N.I. and Ming-li, W., 1999. The effect of sorbed gas on the strength of coal – an experimental study. Geotechnical and Geological Engineering, 17: 387–402.

Bachu, S., 2008. CO_2 storage in geological media: Role, means, status and barriers to deployment. Progress in Energy and Combustion Science, 34(2): 254-273.

Bae, J.-S. and Bhatia, S.K., 2006. High-pressure adsorption of methane and carbon dioxide on coal. Energy & Fuels, 20: 2599-2607.

Baer, D., Thomas, M. and Jones, R., 1984. Influence of stress on H_2S adsorption on iron. Metallurgical and Materials Transactions A, 15(5): 853-860.

Battistutta, E., van Hemert, P., Lutynski, M., Bruining, H. and Wolf, K.-H., 2010. Swelling and sorption experiments on methane, nitrogen and carbon dioxide on dry Selar Cornish coal. International Journal of Coal Geology, 84(1): 39-48.

Beamish, B.B. and Crosdale, P.J., 1998. Instantaneous outbursts in underground coal mines: An overview and association with coal type. International Journal of Coal Geology, 35(1-4): 27-55.

Bennethum, L.S. and Weinstein, T., 2002. Pressures in swelling clay soils. In: C. Di Maio, T. Hueckel and B. Loret (Editors), Chemo-mechanical coupling in clays; From nano-scale to engineering applications. Swets & Zeitlinger, Lisse, pp. 135-147.

Biot, M.A., 1941. General theory of three-dimensional consolidation. Journal of Applied Physics, 12(2): 155-164.

Biot, M.A., 1973. Nonlinear and Semilinear Rheology of Porous Solids. Journal of Geophysical Research, 78(23): 4924-4937.

Boone, T.J., Ingraffea, A.R. and Roegiers, J.C., 1991. Simulation of hydraulic fracture propagation in poroelastic rock with application to stress measurement techniques. International Journal of Rock Mechanics and Mining Sciences & Geomechanics Abstracts, 28(1): 1-14.

Bradshaw, J. et al., 2007. CO_2 storage capacity estimation: Issues and development of standards. International Journal of Greenhouse Gas Control, 1(1): 62-68.

Brenner, D., 1983. In situ microscopic studies of the solvent-swelling of polished surfaces of coal. Fuel, 62(11): 1347-1350.

Briggs, H. and Sinha, R.P., 1932. Expansion and contraction of coal caused respectively by the sorption and discharge of gas. Proceedings of the Royal Society of Edinburgh, 53: 48-53.

Busch, A. and Gensterblum, Y., 2011. CBM and CO_2-ECBM related sorption processes in coal: A review. International Journal of Coal Geology, 87(2): 49-71.

Busch, A., Gensterblum, Y. and Krooss, B.M., 2003. Methane and CO2 sorption and desorption measurements on dry Argonne premium coals: pure components and mixtures. International Journal of Coal Geology, 55: 205-224.

Busch, A., Gensterblum, Y., Krooss, B.M. and Littke, R., 2004. Methane and carbon dioxide adsorption–diffusion experiments on coal: upscaling and modeling. International Journal of Coal Geology, 60: 151-168.

Busch, A., Gensterblum, Y., Krooss, B.M. and Siemons, N., 2006. Investigation of high-pressure selective adsorption/desorption behaviour of CO2 and CH4 on coals: An experimental study. International Journal of Coal Geology, 66: 53-68.

Bustin, R.M., Cameron, A.R., Grieve, D.A. and Kalkreuth, W.D., 1985. Coal petrology: its principles, methods, and applications. Geological Association of Canada; Short Course Notes (8-10 May 1983), 3, Victoria, Britisch Columbia, 230 pp.

Butt, H.-J., Graf, K. and Kappl, M., 2003. Physics and Chemistry of Interfaces. Wiley-VCN Verlag GmbH & Co KGaA, Weinheim, 361 pp.

Cases, J.M. et al., 1992. Mechanism of adsorption and desorption of water vapor by homoionic montmorillonite. 1. The sodium-exchanged form. Langmuir, 8(11): 2730-2739.

Ceglarska-Stefanska, G. and Czaplinski, A., 1991. The effect of limitation free expansion of hard coal on the sorption of carbon dioxide. Archieves of Mining Science, 36(4): 369-378.

Ceglarska-Stefanska, G. and Czaplinski, A., 1993. Correlation between sorption and dilatometric processes in hard coals. Fuel, 72: 413-417.

Cervik, J., 1969. Behaviour of coal-gas reservoirs, US Department of the Interior; Bureau of Mines.

Chaback, J.J., Morgan, W.D. and Yee, D., 1996. Sorption of nitrogen, methane, carbon dioxide and their mixtures on bituminous coals at in-situ conditions. Fluid Phase Equilibria, 117: 289-296.

Cheng, A.H.-D., 1997. Material coefficients of anisotropic poroelasticity. International Journal of Rock Mechanics and Mining Sciences, 34(2): 199-205.

Chikatamarla, L., Cui, X. and Bustin, R.M., 2004. Implications of volumetric swelling and shrinkage of coal in sequestration of acid gases, International Coalbed Methane Symposium, Tuscaloosa, Alabama, USA, pp. 1-22.

Clarkson, C.R., Bustin, R.M. and Levy, J.H., 1997. Application of the mono/multilayer and adsorption potential theories to coal methane adsorption isotherms at elevated temperature and pressure. Carbon, 35(12): 1689-1705.

Clarkson, C.R., Pan, Z., Palmer, I. and Harpalani, S., 2010. Predicting Sorption-Induced Strain and Permeability Increase With Depletion for Coalbed-Methane Reservoirs. SPE Journal, 15(1): 152-159.

Commission of the European Communities, 2008. Proposal for a decision of the European Parliament and of the Council on the effort of Member States to reduce their greenhouse gas emissions to meet the Community's greenhouse gas emission reduction commitments up to 2020. Commission of the European Communities, Brussels.

Condon, J.B., 2006. Surface Area and Porosity Determinations by Physisorption, Measurements and Theory. Elsevier, 274 pp.

Cui, X. and Bustin, R.M., 2005. Volumetric strain associated with methane desorption and its impact on coalbed gas production from deep coal seams. AAPG Bulletin, 89(9): 1181-1202.

Cui, X., Bustin, R.M. and Chikatamarla, L., 2007. Adsorption-induced coal swelling and stress: Implications for methane production and acid gas sequestration into coal seams. Journal of Geophysical Research, 112: B10202.

Cui, X., Bustin, R.M. and Dipple, G., 2004. Selective transport of CO2, CH4, and N2 in coals: insights from modeling of experimental gas adsorption data. Fuel, 83: 293-303.

Davison, J., Freund, P. and Smith, A., 2001. Putting carbon back into the ground, International Energy Agency.

Day, S., Fry, R. and Sakurovs, R., 2008. Swelling of Australian coals in supercritical CO_2. International Journal of Coal Geology, 74(1): 41-52.

Day, S., Fry, R., Sakurovs, R. and Weir, S., 2010. Swelling of Coals by Supercritical Gases and Its Relationship to Sorption. Energy & Fuels, 24(4): 2777-2783.

Deisman, N., Gentzis, T. and Chalaturnyk, R.J., 2008. Unconventional geomechanical testing on coal for coalbed reservoir well design: The Alberta Foothills and Plains. International Journal of Coal Geology, 75(1): 15-26.

Detournay, E. and Cheng, A.H.-D., 1993. Fundamentals of Poroelasticity. In: C. Fairhurst (Editor), Comprehensive Rock Engineering: Principles, Practice and Projects, Vol. II, Analysis and Design Method. Pergamon, pp. 113-171.

Dormans, H.N.M., Huntjens, F.J. and van Krevelen, D.W., 1957. Chemical structure and properties of coal XX - Composition of the individual macerals (Vitrinites, Fusinites, Micrinites and Exinites). Fuel, 36: 321-339.

Du, J. and Olson, J.E., 2001. A poroelastic reservoir model for predicting subsidence and mapping subsurface pressure fronts. Journal of Petroleum Science and Engineering, 30(3-4): 181-197.

Durucan, S., Ahsanb, M. and Shia, J.-Q., 2009. Matrix shrinkage and swelling characteristics of European coals. Energy Procedia, 1(1): 3055-3062.

Durucan, S. and Edwards, J.S., 1986. The effects of stress and fracturing on permeability of coal. Mining Science and Technology, 3: 205-216.

Elder, C.H., 1969. Use of vertical boreholes for assisting ventilation of longwall gob areas. Technical Progress Report 13, US Bureau of Mines, Washington.

Everett, D.H. and Powl, J.C., 1976. Adsorption in slit-like and cylindrical micropores in the henry's law region. A model for the microporosity of carbons. Journal of the Chemical Society, Faraday Transactions 1: Physical Chemistry in Condensed Phases, 72: 619-636.

Every, R.L. and Dell'osso Jr., L., 1972. A new technique for the removal of methane from coal. CIM Bulletin, 65: 143-150.

Feuerstein, S. and John, I.W., 1969. Stress-induced desorption from aluminium, magnesium, and molybdenum. Journal of Applied Physics, 40(8): 3334-3339.

Fitzgerald, J.E. et al., 2005. Adsorption of methane, nitrogen, carbon dioxide and their mixtures on wet Tiffany coal. Fuel, 84: 2351-2363.

French, D.C., Dieckman, S.L. and Botto, R.E., 1993. Three-dimensional NMR microscopic imaging of coal swelling in pyridine. Energy & Fuels, 7(1): 90-96.

Fry, R., Day, S. and Sakurovs, R., 2009. Moisture-Induced Swelling of Coal. International Journal of Coal Preparation and Utilization, 29(6): 298 - 316.

Fulton, P.F., Parente, C.A., Rogers, B.A., Shah, N. and Reznik, A.A., 1980. A laboratory investigation of enhanced recovery of methane from coal by carbon dioxide injection, SPE/DOE Symposium on Unconventional Gas Recovery, Pittsburg.

Gamson, P.D., Beamish, B.B. and Johnson, D.P., 1993. Coal microstructure and micropermeability and their effects on natural gas recovery. Fuel, 72: 87-99.

Gathitu, B.B., Chen, W.-Y. and McClure, M., 2009. Effects of Coal Interaction with Supercritical CO2: Physical Structure. Industrial & Engineering Chemistry Research, 48(10): 5024-5034.

Gensterblum, Y. et al., 2010. European inter-laboratory comparison of high pressure CO_2 sorption isotherms II: Natural coals. International Journal of Coal Geology, 84(2): 115-124.

Gensterblum, Y. et al., 2009. European inter-laboratory comparison of high pressure CO2 sorption isotherms. I: Activated carbon. Carbon, 47(13): 2958-2969.

Gentzis, T., Deisman, N. and Chalaturnyk, R.J., 2007. Geomechanical properties and permeability of coals from the Foothills and Mountain regions of western Canada. International Journal of Coal Geology, 69(3): 153-164.

Goodman, A.L. et al., 2007. Inter-laboratory comparison II: CO_2 isotherms measured on moisture-equilibrated Argonne Premium Coals at 55°C and 15 MPa. International Journal of Coal Geology, 72(3-4): 163-164.

Goodman, A.L. et al., 2004. An inter-laboratory comparison of CO_2 isotherms measured on Argonne Premium Coal samples. Energy & Fuels, 18: 1175-1182.

Goodman, A.L., Campus, L.M. and Schroeder, K.T., 2005. Direct evidence of carbon dioxide sorption on Argonne Premium Coals using attenuated total reflectance-Fourier Transform Infrared spectroscopy. Energy & Fuels, 19: 471-476.

Goodman, A.L., Favors, R.N. and Larsen, J.W., 2006. Argonne Coal structure rearrangement caused by sorption of CO2. Energy & Fuels, 20: 2537-2543.

Gruszkiewicz, M.S. et al., 2009. Adsorption kinetics of CO2, CH4, and their equimolar mixture on coal from the Black Warrior Basin, West-Central Alabama. International Journal of Coal Geology, 77(1-2): 23-33.

Hall, F.E., Zhou, C., Gasem, K.A.M., Robinson Jr., R.L. and Yee, D., 1994. Adsorption of pure methane, nitrogen and carbon dioxide and their binary mixtures on the Wet Fruitland Coal, SPE Eastern Regional Meeting & Exhibition, Charleston, West Virginia, USA, pp. 329-344.

Harpalani, S., 1988. Specimen preperation for testing coal properties. International Journal of Rock Mechanics and Mining Science & Geomechanical Abstracts, 25(5): 327-330.

Harpalani, S. and Chen, G., 1997. Influence of gas production induced volumetric strain on permeability of coal. Geotechnical and Geological Engineering, 15: 303-325.

Harpalani, S. and Mitra, A., 2010. Impact of CO_2 Injection on Flow Behavior of Coalbed Methane Reservoirs. Transport in Porous Media, 82(1): 141-156.

Harpalani, S. and Schraufnagel, R.A., 1990. Shrinkage of coal matrix with release of gas and its impact on permeability of coal. Fuel, 69: 551-556.

Heidug, W.K. and Wong, S.-W., 1996. Hydration swelling of water-absorbing rocks: A constitutive model. International Journal for Numerical and Analytical Methods in Geomechanics, 20: 403-430.

Hile, M.L., 2006. CO_2 sorption by Pittsburgh-seam coal subjected to confining pressure, The Pennsylvania State University, University Park, 102 pp.

Hill, T.L., 1986. An Introduction to Statistical Thermodynamics. Dover Publications, Inc., New York, 508 pp.

Hirsch, P.B., 1954. X-ray scattering from coals. Proceedings of the Royal Society of London. Series A, Mathematical and Physical Sciences, 226(1165): 143-169.

Hol, S., Peach, C.J. and Spiers, C.J., 2011a. Applied stress reduces the CO_2 sorption capacity of coal. International Journal of Coal Geology, 85(1): 128-142.

Hol, S., Peach, C.J. and Spiers, C.J., 2011b. A new experimental method to determine the CO_2 sorption capacity of coal. Energy Procedia, 4: 3125-3130.

Hol, S. and Spiers, C.J., submitted. Competition between adsorption-induced swelling and elastic compression in coal at CO_2 pressures up to 100 MPa. Journal of the Mechanics and Physics of Solids.

Howell, P.G.T. and Boyde, A., 1999. Surface roughness of preparations for backscattered electron-scanning electron microscopy: The image differences and their monte carlo simulation. Scanning, 21(6): 361-367.

Hower, J.C., 2008. Maceral/ microlithotype partitioning with particle size of pulverized coal: Examples from power plants burning Central Appalachian and Illinois basin coals. International Journal of Coal Geology, 73(3-4): 213-218.

Huang, H., Wang, K., Bodily, D.M. and Hucka, V.J., 1995. Density measurements of Argonne Premium coal samples. Energy & Fuels, 9(1): 20-24.

IPCC, 2007. Climate Change 2007: Synthesis Report. In: Core Writing Team, R.K. Pachauri and A. Reisinger (Editors), Contribution of Working Groups I, II and III to the Fourth Assessment Report of the Intergovernmental Panel on Climate Change. IPCC, Geneva, Switzerland, pp. 104.

Israelachvili, J., 1992. Intermolecular & Surface Forces. Academic Press Limited, London, 450 pp.

Israelachvili, J.N. and Pashley, R.M., 1983. Molecular layering of water at surfaces and origin of repulsive hydration forces. Nature, 306(5940): 249-250.

Iwai, Y., Amiya, M., Murozono, T., Arai, Y. and Sakanishi, K., 1998. Drying of coals by using supercritical carbon dioxide. Industrial and Engineering Chemistry Research, 37(7): 2893-2896.

Karacan, C.O., 2003. Heterogeneous sorption and swelling in a confined and stressed coal during CO_2 injection. Energy & Fuels, 17(6): 1595-1608.

Karacan, C.O., 2007. Swelling-induced volumetric strains internal to a stressed coal associated with CO_2 sorption. International Journal of Coal Geology, 72: 209-220.

Karacan, C.O. and Mitchell, G.D., 2003. Behavior and effect of different coal microlithotypes during gas transport for carbon dioxide sequestration into coal seams. International Journal of Coal Geology, 53: 201-217.

Karacan, C.O. and Okandan, E., 2001. Adsorption and gas transport in coal microstructure: investigation and evaluation by quantitative X-ray CT imaging. Fuel, 80(4): 509-520.

Kelemen, S.R. and Kwiatek, L.M., 2009. Physical properties of selected block Argonne Premium bituminous coal related to CO_2, CH_4, and N_2 adsorption. International Journal of Coal Geology, 77(1-2): 2-9.

Kelly, A.A., Groves, G.W. and Kidd, P., 2000. Crystallography and Crystal Defects. John Wiley & Sons.

Kemmere, M.F. and Meyer, T. (Editors), 2005. Supercritical carbon dioxide in polymer reaction engineering. Wiley-VCH, Weinheim.

Khan, M.R. and Jenkins, R.G., 1985. Thermoplastic properties of coal at elavated pressures effect of gas atmospheres, Coal Science: 3rd International Conference, Sidney, Australia, pp. 903-906.

Kim, A.G., 1973. The composition of coalbed gas. RI 7762, US Bureau of Mines, Washington.

Ko, H.-Y. and Gerstle, K.H., 1976. Elastic properties of two coals. International Journal of Rock Mechanics and Mining Sciences & Geomechanical Abstracts, 13: 81-90.

Kolak, J.J. and Burruss, R.C., 2006. Geochemical investigation of the potential for mobilizing non-methane hydrocarbons during carbon dioxide storage in deep coal beds. Energy & Fuels, 20(2): 566-574.

Kramer, D. and Weissmüller, J., 2007. A note on surface stress and surface tension and their interrelation via Shuttleworth's equation and the Lippmann equation. Surface Science, 601(14): 3042-3051.

Krooss, B.M. et al., 2002. High-pressure methane and carbon dioxide adsorption on dry and moisture-equilibrated Pennsylvanian coals. International Journal of Coal Geology, 51: 69-92.

Landau, L.D. and Lifshitz, E.M., 1986. Theory of Elasticity. Elsevier, 187 pp.

Langmuir, I., 1918. The adsorption of gases on plane surfaces of glass, mica and platinum. Journal of the American Chemical Society, 40(9): 1361-1403.

Larsen, J.W., 2004. The effects of dissolved CO_2 on coal structure and properties. International Journal of Coal Geology, 57: 63-70.

Larsen, J.W., Flowers, R.A. and Hall, P.J., 1997. Structural rearrangement of strained coals. Energy & Fuels, 11(5): 998-1002.

Laubach, S.E., Marrett, R.A., Olsen, J.E. and Scott, A.R., 1998. Characteristics and origins of coal cleat: A review. International Journal of Coal Geology, 35: 175-207.

Lehner, F., 1990. Thermodynamics of rock deformation by pressure solution. In: D.J. Barber and P.G. Meredith (Editors), Deformation Processes in Minerals, Ceramics and Rocks. Unwin Hyman Ltd., London, pp. 296-333.

Levine, J.R., 1996. Model study of the influence of matrix shrinkage on absolute permeability of coalbed reservoirs. Geological Society Special Publication, 109: 197-212.

Li, H., Shimada, S. and Zhang, M., 2004. Anisotropy of gas permeability associated with cleat pattern in a coal seam of the Kushiro coalfield in Japan. Environmental Geology, 47: 45-50.

Liu, H.-H. and Rutqvist, J., 2010. A New Coal-Permeability Model: Internal Swelling Stress and Fracture–Matrix Interaction. Transport in Porous Media, 82(1): 157-171.

Low, P.F., 1987. Structural component of the swelling pressure of clays. Langmuir, 3(1): 18-25.

Majewska, Z., Majewski, S. and Ziętek, J., 2010. Swelling of coal induced by cyclic sorption/desorption of gas: Experimental observations indicating changes in coal structure due to sorption of CO_2 and CH_4. International Journal of Coal Geology, 83(4): 475-483.

Majewska, Z. and Ziętek, J., 2007. Changes of acoustic emission and strain in hard coal during gas sorption-desorption cycles. International Journal of Coal Geology, 70: 305-312.

Mares, T.E. et al., 2009. Assessing the potential for CO2 adsorption in a subbituminous coal, Huntly Coalfield, New Zealand, using small angle scattering techniques. International Journal of Coal Geology, 77(1-2): 54-68.

Masel, R.L., 1996. Principles of adsorption and reaction on solid surfaces. John Wiley & Sons Inc., New York, 818 pp.

Mastalerz, M., Drobniak, A., Walker, R. and Morse, D., 2010. Coal lithotypes before and after saturation with CO_2; insights from micro- and mesoporosity, fluidity, and functional group distribution. International Journal of Coal Geology, 83(4): 467-474.

Mavor, M.J., Gunter, W.D. and Robinson, R.L., 2004. Alberta multiwell micro-pilot testing for CBM properties, enhanced methane recovery and CO_2 storage potential, SPE Annual Technical Conference and Exhibition, Houston, Texas, USA, pp. 1-15.

Mazzotti, M., Pini, R. and Storti, G., 2009. Enhanced coalbed methane recovery. The Journal of Supercritical Fluids, 47(3): 619-627.

Melnichenko, Y.B., Radlinski, A.P., Mastalerz, M., Cheng, G. and Rupp, J., 2009. Characterization of the CO_2 fluid adsorption in coal as a function of pressure using neutron scattering techniques (SANS and USANS). International Journal of Coal Geology, 77(1-2): 69-79.

Meyers, A.L., 2002. Thermodynamics of adsorption in porous materials. American Institute of Chemical Engineers Journal, 48(1): 145-160.

Mirzaeian, M. and Hall, P.J., 2006. The interactions of coal with CO2 and its effects on coal structure. Energy & Fuels, 20(5): 2022-2027.

Moffat, D.H. and Weale, K.E., 1955. Sorption by coal of methane at high pressures. Fuel, 34: 449-462.

Morcote, A., Mavko, G. and Prasad, M., 2010. Dynamic elastic properties of coal. Geophysics, 75(6): E227-E234.

Muchnik, S.V., 1974. Advance calculation of the methane sorption isotherms of coals. Journal of Mining Sciences, 6: 112-114.

Munro, R.G., 2001. Effective Medium Theory of the Porosity Dependence of Bulk Moduli. Journal of the American Ceramic Society, 84(5): 1190-1192.

Murray, D.K., 1996. Coalbed methane in the USA: analogues for worldwide development. Geological Society, London, Special Publications, 109(1): 1-12.

Nowak, G.J., 2004. Facies studies of bituminous coals in Poland. International Journal of Coal Geology, 58(1-2): 61-66.

Ottiger, S., Pini, R., Storti, G. and Mazzotti, M., 2008. Measuring and Modeling the Competitive Adsorption of CO2, CH4, and N2 on a Dry Coal. Langmuir, 24(17): 9531-9540.

Ozdemir, E., Morsi, B.I. and Schroeder, K., 2003. Importance of volume effects to adsorption isotherms of carbon dioxide on coals. Langmuir, 19(23): 9764-9773.

Ozdemir, E., Schroeder, K. and Morsi, B.I., 2002. Effect of swelling on the adsorption isotherm of carbon dioxide on coal. Preprints of papers division of fuel chemistry, 47(1): 12-13.

Palmer, I., 2009. Permeability changes in coal: Analytical modeling. International Journal of Coal Geology, 77(1-2): 119-126.

Palmer, I.D. and Mansoori, J., 1998. How permeability depends on stress and pore pressure in coalbeds: A new model. SPE Reservoir Evaluation & Engineering, December: 539-544.

Pan, Z. and Connell, L.D., 2007. A theoretical model for gas adsorption-induced coal swelling. International Journal of Coal Geology, 69: 243-252.

Pan, Z. and Connell, L.D., 2011. Modelling of anisotropic coal swelling and its impact on permeability behaviour for primary and enhanced coalbed methane recovery. International Journal of Coal Geology, 85(3-4): 257-267.

Pan, Z., Connell, L.D. and Camilleri, M., 2010. Laboratory characterisation of coal reservoir permeability for primary and enhanced coalbed methane recovery. International Journal of Coal Geology, 82(3-4): 252-261.

Pegoraro, M., Penati, A. and Clerici, P., 1977. Porosity of membranes consisting of hydrophilic domains in a hydrophobic matrix. Polymer, 18(8): 831-834.

Perkins, J.H. and Cervik, J., 1969. Sorption investigations of methane on coal. Technical Progress Report 14, US Bureau of Mines, Washington.

Pini, R., Ottiger, S., Burlini, L., Storti, G. and Mazzotti, M., 2009. Role of adsorption and swelling on the dynamics of gas injection in coal. J. Geophys. Res., 114.

Pini, R., Ottiger, S., Burlini, L., Storti, G. and Mazzotti, M., 2010. Sorption of carbon dioxide, methane and nitrogen in dry coals at high pressure and moderate temperature. International Journal of Greenhouse Gas Control, 4(1): 90-101.

Pini, R., Ottiger, S., Rajendran, A., Storti, G. and Mazzotti, M., 2006. Reliable measurement of near-critical adsorption by gravimetric method. Adsorption, 12(5): 393-403.

Pone, J.D.N., Halleck, P.M. and Mathews, J.P., 2009a. 3D characterization of coal strains induced by compression, carbon dioxide sorption, and desorption at in-situ stress conditions. International Journal of Coal Geology, 82(3-4): 262-268.

Pone, J.D.N., Halleck, P.M. and Mathews, J.P., 2009b. Sorption capacity and sorption kinetic measurements of CO_2 and CH_4 in confined and unconfined bituminous coal. Energy & Fuels, 23(9): 4688-4695.

Pourier, J.P., 1985. Creep of Crystals. Cambridge University Press, 260 pp.

Prausnitz, J.M., Lichtenthaler, R.N. and Gomes de Azevedo, E., 1986. Molecular thermodynamics of fluid-phase equilibria. Prentice-Hall, Inc., New Jersey, 600 pp.

Pride, S.R. and Berryman, J.G., 1998. Connecting theory to experiment in poroelasticity. Journal of the Mechanics and Physics of Solids, 46(4): 719-747.

Prinz, D. and Littke, R., 2005. Development of the micro- and ultramicroporous structure of coals with rank as deduced from the accessibility to water. Fuel, 84: 1645-1652.

Prinz, D., Pyckhout-Hintzen, W. and Littke, R., 2004. Development of the meso- and macroporous structure of coals with rank as analysed with small angle neutron scattering and adsorption experiments. Fuel, 83: 547-556.

Puri, R. and Yee, D., 1990. Enhanced coalbed methane recovery, SPE Annual Technical Conference and Exhibition, New Orleans, Louisiana.

Radlinski, A.P. et al., 2009a. Dynamic Micromapping of CO_2 Sorption in Coal. Langmuir, 25(4): 2385-2389.

Radlinski, A.P., Busbridge, T.L., Gray, E.M.A., Blach, T.P. and Cookson, D.J., 2009b. Small angle X-ray scattering mapping and kinetics study of sub-critical CO_2 sorption by two Australian coals. International Journal of Coal Geology, 77(1-2): 80-89.

Radlinski, A.P. et al., 2004. Application of SAXS and SANS in evaluation of porosity, pore size distribution and surface area of coal. International Journal of Coal Geology, 59: 245-271.

Ranjith, P.G., Jasinge, D., Choi, S.K., Mehic, M. and Shannon, B., 2010. The effect of CO_2 saturation on mechanical properties of Australian black coal using acoustic emission. Fuel, 89(8): 2110-2117.

Reeves, S.R., 2001. Geological sequestration of CO_2 in deep, unmineable coalseams: An integrated research and commercial-scale field demonstration project, SPE Annual Technical Conference and Exhibition, New Orleans, Louisiana, USA, pp. 1-10.

Renard, F.o. and Ortoleva, P., 1997. Water films at grain-grain contacts: Debye-Hückel, osmotic model of stress, salinity, and mineralogy dependence. Geochimica et Cosmochimica Acta, 61(10): 1963-1970.

Reucroft, P.J. and Patel, K.B., 1986. Gas-induced swelling in coal. Fuel, 65: 816-820.

Reznik, A.A., Singh, P.K. and Foley, W.L., 1984. An analysis of the effect of CO2 injection on the recovery of in situ methane from bituminous coal: An experimental simulation. SPE Journal, October: 521-528.

Rice, D.D., Clayton, J.L. and Pawlewicz, M.J., 1989. Characterization of coal-derived hydrocarbons and source-rock potential of coal beds, San Juan Basin, New Mexico and Colorado, U.S.A. International Journal of Coal Geology, 13(1-4): 597-626.

Robertson, E.P. and Christiansen, R.L., 2005. Modelling permeability in coal using sorption-induced strain data, SPE Annual Conference and Exhibition, Dallas, Texas, USA, pp. 1-10.

Romanov, V., Soong, Y. and Schroeder, K., 2006a. Volumetric effects in coal sorption capacity measurements. Chemical Engineering Technology, 29(3): 368-374.

Romanov, V.N., Goodman, A.L. and Larsen, J.W., 2006b. Errors in CO2 adsorption measurements caused by coal swelling. Energy & Fuels, 20(1): 415-416.

Ross, D.J.K. and Bustin, M.R., 2007. Impact of mass balance calculations on adsorption capacities in microporous shale gas reservoirs. Fuel, 86(17-18): 2696-2706.

Rouzaud, J.-N., 1990. Contribution of Transmission Electron Microscopy to the study of the coal carbonisation processes. Fluid Processing Technology, 24: 55-69.

Ruff, O. and Geselle, P., 1936. Das Verhalten von Steinkohlen bei der Aufnahme und Abgebe von Kohlensaeure. Zeitschrift für das Berg-, Hütten-, und Salinenwesen im Deutschen Reich, 84(10): 425-436.

Sakurovs, R., Day, S. and Weir, S., 2009. Causes and consequences of errors in determining sorption capacity of coals for carbon dioxide at high pressure. International Journal of Coal Geology, 77(1-2): 16-22.

Sakurovs, R., Day, S., Weir, S. and Duffy, G.J., 2007. Application of a modified Dubinin-Radushkevich equation to adsorption of gases by coals under supercritical conditions. Energy & Fuels, 21(2): 992-997.

Scherer, G.W., 1986. Dilatation of porous glass. Journal of the American Ceramic Society, 69(6): 473-480.

Schroeder, K., Ozdemir, E. and Morsi, B.I., 2002. Adsorption capacity of carbon dioxide on Argonne Premium coals. Preprints of Papers Division of Fuel Chemistry, 47(1): 10-11.

Schutjens, P.M.T.M., 1991. Experimental compaction of quartz sand at low effective stress and temperature conditions. Journal of the Geological Society, 148(3): 527-539.

Shi, J.Q. and Durucan, S., 2003. A bidisperse pore diffusion model for methane displacement desorption in coal by CO2 injection. Fuel, 82: 1219-1229.

Shi, J.Q. and Durucan, S., 2005. A model for changes in coalbed permeability during primary and enhanced methane recovery. SPE Reservoir Evaluation & Engineering: 291-299.

Shibaoka, M., Stephens, J.F. and Russel, M.J., 1979. Microscopic observations of the swelling of a high-volatile bituminous coal in response to organic solvents. Fuel, 58(7): 515-522.

Siemons, N. and Busch, A., 2007. Measurement and interpretation of supercritical CO_2 sorption on various coals. International Journal of Coal Geology, 69: 229-242.

Sircar, S., 1999. Gibbsian surface excess for gas adsorption - revisited. Industrial & Engineering Chemistry Research, 38(10): 3670-3682.

Siriwardane, H. et al., 2009. Influence of carbon dioxide on coal permeability determined by pressure transient methods. International Journal of Coal Geology, 77(1-2): 109-118.

Solano-Acosta, W., Mastalerz, M. and Schimmelmann, A., 2007. Cleats and their relation to geologic lineaments and coalbed methane potential in Pennsylvanian coals in Indiana. International Journal of Coal Geology, 72(3-4): 187-208.

Span, R. and Wagner, W., 1996. A new equation of state for carbon dioxide covering the fluid region from the triple-point temperature to 1100 K at pressures up to 800 MPa. Journal of Physical and Chemical Reference Data, 25(6): 1509-1596.

Steriotis, T.A. et al., 2008. In situ neutron diffraction study of adsorbed carbon dioxide in a nanoporous material: Monitoring the adsorption mechanism and the structural characteristics of the confined phase. Physical Review B (Condensed Matter and Materials Physics), 78(11): 115424-10.

Stevenson, M.D., Pinczewski, W., Somers, M. and Bagio, S., 1991. Adsorption/desorption of multicomponent gas mixtures on coal at in-seam conditions, SPE Asia-Pacific Conference, Perth, Western Australia.

Strapoc, D., Schimmelmann, A. and Mastalerz, M., 2006. Carbon isotopic fractionation of CH4 and CO2 during canister desorption of coal. Organic Geochemistry, 37: 152-164.

Tambach, T.J., Mathews, J.P. and van Bergen, F., 2009. Molecular Exchange of CH_4 and CO_2 in Coal: Enhanced Coalbed Methane on a Nanoscale. Energy & Fuels, 23(10): 4845-4847.

Terry, R.C., 1978. Producing methane from coal in situ. In Situ Technology, Inc., Denver, CO, United States of America, pp. 8.

Thompson, M. and Willis, J.R., 1991. A Reformation of the Equations of Anisotropic Poroelasticity. Journal of Applied Mechanics, 58(3): 612-616.

Tuin, G. and Stein, H.N., 1995. The Excess Gibbs Free Energy of Adsorption of Sodium Dodecylbenzenesulfonate on Polystyrene Particles. Langmuir, 11(4): 1284-1290.

Unsworth, J.F., Fowler, C.S. and Jones, L.F., 1989. Moisture in coal : 2. Maceral effects on pore structure. Fuel, 68(1): 18-26.

USEIA, 2010. Annual U.S. Coalbed Methane Production 1990-2009. US Energy Information Administration.

van Bergen, F., Hol, S. and Spiers, C., 2009a. Stress-strain response of pre-compacted granular coal samples exposed to CO_2, CH_4, He and Ar. In: F. van Bergen (Editor), Effect of coal matrix swelling on Enhanced Coalbed Methane production - A field and laboratory study. Utrecht University, Utrecht, pp. 119-144.

van Bergen, F., Pagnier, H. and Krzystolik, P., 2006. Field experiment of enhanced coalbed methane-CO_2 in the upper Silesian basin of Poland. Environmental Geosciences, 13(3): 201-224.

van Bergen, F., Spiers, C., Floor, G. and Bots, P., 2009b. Strain development in unconfined coals exposed to CO_2, CH_4 and Ar: Effect of moisture. International Journal of Coal Geology, 77(1-2): 43-53.

van der Meer, B. and Egberts, P., 2008. Calculating subsurface CO_2 storage capacities. The Leading Edge, 27(4): 502.

van Hemert, P., Bruining, H., Rudolph, E.S.J., Wolf, K.-H.A.A. and Maas, J.G., 2009. Improved manometric setup for the accurate determination of supercritical carbon dioxide sorption. Review of Scientific Instruments, 80(3): 035103.

van Krevelen, D.W., 1993. Coal: Typology - Physics - Chemistry - Constitution. Elsevier.

van Wageningen, W.F.C., Wentinck, H.M. and Otto, C., 2009. Report and modeling of the MOVECBM field tests in Poland and Slovenia. Energy Procedia, 1(1): 2071-2078.

Vandamme, M., Brochard, L., Lecampion, B. and Coussy, O., 2010. Adsorption and strain: The CO_2-induced swelling of coal. Journal of the Mechanics and Physics of Solids, 58(10): 1489-1505.

Viete, D.R. and Ranjith, P.G., 2006. The effect of CO_2 on the geomechanical and permeability behaviour of brown coal: Implications for coal seam CO_2 sequestration. International Journal of Coal Geology, 66: 204-216.

Viete, D.R. and Ranjith, P.G., 2007. The mechanical behaviour of coal with respect to CO_2 sequestration in deep coal seams. Fuel, 86(17-18): 2667-2671.

Walker Jr., P.L., Verma, S.K., Rivera-Utrilla, J. and Davis, A., 1988. A direct measurement of expansion in coals and macerals induced by carbon dioxide and methanol. Fuel, 67: 719-726.

Walsh, J.B., 1965. The Effect of Cracks on the Compressibility of Rock. J. Geophys. Res., 70(2): 381-389.

Wang, H.F., 2000. Theory of linear poroelasticity with applications to geomechanics and hydrogeology. Princeton University Press, Princeton, 287 pp.

Wang, S., Elsworth, D. and Liu, J., 2011. Permeability evolution in fractured coal: The roles of fracture geometry and water-content. International Journal of Coal Geology, 87(1): 13-25.

White, C.M. et al., 2005. Sequestration of carbon dioxide in coal with enhanced coalbed methane recovery - A review. Energy & Fuels, 19(3): 659-724.

Wold, M.B., Connell, L.D. and Choi, S.K., 2008. The role of spatial variability in coal seam parameters on gas outburst behaviour during coal mining. International Journal of Coal Geology, 75(1): 1-14.

Yamaguchi, S., Ohga, K., Fujioka, M., Nako, M. and Muto, S., 2006. Field experiment of Japan CO_2 geosequestration in coal seams project (JCOP). In: J.J. Gale, N. Rokke, P. Zweigel and H. Svenson (Editors), 8th International Conference on Greenhouse Gas Control Technologies. Elsevier, Trondheim, Norway.

Yi, J., Akkutlu, I.Y., Karacan, C.Ö. and Clarkson, C.R., 2009. Gas sorption and transport in coals: A poroelastic medium approach. International Journal of Coal Geology, 77(1-2): 137-144.

Yu, H., Guo, W., Cheng, J. and Hu, Q., 2008. Impact of experimental parameters for manometric equipment on CO2 isotherms measured: Comment on "Inter-laboratory comparison II: CO2 isotherms measured on moisture-equilibrated Argonne premium coals at 55°C and up to 15 MPa" by Goodman et al. (2007). International Journal of Coal Geology, 74(3-4): 250-258.

Zhang, J., Bai, M. and Roegiers, J.C., 2003. Dual-porosity poroelastic analyses of wellbore stability. International Journal of Rock Mechanics and Mining Sciences, 40(4): 473-483.

Zhang, J. et al., 2002. Study on intermolecular interactions in supercritical fluids by partial molar volume and isothermal compressibility. The Journal of Supercritical Fluids, 22(1): 15-19.

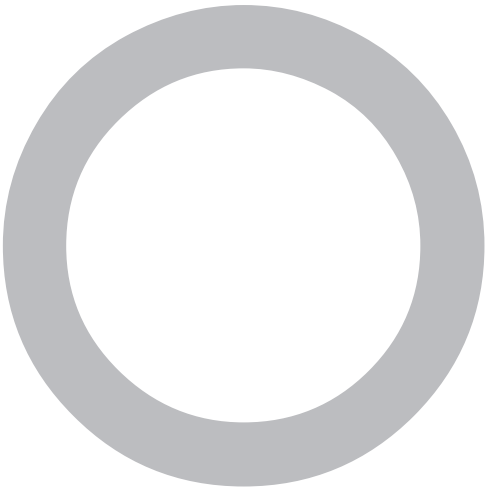

Summary

Summary

Coal swells when it adsorbs CO_2. The stress-strain behaviour associated with adsorption is of key importance in determining the feasibility of extracting methane from coal via Enhanced Coalbed Methane production. ECBM involves injection of preferentially sorbing carbon dioxide (CO_2) into the target coal seam, coupled with recovery of desorbing methane (CH_4). It and thus offers not only a promising way of producing CH_4 from coalbeds but also a potential means of geologically storing CO_2, and hence reducing CO_2 emissions. However, almost all field experiments performed to date, show major injectivity reductions, suggesting that a strong coupling exists between CO_2 sorption, changes in the mechanical state of the coal matrix and changes in the transport properties of the system. Unfortunately, the fundamental physical processes controlling this coupling are very poorly understood.

The motivation for the present thesis, introduced in **Chapter 1**, was to help fill this knowledge gap, providing a basis to advance existing ECBM reservoir "simulators" towards predictive reservoir models. The approach adopted involves both theoretical developments and mechanical tests, performed at 40 °C and CO_2 pressures in the range 0-100 MPa. All experiments were performed on Brzeszcze high volatile bituminous coal (seam 364) obtained from the ECBM pilot project, RECOPOL, conducted in Poland in 2004-2005.

The first issue addressed in this thesis (**Chapter 2**) is the direct effect of the application of an effective stress, over and above an applied CO_2 pressure, on the adsorption of CO_2 by coal matrix material. To investigate this, I performed one-dimensional (oedometric) compression experiments on pre-compacted, porous aggregates of Brzeszcze matrix material at CO_2 pressures of 10-20 MPa. The experiments showed that the application of an effective stress of 35 MPa results in a reduction of CO_2 sorption capacity by 5-50 %. This effect was accompanied by a reduction in apparent axial stiffness of the samples by about 33 % from 1.52 to 0.95 GPa. The processes responsible for desorption and the change in apparent stiffness were investigated by deriving a thermodynamic model accounting for the *PV*-work term associated with swelling of coal against a hydrostatic stress applied to the solid. The model predicts a similar reduction of adsorption capacity to that determined in the laboratory.

In **Chapter 3**, the volumetric strain response of coal matrix material to CO_2 pressure was investigated under conditions of zero effective stress. Dilatometry experiments were performed, using a high-pressure eddy-current sensor, on mm-scale cylindrical coal matrix samples at a constant temperature of 40 °C and CO_2 pressures up to 100 MPa. The experiments showed that pre-exposed coal matrix samples deform reversibly, but

anisotropically over the range of CO_2 pressures used. Expansion perpendicular to the bedding was about 1.4 times higher than the more or less isotropic expansion measured in the bedding plane. Net volumetric strains were characterised by expansion below 10-20 MPa of CO_2 pressure and contraction at higher CO_2 pressures, demonstrating direct competition between purely adsorption-induced swelling, dominating at low pressures, versus linear elastic compression of the coal matrix, which dominates at high pressures. A combined thermodynamic swelling plus elastic compression model was developed that includes this competitive behaviour, assuming the adsorption-induced swelling to be linearly related to adsorbed CO_2 concentration. Good agreement was found between the model and our experimental data. The total volumetric strain occurring under unconfined conditions can thus be realistically modelled as the sum of an adsorption-related expansion term and an elastic compression term.

An additional issue in determining the coupled stress-strain-adsorption response of coal matrix material exposed to CO_2 is the need to accurately determine sorption capacity. Conventional manometric and gravimetric sorption techniques involve uncertainties that affect the accuracy of determinations of the CO_2 sorption capacity of coal. In **Chapter 4**, we report a new method to determine the total uptake of CO_2 by coal matrix material (*i.e.* the sum of pore filling and adsorption capacity). This method obviates use of the Equation of State (EoS) for CO_2, and requires no volumetric corrections to account for sample swelling. The method involves enclosing an individual CO_2-saturated sample in a ductile metal capsule and capturing its CO_2 content directly. The method yielded Langmuir-like CO_2 uptake curves for the total CO_2 content of the coal matrix material tested. Manometric data for a subset of the samples showed 20-30 % lower mean uptake values. The differences between the two methods are attributed to i) random errors and uncertainties in the EoS in the manometric dataset at low CO_2 pressures (3-9 MPa), and ii) systematic errors, due to erroneous trapping of free CO_2, dominating in the capsule dataset at high CO_2 pressures (>9 MPa). The method proved useful for location-specific sorption determinations at CO_2 pressures below 9 MPa, but improvement of the capsule technique is needed to yield reliable data at high CO_2 pressures.

A general thermodynamic model for the effect of a 3-D stress state on adsorbed CO_2 concentration was developed in **Chapter 5**. The model predicts that application of a general compressive stress state σ_{ij} to the solid framework of the coal matrix material, over and above the fluid pressure P, generates a reduction in the site occupancy, and therefore in adsorbed concentration. This prediction was confirmed by a preliminary hydrostatic experiment performed on a 25 mm cylindrical sample of Brzeszcze coal at 40 °C and at 15 MPa CO_2 pressure, applying an effective hydrostatic stress of 1-35 MPa. The experiment showed that adsorption capacity was reduced by almost 10 % at 25 MPa effective stress. The theory was finally extended to develop a constitutive equation describing the full coupling between stress, strain and adsorption behaviour

of coal matrix material exposed to CO_2. This constitutive equation provides a realistic basis for modelling stress-strain-sorption-permeability evolution and CO_2 movement under *in situ* ECBM conditions, including effects of self-stressing by constrained swelling. The principal conclusion drawn is that while the *in situ* stress initially present in coal seams will significantly reduce the sorption capacity of coal for CO_2 (~10-20%), self-stressing accompanying swelling upon CO_2 injection leads to an even greater effect (up to 30 %) which needs to be taken into account in ECBM reservoir modelling.

Chapter 6 focuses on irreversible side-effects, such as permanent swelling and changes in equilibration time, which may occur in response to the exposure of coal matrix material to CO_2. I attempted to establish the microphysical processes that underlie these effects, in order to predict whether they are likely to occur *in situ*. Dilatometry experiments were performed on mm-scale, fresh coal matrix samples, which were exposed to CO_2 in multiple runs. Substantial hysteresis was observed in expansion versus CO_2 pressure behaviour measured during the first (or second) exposure of the samples to CO_2, accompanied by minor permanent shrinkage, with the largest permanent strain and largest strain hysteresis occurring in the direction perpendicular to the bedding. Moreover, dilatometric equilibration of the samples took three to five times longer in the first than in subsequent CO_2 pressurisation cycles. Microstructural analysis showed that exposure resulted in the formation and propagation of microfractures, mostly delaminating the bedding planes and roughly following maceral interfaces or the maceral fabric. It was inferred that non-uniform access of CO_2, hence non-uniform swelling, plus a differential response of different coal macerals caused the hysteresis, permanent strain and microfracturing in the first or second exposure cycles. The thereby improved accessibility to CO_2 caused the observed decrease in equilibration rate. No evidence was found that CO_2-induced plasticisation of the coal structure played any role in the behaviour observed. Simple mechanical considerations imply that at *in situ* effective stresses, *e.g.* 25-35 MPa at a depth of 1000-1500 m, adsorption-induced microfractures will not form. It is concluded that, at *in situ* stresses, injection of CO_2 into coal, while leading to differential swelling strains within the material, will not generate significant microfracture permeability, and that full penetration by, and equilibration of the coal matrix with CO_2 will generally be prevented.

Chapter 7 summarises this thesis and considers several important implications of the results obtained for ECBM. First, effective *in situ* stresses in the range 25-35 MPa will directly reduce the sorption capacity of the coal matrix significantly. Second, the effect of "self-stressing" as a result of adsorption of CO_2 by coal under the conditions of restricted or zero strain (*i.e.* fully constrained conditions) will more than double the expected *in situ* stresses under typical (E)CBM reservoir conditions. This leads to an additional reduction in CO_2 uptake. Third, the CO_2 access problem remains a major problem for ECBM operations, especially in the case of stiff, highly swelling coals

situated at (unmineable) depth. Major improvements in access to the coal matrix by CO_2 can probably only be achieved by creating space to accommodate coal swelling. The required removal of coal mass, or creation of void volume, may be achievable either by hydrofracturing and injection of solvents to remove either organic or mineral components, by performing active mining of the coal and/or the over- or underlying strata, or possibly by pore pressure depletion of porous sediments enclosing the target coal seams. **Chapter 7** and the thesis as a whole is concluded with a summing up of remaining questions and suggestions for future research.

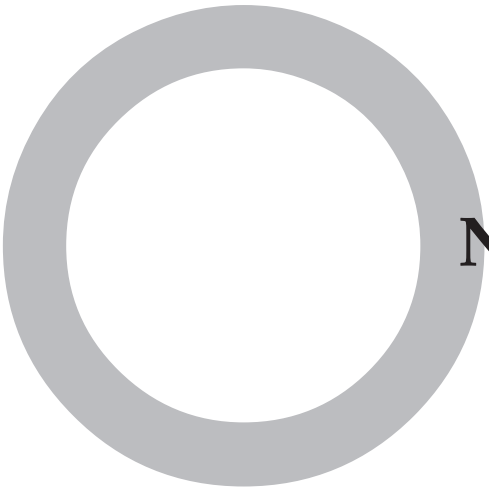

Samenvatting voor een algemeen publiek

Onderdelen van deze samenvatting zijn verschenen als artikel in Ublad 33 (38), de krant van de Universiteit Utrecht. Dit betrof het resultaat van een cursus Wetenschapscommunicatie die gegeven werd door journalist Liesbeth den Bakker.

Samenvatting

Olie- en gasproducenten proberen al enige jaren om koolstofdioxide te injecteren in oude gasvelden. Koolstofdioxide verdwijnt op die manier in de poriën van zandsteenlagen, de plek waar vroeger het aardgas zat. Uit eerste veldprojecten, maar voornamelijk uit laboratoriumexperienten, blijkt dat de ondergrondse opslag van koolstofdioxide in aardlagen mogelijk is, mits deze lagen geologisch geschikt zijn voor de opslag. Ze mogen niet lekken, mogen geen ongewenste chemische reacties aangaan met koolstofdioxide en moeten mechanisch stabiel blijven. Met dat laatste bedoelen we dat koolstofdioxide de laag niet te veel mag laten verzakken of uitzetten.

Samen met Shell, TNO en de EU werkt de Universiteit Utrecht al enige jaren mee aan onderzoek naar een andere mogelijkheid: de injectie van koolstofdioxide in steenkool. Hoewel steenkool voor veel landen nog een brandstof op zich is, ligt het op sommige plaatsen zó diep, dat delven niet mogelijk of niet rendabel is. Op die plekken zou koolstofdioxide kunnen worden opgeslagen.

Steenkool heeft een groot netwerk van verschillende maten poriën en scheurtjes ('cleats'). In de poriën zit vaak aardgas. Dit gas bestaat voor meer dan negentig procent uit methaan (CH_4) dat geadsorbeerd ('geplakt') zit aan de wanden van die poriën, maar ook vrij in de poriën zweeft. Omdat koolstofdioxide sterker adsorbeert dan methaan, kan het methaanmoleculen verdringen. Door de injectie van koolstofdioxide stroomt het methaan door de poriën en breukjes naar het aardoppervlak via een boorput. Op die manier zorgt de opslag van koolstofdioxide in steenkool voor de productie van aardgas.

Toch zitten er een paar haken en ogen aan de opslag in steenkool. Wetenschappers zijn er niet over uit of koolstofdioxide goed injecteerbaar is en of het voldoende hecht aan het porieoppervlak door adsorptie. Om dit goed te bepalen is het van essentieel belang om processen zoals adsorptie, maar ook het volumetrische gedrag of de vervorming van steenkool te begrijpen, in het bijzonder bij de druk en temperatuur condities die in de ondergrond heersen ('*in situ* conditions'). Een factor die daarin mogelijk een belangrijke rol speelt is het effect van spanning ('stress'). Met spanning bedoelen we de extra druk die op de steenkool wordt uitgeoefend door het gewicht van bovenliggende aardlagen. Zolang we de koppeling tussen de effecten van spanning, vervorming en adsorptie niet begrijpen, is een goede voorspellen van de opslagcapaciteit, maar ook de selectie van de juiste injectietechnieken, niet voldoende mogelijk.

Om de koppeling tussen spanning, vervorming en adsorptie te begrijpen, heb ik meer dan vier jaar onderzoek gedaan in het Hoge Druk en Temperatuur Laboratorium (HPT-lab) van de Faculteit Geowetenschappen van de Universiteit Utrecht. Het laboratorium is ideaal voor dit soort problemen, aangezien de experimenten die we

daar uitvoeren nabootsen wat er in een diepliggende steenkoollaag plaatsvindt. Zo staan er compactieapparaten, pompen, gasflessen en ovens, waarmee ik koolstofdioxide in de steenkool pers en met de modernste technieken de effecten daarvan meet.

De resultaten van mijn onderzoek naar de koppeling tussen spanning, vervorming en adsorptie laten het volgende zien:

1. Een nieuwe methode om de hoeveelheid koolstofdioxide te bepalen die kan worden opgenomen door steenkool, zonder hier spanning op uit oefenen, presenteer ik in **Chapter 4**. De methode laat op een nieuwe manier zien dat adsorptie verreweg het belangrijkste opnameproces is.
2. De opname van koolstofdioxide door steenkool, zonder hier spanning op uit oefenen, zorgt voor zwelling, die lineair gekoppeld kan worden aan de hoeveelheid adsorptie (**Chapter 3**). Dit geeft aan dat de oorzaak van zwelling in de adsorptie van koolstofdioxide ligt. Om deze relatie te leggen, heb ik wél laten zien dat de gemeten zwelling moet worden gecorrigeerd voor een elastische compressie die veroozaakt wordt door de hoge gasdruk tijdens ons experiment (max. 100 MPa=1000 bar).
3. De spanning die in de ondergrond aanwezig is (door het gewicht van bovenliggende aardlagen) reduceert de hoeveelheid koolstofdioxide die steenkool kan adsorberen met 5-50 %. Dit toon ik aan met experimenten waarin ik het gas uit steenkoolpoeder pers door middel van een stalen zuiger (**Chapter 2**). Thermodynamische berekeningen, die de relatie leggen tussen spanning en adsorptie, laten zien dat dit effect zelfs quantitatief te voorspellen is. Spanning oefent 'arbeid' uit op de steenkool, dat het moelijker maakt voor een koolstofdioxidemolecuul om geadsorbeerd te blijven. Het volledige thermodynamische model wordt afgeleid in **Chapter 5**, en voorspelt dat de adsorptiecapaciteit door spanning wordt verlaagd, maar ook dat de beperkte zwelruimte in de ondergrond er voor zorgt dat zich spanningen ontwikkelen als gevolg van adsorptie en zwelling. Een enkel experiment, uitgevoerd op een stapel steenkoolschijven van 2,5 cm doorsnede en 0,5 cm dik, toont opnieuw aan dat het aanbrengen van spanning op steenkool, in evenwicht met koolstofdioxide, de hoeveelheid adsorptie verlaagt, in dit geval met ongeveer 10 %. De opslagcapaciteit van steenkoollagen in de ondergrond, waar de spanning heerst, is dus substantieel lager dan aanvankelijk gedacht.
4. De experimenten in **Chapter 6** laten zien dat er permanente volumeveranderingen in steenkool plaatsvinden, die veroorzaakt worden door de vorming van kleine, ongevaarlijke breukjes ('microfractures'). Die microbreukjes vormen door verschillen in het specifieke adsorptie- en zwelgedrag van 'maceralen' waaruit steenkool bestaat (maceraal is zoals een mineraal in kristallijne gesteenten), en zorgen ervoor dat gedurende het experiment het steenkoolmateriaal steeds beter toegankelijk wordt voor koolstofdioxide. Omdat door de aanwezigheid van spanning in de ondergrond zulke breukjes moeilijk zullen opengaan, en dus de toegankelijkheid laag blijft, zal een deel van de steenkool niet in aanraking kunnen komen met koolstofdioxide. Ook dit proces zorgt voor een reductie van de netto opslagcapaciteit.

Het onderzoek eindigt niet optimistisch voor de haalbaarheid van koolstofdioxideopslag in steenkool. Mijn laboratoriumexperimenten laten zien dat steenkool moeilijk toegankelijk zal zijn, en een sterk lagere opslagcapaciteit kent dan aanvankelijk gedacht. Dit wordt uiteindelijk veroorzaakt door de aanwezigheid van spanning. Waarschijnlijk is de enige oplossing voor dit probleem om ergens om de steenkool heen, of in de steenkool, ruimte te creëren voor volumetrische effecten als zwelling en de vorming van microbreukjes. Toekomstig onderzoek zet hierop in, waarbij opnieuw een goede samenwerking tussen bedrijven, onderzoeksorganisaties en de universiteit nodig is. Alleen als het creëren van ruimte succesvol blijkt, dan kan de ondergrondse opslag van koolstofdioxide in steenkool een bijdrage leveren aan het reduceren van broeikasgasconcentraties in de atmosfeer. Een sterke motivatie voor slagen, is dat we bij succes bruikbaar aardgas cadeau krijgen.

Sander Hol
November 2011

Ackowledgements

Ackowledgements

Nature has always fascinated me tremendously, although it took a while to get conscious of that. Of course the nice colours and shapes that nature produces are a feast for the eye, but after many years of learning and learning one starts to appreciate its complex systematics also. Walking a boundary where 'wonder for the beauty of the unknown' lies on one side, and where 'the scientific known' lies on the other, has become almost addictive. Yet, it is this that has brought me to the present result, my thesis. In walking my path, I have been supported by many many people in different ways. All of them have contributed in more or lesser extends to my development. Their criticism has been good for me, their encouragements stimulating. I would like to thank several persons in specific.

I could not have reached this goal without the help of my supervisors **Chris Spiers** and **Colin Peach**. Both played a different role. **Chris**, my promotor, you have shown me how proper science is done. Thank you for that, because you played a major role in turning me from being quite opinionated into a creative scientist. We shared many laughs, irritations and joys. We both felt the liberty to be honest with each other in dealing with issues, which always worked out well. I thank you for the group you have been developing over the years, the Experimental Rock Deformation group. Something special and energetic is in this group, which is a mixture of the positive attitude of its group members, the experience, as well as the good science. I have enjoyed every moment of my work! **Colin**, my co-promotor, I thank you for all the help you gave me with your clear understanding of science and technology. Your knowledge of the techniques we use in the HPT lab has been extremely valuable. You have always given me backup; you are person to count on. That is not only true for the science-aspect of things, but also interpersonally. Thank you!

In my work, I have appreciated the combination of science and societal relevance enormously. This thesis is an example of the fact that such a combination is possible. Investigating the topic of ECBM, and getting involved in applied research, all started with meeting **Frank van Bergen**. Frank, you introduced me into this field of research, and have shared many of your contacts, as well as much of your resources and time, to guide me. You will undoubtedly recognize the development I went through, haha. I thank you sincerely for everything you have done!

The HPT lab, in which I have worked with pleasure every day, has been the domain of great people for all the years that I have been there, all with different characters and specific qualities. On the technical front I like to thank **Peter van Krieken**, **Gert Kastelein** and **Eimert de Graaff** for their support. In the different research chapters several new methods were developed. All of you played a major role in this, be it in using specific modified pressure vessels (Gert), measuring techniques and microscopy (Peter), or electronic equipment (Eimert). Thanks for this! Eimert, I like to highlight your major efforts on the gold capsules and the dilatometer. The development of these techniques has given us often headaches, but the results proved good. Also I like to

thank **Hans de Bresser**. Hans, although you were no official supervisor, you have been there for me in times when science was the topic, but also when understanding was needed from a family man. Much appreciated! I thank **Magda Mathot-Martens**, our group secretary. Magda, you are fantastic for the HPT group, and I mean that. Thanks for all the calmness, accuracy and kindness in you approach. The smoothness you bring into many organizational operations is exceptional. I thank my colleagues **Suzanne** (my paranimf), **Esther**, **Saskia**, **Emilia**, **Reinier**, **André**, **Jon**, **Amir**, **Loes**, **Sabine**, **Tim**, **Sander**, **Anne**, **Sabrina**, **Ken**, **Nawaz**, **Ross**, **Elisenda**, and **Bart**. I had great times in the lab working with you. I also enjoyed the many discussions and laughs we had!

My project was funded by Shell. I the past years I worked closely with **Rick Wentinck**. Rick, thank you for all the nice discussions! Also, being a Shell-coordinator of my project, thanks for the time you have given me to do things scientific, and not by filling tick boxes. That freedom has been very stimulating. I thank all other Shell staff members who have supported me in various ways: **Claus Otto**, **Niels van Wageningen** and **Andreas Busch**.

The department of Earth Sciences is thanked as well for all the years I had the opportunity to work there. **Margot Stoete** and **Ria van der Linden** are thanked for their quick support in the last days before submission of this thesis. I also like to thank the Structural Geology Group members. I would like to thank them for their scientific support, but also for the nice time I had. I particular, I would like to thank **Martyn Drury** and **Gill Pennock** for our collaboration on the coal front, and further **Reinoud**, **Côme** and **Maartje**.

Harry Veld and **Katrin Reimer**, working in the rock characterisation laboratory of TNO, are thanked for answering my many questions. My collaboration with RWTH Aachen was in particular with **Yves Gensterblum** and **Bernd Krooss**. I thank you both for your hospitality and friendship in the past years. We will undoubtedly see each other in the future!

Finally, I like to thank my family. It is difficult to find words that express the support I felt in the past years, but I will give it a try in Dutch. **Kees** en **Marga**, papa en mama, jullie hebben mij heel veel geleerd. Ik heb jullie liefde en steun altijd enorm gevoeld! Bedankt! Ook **Maarten** (mijn paranimf), **Marleen** en **Betty** wil ik bedanken voor alle interesse in mijn werk. **Maartje**, mijn lieve vrouw, je bent er altijd voor mij. We zijn door veel heen gegaan de laatste jaren. De vele keren dat ik in het weekend werkte waren vreselijk, ook de onzekerheid of dat nodig was in de weekenden daarna. Toch bewonder ik onszelf, maar vooral jou, dat we konden genieten van de tijd samen. Bedankt dat je zo geduldig bent gebleven. Ik hou van je! Je bent een prachtvrouw! Als laatste, **Emma**. Je hebt natuurlijk niets van mijn werk begrepen, maar met jou voel ik een sterke band door de liefde voor de natuur. Onder jouw eerste woordjes waren 'buiten', 'zon' en 'vogel'. Je weet heel goed aan te geven wat er in je omgaat. Ik hoop dat jij je ontwikkelt zoals je dat zelf wilt. Bedankt voor de pret van alledag!

CURRICULUM VITAE (education)
SANDER HOL

Date of birth:	26 October 1979
1992-1998:	Secondary education, Bornego College, Heerenveen
1998-1999:	HTS (BSc-level) Bouwkunde, Civiele Techniek en Verkeerskunde, Noordelijke Hogeschool, Leeuwarden (not finished)
1999-2000:	Propaedeutics Earth Sceinces, Utrecht University, Utrecht
2000-2007:	MSc Earth Sciences, specialised in Earth Materials / Experimental Rock Deformation, Utrecht University, Utrecht
2007-2011:	PhD Experimental Rock Deformation, Utrecht University, Utrecht